Orbital forcing and climate response: astronomically-tuned age models and stable isotope records for the Oligocene-Miocene

Helen Beddow-Twigg

Utrecht Studies in Earth Sciences 106

Members of the dissertation committee

Prof. Dr. B.S. Wade
Department of Earth Sciences, University College London
London, United Kingdom

Prof. Dr. H. Pälike
MARUM, Bremen University
Bremen, Germany

Prof. Dr. W. Krigjsman
Department of Earth Sciences, Utrecht University
Utrecht, Netherlands

Prof. Dr. A. Sluijs
Department of Earth Sciences, Utrecht Univesity
Utrecht, Netherlands

Dr. Ann Holbourn
Institute of Geoscience, Kiel University
Kiel, Germany

ISBN 978-90-6266-425-2
Utrecht Studies in Earth Sciences (USES) No. 106

Cover: Jökulsárlón, Iceland. Photo by Janneke van Ginkel, cover design by Margot Stoete (Faculty of Geosciences, Utrecht University)

Printed in the Netherlands by CPI, Zutphen.

Orbital forcing and climate response: astronomically tuned age models and stable isotope records for the Oligocene-Miocene

Orbitaal forcering en klimaat respons: Astronomisch gekalibreerde ouderdomsmodellen en stabiele isotopen reeksen voor het Oligoceen-Mioceen
(met een samenvatting in het Nederlands)

Proefschrift

ter verkrijging van de graad van doctor aan de Universiteit Utrecht op gezag van de rector magnificus, prof.dr. G.J. van der Zwaan, ingevolge het besluit van het college voor promoties in het openbaar te verdedigen op vrijdag 27 mei 2016 des middags te 2.30 uur

door

Helen Mary Beddow-Twigg

geboren op 27 januari 1986 te Londen, Verenigd Koningkrijk

Promotor:

Prof. dr. L.J. Lourens

This research was supported by the Netherlands Organization for Scientific Research (NWO-ALW grant no. 865.10.001)

Contents

Chapter 1:

Introduction, background and aims

"Nothing endures but change"

Heraclitus

1 Introduction, background and aims

1.1 Thesis overview

The primary aim of this thesis is to reconstruct the evolution of the cryosphere, global ocean temperatures and the carbon cycle during the Oligocene-Miocene interval; using high-resolution foraminiferal stable isotope records with accurate chronological control provided by astronomically tuned age models.

The introduction describes the Oligocene-Miocene interval studied and it's climatic context within the Cenozoic, presents the materials and methodologies used to create stable isotope records and astronomically tuned age models and outlines the content of the four central chapters that constitute the main body of work for the thesis.

1.2 Climate evolution during the Oligocene-Miocene

1.2.1 Cenozoic climate evolution

Over the last 65 million years, climate has evolved from a "greenhouse" scenario, with warm global temperatures and no ice sheets at the poles, to an "icehouse scenario", dominated by large continental ice sheets (*Zachos et al.*, 2001) (Fig. 1) Understanding how Cenozoic climate evolved, and untangling the mechanisms operating between the cryosphere, ocean circulation, the carbon cycle and orbital forcing is key to understanding the climate today, something that is becoming increasingly important in light of current anthropogenic climatic change, and its impact on our global society.

In order to predict climatic response to rapidly increasing levels of atmospheric CO_2, and the potential impacts on global temperatures, ocean circulation and the extent of the Antarctic and Greenland ice sheets, we need to understand how these components of Earth's climate interacted and evolved in the past.

Earth's climate changes continuously, as the boundary conditions governing global climate constantly change, on time scales ranging from years to millions of years. On long-term time scales (10^5 to 10^6 year), climatic change is driven by the slow movement of tectonic plates, producing gradual change in the global carbon cycle through rates of weathering and carbon burial, and controlling sea level and ocean circulation patterns through the geographical distribution of the continents. The slow continuous change in boundary conditions has an impact on climate sensitivity, leading to changes in climate response throughout Earth's history. The long-term trend across the Cenozoic has been a shift towards colder temperatures, and an increase in continental ice sheet growth, tectonically driven by the gradual decrease in atmospheric CO_2 levels [*Deconto and Pollard*, 2003; *Houben et al.*, 2012] most likely through increasing weathering rates due to the uplift of the Tibetan plateau [*Raymo et al.,* 1988; *Raymo and Ruddiman*, 1992], and the closure and opening of oceanic gateways, in particular the isolation of Antarctica and subsequent development of the circumpolar current [*Kennett*, 1977; *Barker*, 2001; *Scher and Martin*, 2006]. Modeling studies have indicated that the major factor driving long-term Cenozoic cooling is the steady decrease in atmospheric CO_2 [*Deconto and Pollard*, 2003; *Deconto et al.*, 2008]. From the beginning of the Cenozoic, to pre-industrial levels, atmospheric pCO2 has declined from over

2000 ppm to ~280 ppm [*Pearson,* 2000, 2009; *Pagani*, 2005; *Bijl et al.*, 2010, *Foster et al.*, 2012, *Zhang et al.*, 2013 *Greenop et al.*, 2014]. The timing of the opening of the drake passage leading the isolation of Antarctica and the inception and intensification of the circumpolar current are less well constrained, but were likely open to the extent that the Antarctic circumpolar current (ACC) had developed by the late Eocene [*Livermore et al.*, 2005; *Scher and Martin*, 2006] and the first prominent ice sheets were established on Antarctica at ~34 Ma, at the Eocene-Oligocene boundary [*Shackleton and Kennett*, 1975; *Kennett and Shackleton*, 1976; *Miller et al.*, 1987; 1991; *Zachos et al.*, 1992; *Ivany et al.*, 2006; *Wilson et al.*, 2012].

Superimposed over the long-term Cenozoic trend towards colder global temperatures and the growth of continental ice sheets at both poles are a series of more extreme climatic events and higher frequency near-periodic variations on a range of timescales. Some climate events are extreme and are either transitional and represent climate moving over a threshold into a colder state, or transient aberrations standing out against the long-term global climate mean. Periodic variation oscillating around the global climate mean occurs on time-scales related to orbital cycles, driven by gravitational interactions between other planets and astronomical bodies within the solar system. [*Hays et al.*, 1976].

1.2.2 The Oligocene-Miocene interval

The Oligocene to middle Miocene interval (~34-13 Ma) is bracketed by two major cooling steps in Cenozoic climate evolution; the inception of permanent continental ice sheets on Antarctica

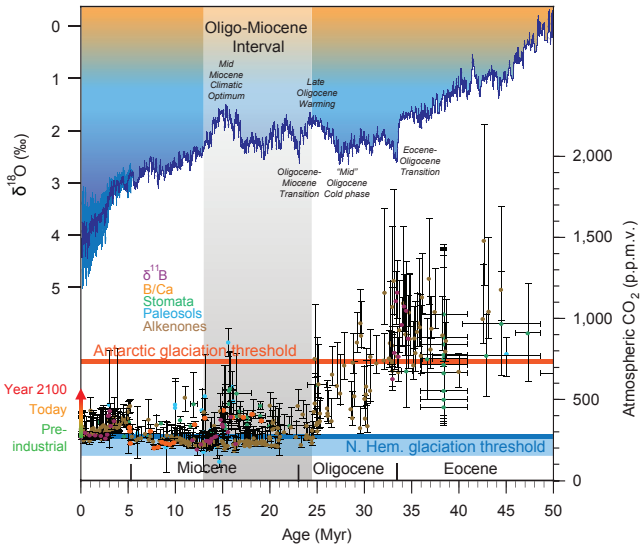

Figure 1.1. *Compilation of benthic $\delta^{18}O$ and atmospheric CO_2 estimates for the Cenozoic. Benthic $\delta^{18}O$ is a global compilation using data from Lisiecki and Raymo [2005] and Zachos et al. [2008]. Carbon dioxide estimates are derived from alkenones, boron isotopes, B/Ca, leaf stomata and paleosols [Ehkart et al., 1999; Kürschner et al., 2008; Beerling et al., 2009; Beerling and Royer, 2011; Pearson et al., 2009; Triparti et al., 2009; Retallack et al., 2009; Foster et al., 2012; Zhang et al., 2013]. The orange line represents an estimated CO_2 threshold for Antarctic glaciation, and the blue line an estimated CO_2 threshold for northern hemisphere glaciation [Deconto et al., 2008]. The grey bar represents the studied interval. This figure is modified from Liebrand, [2015] [unpublished dissertation].*

at the Eocene-Oligocene boundary, and the Middle Miocene Climate Transition (MMCT) at ~14 Ma, a fundamental step in the development of modern cryosphere systems (Fig. 1) [*Kennett and Shackleton, 1976*; *Miller et al*., 1987; *Zachos et al*., 2001; *Coxall and Wilson*, 2011; *Holbourn et al*., 2013, 2014]. Long-term climate follows a general cooling trend towards cooler global temperatures and ice-sheet growth, punctuated by a notable reversal at the Miocene Climatic Optimum (MCO) between 17 and 15 Ma, a 2 Myr shift towards global warmth [*Zachos et al*., 2001; *Holbourn et al*., 2005, 2007, 2013, 2014, 2015]. During the Oligocene-Miocene interval, there is evidence for the presence of ice-sheets in the southern hemisphere [*Ehrmann and Mackensen*, 1992; *Zachos et al*., 1992, 1994; *Flower and Kennett*, 1994; *Ivany et al., 2006*; *Pekar and Deconto*, 2006], although the exact extent and location of ice on Antarctica is not fully constrained [*Wilson and Luyendyk*, 2009]. The Oligocene-Miocene interval is generally interpreted as a unipolar climate system, with limited evidence for the presence of ice in the Northern Hemisphere [*Moran et al*., 2006].

By the Oligocene-Miocene, Antarctica was geographically isolated [*Livermore et al*., 2005; *Scher and Martin*; 2006], but the Central American seaway (CAS) between the two American continents linking the Pacific and the Atlantic did not fully close until the late Miocene [*Molnar*, 2008; *Montes et al*., 2015]. The opening of the drake passage and the development of the ACC had led to the thermal isolation of Antarctica and the build-up of ice sheets beginning at ~34 Ma [*Scher and Martin*; 2006; *Coxall and Wilson*, 2011]. Most of the deep ocean water was supplied by the Southern Ocean, with the development of an additional deep-water source in the North Atlantic possibly beginning in the Eocene [*Katz et al*., 2011; *Hohbein et al*., 2012], but is definitively present in the deep waters of the equatorial Atlantic by the Late Oligocene-early Miocene [*Woodruff and Savin*, 1989; *Billups et al*., 2002; *Pälike et al*., 2006; *Liebrand et al*., 2011].

1.2.3 Major Oligocene-Miocene climate events

1.2.3.1 The OMT

The Oligocene-Miocene transition (OMT) is a large, transient (~200 kyr) cooling event, present in the benthic $\delta^{18}O$ record of ~1‰, inferred as a drop in global deep-sea temperatures, and an increase in ice volume on Antarctica, occurring close to the Oligocene-Miocene boundary [*Woodruff and Savin*, 1989; *Miller et al.,* 1991; *Zachos et al.,* 1997]. The OMT represents a climate shift from relatively warm global temperatures and low amplitude climate variability in the late Oligocene, towards high amplitude, rapid climate variability in the early Miocene reflecting large-scale temperature and ice volume fluctuations [*Shackleton et al*., 2000; *Zachos et al*., 2001; *Billups et al*., 2004; *Pälike et al*., 2006a, 2006b; *Liebrand et al*., 2011; *Holbourn et al*., 2015].

1.2.3.2 The MCO (~15-17 Ma)

The Miocene Climatic Optimum (MCO) is a 2 Myr long period of global warmth in the "ice-house" interval of the Cenozoic, and presents an intriguing reversal in the long-term trend towards cooler conditions and continental ice growth. As one of the most geologically recent intervals of global warmth, potentially driven by an increase of atmospheric CO_2, understanding the MCO is important in the context of current anthropogenic-driven global warming. The most likely driver of global warmth at the MCO is sustained volcanic outgassing leading to elevated pCO_2 levels across the Early to Middle Miocene, triggering climatic warming and subsequent climatic effects [*Foster et al*., 2012; *Zhang et al*., 2013, *Holbourn et al*., 2007; 2015]. Estimates of atmospheric CO_2 do indicate an increase across the MCO, however, these estimates appear to be relatively low, suggesting the presence of a dynamically responding Antarctic ice sheet to account for changes seen

in the $\delta^{18}O$ record [*Kurschner et al.*, 2008; *Foster et al.*, 2012; *Zhang et al.*, 2013]. As one of the most geologically recent intervals of global warmth, potentially driven by an increase of atmospheric CO_2, understanding the MCO is important in the context of current anthropogenic-driven global warming.

1.2.3.3 The MMCT (14.2-18.8 Ma)

The MCO is followed by a general shift towards cooler, more glaciated climate conditions culminating in large cooling step beginning at 14.2 Ma, The Middle Miocene Climatic Transition (MMCT). The MMCT is the second of three major Cenozoic cooling steps across the "greenhouse" to "icehouse" climate transition, associated with a ~1% shift in the $\delta^{18}O$ isotope record and a large expansion of the East Antarctic Ice Sheet (EAIE) at ~13.8-13.9 Ma [*Flower and Kennett*, 1994; *Shevenell et al*, 2004; *Tian et al.*, 2013; 2014]. It represents an important shift towards modern climate conditions, culminating in the eventual inception of northern hemisphere glaciation between ~3.2 and 2.7 Ma [*Maslin et al.*, 1998; *Mudelsee and Raymo*, 2005; *Lisiecki and Raymo*, 2005; *Bailey et al.*, 2013], with the development of major evolutionary steps towards modern flora and fauna [*Zachos et al., 2001*; *Kurschner et al.*, 2008]. Three main mechanisms have been proposed to explain the MMCT; 1) deep ocean circulation changes driven by tectonic processes [*Woodruff and Savin*, 1989; *Hamon et al.*, 2013] 2) the drawdown of atmosphere *p*CO2 across a climate threshold, potentially driven by an increase in burial rates [*Vincent and Berger*, 1985, *Flower and Kennett*, 1993, *Shevenell et al.*, 2004; *Foster et al.*, 2012, *Badger et al.*, 2013; *Zhang et al.*, 2013] 3) changes in insolation driven by favorable orbital configurations for ice-sheet growth [*Shevenell et al.*, 2004, 2008; *Holbourn et al.*, 2013, 2015].

1.2 Ocean sediment cores and stable isotope proxy records

1.2.1 Ocean drilling

Beyond instrumental records, which go back around 130 years, we do not have direct observations of the physical and geochemical characteristics of Earth's climates of the past. In place of direct measurements of climatic conditions, we use preserved physical characteristics of earth's past environment as an indirect proxy measurements of climate information to piece together an approximation of Earth's past climate. Ocean sediments are deposited nearly continuously throughout the Earth's oceans, stretching back millions of years in some places, providing a valuable archive of climate proxy information. Since the formation of Deep Sea Drilling Project (DSDP) in 1967, scientific ocean drilling has been providing access to these deep-sea sedimentary archives, providing invaluable records of past climate information for paleoclimate studies stretching back millions of years [*Pearson,* 2012]. The cores within this thesis have been provided by later generations of the scientific drilling program, the Ocean Drilling Program (ODP) and its current iteration, the Integrated Ocean Drilling Program (IODP). The contribution of ocean drilling to our knowledge of the earth' history has been monumental and provided much of our current understanding about the Cenozoic, the most recent geological epoch.

1.2.2 Stable isotopes as a climate proxy

Carbon ($\delta^{13}C$) and oxygen ($\delta^{18}O$) isotope ratios, measured in biogenic calcite, are one of the oldest established and most widely used methods for tracking the evolution of past climates. The main source of biogenic calcite used to measure carbon and oxygen isotope ratios are foraminiferal shells. Foraminifers are mostly marine microorganisms, which are ubiquitous throughout the Earth's

oceans, both vertically throughout the water column, from the sea surface to several cm below the seafloor, and geographically, from the tropics to the poles. They secrete tests (shells) constructed predominantly of calcite ($CaCO_3$), which float to the sea floor (planktonic) or remain in situ (benthic) when the organisms die and are subsequently preserved in marine sediments. The $\delta^{18}O$ and $\delta^{13}C$ components of the $CaCO_3$ tests reflect the $\delta^{18}O$ and $\delta^{13}C$ values of the seawater they are formed in, meaning that they record environmental information about the properties of seawater they were formed in, at the time they were formed. The original climate signal can be preserved potentially for millions of years, creating a geographically diverse and continuous archive of climate information in sea floor sediments stretching back millions of years. Our present level of knowledge and understanding of paleoclimate change and events during the Cenozoic has relied extensively on foraminiferal $\delta^{18}O$ and $\delta^{13}C$ stable isotope records since measurement techniques were pioneered in the middle of the last century [*Urey*, 1947; *Emilliani*, 1955].

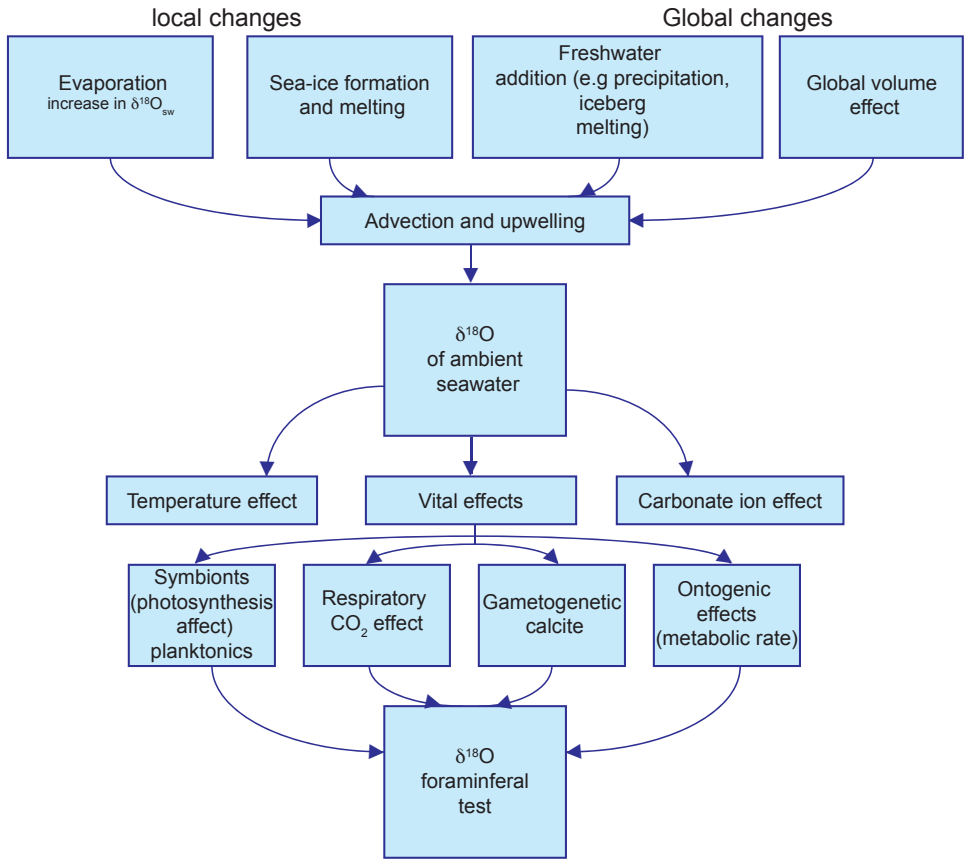

Figure 1.2. *Schematic view of environmental and biological factors determining the $\delta^{18}O$ of foraminifera, adapted from figures in Rohling and Cooke, [1999] and Ravelo and Hillaire-Marcel, [2007].*

1.2.2.1 *Oxygen isotopes*

The oxygen isotopic composition of a foraminiferal test is reflects the oxygen isotopic composition of the surrounding seawater in which it calcifies (Fig. 2). The $\delta^{18}O$ of seawater varies over time, and with geographical distribution. The isotopic composition of the seawater is influenced on a global scale by the extent of ice sheet growth, and on a more local scale by changes in salinity caused by regional changes evaporation and precipitation, the influences of other water masses and upwelling of deeper waters. The $\delta^{18}O$ of the global ocean reflects ice volume changes due to a process known as Raleigh fractionation, where ^{18}O, as the heavier isotope, is preferentially precipitated before ^{16}O, with increasing latitude and altitude, meaning that the ice sheets are depleted ^{18}O. As a result, during glacial periods, the global ocean has relatively enriched $\delta^{18}O$ values. This means that as ice growth increases on the continents, $\delta^{18}O_{sw}$ increases, and when ice melts, $\delta^{18}O_{sw}$ decreases. Foraminifera therefore record the change in ice volume as a component of their $\delta^{18}O$ signal. The oxygen isotopic composition of a foraminiferal test is also dependent on the temperature at which it calcifies. Higher temperatures offset the $\delta^{18}O$ ratio of the foraminifera from the $\delta^{18}O$ of the seawater to lower values, and lower temperatures to higher $\delta^{18}O$ values.

Regional processes relating to evaporation and precipitation rates and the formation of sea-ice also affect $\delta^{18}O_{sw}$. The lighter oxygen isotope, ^{16}O, evaporates preferentially, leaving regions with high levels of evaporation relatively enriched in $\delta^{18}O$. Sea-ice is enriched in $\delta^{18}O$ relative to the surrounding seawater, causing strong seasonal variability as sea-ice forms and melts throughout the year [*Macdonald et al*., 1995; *Rohling and Cooke*, 2001]. The global distribution of $\delta^{18}O_{sw}$ is controlled by the mixing and advection of water masses from different sources, with $\delta^{18}O_{sw}$ values controlled by regional processes such as evaporation precipitation budgets, the influence of freshwater run-off, the formation of sea-ice and upwelling.

To produce an oxygen isotope value, we measure the ratio of the two most common isotopes of oxygen, ^{16}O and ^{18}O, relative to a standard, Vienna Pee Dee Belemite (VPDB) or Vienna Standard Mean Ocean Water (SMOW). The δ values is defined as:

$$\delta sam = \frac{Rsam - Rstd}{Rstd} \times 1000$$

where *sam* is the value of the sample, and *std* is the value of the standard.

1.2.2.2 *Carbon isotopes*

The ratio of carbon isotopes ($\delta^{13}C$) present in biogenic calcite is also widely used in paleoclimate studies to track shifts in the marine carbon cycle, relating to changes in paleo productivity, carbon burial and atmospheric – surface ocean CO_2 exchange (Fig. 3) [*Shackleton*, 1977]. The carbon isotopic composition of foraminiferal shells reflects the amount of dissolved inorganic carbon (DIC) of the seawater in which they calcified, but due to the influence of vital effects caused by biological and kinetic fractionation, they are not in isotopic equilibrium with seawater [*Ravelo and Hillaire-Marcel, 2007*].

The $\delta^{13}C$ of DIC of seawater changes in relation to the global carbon cycle, tracking the partitioning and transfer between different sources and sinks of carbon in the atmosphere, the ocean, the biosphere and ocean sediments. It varies for two main reasons, 1) the distribution and biological cycling of nutrients, and 2) the exchange of CO_2 between the atmosphere and the surface ocean. The distribution and biological cycling of nutrients is the main control on the extent of the biosphere. During photosynthesis, plants preferentially take up the lighter isotope ^{12}C over ^{13}C,

so an increase in the biosphere will remove isotopically light carbon and store it in the biosphere, leading to an enrichment of $\delta^{13}C$ values in the other carbon pools. In the ocean, an increase in nutrient concentrations leads to an increase in productivity and uptake of ^{12}C in the surface waters, which is then released at the sea floor when the marine organisms die, sink to the sea floor and decompose, transferring depleted carbon from the surface waters into the deep ocean. The second important factor that affects the $\delta^{13}C$ of DIC is the preferential uptake of ^{12}C into the atmosphere during atmosphere surface ocean CO_2 exchange, leading to an enrichment of the surface waters in ^{13}C, which alters the $\delta^{13}C$ of DIC.

We measure the ratio of the two most common isotopes of carbon, ^{12}C and ^{13}C, relative to a standard, using the same equation as shown above for the $\delta^{18}O$ values.

1.2.2.3 Foraminiferal stable isotope records

Benthic foraminifera live both on the sea floor and in the first ~20 cm of ocean sediments, and record the isotopic composition of the deep ocean ambient seawater surrounding them [*Pearson*, 2012]. High-resolution benthic stable isotope records have been the primary stratigraphic tool used

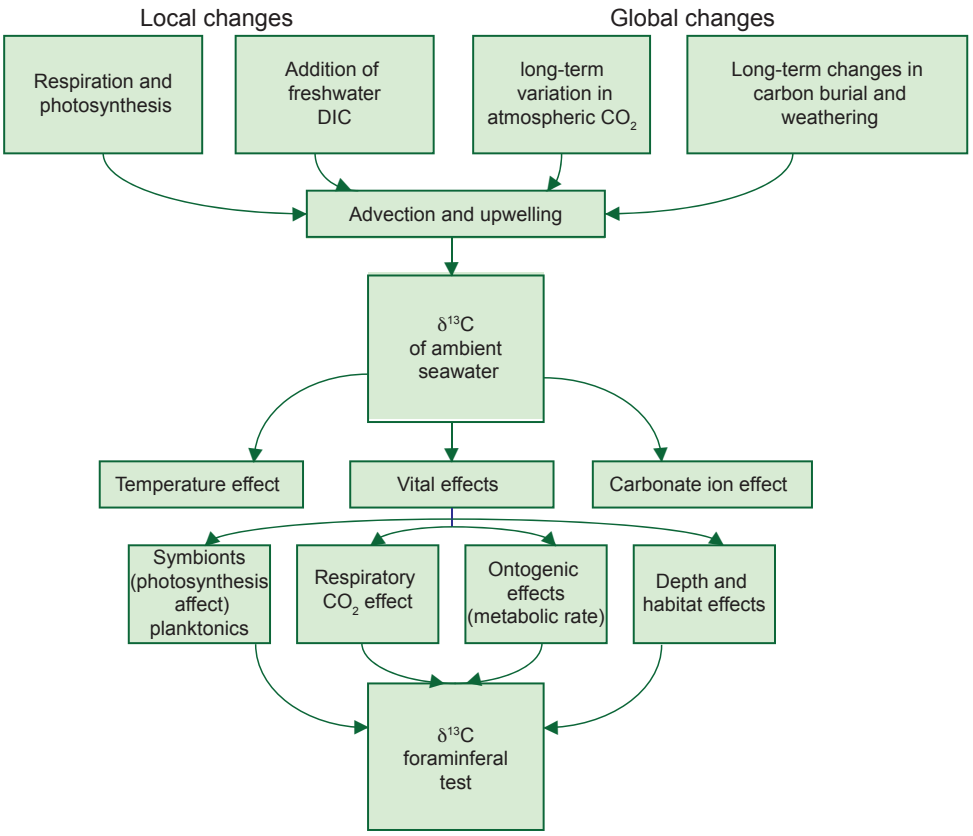

Figure 1.3. *Schematic view of environmental and biological factors determining the $\delta^{13}C$ of foraminifera, adapted from figures in Rohling and Cooke, [1999] and Ravelo and Hillaire-Marcel, [2007].*

to reconstruct past climates in detail and have been fundamental in tracking the temporal evolution of Cenozoic temperature, cryosphere and marine carbon cycle changes.

Planktonic foraminifera live in the surface waters of the ocean at a range of depths in the upper ~500m of the water column, from the sea surface to the lower thermocline, dependent on their ecology and life cycle (*Hemleben et al*., 1989; *Pearson*, 2012; *Friedrich et al*., 2012). This means that planktonic foraminifera live and calcify at a range of temperatures, between 8 and 29° C [*Birch et al*., 2013], from an inter-species level down to the level of an individual foraminifer. Like benthic foraminifera, planktonic foraminiferal stable isotope values are dependent on the isotopic composition of the surrounding seawater, and the temperature at which they calcify. Interpreting stable isotope values derived from planktonic foraminifera is based on the assumption that planktonic foraminifera shells are isotopically similar to the surrounding seawater in which they calcified. For planktonic foraminifera, this means that interpreting the record relies heavily on knowing the depth of the water column in which the foraminifera calcified. If we can infer the depth at a species of planktonic foraminifera calcified, using size fractions to constrain foraminifera to an particular stage of their life cycle, planktonic foraminiferal stable isotope records have the potential to reconstruct the vertical stable isotope gradients present in the water column and track the evolution of sea surface temperatures and the global ice volume signal [*Rohling and Cooke*, 1999].

1.3 Astronomical age models

1.3.1 Orbital variation

There are semi-periodic variations within Earth's orbit around the sun, which occur due to the gravitational effects of the sun, moon, and other planets in the solar system. These orbital variations produce small but significant changes in the seasonal and geographical distribution of insolation, the net amount of solar radiation received at the top of earth's atmosphere. Orbital forcing produces a steady and predictable rhythm in global climate so much so that it has been referred to as the 'pacemaker' or the 'heartbeat' of Earth's climate (*Hays et al*, 1976; *Pälike et al*, 2006b).

Orbital forcing can be divided into three main components – eccentricity, obliquity and precession (Fig. 4) [*Berger*, 1980; *Laskar et al.,* 2004]. Eccentricity describes how much the shape of Earth's orbit around the sun deviates from a perfect circle. The elliptical shape of Earth's orbit controls the length of the seasons. Earth travels faster in its orbit when it is closer to the sun (perihelion) and travels slower when it is further away from the sun (aphelion), which leads to an adjustment in the length of summer and winter and in the amount of insolation received during the seasons. Variability in the eccentricity of the earth occurs at three main periodicities, 405 kyr, 96 kyr and 127 kyr).

Obliquity is defined as the angle between earth's rotational axis and the plane of the Earth's orbit, varying between 22 and 24.5°. Obliquity determines the geographical distribution of solar insolation between the seasons. When obliquity increases, a higher amount of insolation is received in summer, and a lower amount of insolation in winter, and vice versa when obliquity decreases. Obliquity varies with a dominant periodicity of 41 kyr, and secondary periodicities of 54 and 29 kyr.

Climatic precession describes the seasonal timing of aphelion and perihelion, which varies due to the rotation of Earth's rotational axis in combination with the opposite rotation of the Earth's orbit on the orbital plane. Climatic precession varies at dominant periodicities of 23.7, 22.4 and 19 kyr, and its amplitude is modulated by eccentricity.

Together, these three main astronomical components determine the length of the seasons and the geographical and seasonal amount of insolation received across the Earth, producing oscillations in climate on astronomical time-scales, which are recorded in the sedimentary archive.

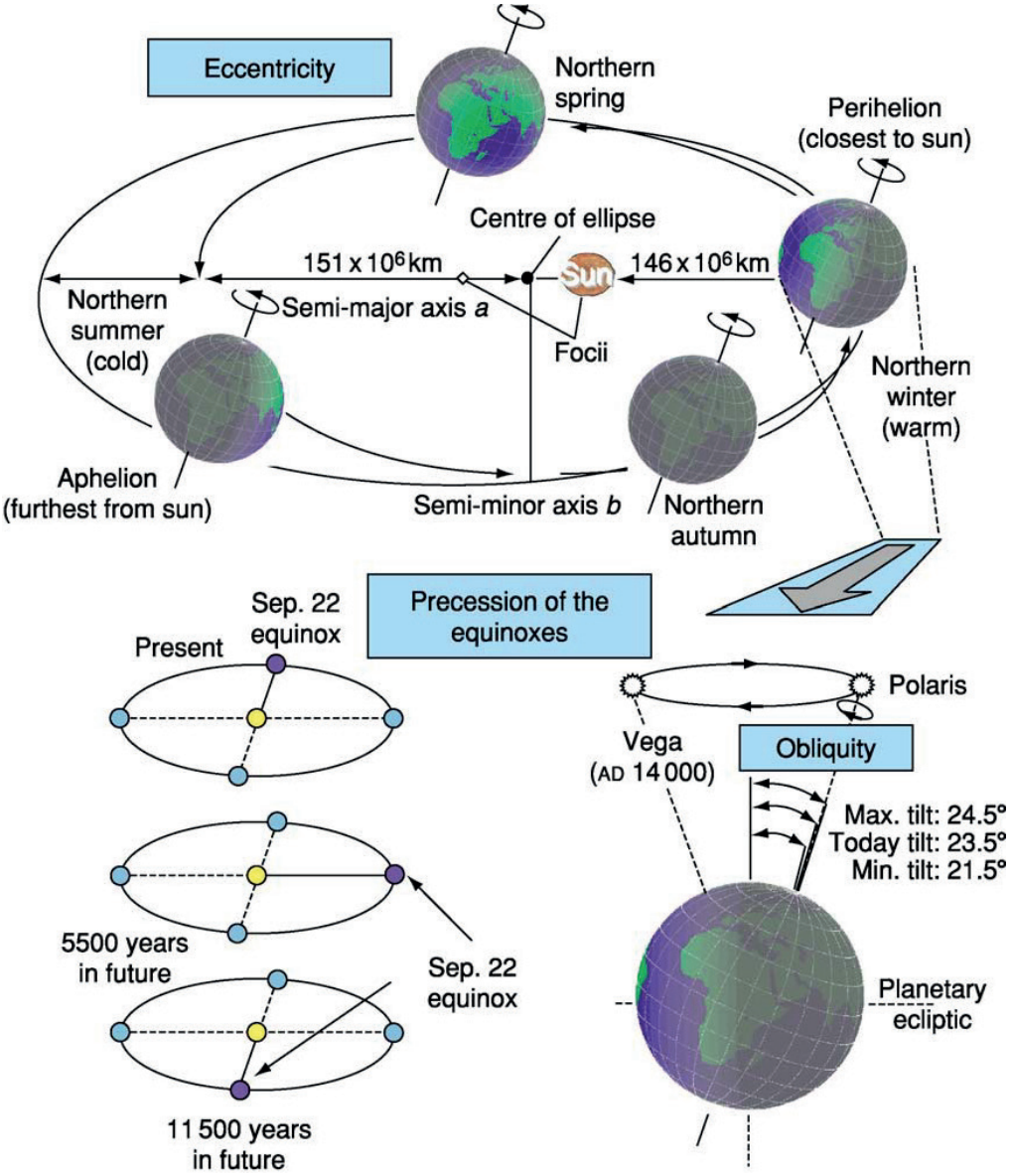

Figure 1.4. *The three main astronomical components of orbital variation. Eccentricity describes the elliptical shape of Earth's orbit; obliquity describes the tilt of Earth's axis with respect to earth's orbital plane and precession describes the seasonal position of the equinoxes. This figure is reproduced directly from Pälike, 2005.*

1.3.2 Astronomically paced climate evolution

Glacial-interglacial cycles exhibit variation at frequencies related to all three components of orbital variation [*Imbrie et al.*, 1984], One of the first astronomical explanation for ice ages was produced by *Croll* [1875] who suggested the ice ages were primarily caused by precession-controlled changes in winter insolation and mathematically linked the ice ages to an astronomical solution by *Le Verrier* [1856]. These early theories were refined by *Milankovitch* [1941], who suggested that the distribution of summer insolation at 65°N is critical to the growth and decline of ice sheets at high latitudes and is controlled primarily by precession. After the landmark paper by *Hays et al.* [1976] 'Milankovitch theory' became widely accepted as the model explaining ice sheet advance and retreat. *Hays et al*, [1976] statistically confirmed the link between global ice volume and orbital variations and opened up the possibility of astronomically forced climate cycles as an independent means of dating. It has now been widely established that climatic variation at astronomical frequencies is present throughout climate proxy records for the Cenozoic and beyond, indicating that orbital forcing played a significant role in global climate evolution [e.g. *Imbrie et al.*, 1984; *Bassinot et al.*, 1994; *Herbert*, 1995; *Zachos et al., 2001; Holbourn et al., 2004; Lisiecki and Raymo, 2005*].

1.3.3 Age models and Astronomical tuning

In order to accurately reconstruct past climates, and to figure out cause and effect in Earth's climate feedback systems, we need precise and accurate time control. Since the link between orbital variation and climate has been confirmed [*Hays et al.*, 1976], research has focused on the potential of isotope stratigraphy as an independent means of dating, in particular when combined with magnetostratigraphic and biostratigraphic measurements from the same site or section [*Shackleton and Opdyke*, 1973; *Hilgen et al.*, 1995; *Krijgsman et al.*, 1999; *Hilgen et al.*, 2000; *Billups et al.*, 2004; *Pälike et al*, 2006b; *Mourik et al.*, 2011]. The application of orbital tuning to paleoclimate data has changed the way geologic time scales can be constructed by allowing unprecedented accuracy, resolution, and stability and completely underpins the Neogene and parts of the Paleogene time scale in *A Geologic Time Scale 2012* (GTS2012) (*Gradstein et al.*, 2012).

To create a time scale for paleoclimate datasets using an astronomical signal, we need to translate a climate proxy signal from the depth domain into the time domain by aligning the stratigraphic climate proxy signal to a target orbital curve. A lithological or geochemical dataset is selected as a tuning signal, and maxima and/or minima aligned to maxima and/or minima in the astronomical curve, based on a either one of or a combination of three main astronomical components; eccentricity, obliquity and precession. The most recent astronomical solution is reliable back to ~ 50 Ma for eccentricity, allowing development of astronomically tuned records well into the Paleogene [*Laskar et al.,* 2011a,b; *Westerhold et al.*, 2015]

1.4 Research objectives and thesis outline

1.4.1 Research objectives

The main research objectives of this thesis are:

- To produce high resolution benthic stable isotope records across the Oligocene-Miocene interval, which resolve climate variability in detail on astronomical timescales. In particular, we focus on reconstructing the evolution of the Antarctic ice sheet and deep-sea temperatures across this interval, resolving small-scale ice sheet expansions/temperature variations at

astronomical periodicities and identifying corresponding shifts in the deep carbon reservoir and their relationship to global climate change.

- To identify the dominant astronomical periodicities present in the sedimentary record during the Oligocene-Miocene interval, and produce astronomically tuned age models, enabling us to accurately quantify rates of change across key climate transitions. Our astronomical timescales have the potential to contribute to the next generation geologic time scale (GTS), in particular for the early Miocene interval between ~16 and 23 Ma, which is based on spreading rates and is not astronomically calibrated in the current iteration, GTS2012 [*Hilgen et al*., 2012]

- To produce the first planktonic foraminiferal stable isotope record for the OMT interval, recreating vertical carbon and oxygen gradients in the Pacific and allowing investigation of astronomical periodicities present in the thermocline and surface waters.

1.4.1.1 Thesis Outline

We bring together benthic and planktonic high-resolution foraminiferal stable isotope records from the Atlantic and the Pacific, covering the time period 24.2 Ma – 13.24 Ma, capturing major Cenozoic climate events and transitions at the OMT, the MCO and the MMCT. We compare these records to pre-existing high-resolution stable isotope records from the Atlantic, Pacific and Southern oceans, providing new insights into the onset and amplitude of astronomically paced variability and climatic events between the Pacific and Atlantic basins and contributing towards the development of a more geographically representative global climate record.

The four central chapters that constitute the main body of work for this thesis are outlined below:

In **chapter two**, we present a high-resolution (3.6 kyr) benthic stable isotope record from IODP site U1334, in the equatorial pacific. The data are presented on a magenetostratigraphic age model, in order to assess the astronomical periodicities present in the dataset without introducing spectral power by tuning. We compare our data with data from four other high-resolution stable isotope records from the Pacific and the Atlantic basins. We align the data in the depth domain, and place all datasets on the magenetostratigraphic age model, creating a benthic Oligocene-Miocene stacked record.

This chapter has been published as: *Beddow, H. M., D. Liebrand, A. Sluijs, B. S. Wade, and L. J. Lourens* (2016), Global change across the Oligocene-Miocene transition: High-resolution stable isotope records from IODP Site U1334 (equatorial Pacific Ocean), *Paleoceanography*, *31*, doi:*10.1002/2015PA002820*.

In **Chapter three**, we present two independent astronomically tuned age models for IODP site U1334. The age models are created using $CaCO_3$ est (%) as a tuning signal for our first age model option, and $\delta^{13}C$ as a tuning signal for our second age model option. We discuss the implications of assumptions we make when constructing age models and assess the astronomical periodicities and spectral power present in the datasets within each age model. We use spreading rates as an independent check on our age models, and find that the $CaCO_3$ tuned age model is more consistent with an assumption of constant or constantly changing spreading rates.

In **Chapter four**, we produce the first high-resolution planktonic stable isotope record for IODP site U1334, across the OMT interval from 21.96-24.15 Ma. We compare our planktonic record with the benthic record produced in chapter one, on the age model created in chapter two, and discuss the evolution of pacific surface-deep water gradients. We find expansions in thermocline

– deep water gradients are paced by ~110 kyr eccentricity cycles, suggesting an increase in export productivity during glacial maxima during cooler, glaciated climate conditions.

In **Chapter five**, we present a high-resolution, astronomically tuned benthic foraminiferal stable isotope record for ODP site 1264, in the south-east Atlantic, from 13.24 – 18.9 Ma, covering the MCO and MMCT. We find a negative shift in the $\delta^{18}O$ record indicating a warming/deglaciation on Antarctica at ~17.1 Ma (the MCO), and a positive shift indicating rapid cooling/glaciation of Antarctica at ~13.8 Ma (the MMCT). Throughout this interval we find high-amplitude (~1‰) variability on 405 kyr and ~110 kyr astronomical time-scales. Together with other records from this time interval located in the Pacific, which show similar features, the data strongly suggests a highly dynamic global climate system during the early to middle Miocene.

Chapter 2:

Global change across the Oligocene-Miocene Transition: high-resolution stable isotope records from IODP Site U1334 (equatorial Pacific Ocean).

Abstract

The Oligocene-Miocene Transition (OMT) (~23 Ma) is interpreted as a transient global cooling event, associated with a large-scale Antarctic ice sheet expansion. Here, we present a 2.23 Myr long high-resolution (~3 kyr) benthic foraminiferal oxygen and carbon isotope ($\delta^{18}O$ and $\delta^{13}C$) record from Integrated Ocean Drilling Program Site U1334 (eastern equatorial Pacific Ocean), covering the interval from 21.91 to 24.14 Ma. To date, five other high-resolution benthic foraminiferal stable isotope stratigraphies across this time-interval have been published, showing a ~1‰ increase in benthic foraminiferal $\delta^{18}O$ across the OMT. However, these records are still few and spatially limited and no clear understanding exists of the global versus local imprints. We show that trends and the amplitudes of change are similar at Site U1334 as in other high-resolution stable isotope records, suggesting that these represent global deep-water signals. We create a benthic foraminiferal stable isotope stack across the OMT by combining Site U1334 with records from ODP Sites 926, 929, 1090, 1264 and 1218 to best approximate the global signal. We find that isotopic gradients between sites indicate inter- and intra-basinal variability in deep-water masses, and in particular note an offset between the equatorial Atlantic and the equatorial Pacific, suggesting that a distinct temperature gradient was present during the OMT between these deep water masses at low latitudes. A convergence in the $\delta^{18}O$ values between infaunal and epifaunal species occurs between 22.8 and 23.2 Ma, associated with the maximum $\delta^{18}O$ excursion at the OMT, suggesting climatic changes associated with the OMT had an effect on interspecies offsets of benthic foraminifera. Our data indicates a maximum glacioeustatic sea level change of ~50 m across the OMT.

2.1 Introduction

The Oligocene-Miocene Transition (OMT; ~23 Ma) is characterised by a ~1 ‰ positive excursion in marine benthic foraminiferal $\delta^{18}O$ records. This $\delta^{18}O$ increase is inferred as a large-scale, rapid expansion in ice volume on Antarctica, and an accompanied drop in high-latitude and deep ocean temperatures [*Woodruff and Savin*, 1989; *Miller et al.,* 1991; *Zachos et al.,* 1997]. Across the OMT, the benthic $\delta^{18}O$ record shifts from relatively low amplitude climate variability in the late Oligocene, towards high amplitude, rapid climate variability in the early Miocene [*Zachos et al*., 2001; *Billups et al*., 2004; *Pälike et al*., 2006a, 2006b; *Liebrand et al*., 2011; *Holbourn et al*., 2015]. The late Oligocene interval is interpreted as a time of relatively warm global temperatures and low Antarctic ice volume, whereas the early Miocene record is thought to reflect large-scale temperature and ice volume fluctuations [e.g., *Miller et al*., 1991; *Zachos et al*., 2001, *Shevenell and Kennet*, 2007; *Mawbey and Lear*, 2013].

Stable isotope records across the OMT come primarily from Ocean Drilling Program (ODP) sites located in the Atlantic Ocean, whereas the Pacific Ocean is comparatively understudied. While the benthic foraminiferal stable isotope record from Pacific Ocean Site 1218 provided detailed time control of the entire Oligocene, it is less evenly sampled and of lower-resolution after the OMT [*Lear et al*., 2004; *Pälike et al*., 2006b]. The Pacific Ocean plays a dominant role in the global transport of heat and salt and represents the largest reservoir of carbon in the exogenic carbon pool strongly influencing the global carbon cycle, predominantly through regionally high primary productivity

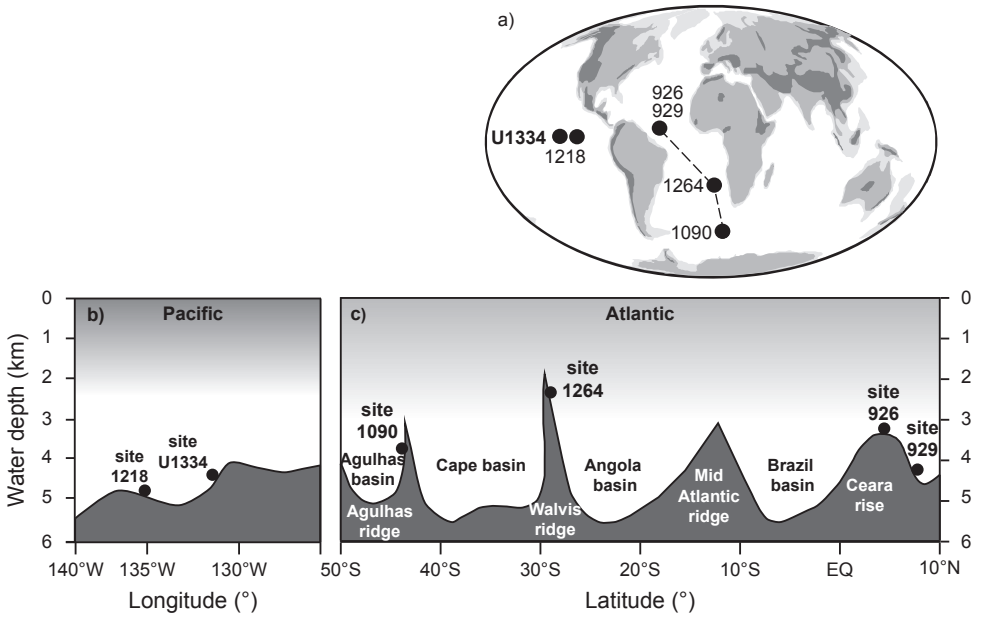

Figure 2.1. *(a) Location of IODP Site U1334 with reference to ODP Sites 1264, 1218, 926, 929 and 1090. Schematic transects indicating location and depth of sites included within this study through b) the eastern equatorial Pacific and c) the current equatorial and southern Atlantic Ocean. Black dots indicate drill locations. Transects were constructed using ocean data view [Schlitzer, 2010, adapted from Liebrand et al, 2011]*

[*Lyle et al.*, 2008]. The Integrated Ocean Drilling Program (IODP) revisited the equatorial Pacific during the Pacific Equatorial Age Transect (PEAT) Expeditions 320/321 to broaden current understanding of Cenozoic climate and carbon cycle history [*Lyle et al.*, 2010]. Here, we present a 2.3 Myr high-resolution (3 kyr) benthic foraminiferal stable isotope record from IODP Site U1334, covering the interval 21.91-24.14 Ma, providing a fresh opportunity to study the OMT in the Pacific Ocean, and to compare it on both an intra-basin scale, to Site 1218, and inter-basin scale, to sites from the Atlantic Ocean [*Zachos et al.*, 2001; *Billups et al.*, 2004; *Pälike et al.*, 2006a, b; *Liebrand et al.*, 2011]. A well-defined magnetostratigraphy is available for Site U1334 [*Channell et al.*, 2013], which forms the basis of our untuned age model used to evaluate climatic change across the OMT.

2.2 Site description

The main objective of PEAT Expeditions 320 and 321 was to recover sediments deposited across the equatorial zone from 56 Ma-present for the purpose of creating a continuous Pacific 'Megasplice', allowing for focus in high-resolution on critical intervals of Cenozoic climatic change [*Pälike et al.*, 2010]. A shallow Paleogene calcite compensation depth (CCD) has made obtaining well-preserved carbonate sediments during this stratigraphic interval challenging, however IODP Expedition 320 recovered a unique sedimentary archive encompassing most major Cenozoic glaciations, including the OMT. Pelagic clays, nannofossil oozes and nannofossil chalks of early Miocene to late middle Eocene age, deposited on ~38 Ma-old oceanic crust, were recovered from three holes drilled at IODP Site U1334 (7°59.998`N, 131°58.408`W), which is situated 4794 meters below sea level (mbsl). Oligocene to Miocene sediments at Site U1334 are primarily made up of nannofossil ooze and chalk [*Pälike et al.*, 2010]. The site is estimated to have been positioned at ~4200 meters water depth during the OMT, ~500 m above the CCD [*Pälike et al.*, 2010; *Pälike et al.*, 2012]. Within this study, we analyze a section of Site U1334 stretching from 77.74 CSF in hole A (core depth below sea floor, equivalent to meters below sea floor or mbsf) to 104.17 CSF in hole B. On the revised splice of Site U1334 [*Westerhold et al.*, 2012], this section runs from 88.93 CCSF-A (core composite depth below seafloor) (U1334A-9H-3) to 121.29 CCSF-A (U1334B-11H-5). Shipboard data indicate $CaCO_3$ concentrations are consistently high within this section, ranging from 74-95 wt % [*Pälike et al.*, 2010].

Sites selected for global comparison within this study, with the exception of Site 1218, are located in or near the Atlantic Ocean forming a geographic distribution from the Atlantic sector of the Southern Ocean to the equatorial Atlantic (Fig. 1). We compare the composite record from Site U1334 with data from ODP Sites 926 (Hole B, 3598 mbsl) and ODP Site 929 (Hole A, 4358 mbsl), drilled at Ceara Rise in the equatorial western Atlantic [*Zachos et al.*, 2001; *Pälike et al.*, 2006a], ODP Site 1090 (composite of Holes D and E, 3699 mbsl) from the Agulhas Ridge in the Atlantic sector of the Southern Ocean [*Billups et al.*, 2004] and ODP Site 1264 (composite of Holes A and B, 2505 mbsl), from the Walvis Ridge in the south-eastern Atlantic Ocean [*Liebrand et al.*, 2011]. For a regional equatorial Pacific comparison, we compare our results from Site U1334 with those obtained from ODP Site 1218 (composite of Holes A, B and C, 4827 mbsl) [*Lear et al.*, 2004; *Pälike et al.*, 2006b], located ~370 km southeast of Site U1334, 28 mbsl deeper than Site U1334 (Fig. 1).

2.3 Methods

The revised splice of Site U1334 [*Westerhold et al.*, 2012] was followed during sampling. Samples of approximately 7.5 cm^3 (quarter-core 1 cm slices) of sediment at 4 cm intervals were taken from 88.93 to 121.29 CCSF-A, covering the complete OMT interval. The samples were freeze-dried, washed over 38 µm, 63 µm and 150 µm sieves, and oven-dried at 40ºC. Weights were recorded before and after all sample-processing steps. Samples were dry-sieved and two benthic foraminifera species, *Cibicidoides mundulus* and *Oridorsalis umbonatus,* were picked from the 250-355 µm size fraction to avoid juvenile specimens with potentially different isotopic compositions, resulting from variability in vital effects between specimens of different age [*Schmiedl et al*, 2004]. Between 1 and 6 foraminifera were picked, crushed to obtain a homogeneous sub-sample and ultrasonically cleaned for two seconds while suspended in ethanol. Excess ethanol was pipetted out and the samples dried overnight at 40°C.

Stable isotope analyses were conducted at the Faculty of Geosciences, Utrecht University, using a Thermo-Finnigan Kiel III automated preparation system coupled to a Thermo-Finnigan MAT 253 mass spectrometer. The standard NBS-19 and an in-house marble standard "Naxos" were used to calibrate isotope values to Vienna Pee Dee Belemnite (VPDB). Analytical precision is 0.03 ‰ and 0.08 ‰ for $\delta^{13}C$ and $\delta^{18}O$, respectively. The standard error derived from running replicate analyses of the samples (15% of the dataset) is 0.32 ‰ and 0.33 ‰ (Fig S3, Supporting Information). The standard error from the correction factor between the two species is 0.52 ‰ and 0.45 ‰ for $\delta^{13}C$ and $\delta^{18}O$ respectively. Minimal removal of outliers was performed by eye from both stable isotope data sets; 8 values were removed from the *C. mundulus* dataset and 13 from the *O. umbonatus* dataset (Fig S2, Supporting Information).

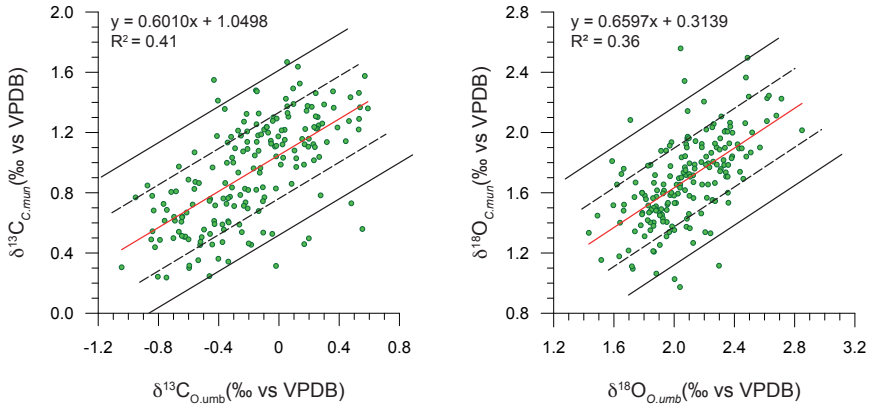

Figure 2.2. *Paired isotope analyses of Cibicidoides mundulus and Oridorsalis umbonatus (n=187). The ordinary least squares regression line is based on the entire data set. The green data points represent data from Site U1334 (this study). The dashed black lines represent 1σ standard deviation (99%), the solid black lines represent 2σ standard deviation (95%).*

2.4 Results

2.4.1 Interspecies comparison

Oligocene-Miocene foraminifera present at Site U1334 have moderate to good preservation [*Pälike et al.*, 2010; *Edgar et al.*, 2013]. *Cibicidoides mundulus* is present in most samples and is measured within this study as the main species, however in some samples *C. mundulus* is scarce or even absent. The scarcity is most likely a result of the quarter-core sample size and/or reflects overall low epifaunal foraminiferal abundances. Owing to the scarcity of *C. mundulus* we use *Oridorsalis umbonatus* to fill gaps in our *C. mundulus* record and obtain a high-resolution record. Specimens of *O. umbonatus* are ubiquitous at Site U1334 throughout the Oligocene-Miocene interval and are also used in other high-resolution stable isotope records across the OMT [*Billups et al.*, 2004].

We compare pairs of *O. umbonatus* and *C. mundulus* stable isotope values from 187 samples to calculate interspecies offsets across the OMT using an ordinary least squares linear regression (Fig. 2). This linear regression implies correction factors of *C. mundulus* = (0.60 x *O. umbonatus*) + 1.05 (± 0.10) and *C. mundulus* = (0.66 x *O. umbonatus*) + 0.31 (± 0.12) with R^2 values of 0.41 and 0.36 for $\delta^{13}C$ and $\delta^{18}O$ respectively. Spearman's rank correlation of the relationship between *C. mundulus* and *O. umbonatus* values from the same sample show a statistically significant relationship (> 99%), yielding a coefficient of $\rho = 0.65$ for the $\delta^{13}C$ values, and $\rho = 0.63$ for the $\delta^{18}O$ values. The 95% confidence interval on the slope of the regression line is ± 0.71 and ± 0.79 for $\delta^{13}C$ and $\delta^{18}O$ respectively. The sign of the corrections applied to *O. umbonatus* values is in agreement with previous estimates [*Shackleton et al.*, 1984; *Katz et al.*, 2003; *Billups et al.*, 2004 *Coxall and Wilson*, 2011] (Table 1, see also Figs S4 and S6, Supporting Information).

After correcting for the offset between the two species, we obtain benthic foraminiferal $\delta^{13}C$ and $\delta^{18}O$ composite records for Site U1334 (Fig. 3). Although the correlation coefficients between the individual *O. umbonatus* and *C. mundulus* records are low, the offset between *C. mundulus* and *O. umbonatus* appears to be fairly consistent in the depth domain during the late Oligocene and early Miocene, with *O. umbonatus* values on average 0.5 ‰ higher in $\delta^{18}O$ and 1.1 ‰ lower in the $\delta^{13}C$ than the *C. mundulus* values. The *C. mundulus* $\delta^{18}O$ values, however, indicate a greater range of variability (0.97-2.71 ‰), compared to the corrected *O. umbonatus* $\delta^{18}O$ values (0.90-2.23 ‰). From ~101 to ~107 CCSF-A, in the $\delta^{18}O$ record, the offset between the two species is reduced to on average 0.4 ‰, as *C. mundulus* values shift towards higher $\delta^{18}O$ values with a greater amplitude than the corresponding *O. umbonatus* values (Fig. 3 and 4).

To assess the validity of applying the correction factor shown in Fig. 2, we performed a sensitivity study to see how robust the record is, and how much trends and variability within the record are affected by potential error introduced by using the correction factor. We applied previously reported correction factors [*Shackleton et al.*, 1984; *Katz et al.*, 2003; *Billups et al.*, 2004; *Coxall and Wilson*, 2011] to the *O. umbonatus* values from Site U1334, resulting in *O. umbonatus* values with a variability of 0.58 ‰ for $\delta^{13}C$ and 0.28 ‰ for $\delta^{18}O$. Wavelet analyses on the subsequent records showed virtually identical results, indicating that periodicities of change within the record (and their relative amplitudes with respect to each other) are not sensitive to the correction factor used (Fig S4, S5, S6 and S7 Supporting Information).

2.4.2 Age model

Site U1334 provides a complete magnetostratigraphy for the OMT interval (Fig. 3 and 5) [*Channell et al.*, 2013]. By assigning the most recent GTS2012 [*Hilgen et al.*, 2012; *Vandenberghe et al.*, 2012] polarity chron ages to the magnetic reversals at Site U1334, we fit a third order polynomial

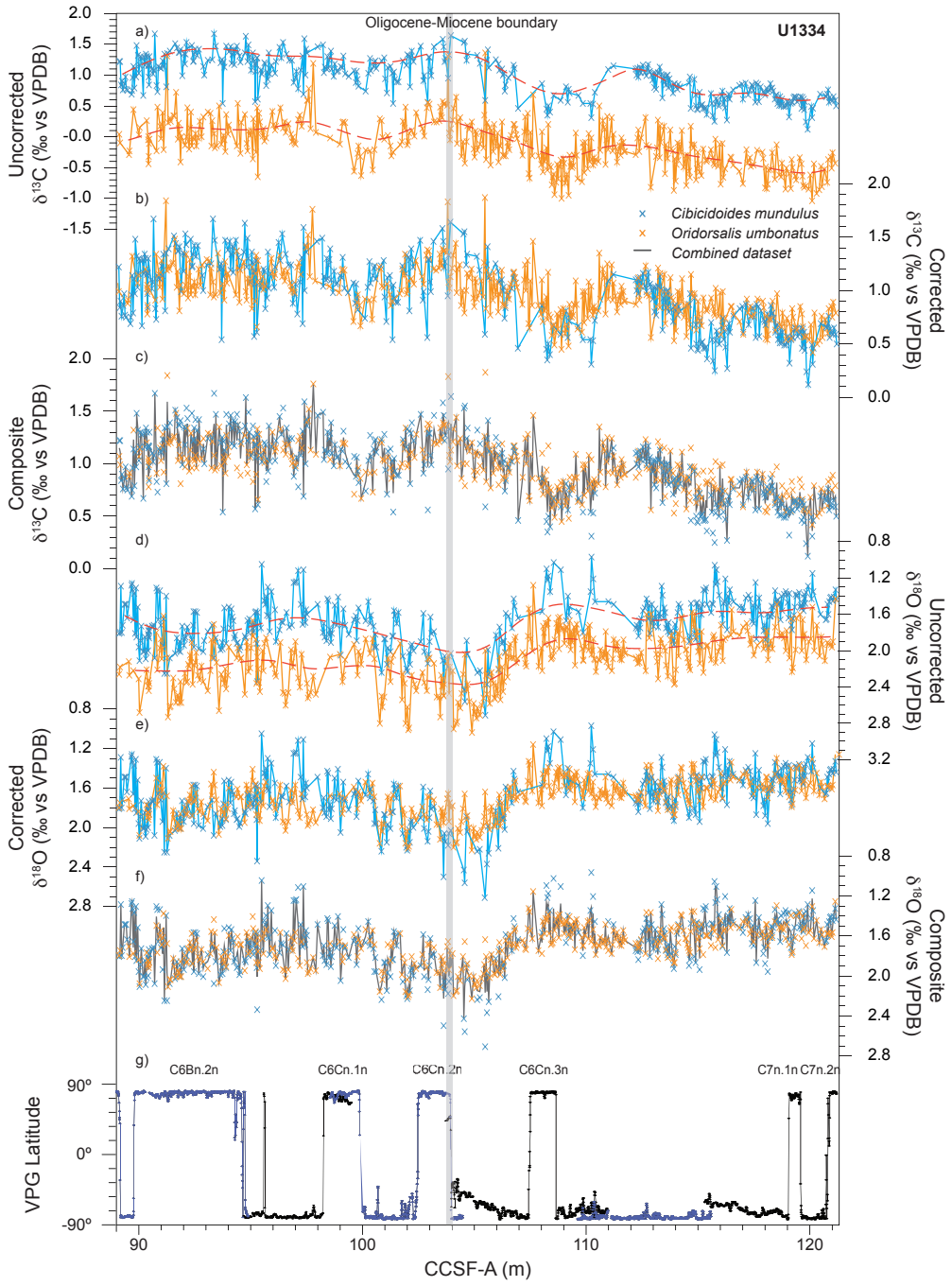
Oligocene-Miocene boundary
U1334
a)
b)
c)
d)
e)
f)
g)
Cibicidoides mundulus
Oridorsalis umbonatus
Combined dataset
Uncorrected δ13C (‰ vs VPDB)
Corrected δ13C (‰ vs VPDB)
Composite δ13C (‰ vs VPDB)
Uncorrected δ18O (‰ vs VPDB)
Corrected δ18O (‰ vs VPDB)
Composite δ18O (‰ vs VPDB)
VPG Latitude
C6Bn.2n
C6Cn.1n
C6Cn.2n
C6Cn.3n
C7n.1n
C7n.2n
CCSF-A (m)

to the 14 depth-to-age magnetostratigraphic tie-points, which results in a near-linear depth-to-age conversion (Fig. 5). The average sedimentation rate is 14.5 m/Myr, with a maximum rate of 15.2 m/Myr and a minimum rate of 12.8 m/Myr. By fitting a 3rd order polynomial through the GTS2012 polarity ages, we prevent the introduction of spectral power on higher astronomical frequencies (i.e. >10 cycles/Myr), although it should be taken into consideration that the GPTS2012 does consider astronomically tuned ages [*Billups et al.*, 2004; *Pälike et al.*, 2006a] for their age calculations of the paleomagnetic reversals [*Hilgen et al.*, 2012; *Vandenberghe et al.*, 2012]. On the magnetostratigraphic age model, our stable isotope records cover the interval 21.91-24.14 Ma with a mean sample resolution of 3.6 kyr (Fig. 5).

2.4.3 Stable oxygen and carbon isotope composite records

Within this study, we have chosen to focus on the composite high-resolution two-species dataset from Site U1334 (Fig. 3), in order to identify and compare trends and patterns present in the Site U1334 dataset with other high-resolution stable isotope records across the OMT. Following removal of outliers, the complete record contains 614 values, of which 200 values are *C. mundulus* values, 227 are *O. umbonatus* values corrected to *C. mundulus*, and 187 are values derived from correcting *O. umbonatus* to *C. mundulus*, and then taking an average between the corrected *O. umbonatus* and the *C. mundulus* values. The record using values averaged between the corrected *O. umbonatus* values and *C. mundulus* values has a higher signal to noise ratio than the record constructed using *C. mundulus* values preferentially, with corrected *O. umbonatus* values only present in the dataset where no *C. mundulus* data are available. Several peaks in the *C. mundulus* record are not replicated in the *O. umbonatus* record, in particular across the transition. The aim of this paper is to discuss the trends and patterns between records, so we have chosen to use the dataset with values averaged between both species for samples where both values are present.

The most prominent feature in the composite stable isotope records is the large positive excursion in the $\delta^{18}O$ dataset, beginning with a steep shift towards more positive values at 23.2 Ma (107.3 CCSF-A) followed by peak positive values (2.43 ‰) occurring at 23.03 Ma (104.5 CCSF-A) (Figs. 3 and 5). We identify the prominent shift and subsequent recovery as the inception and termination of the OMT. The OMT divides the record into two distinct phases; a period of lower $\delta^{18}O$ and $\delta^{13}C$ values with low amplitude variability (~0.5 ‰ and ~0.4 ‰ for $\delta^{18}O$ and $\delta^{13}C$ respectively) prior to the excursion, from 23.03 -24.14 Ma (~ 107.3 to 121.3 CCSF-A), and a shift towards more positive values and rapid, high amplitude variability (~1.0 ‰ and ~0.6 ‰ for $\delta^{18}O$ and $\delta^{13}C$ respectively) after the excursion from 21.91-22.9 Ma (~ 88.9 -102.6 CCSF-A). Variability in the $\delta^{13}C$ record is noticeably smaller (between 0.1 and 0.4 ‰) than in the $\delta^{18}O$ record [*Zachos et al.*, 2001; *Pälike et al.*, 2006a].

Figure 2.3. *Site U1334 benthic foraminiferal stable isotope records on the CCSF-A depth scale based on the splice by Westerhold et al. [2012]. Shown are Cibicidoides mundulus and uncorrected Oridorsalis umbonatus $\delta^{13}C$ records (Red dashed lines indicate long-term SiZer smooths) (a), C. mundulus and corrected O. umbonatus $\delta^{13}C$ records, based on the correction factor shown above in Fig. 2 (b) the combined composite $\delta^{13}C$ record used within this study (c), Cibicidoides mundulus and uncorrected Oridorsalis umbonatus $\delta^{18}O$ records (d), C. mundulus and corrected O. umbonatus $\delta^{18}O$ records, based on the correction factor shown above in Fig. 2 (e), and the combined composite $\delta^{18}O$ record used within this study. Blue crosses indicate C. mundulus values, orange crosses O. umbonatus values. Site U1334 VPG latitudes (g) have been previously published by Channell et al. [2013]. Alternate holes are coloured blue/black in the VPG latitude plot.*

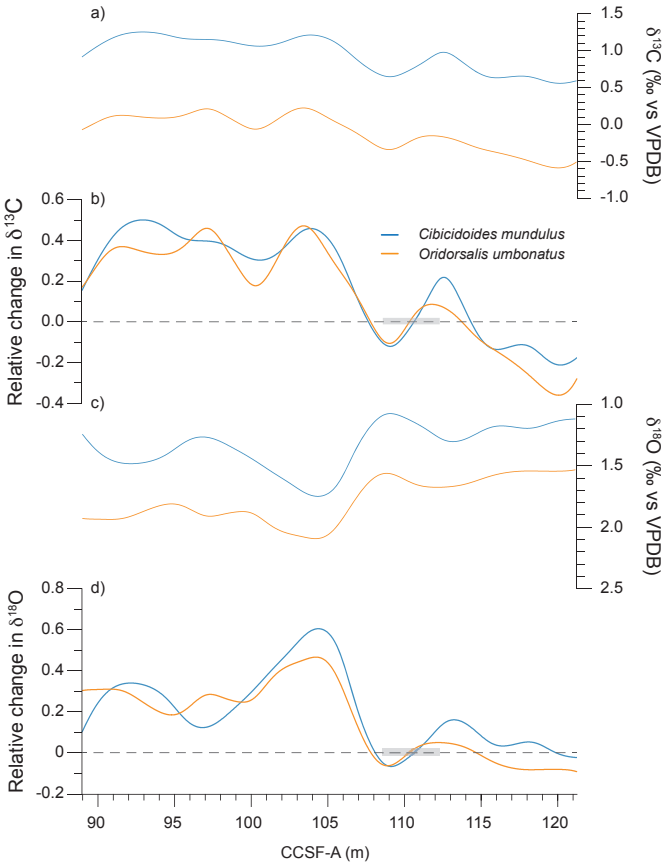

Figure 2.4. *Statistically smoothed Cibicidoides mundulus and uncorrected Oridorsalis umbonatus $\delta^{13}C$ datasets created using SiZer indicating the long-term (>250 kyr) trend (a). Relative change in Site U1334 Cibicidoides mundulus and uncorrected Oridorsalis umbonatus $\delta^{13}C$ datasets (b) based on the long-term SiZer smooths, calculated using a baseline average determined between 108.70 and 112.20 CCSF-A (grey shaded box). Statistically smoothed Cibicidoides mundulus and uncorrected Oridorsalis umbonatus $\delta^{18}O$ datasets created using SiZer indicating the long-term (>250 kyr) trend (c). Relative change in Site U1334 Cibicidoides mundulus and uncorrected Oridorsalis umbonatus $\delta^{18}O$ datasets (d) based on the long-term SiZer smooths, using a baseline average determined between 108.70 and 112.20 CCSF-A (grey shaded box).*

2.4.4 Time series analysis

The benthic foraminiferal $\delta^{13}C$ and $\delta^{18}O$ time series both exhibit amplitude variability on astronomical frequencies (Fig. 6). To illustrate the evolution of astronomical cyclicity through time, we convert our time series into the time-frequency domain using wavelet analyses [*Torrence & Compo*, 1998] (Fig. 6). Prior to analysis, the data were linearly detrended, resampled at a 5 kyr time-step and long-term trends (periods longer than 600 kyr) were removed using a Gaussian notch filter, with version 2 of the software package AnalySeries [*Paillard et al.*, 1996]. In addition, we calculate a 'family of smooths" on our isotope chronology using a space-scale statistical programme SiZer (Significant Zero crossing of derivatives) [*Chaudhuri and Marron*, 1999], to quantify features in the dataset that stand out above the background noise. Of the 41 smooths calculated by SiZer we

have selected the 31st and the 24th smooths as they resolve variability on ~100 kyr and >400 kyr timescales, respectively. We will refer to these from this point on in the text as the short-term smooth and long-term smooth. The first set is used to better resolve the orbital components of the records (Fig. 6 solid blue line) whereas the second set is used to track climate variability on long-term (>400 kyr) timescales (Fig. 6 dashed red line).

Our wavelet analyses show that both isotope records are paced by the long (400 kyr) and short (95-125 kyr) periods of eccentricity, with intervals of obliquity (41 kyr) paced variability (Fig. 6). Prior to the inception of the OMT glaciation, long period eccentricity variability is prominent, particularly in the $\delta^{13}C$ record, with amplitude variability of 0.4 to 0.8 ‰. After the termination, both $\delta^{18}O$ and $\delta^{13}C$ exhibit increased amplitude variability with typical amplitudes of 0.5 to 1.0 ‰ on short-term eccentricity frequencies (95-125 kyrs). Significant ~100 kyr and 41 kyr power increases during the OMT and into the early Miocene in both datasets, whereas the 41 kyr signal appears in the wavelet spectrum when the ~100 kyr signal present in the dataset is weakest (Fig. 6).

2.4.5 Global benthic stacked records for $\delta^{13}C$ and $\delta^{18}O$ across the OMT

To create the best approximation of the global isotope signals, we align our data in the depth domain with existing high-resolution benthic foraminiferal stable isotope records from ODP Sites 926, 929, 1090, 1218 and 1264 [*Zachos et al.*, 2001; *Billups et al.*, 2004; *Pälike et al.*, 2006a; *Pälike et al.*, 2006b; *Liebrand et al.*, 2011] and create a benthic stack across the OMT. We first correlate the records in the depth-domain to Site U1334 using a minimal number of manually selected correlation points and subsequent automated alignment through the application of the Match software package [*Lisiecki and Lisiecki*, 2002] (Supporting Information). In addition, we utilised an existing correlation of physical property data from the Pacific Sites 1218 and U1334 [*Westerhold et al.*, 2012]. After all records have been placed on the Site U1334 CCSF-A depth scale, we assigned the ages of our magnetostratigraphic age model to all records. The resulting time series for each site allows the comparison of the available magnetostratigraphies, Site 1218 [*Lanci et al.*, 2004; *Lanci et al.*, 2005; *Pälike et al.*, 2006b], Site 1090, [*Channell et al.*, 2003; *Billups et al.*, 2004] and Site 1265 [*Bowles*, 2006], with that of Site U1334 [*Channell et al.*, 2013] along a common age scale. At Site 1264, no reliable magnetostratigraphy was recovered, so the magnetostratigraphic data from nearby ODP Site 1265 (3083 mbsl) was transferred by pattern matching magnetic susceptibility and colour reflectance records [*Liebrand et al.*, 2011]. All reversals, in particular the base of Subchron C6Cn.2n,

Table 2.1. *Correction factors.*

Study	Correction factor $\delta^{13}C$	Correction factor $\delta^{18}O$
This study	*Cib* = (0.60 x *Orid*) + 1.05 (± 0.10)[a]	*Cib* = (0.66 x *Orid*) + 0.31 (± 0.12) [a]
Shackleton et al., [1984]	+1.0 ‰	-0.5 ‰
Katz et al., [2003]	+0.72 ((±0.06 ‰) [a]	-0.28 (±0.06 ‰) [a]
Billups et al., [2004]	+1.3 (±0.37 ‰) [b]	-0.4 (±0.27 ‰) [b]
Coxall and Wilson, [2011]	+1.3 ‰	-0.34 ‰

[a] The uncertainty is 2x the standard error of the mean. [b] The uncertainty is the standard deviation *Cib* = *Cibicidoides mundulus. Orid* = *Oridorsalis umbonatus*.

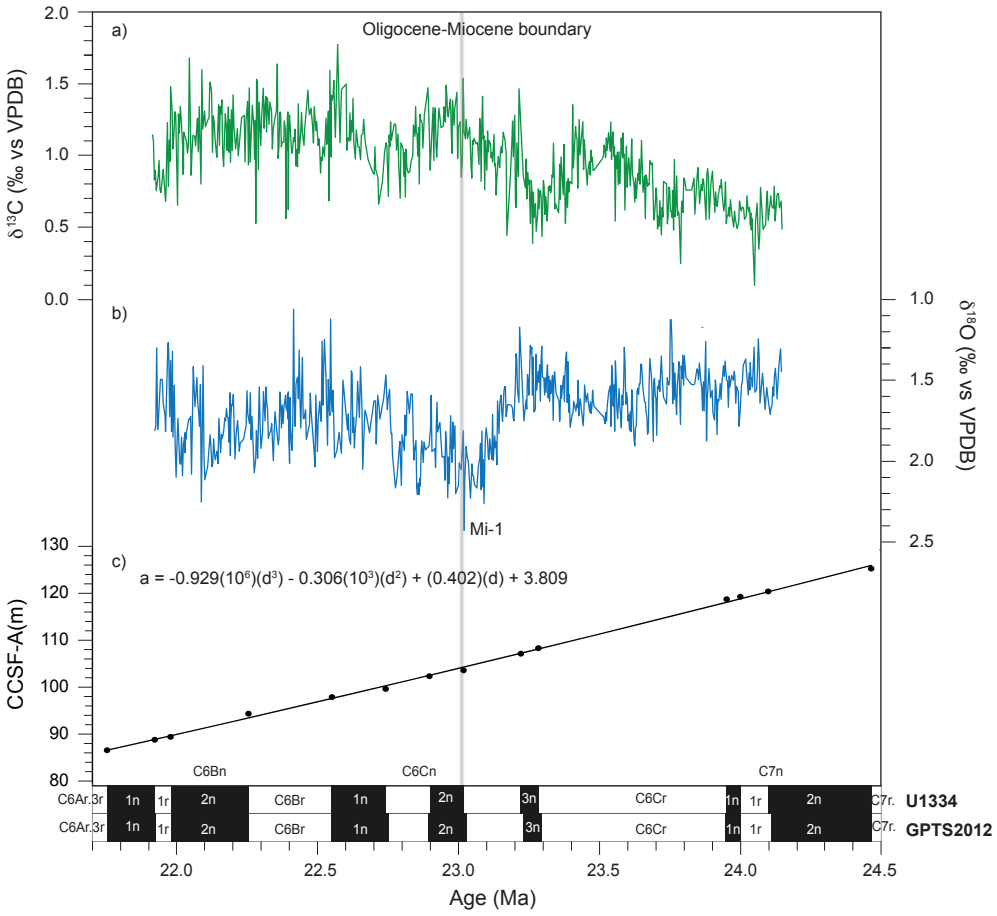

Figure 2.5. *Site U1334 composite benthic foraminiferal stable isotope records of $\delta^{13}C$ (a) and $\delta^{18}O$ (b). Magnetic reversal data from Site U1334 placed on the third order polynomial age model (c) compared to ages published in GTS2012 [Hilgen et al., 2012; Vandenberghe et al., 2012]. The grey shaded line represents the Oligocene/Miocene boundary.*

marking the base of the Miocene, are clearly consistent with the magnetostratigraphies from Sites 1218, 1090 and 1265 (Figs. 7 and 8).

As reference for our comparison, we have constructed a composite global stack across the OMT by averaging the benthic foraminiferal stable isotope records of IODP Site U1334 and ODP Sites 926, 929, 1090, 1218 and 1264. Sites 926, 929, 1218 and 1264 are constructed using *Cibicidoides* spp. and Sites U1334 and 1090 are constructed using both *Cibicidoides* spp. and *O. umbonatus* corrected to *C. mundulus*. No corrections are applied for species offsets between records when constructing the stacked record. All analysed records have a sampling resolution of <10 kyrs. The composite stable isotope stack is created by resampling each record at 5 kyr intervals using AnalySeries, to approximate the true sampling resolution (i.e. not under sample) of the best resolved records and subsequently calculating an equal-weighted average of the six aligned $\delta^{18}O$ and $\delta^{13}C$ records. The maximum value in the $\delta^{18}O$ stack is 2.21 ‰ and the minimum is 1.79 ‰ (Fig. 7). In the $\delta^{13}C$ stack,

the maxima and minima are 1.89 ‰ and 0.52 ‰ respectively (Fig. 8). The stacked record captures the full extent of the ~1 ‰ shift that occurs in the benthic $\delta^{18}O$ signal across the OMT. Although the sites used are few, and spatially limited (no data from the North Atlantic and only one fully high-resolution site from the Pacific), the stack is the best global averaged stable isotope signal across the OMT currently possible.

2.5 Discussion

The benthic foraminiferal $\delta^{18}O$ signal is a function of the isotopic composition of local seawater $\delta^{18}O$ and water temperature at the site of calcification. Consistency in both shape and amplitude between the six records across the OMT indicates a true global signal present in the records from Site U1334. Deconvolving the benthic foraminiferal $\delta^{18}O$ signal into separate components driven by ice volume changes and temperature requires other independent temperature proxies, such as Mg/Ca [*Lear et al.*, 2004; *Mawbey and Lear*, 2013] or inverse modelling techniques, including ice-sheet models for the loci of significant land-ice in both hemispheres [*De Boer et al.*, 2010, 2012]. These studies indicate that 50% or more of the benthic $\delta^{18}O$ signal is driven by changes in Antarctic ice volume. This equates to an average sea level fall of 50m or more according to a combined benthic $\delta^{18}O$ and Mg/Ca study of Site 926 records [Mawbey and Lear 2013] and estimates of 35-40m based on inverse modelling of benthic $\delta^{18}O$ from Site 1264 [*Liebrand et al.* 2011].

2.5.1 Changes in $\delta^{18}O$ offset between infaunal and epifaunal species at site U1334

We recognise that the use of two species that exhibit different paleoecological habitats, i.e. epifaunal (*C. mundulus*) and shallow infaunal (*O. umbonatus*), as done within this study and that of Site 1090 [*Billups et al.*, 2004], may influence amplitude variability in the benthic stable isotope records. This may, in turn, complicate the interpretation of the short-term variability in the water masses and climates investigated. In particular, we found a reduction in the $\delta^{18}O$ offset between *C. mundulus* and *O. umbonatus* occurring within the interval between 108.70 and 112.20 CCSF-A (~ 22.8-23.2 Ma), coincident with the positive $\delta^{18}O$ excursion present at the OMT as reflected in both single species records (Fig. 3). The deviation is caused by a larger shift in *C. mundulus* values (epifaunal) (1.1 ‰) than in *O. umbonatus* values (infaunal) (1.0 ‰) across the glacial interval. The reduction in the offset between the two species is clear in $\delta^{18}O$, but minimal in the $\delta^{13}C$ record and we find greater variation in $\delta^{18}O$ interspecies offsets.

We compare the relative change in amplitude across the OMT in the *Cibicidoides mundulus* and uncorrected *Oridorsalis umbonatus* $\delta^{13}C$ and $\delta^{18}O$ datasets, calculated by using the long-term SiZer smooths (Fig. 3) and a baseline average determined between 108.70 and 112.20 CCSF-A (Fig. 4). We find that both $\delta^{13}C$ datasets have a similar relative change in amplitude across the OMT, but in the *C. mundulus* $\delta^{18}O$ dataset the OMT has a relative amplitude of ~ 0.6 ‰, and the *O. umbonatus* dataset has a smaller relative amplitude of ~ 0.4 ‰.

We note a similar reduction in interspecies $\delta^{18}O$ gradients between *C. mundulus* and *O. umbonatus* occurred across the Eocene-Oligocene boundary at Pacific Site 1218, during a positive shift in $\delta^{18}O$ associated with the inception of permanent ice-sheets on Antarctica (*Coxall and Wilson*, 2011). Although it is a very different setting, changes in offsets between the two species have also been noted across the LGM [*Thornalley et al.*, 2015], suggesting that these offsets relate to glacial maxima.

Offsets in stable isotope signals between different benthic foraminifera species are often attributed to differences in metabolic fractionation or 'vital effects'. Fluctuations in stable isotope offsets between epifaunal and infaunal species are associated with changes in deep-water oxygenation, organic matter fluxes and pore water DIC concentration, and vertical microhabitat shifts [*McConnaughey,* 1989 a, b; *McConnaughley et al,* 1997*; Schmiedl et al.*, 2004]. The $\delta^{18}O$ offset between *C. mundulus* and *O. umbonatus* is not constant through time, and the reduced offset present between 101 and 107 CCSF-A (Fig. 3) and could reflect a carbonate ion effect on the benthic $\delta^{18}O$ isotope signal during the OMT, where a decrease in *p*H could lead to the $\delta^{18}O$ of foraminiferal shells becoming isotopically heavier [*Zeebe,* 1999]. Many studies focus on the implications of the carbonate ion effect for trace metals, suggesting *O. umbonatus* is a reliable species for Mg/Ca and other trace metal species by reasoning that, as an infaunal species, it is protected from fluctuations in the CCD by a buffering effect [*Elderfield et al,* 2010; *Brown et al.*, 2011; *Mawbey and Lear*, 2013], however, few studies have considered the influence of the carbonate ion effect on benthic stable isotopes. A study of the carbonate ion effect across the PETM suggests that increases in *p*H across climate transitions could potentially dampen the magnitude of climate excursions recorded in benthic stable isotope signals [*Uchikawa and Zeebe,* 2010]. Culture studies (e.g., *Diz et al.*, 2012), however, suggest that the carbonate ion effect affects $\delta^{18}O$ to a much lesser extent than $\delta^{13}C$, and as our offset in $\delta^{13}C$ is consistent across the OMT, an alternative mechanism may be controlling the change in interspecies offsets across the OMT.

Fluctuations in $\delta^{18}O$ inter-species offsets could be indicative of variations in carbonate ion concentration or early diagenetic processes [*Schmiedl and Mackensen*, 2006; *Hoogakker et al.*, 2010] associated with the shift in climate across the OMT at Site U1334. This suggests that a change in the relationship between the $\delta^{18}O$ values of infaunal species *O. umbonatus* and the epifaunal species *C. mundulus* is linked to the climatic changes occurring during the positive $\delta^{18}O$ excursion, notably deep-water cooling. However, few data exist on the impact of glacial-interglacial changes on species offsets in benthic foraminiferal stable isotope signals in deep sea cores, or on multispecies records from the same cores extending beyond the LGM [*Vidal et al., 2004*; *Schmiedl and Mackensen*, 2006; *Friedrich et al.*, 2006; *Hoogakker et al.*, 2010], making it difficult to pinpoint mechanisms controlling Cenozoic changes in the $\delta^{18}O$ gradient between benthic foraminiferal species**.**

2.5.2 Inter-basin comparison of the OMT

All Pacific and Atlantic high-resolution records throughout the OMT interval show a notable similarity in the shape and amplitude of large and small-scale features in the datasets and short-term and long-term smooths created using SiZer (Figs. 7 and 8). As changes in ice volume should have an equal effect on the $\delta^{18}O$ of all water masses, the global signal in the $\delta^{18}O$ records should be comparable, with differences in $\delta^{18}O$ between records implying a change in deep ocean circulation patterns, regional changes in water mass temperature, or changes in the relationship between salinity and $\delta^{18}O$, taking offsets between labs (which can be up to 0.2 ‰) into account [*Ostermann and Currie*, 2002]. All six records exhibit peak positive $\delta^{18}O$ values that are often referred to as the Mi-1 isotope zone, or "Mi-1", which has been identified previously in a number of OMT records (*Miller et al.*, 1991; *Billups et al.*, 2004; *Pälike et al*, 2006b). The peak positive values (Mi-1) at Site U1334 occur at 23.02 Ma, just prior to Chron C6cn.2n, the marker for the Oligocene/Miocene boundary, making it a late Oligocene event rather than a Miocene event (Figs. 5 and 7).

Absolute (range from maxima to minima) values of the amplitude of the positive $\delta^{18}O$ excursion at the OMT range between 1.0 ‰ (Site 1264) and 1.4 ‰ (Site 1090). We measure the absolute amplitude of the OMT in each record by taking the difference between the minimum value

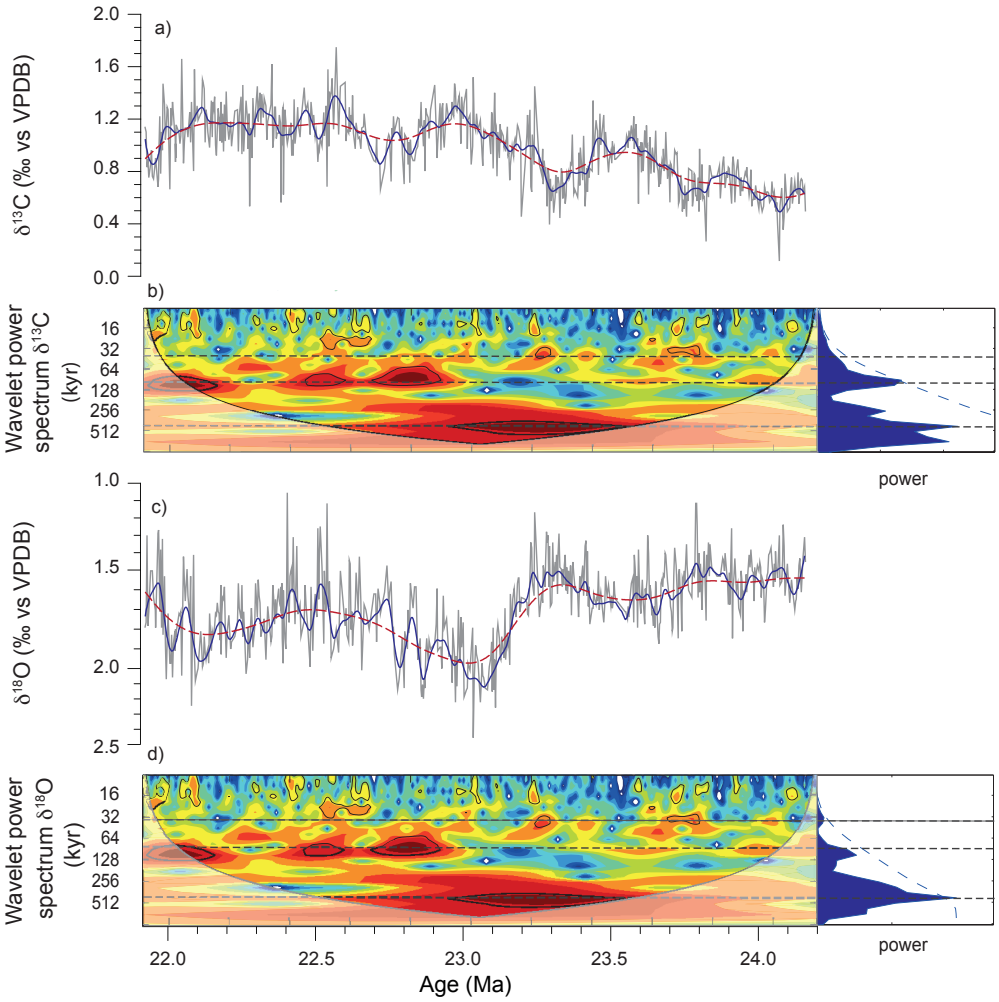

Figure 2.6. *Site U1334 composite benthic foraminiferal stable isotope records of $\delta^{13}C$ (a) and $\delta^{18}O$ (c) including two statistical smoothes (blue and dashed red lines) created using SiZer. Wavelet analysis with 95% confidence levels calculated for $\delta^{13}C$ (b) and $\delta^{18}O$ (d), calculated using an adapted script from Torrence and Compo, [1998]. Data were resampled, notch-filtered and linearly detrended prior to wavelet analysis.*

at 23.2 Ma, where the shifts towards more positive $\delta^{18}O$ values begins, and the maximum value during the OMT at ~23.0 Ma. One factor to consider with regards to measuring the amplitude of an event using absolute values is that picking a precise point at which the transition starts can be arbitrary, and choosing different points in the dataset to define the beginning of a transition can lead to different estimates for the absolute amplitude of the event [*Mudelsee et al.*, 2014]. We use the short and long-term SiZer smooths to distinguish the underlying structure of the dataset from the background noise; to pinpoint the beginning of the positive $\delta^{18}O$ shift at the OMT, and to compare the relative amplitude change during the glaciation between records [*Bohaty et al.*, 2012]. Focusing on differences in the amplitude of the isotope excursion during the OMT using statistically

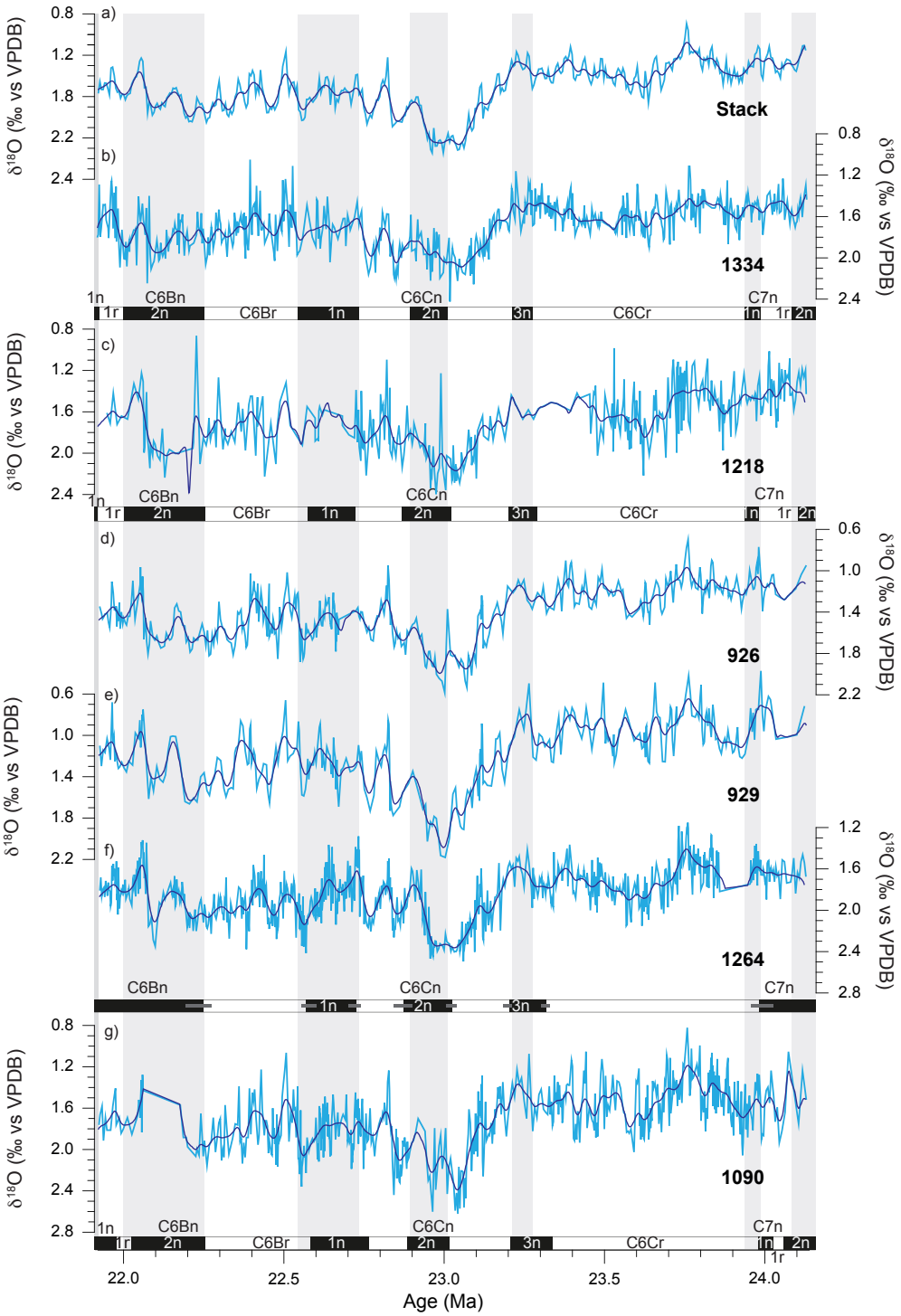
a)
Stack
b)
1334
c)
1218
d)
926
e)
929
f)
1264
g)
1090
δ18O (‰ vs VPDB)
C6Bn
C6Br
C6Cn
C6Cr
C7n
1n
1r
2n
3n
Age (Ma)
22.0
22.5
23.0
23.5
24.0

smoothed SiZer data avoids putting too much emphasis on extreme stable isotope values, which might lead to an over- or underestimation of differences in amplitude between sites [*Mudelsee et al.*, 2014].

Site 1090 has the largest absolute amplitude across the OMT in terms of maximum and minimum individual $\delta^{18}O$ values (1.4 ‰) (Fig. 7), but looking at the smoothed dataset (Fig. 9), equatorial Atlantic Site 929 experiences the largest relative change across the OMT. The relative change in $\delta^{18}O$ at Site 929 across the OMT is 0.85 ‰, relative to a baseline determined by averaging $\delta^{18}O$ values between 23.30 and 23.55 Ma. This is 0.2 ‰ larger than the relative change at Site 926, which is located near to but 760 m shallower than Site 929. Site 1090 has a relative change in $\delta^{18}O$ of 0.6 ‰, and Sites 1218, 1264 and U1334 all have a relative change of 0.5 ‰. Comparing the relative amplitude of the sites indicates that the equatorial Atlantic sites experienced the largest change in $\delta^{18}O$ values compared to Pacific Sites. Using the long-term SiZer smooth of our stacked record to estimate relative change in $\delta^{18}O$ across the OMT, we find a value of 0.6 ‰ (Fig. 7), which agrees with a previously published study, which gives the same figure for an overall weighted mean from 15 high and low resolution records [*Mudelsee et al.*, 2014]. We note that the small relative amplitude at Site U1334 could an artefact of the way the record was constructed using the two species, taking into account the change in the offset between the two species from 22.8-23.2 Ma. The 0.5 ‰ relative change in amplitude in the $\delta^{18}O$ dataset is an average of the *C. mundulus* and *O. umbonatus* datasets. The *C. mundulus* dataset has a relative change in amplitude of 0.6% (Fig. 4), which is in better agreement with the value given by the stacked record and the study from *Mudelsee et al.,* [2014]. Comparing relative change in $\delta^{18}O$ values across the OMT suggests that the upper limit of ice volume change present within the $\delta^{18}O$ signal across the OMT can be constrained to 0.6 ‰, which would equate to a maximum ~ 50m of sea level fall, assuming an ice sheet $\delta^{18}O$ identical to today [*Fairbanks and Mathews*, 1978]. If the $\delta^{18}O$ of the expanding ice sheet during Mi-1 was higher than today, which can be expected from presumably reduced Rayleigh distillation by atmospheric water transport in a warmer world than the present day then this estimate could be slightly larger. This would suggest that sea-level change across the OMT is in the mid-range of previous estimates, which vary from 30-90m [*Miller et al.,* 1991; *Pekar et al.*, 2002; *Liebrand et al.*, 2011; *Mawbey and Lear*, 2013].

Significant ~100 kyr amplitude variability present in all $\delta^{18}O$ datasets during the early Miocene suggests short-period eccentricity controlled expansion/contraction of the geographical extent and mass of the Antarctic ice sheet (Fig. 6) [*Zachos et al.*, 2001; *Liebrand et al.*, 2011]. Low ~100 kyr amplitude variability during the positive isotope excursion and suggested glacial expansion across the OMT indicates a stable period of maximum ice volume and persistent low temperatures. More significant ~100 kyr variability occurring in the early Miocene is superimposed on a long-

Figure 2.7. *Comparison of Site U1334 with previously published high-resolution benthic foraminiferal $\delta^{18}O$ records, with magnetic reversal data plotted underneath, adjusted to Site U1334 age model. Dark blue lines are a statistical smooth created using SiZer. Plotted above is the benthic foraminiferal isotope stack (a) IODP Site U1334 (b) [Channell et al., 2013], ODP Site 1218 (c) [Lanci et al., 2004; Lear et al., 2004; Pälike et al., 2006b] ODP Sites 926 (d) and 929 (e) [Flower et al., 1997a; Zachos et al., 1997, 2001; Paul et al., 2000; Pälike et al., 2006a; Shackleton et al., 2000], Site 1264 (f) [Liebrand et al., 2011] and Site 1090 (g) [Channell et al., 2003; Billups et al., 2002, 2004]. The magnetostratigraphy for Site 1264 is transferred from Site 1265 [Bowles, 2006]. The datasets have been aligned at depth using the Match software package [Lisiecki and Lisiecki, 2002] (Supporting information) and all datasets then placed on the Site U1334 magnetostratigraphic age model.*

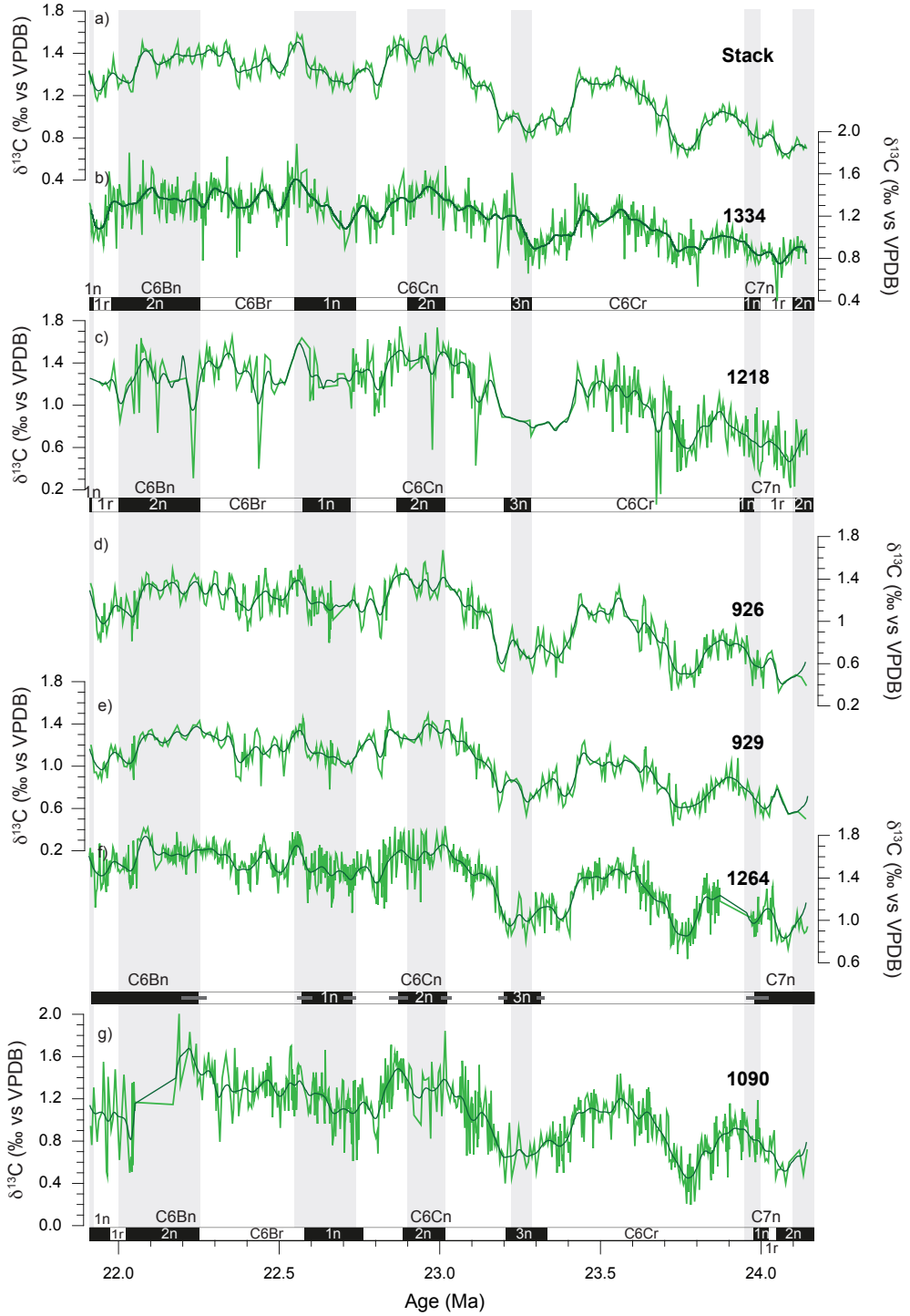
a)
Stack
b)
1334
c)
1218
d)
926
e)
929
f)
1264
g)
1090
δ13C (‰ vs VPDB)
1n
C6Bn
C6Cn
C7n
1r
2n
C6Br
3n
C6Cr
22.0
22.5
23.0
23.5
24.0
Age (Ma)

term trend in ice-sheet decay and relatively higher global temperatures. Strong ~100 kyr cyclicity is particularly clear during the termination phase of the transient glaciation across the OMT. All six sites show a clear increase in the amplitude of ~100 kyr variability after the termination, although the amplitude of the response differs between basins. In particular, directly after the OMT, three prominent ~100 kyr cycles are present in all records but are clearest at Sites U1334 and 1264 (Figs. 6 and 7). At 22.7 Ma, Site 1264 has notably high amplitude ~100 kyr cycle relative to the other five sites, which appears to be a regional feature unique to this record. The strong shift towards more negative $\delta^{18}O$ values at Site 1264 around 22.7 Ma results in reduced gradients between Site 1264 and the Pacific and Southern Ocean sites (Fig. 9) and is associated with variability on 400 kyr timescales, coinciding with the termination phase of the transient glaciation across the OMT.

Comparing the short-term smooths between 22.6 and 22.9 Ma (Fig. 7), $\delta^{18}O$ values at Site 1264 decrease compared to values earlier in the record between 21.9 Ma-22.6 Ma and return to almost late Oligocene baseline values. The other five sites do not show a similar return to pre-OMT values, although Sites 926 and 929 also exhibit a decrease in values directly after the termination comparative to the youngest part of the record [*Zachos et al.*, 2001]. These comparatively low $\delta^{18}O$ values at Site 1264 appear untypical compared to the other early Miocene records. A slight return towards warmer conditions after the OMT recovery phase has been noted in previous studies [*Zachos et al.*, 2001; *Lear et al.*, 2004; *Mawbey and Lear,* 2013; *Mudelsee et al.*, 2014], suggesting a non-linear and dynamic response present in the climate system [*Zachos et al.*, 2001]. This signal could be particularly prominent at Site 1264 due to more positive late Oligocene $\delta^{18}O$ values at Site 1264, which suggest colder/more saline bottom water conditions, relative to the other five sites. Site 1264 consistently has the most positive (baseline) $\delta^{18}O$ values of all six sites, and during the OMT, the other sites move towards the more positive (colder/more saline) $\delta^{18}O$ values at Site 1264 (Fig. 9).

The maximum $\delta^{13}C$ values occur at all six sites ~30 kyr after the peak $\delta^{18}O$ values of the OMT, due to a global shift in the carbon cycle either triggered by or coincident with the expansion of the Antarctic Ice Sheet [*Hodell and Woodruff*, 1994; *Diester-Haass et al.*, 2011]. We calculated the relative change in $\delta^{13}C$ on the long-term smooths across the OMT for all six sites, relative to a baseline determined by averaging $\delta^{13}C$ values between 23.30 and 23.55 Ma. Across the glaciation, the range in relative amplitudes in the long-term $\delta^{13}C$ smooths between all six sites is minor (0.3-0.5 ‰) (Fig. 9). After this shift across the OMT, the $\delta^{13}C$ baseline is distinctly offset towards more positive values in all datasets (Fig. 9), a $\delta^{13}C$ stable isotope feature previously described as the Oligocene-Miocene Carbon Maximum [*Hodell and Woodruff*, 1994]. The long and short-term smoothed datasets in the $\delta^{13}C$ record show the clear imprint of the long period eccentricity forcing prior to and during the OMT (Figs. 6 and 8). The strong response at the 400 kyr frequency seen in

Figure 2.8. *Comparison of Site U1334 with previously published high-resolution benthic foraminiferal $\delta^{13}C$ records, with magnetic reversal data plotted underneath, adjusted to Site U1334 age model. Dark green lines are a statistical smooth created using SiZer. Plotted above is the benthic foraminiferal stable isotope stack (a) IODP Site U1334 (b) [Channell et al., 2013] ODP Site 1218 (c) [Lanci et al., 2004; Lear et al., 2004; Pälike et al., 2006b] ODP Sites 926 (d) and 929 (e) [Flower et al., 1997a; Zachos et al., 1997, 2001; Paul et al., 2000; Pälike et al., 2006a; Shackleton et al., 2000], Site 1264 (f) [Liebrand et al., 2011] and Site 1090 (g) [Channell et al., 2003; Billups et al., 2002, 2004]. The magnetostratigraphy for Site 1264 is transferred from Site 1265 [Bowles, 2006]. The datasets have been aligned at depth using the Match software package [Lisiecki and Lisiecki, 2002] (Supporting information) and all datasets then placed on the Site U1334 magnetostratigraphic age model.*

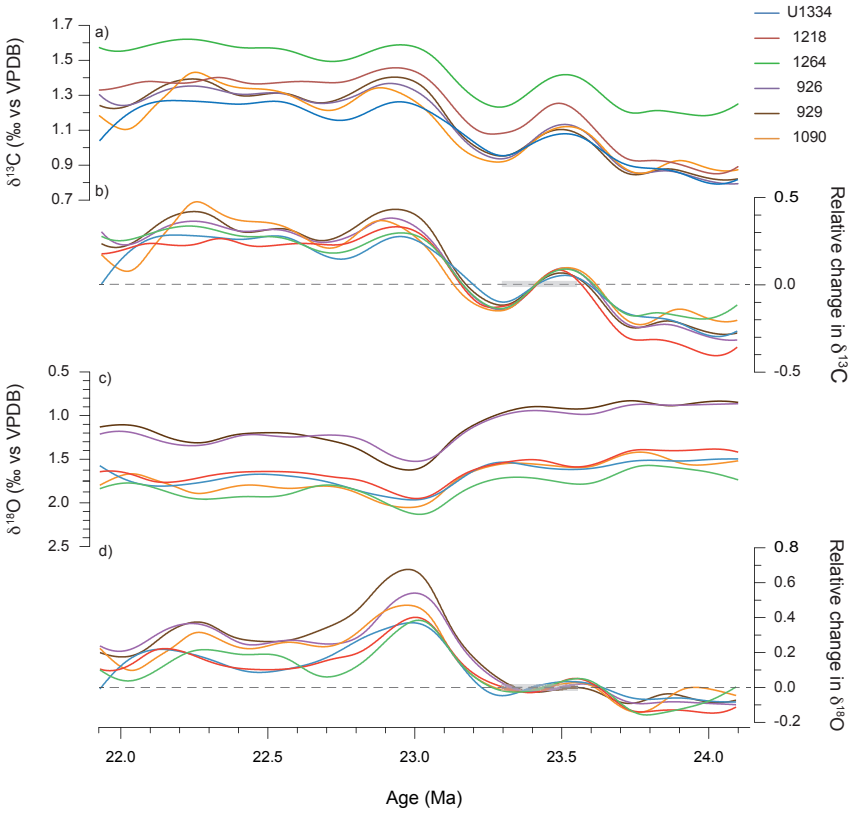

Figure 2.9. *Statistically smoothed $\delta^{18}O$ datasets from Site U1334 (this study) and previously published datasets from Sites 1218, 926, 929, 1264 and 1090 indicating the long-term (>250 kyr) trend (a). Relative change in $\delta^{18}O$ record based on long-term $\delta^{18}O$ SiZer smooths, using a baseline average determined between 23.3 and 23.5 Ma (grey shaded box) (b). Statistical smoothed $\delta^{13}C$ datasets from Site U1334 (this study) and previously published datasets from Sites 1218, 926, 929, 1264 and 1090 indicating the long-term (>250 kyr) trend (c). Relative change in $\delta^{13}C$ record based on long-term $\delta^{18}O$ SiZer smooths, using a baseline average determined between 23.3 and 23.5 Ma (grey shaded box) (d).*

the $\delta^{13}C$ record is a consistent global feature of climate during the Oligocene and Miocene [*Zachos et al.*, 2001; *Wade and Pälike*, 2004; *Pälike et al.*, 2006a; *Holbourn et al.*, 2013, 2015].

2.5.3 Isotopic gradients between sites

On an intra-basin scale, the offset in $\delta^{18}O$ between Sites U1334 and 1218 on astronomical time-scales is small at 0.1 ‰, although the offset increases across the OMT (Fig. 9). The similarity between the Pacific sites is unsurprising, as they are geographically close and from similar water depths. Preservation issues can be discounted as an explanation for the difference between the sites across the OMT, as foraminifera from Site 1218 have very good preservation across this time period [*Lyle et al., 2002; Edgar et al., 2013*]. The offset is within the limit suggested to account for different laboratory practices [*Ostermann and Currie, 2002*] but this does not explain an increase in the offset across the OMT. Either Site 1218 does not record the full extent of the coldest points during the

OMT, or, in the equatorial Pacific, local variation exists in bottom water temperatures based on depth.

The long-term $\delta^{18}O$ SiZer smooths (Fig. 9) indicate that the six records fall into two distinct groups. The equatorial Atlantic Sites 926 and 929 form one group, which is offset from the other four high-resolution records to consistently lighter $\delta^{18}O$ values, indicating that the seafloor at these equatorial Atlantic sites was bathed within relatively warm and/or a $\delta^{18}O$ depleted water mass [*Billups et al.*, 2002]. Site 926 and 929 are relatively constantly offset by ~1 ‰ from the equatorial Pacific Site U1334 and 1218. The offset between the lighter $\delta^{18}O$ values in the equatorial Atlantic and the heavier $\delta^{18}O$ values equatorial Pacific could be related to temperature, suggesting equatorial Pacific bottom waters were colder than equatorial Atlantic bottom waters. This supports previous suggestions of the existence of a warmer deep-water mass present in the North Atlantic across the OMT [*Woodruff and Savin*, 1989; *Billups et al.*, 2002].

The second group of $\delta^{18}O$ records consists of the sub-Antarctic Southern Ocean Site 1090, the two Pacific Sites, 1218 and U1334 and the south-east Atlantic Site 1264, although 1264 exhibits some differences in $\delta^{18}O$ values from the other three sites. Sites 1218, 1264 and U1334 bear a close similarity to Site 1090, suggesting an Antarctic sourced water mass was present at all three sites. Site 1264 consistently has the most positive $\delta^{18}O$ values, a surprising result given that it is the shallowest site. One possible explanation is the presence of a more saline (high $\delta^{18}O$) water mass at Site 1264. During the glaciation at the OMT, gradients between Site 1264 and the Southern Ocean and Pacific sites (1090, 1218 and U1334) reduce, and remain smaller into the early Miocene.

Deep ocean $\delta^{13}C$ gradients between basins are negligible across the OMT, regardless of changes in ocean circulation. The low gradients in $\delta^{13}C$ are attributed to a generally low-nutrient ocean [*Delaney and Boyle*, 1987; *Wright et al.*, 1991; *Billups et al.*, 2002]. However, we observe some differences between the sites. Carbon isotope gradients between the deeper Sites U1334, 1218, 926, 929 and 1090 are small, but Site 1264 is offset from the other sites by ~ +0.5 ‰ (Fig. 9). The difference in $\delta^{13}C$ gradients between Site 1264 and the other five sites is most likely due to its shallower water depth location [*Liebrand et al.*, 2011]. In this respect, it is interesting to note that Site 1264 revealed a weak imprint of obliquity in both stable isotope records across the OMT [*Liebrand et al.*, 2011] compared to the equatorial, though deep water, Sites 926 and 929 [*Flower et al.*, 1997; *Paul et al.*, 2000] (Fig. 9). Our findings at Site U1334 confirm a distinct obliquity imprint in both $\delta^{18}O$ and $\delta^{13}C$ during the OMT in the deep waters of the Pacific (Fig. 6), indicating that most likely the obliquity signal is transferred from high-latitudes (i.e. Antarctica) to the equator primarily through deep-water masses. Alternatively, Site 1264 has low sedimentation rates, which could distort the preservation of higher frequency astronomical cycles and lead to a weak obliquity signal. After the OMT, $\delta^{13}C$ values at all sites increase and show greater variability, and the imprint of the 400 kyr eccentricity cycle is less easy to distinguish, in particular the Pacific/Southern Ocean sites have a more variable $\delta^{13}C$ signal.

2.6 Conclusions

We have constructed new high-resolution (~ 3 kyr) benthic foraminiferal stable isotope records in the equatorial Pacific basin, and compare these datasets to other high-resolution records from different ocean basins to evaluate global and regional climate variability across the OMT. We find that the benthic foraminiferal stable isotope records from IODP Site U1334 are remarkably consistent with previously published records, confirming the global nature of the $\delta^{18}O$ signal in

the Pacific. Peak $\delta^{18}O$ values associated with the OMT (i.e. Mi-1 oxygen isotope zone) occur in the latest Oligocene prior to the Oligocene/Miocene boundary. Gradients between sites suggest that the high-resolution records fall into two groups, dominated by two different water masses, supporting previous suggestions of the existence of deep-water formation in the North Atlantic during the Oligocene-Miocene. We find pervasive cyclicity at long and short period eccentricity frequencies (400 and ~100 kyr) and confirm a distinct obliquity imprint (41 kyr) present in the stable isotope records at Site U1334. We find an offset in $\delta^{18}O$ records between the deep equatorial Atlantic and deep equatorial Pacific basins, which suggests a temperature gradient is present between the equatorial Pacific bottom waters and the equatorial Atlantic bottom waters across the OMT.

Acknowledgements

This research used samples provided by the Integrated Ocean Drilling Program (IODP), collected by the staff, crew and scientists of IODP Expedition 320/321. We thank Dominika Kasjanuk, Arnold van Dijk, Maxim Krasnoperov and Jan Drenth for laboratory assistance, and Vittoria Lauretano, Stefanie Kaboth, Frits Hilgen, Heiko Pälike and Steve Bohaty for useful discussions. We thank Ann Holbourn, and two anonymous reviewers for constructive and helpful reviews. This research was supported by NWO VICI grant no. [865.10.001] awarded to L. J. Lourens. A. Sluijs thanks the European Research Council (ERC) under the European Union Seventh Framework Program for ERC Starting Grant #259627. B. Wade was supported by the Natural Environment Research Council reference NE/G014817. This work was carried out under the program of the Netherlands Earth System Science Centre (NESSC). Data are available in the supporting information tables and online through Pangaea.

Chapter 3:

Astrochronology and orbital forcing across the Oligocene-Miocene transition: tuned stable isotope records from eastern equatorial Pacific Site U1334

Abstract

Astronomical tuning approaches for Cenozoic climate proxy records vary within the published literature. Different approaches can have major implications for ages and pacing theories derived from tuned age models. We present two independent astronomically tuned age model options for the interval covering the Oligocene-Miocene Transition (OMT) at IODP Site U1334, in the equatorial Pacific Ocean to assess the effect of different tuning approaches for the pacing of events across the OMT. In our first tuning, we use $CaCO_3$ % weight estimates as a tuning signal and in a second tuning approach we use the benthic stable carbon isotope record as a tuning signal. We use these two independent astronomically tuned age models to evaluate the implications of tuning assumptions on the duration and age of the studied interval. Moreover, we compare the effect of each age model on astronomical periodicities, as well as coherency and phase relations in the datasets. The age model based on estimated wt% $CaCO_3$ produces a duration of 2.19 Myr for the studied interval, ranging from 21.96 to 24.15 Ma. The age model based on benthic foraminiferal $\delta^{13}C$ produces a duration of 2.11 Myr, ranging from 22.10 to 24.21 Ma. We identify 405 kyr and ~110 kyr eccentricity periodicities as the dominant astronomical signals present in the $CaCO_3$ est. (%) and benthic foraminiferal stable isotope datasets, with intermittent intervals of 41 kyr obliquity. Comparison to independent astronomically tuned age models implies that the wt% $CaCO_3$-based age model is in better agreement with previous tuning approaches. In contrast, the $\delta^{13}C$-based age model presents an alternative tuning option for the early Miocene, where 405 kyr variability in the benthic $\delta^{13}C$ and $\delta^{18}O$ records is completely in-phase with eccentricity. New tectonic plate-pair spreading rate-based ages provide independent time control for the Oligocene-Miocene, and indicate that the $CaCO_3$ tuned age model provides polarity chron ages that are consistent with the assumption of constant spreading rates. This confirms earlier tuning approaches that also preferred local/regional tuning signal over globally integrated isotope records, which are known to produce significant lags relative to eccentricity as a result of non-linear feedbacks. The new astronomically tuned ages for the polarity chrons at Site U1334 have implications for the next generation GTS, as polarity chron C6Bn.1n to polarity chron C6Cn.1r are not astronomically calibrated in GTS2012, the current iteration of the GTS.

3.1 Introduction

Over the last 65 million years, climate has gradually shifted from a period of global warmth without major ice sheets, punctuated by events of extreme warmth, to a climate dominated by large continental ice sheets, punctuated by more extreme climate events of large-scale glaciation, or increases in global warmth (*Zachos et al.*, 2001). The Oligocene-Miocene Transition (OMT, ~23 Ma), is a large, transient glaciation event, occurring at the Oligocene-Miocene boundary, marked in oxygen isotope ratios ($\delta^{18}O$) of benthic foraminifera as a positive excursion of ~ 1‰ (per mil), generally interpreted as an interval of deep-sea cooling and increased ice volume on Antarctica [*Woodruff and Savin*, 1989; *Miller et al.,* 1991; *Zachos et al.,* 1997]. The OMT marks a change on secular time-scales in the way the climate system operates, from low-amplitude climate variability in the late Oligocene to higher amplitude climate variability in the early Miocene [*Zachos et al.*, 2001; *Billups et al.*, 2004; *Pälike et al.*, 2006a, 2006b, *Liebrand et al.*, 2011].

Precise and accurate time-control on climate proxy records is necessary to reconstruct and understand Earth's past climate in detail. Previously published high-resolution astronomically tuned age-models for the OMT have been based on a mix of eccentricity, obliquity and precession as tuning targets, using lithological data and benthic foraminiferal stable isotopes as a tuning signal [*Shackleton et al.*, 2000; *Zachos et al.*, 2001; *Billups et al.*, 2004; *Pälike et al.*, 2006a, 2006b]. More recently, a high-resolution astronomically tuned record was generated for ODP Site 1264, using eccentricity as the sole tuning target, and lithological data as the tuning signal [*Liebrand et al.*, submitted]. Despite this progress, uncertainties regarding the precision and accuracy of astronomical age models limit the constraints on rates of climate change. Assumptions inherent to the available astronomical tunings have implications for determining the timing and duration of events, as well as the astronomical frequencies and phase relationships present within climate proxy datasets.

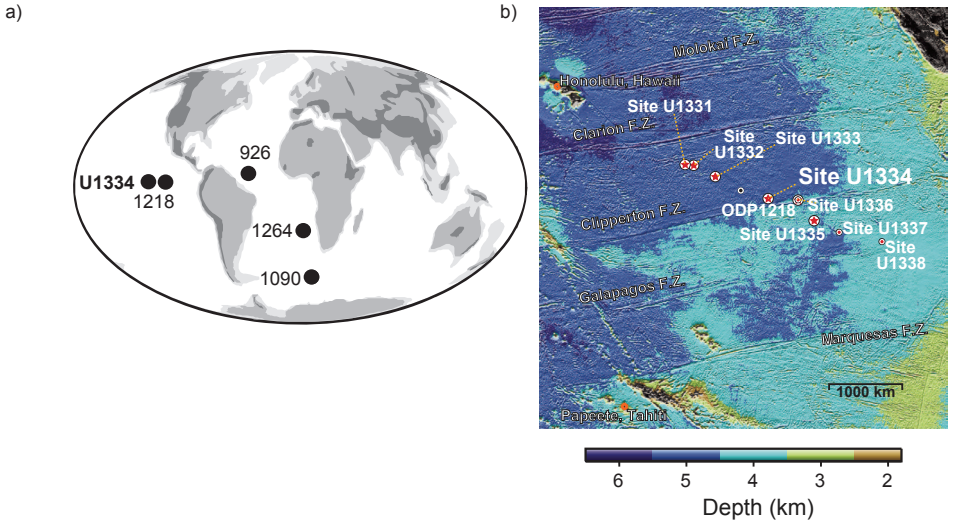

Figure 3.1. *(a) Location of IODP Site U1334 with reference to ODP Sites 1264, 1218, 926, 929 and 1090. (b) Bathymetric overview map of Site U1334 and PEAT drilling locations, with previous ODP and DSDP sites, including ODP Site 1218 [adapted from Pälike et al., 2010.]*

In the Neogene section of the Geologic Time Scale 2012 (GTS2012), numerical ages and durations for polarity chrons from Chron C5C (middle Miocene) to Chron C6Cn.2n at the Oligocene-Miocene boundary are still derived from fitting spreading rate models without astronomical calibration [*Hilgen et al.*, 2012, *Gradstein et al.*, 2012]. Calibrating early to middle Miocene magnetostratigraphies with cyclostratigraphic ages will allow tighter constraints of chron ages and duration in the next iteration of the GTS, and potentially replace current ages. In addition, such initiatives might address the stability of obliquity and precession periods for age >10 Ma, which at present remains uncertain due to limitations in constraining tidal dissipation values and dynamical ellipticity [*Lourens et al.,* 2004*; Husing et al.,* 2007*; Zeeden et al.*, 2014].

Here, we present two independent astronomically tuned age models for previously published high-resolution OMT records from IODP Site U1334, in the eastern equatorial Pacific, based on the alignment of $CaCO_3$ est (%) and benthic foraminiferal $\delta^{13}C$ data to eccentricity [*Beddow et al.*, 2016]. Subsequently, we use our astronomically tuned benthic foraminiferal stable isotope records to assess climate response at orbital frequencies across the OMT at Site U1334 and compare our record with existing high-resolution benthic foraminiferal stable isotope records from both the Atlantic and Pacific ocean basins [*Shackleton et al.*, 2000; *Zachos et al.*, 2001; *Billups et al.*, 2004; *Pälike et al.*, 2006a, 2006b, *Liebrand et al.*, submitted]. We evaluate the implications of tuning signal choices and discuss the ramifications of assumptions made when producing astronomically tuned age models, using sea floor spreading rates as an independent test for our two astronomical age models.

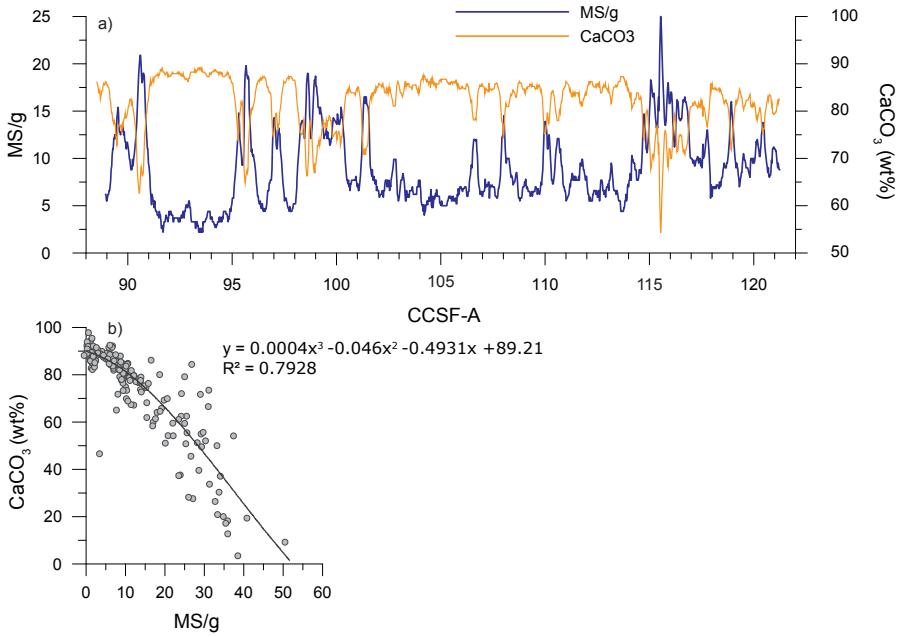

Figure 3.2. *Calibration between the shipboard Magnetic Susceptibility record and shipboard coulometric $CaCO_3$ measurements to obtain a record of $CaCO_3$ estimates (%). Magnetic susceptibility and $CaCO_3$ est. (%) are plotted against CCSF-A in panel (a). The relationship between coulometric $CaCO_3$ measurements and Ms/g was calculated using ordinary least squares linear regression, with an r^2 value of 0.79 (b).*

3.2 Materials

3.2.1 Site description

Site U1334, positioned in the eastern equatorial Pacific (4794 meters below sea level (mbsl), 7°59.998'N, 131°58.408'W) was recovered in 2009 by Integrated Ocean Drilling Program (IODP) expeditions 320/321 (Fig.1). Upper Oligocene and lower Miocene sediments were deposited at a paleodepth of ~4200 meters below sea level (mbsl) and comprise of nannofossil ooze and chalk [*Pälike et al.*, 2010, 2012].

3.2.2 Benthic stable isotope records and Magnetostratigraphic age model

A benthic foraminiferal stable isotope record has been constructed from a splice of Holes A, B and C drilled at Site U1334 to create a continuous core composite depth (m) below seafloor (CCSF-A, equivalent to metres composite depth) depth scale (Fig. 3) [*Westerhold et al.*, 2012]. At Site U1334, a complete and extended Oligocene-Miocene section was recovered, with a well-defined magnetostratigraphy [*Channell et al.*, 2013] (Fig. 3). We use the stable isotope dataset of *Beddow et al.* [2016], based on the *Oridorsalis umbonatus* and *Cibicidoides mundulus* benthic foraminifera species. A correction factor derived from the analysis of 180 pairs of for inter-species isotope value comparison was applied and *O. umbonatus* values were corrected to *C. mundulus* values based on ordinary least squares linear regression [*Beddow et al.*, 2016]. The benthic stable isotope datasets at Site U1334 were placed on a magnetostratigraphic age model created by fitting a third-order polynomial through 14 magnetostratigraphic age-depth tie-points identified at Site U1334 (Table 1 and Fig. 4), and gives the Site U1334 $CaCO_3$ est. (%) stable isotope dataset an age of 21.91 to 24.14 Ma (Fig. 3) [*Channell et al.*, 2013; *Beddow et al.,* 2016].

3.3 Methods

3.3.1 Coulometric $CaCO_3$ and magnetic susceptibility

For a high-resolution estimated wt% $CaCO_3$ record, we calibrated shipboard magnetic susceptibility (MS) to shipboard coulometric $CaCO_3$ measurements for Site U1334 [*Pälike et al.*, 2010]. Minimum MS (SI unit) values correspond to maximum $CaCO_3$ values. The relationship between coulometric $CaCO_3$ measurements and MS (SI unit) was calculated using a third order polynomial fit, with an r^2 value of 0.79 (Fig. 2).

3.3.2 Spectral analysis

We conduct spectral analysis methods on the benthic foraminiferal $\delta^{13}C$ and $\delta^{18}O$ and the $CaCO_3$ est. (%) datasets in the depth domain, on the magnetostratigraphic age model and on both astronomical age model options presented here. Prior to analysis, the data were re-sampled, linearly detrended and long-term trends longer than 6m or 600 kyr were removed using a notch-filter in version 2 of the software package AnalySeries [*Paillard et al.*, 1996]. Blackman Tukey spectral analysis was used to identify dominant periodicities present within the data, which were then filtered using a Gaussian filter using AnalySeries. Cross-spectral analysis identifying coherency and phase relationships between the astronomical target and the datasets were performed at 95% significance in AnalySeries. Evolutive spectra are produced using the program MATLAB.

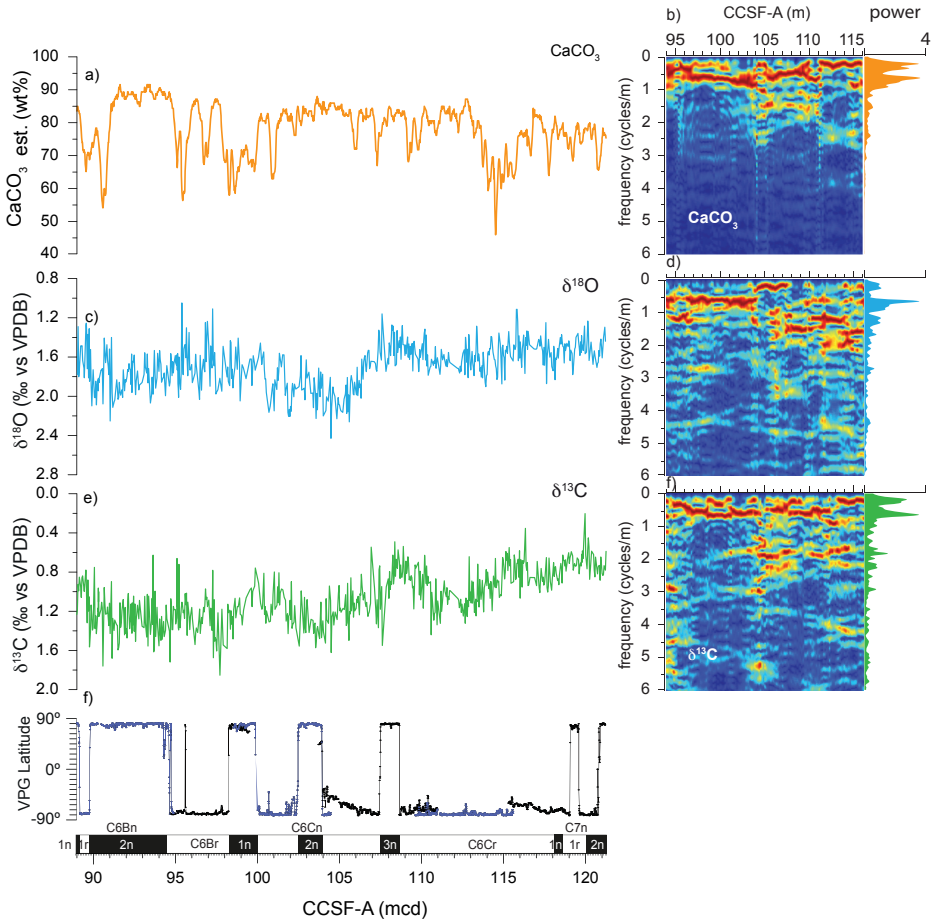

Figure 3.3. *Site U1334 datasets, evolutive spectra and power spectra against depth in CCSF-A (m) based on the splice by Westerhold et al. [2012]. Site U1334 $CaCO_3$ est. weights (%) are plotted in panel (a), and $CaCO_3$ est. (%) evolutive and power spectra are plotted in panel (b). The benthic foraminiferal $\delta^{18}O$ dataset is plotted in panel (c) and $\delta^{18}O$ evolutive and power spectra in panel (d). The benthic foraminiferal $\delta^{13}C$ dataset is plotted in panel (e) and $\delta^{13}C$ evolutive and power spectra in panal (f). Site U1334 VPG latitudes (g) have been previously published by Channell et al. [2013]. Alternate holes are coloured blue/black in the VPG latitude plot.*

3.4 Results

3.4.1 $CaCO_3$ est.

Variability in the $CaCO_3$ est. ranges between 54% and 88% of the dry sediment. $CaCO_3$ est. values dip below 70% in the upper Oligocene, between 114.9 and 116.2 m CCSF-A, with a minimum value of 54% occurring at 115.5 m CCSF-A (Fig. 3). From 116.2 m CCSF-A to 121.9 m CCSF-A, the $CaCO_3$ est. content varies between 61 and 83%. Changes in $CaCO_3$ est. content are generally twice as large in the early Miocene section of the record, between 88.95 and ~102 m CCSF-A, varying by

~40% with several minima in the record dipping below 70%. Between ~102 and ~106 m CCSF-A (the OMT) the $CaCO_3$ record shows little variability.

3.4.2 Spectral analyses in the depth domain

The power spectra of the $CaCO_3$ est. (%) record reveal strong spectral peaks at 0.2 cycles/m and 0.65 cycles/m (Fig. 3). These correspond to similar peaks found in the benthic foraminiferal $\delta^{13}C$ and $\delta^{18}O$ depth series at 0.15 cycles/m and 0.65 cycles/m. Smaller peaks are present at 1.83 cycles/m and 2.8 cycles/m (Fig. 3). High-amplitude cycles with low frequencies are present in all datasets with a 1:4 ratio, suggesting a strong influence from eccentricity forcing. This interpretation of strong eccentricity cyclicity present in all datasets is supported by the application of the initial magnetostratigraphic age model, which indicates spectral power is present in the $CaCO_3$ est. (%) and benthic $\delta^{13}C$ and $\delta^{18}O$ datasets at 405 kyr and ~110 kyr periodicities (Fig. 5) [*Beddow et al.*, 2016].

3.4.3 Astronomical tuning of Site U1334

We generate astronomically tuned age models for Site U1334 stretching from 88.93 CCSF-A (U1334A-9H-3) to 121.29 m CCSF-A (U1334B-11H-5), covering the complete OMT interval [*Westerhold et al.*, 2012]. To create an astronomically tuned stable isotope dataset for Site U1334, we consider two climatic proxy records, $CaCO_3$ est. (%) and benthic foraminiferal $\delta^{13}C$ as options for our tuning signal, and have constructed two independent tuned astronomical age models for Site U1334. As a starting point for tuning Site U1334 across the OMT, we used our initial magnetostratigraphic age model based on the GTS2012 [*Beddow et al*, 2016; *Vandenberghe et al.*, 2012; *Hilgen et al.*, 2012; *Channel et al.*, 2013] to assess the presence of astronomical variability in the data.

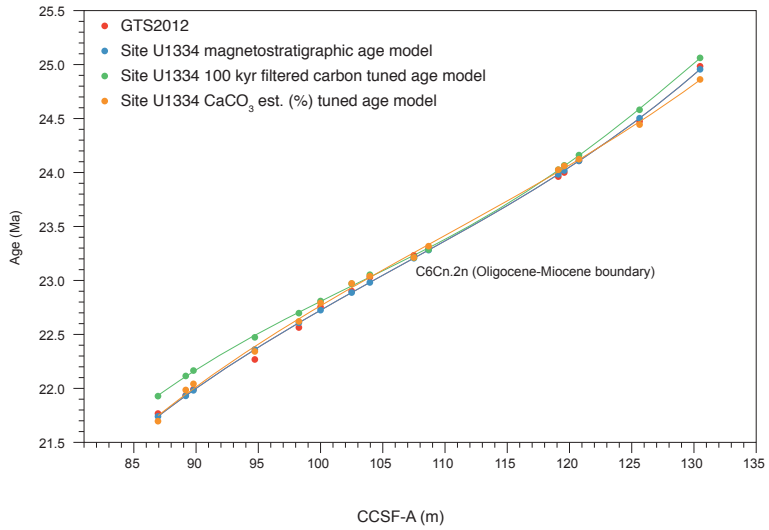

Figure 3.4. *Depth vs age plots for Site U1334, with magnetochron ages derived from GTS2012 (Vandenberghe et al., 2012; Hilgen et al., 2012) and the three independent age models discussed within this study. Magnetochrons are plotted as coloured circles, and the lines represent a third order polynomial fit.*

3.4.3.1 *Magnetostratigraphic age model*

Based on the initial age model, evolutive and power spectra demonstrate that the $CaCO_3$ est. (%) and benthic $\delta^{13}C$ and $\delta^{18}O$ records are dominated by 405 kyr and ~110 kyr eccentricity periodicities, with short intervals of significant response at shorter periodicities (higher frequencies) (Fig. 5). In addition, we filtered long (405 kyr) and short (~110 kyr) eccentricity related cycles of the $CaCO_3$ est. (%) and $\delta^{13}C$ records (Figs. 6a and 7a). We observe slightly more than 5 cycles (~5.25-5.5) related to long eccentricity in both the filtered $\delta^{13}C$ and $CaCO_3$ est. (%) records. Based on the bandpass filtering, we further find a small difference in the number of short eccentricity-related cycles present in the datasets, namely 23 in the $CaCO_3$ est (%) record, and 21 in the $\delta^{13}C$ record. This is unsurprising as the exact number is often very sensitive to the width of the bandpass filter. In the La2011 solution, we notice 5.5 405 kyr cycles and 22 short eccentricity cycles in the interval between 21.91 and 24.14 Ma.

3.4.3.2 *Astronomical target curve*

As our astronomical target curve, we chose eccentricity only, as time-series analyses in the depth domain and on our initial age model indicate that eccentricity is the dominant astronomical frequency present in our records, whilst lower periodicities are only intermittently expressed (Fig. 7). This is a departure from previously published OMT astronomical tuning strategies for high-resolution benthic stable isotope records, which have been constructed based on tuning to target-curves that are composed of a mix of eccentricity, obliquity and precession (Table 2) [*Shackleton et al*, 2000; *Zachos et al*, 2001; *Billups et al*, 2004; Pälike *et al*, 2006a, 2006b], and follows the strategy of *Liebrand et al.* [submitted]. The eccentricity time series was obtained from the most recent astronomical solution, La2011 which is reliable back to ~50 Ma [*Laskar et al.,* 2011a, 2001b; *Westerhold et al*., 2012b]. For the OMT interval, the solution is not significantly different from La2004 solution [*Laskar et al.*, 2004], which was used to generate previous astronomically tuned high-resolution age models for this time interval [*Pälike et al.*, 2006a,b].

3.4.3.3 *Astronomical tuning of the $CaCO_3$ record*

For our first tuning approach, we selected the $CaCO_3$ est. (%) record as a lithological tuning signal to construct an astronomically tuned age model. Using $CaCO_3$ est (%) as a tuning signal allows us to assess astronomical variability present within the benthic foraminiferal stable isotope datasets independent of tuning assumptions.

The initial magnetostratigraphic age model is a starting point for a more detailed calibration of maxima in $CaCO_3$ est. (%) to ~110 kyr eccentricity minima. Eccentricity minima represent the roundest orbits of the Earth around the Sun, which are on average least perturbed by the gravitational pull of the other planets and asteroids [*Berger*, 1980; *Laskar et al.,* 2004]. These astronomical configurations are relatively brief, appearing as clear, sharp points in the eccentricity solution (Fig. 6). We assume that the $CaCO_3$ est. (%) record is directly in anti-phase with eccentricity, as we find that in the depth domain and on the initial age model $CaCO_3$ maxima generally correspond with positive $\delta^{18}O$ and $\delta^{13}C$ values (i.e. cooler, more glacial periods), which are generally linked to eccentricity minima [*Zachos et al*., 2001].

We visually identify 23 complete short (~110 kyr) eccentricity cycles within our initial magnetostratigraphic age model using a Gaussian filter. As the $CaCO_3$ est. (%) record has clearly delineated maxima and minima on ~110 kyr timescales, we match maxima in the $CaCO_3$ record directly to minima in the La2011 eccentricity time series (Fig. 6c), taking the expression of the 405 kyr eccentricity cycle into account in addition.

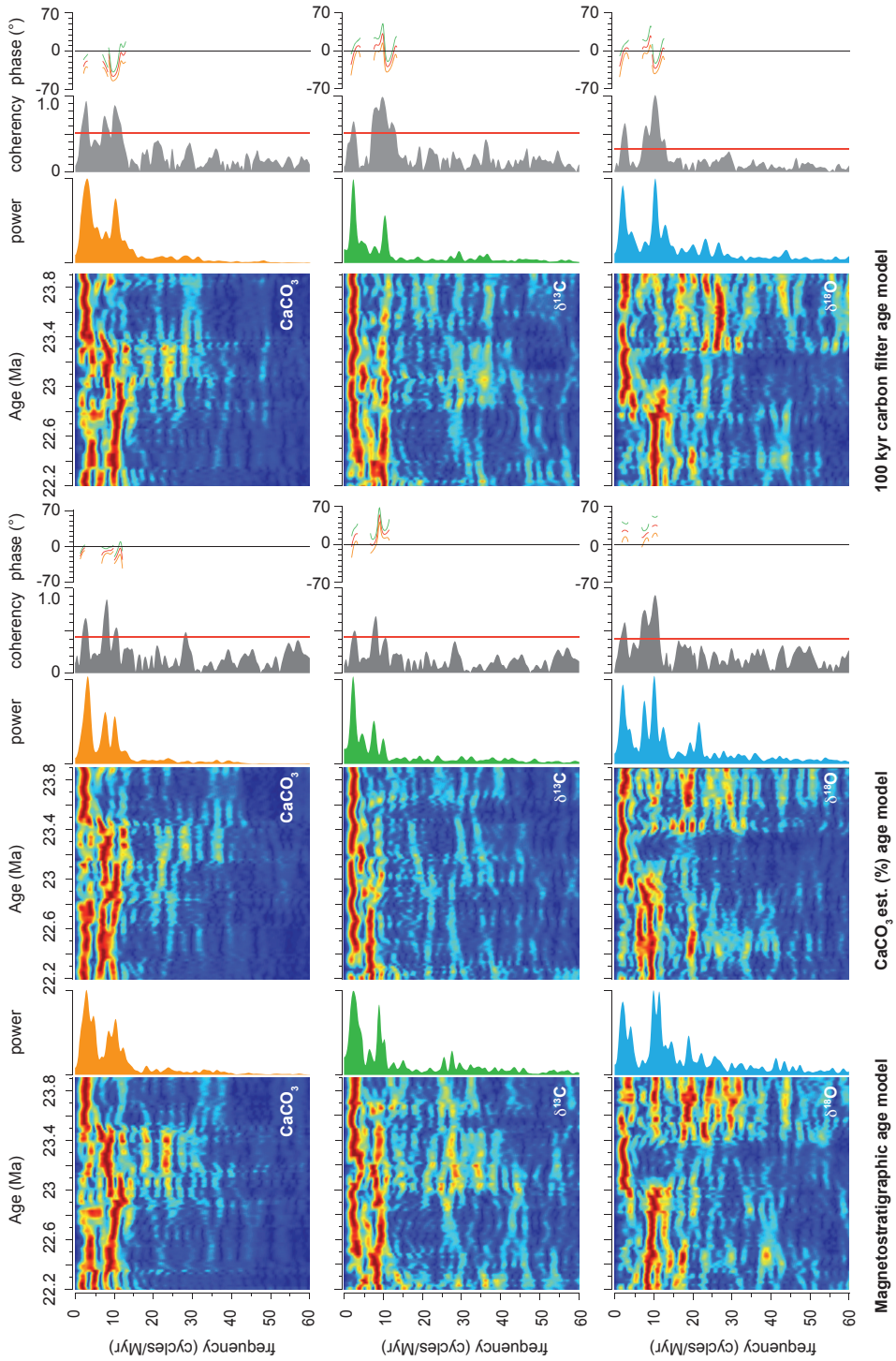
Age (Ma)
power
coherency
phase (°)
CaCO3
δ13C
δ18O
frequency (cycles/Myr)
Magnetostratigraphic age model
CaCO3 est. (%) age model
100 kyr carbon filter age model

Based on the $CaCO_3$ tuned age model option, the $CaCO_3$ est. (%) and stable isotope records from Site U1334 span the interval 21.96 to 24.15 Ma (2.19 Myr duration). Sedimentation rates vary around an average value of ~16 m/Myr, between 8.5 and 21.6 m/Myr, with higher sedimentation rates during the OMT (Fig. 6). This gives an average sample resolution of 3.6 kyr for the benthic foraminifer isotope records.

Evolutive analyses of $CaCO_3$ est. (%), $\delta^{13}C$ and $\delta^{18}O$ indicate that the dominant periodicity in all three records is at 405 kyr. In the $CaCO_3$ evolutive spectrum, the 405 kyr signal is relatively weak during the OMT (Fig. 5). In the $\delta^{13}C$ and $\delta^{18}O$ evolutive spectra we see the opposite, with weaker significance at all shorter periodicities relative to power at the 405 kyr cycle during the OMT. Power at the ~110 kyr periodicity increases after the OMT in all three records, particularly in the $\delta^{18}O$ record, where it becomes stronger than the 405 kyr signal, and we can identify power at both short eccentricity cycles (125 and 95 kyr) in the $CaCO_3$ and $\delta^{18}O$ datasets. In the $\delta^{13}C$, the evolutive and power spectra indicate short eccentricity forcing is more significant at the 125-kyr periodicity, compared to the 95-kyr component. We find intermittent power present at a ~ 50 kyr periodicity, which is either related to the obliquity cycle, and offset/transferred towards a longer periodicity, or to the first harmonic of the short eccentricity cycle [*King*, 1996]. It is strongest in the $\delta^{18}O$ datasets, where we can identify two main phases with significant power at a ~50 kyr periodicity between ~23.5and ~23.8 Ma and ~22.4 and ~22.6 Ma.

Cross-spectral analyses indicate that $CaCO_3$ est. (%), $\delta^{18}O$ and $\delta^{13}C$ are significantly coherent (99%) with eccentricity at the 405 kyr long and 125 and 95 kyr short eccentricity cycles (Fig. 5). Phase estimates of $\delta^{13}C$ with respect to eccentricity indicate that on the $CaCO_3$ astronomically tuned age model, $\delta^{18}O$ lags eccentricity by 23-27º (20-35 kyr) at the 405 kyr period and 4-50º (2-18 kyr) at the ~110 kyr periodicity, whilst $\delta^{13}C$ lags eccentricity by 23-28º (19-38 kyr) at the 405 kyr periodicity and 13-23º (5-8 kyr) and 34-36º (8-10 kyr) at the 125 kyr and 95 kyr short eccentricity cycles respectively (Fig. 5). $CaCO_3$ is roughly in phase with eccentricity by -2 to -18º (0-7 kyrs) at the 405 kyr periodicity, and by 0 to -18º (0-7 kyrs) and -1 to -27º (0-7 kyrs) at the 125 kyr and 96 kyr short eccentricity cycles respectively.

3.4.3.4 Astronomical tuning of the $\delta^{13}C$ record

An important consequence of our $CaCO_3$ astronomically tuned age model is that eccentricity-related variability within the $\delta^{13}C$ record is not in phase with the eccentricity time series [*Laskar et al., 2011* a,b] (Fig. 7b). In the early Miocene, on both the initial age model and the $CaCO_3$ tuned age model, the phasing between the 405 kyr eccentricity signal and the 405 kyr eccentricity filter of $\delta^{13}C$ shifts and becomes out of phase. This is not consistent with current ideas about the eccentricity pacing of the carbon cycle during the Oligocene-Miocene [*Holbourn et al*., 2004, 2013; *Pälike et al*., 2006a,b].

As an alternative astronomical tuning approach, we used the $\delta^{13}C$ record as tuning signal. An important constraint for our second tuning approach is given by the relatively strong 405 kyr signal

Figure 3.5. *Evolutive analyses, power spectra and coherence and phase plots for all three age models discussed within this study. Prior to analysis, the $CaCO_3$ data are resampled at a time step of 2 kyr, the benthic foraminiferal data are resampled at a time step of 4 kyr and periodicities larger than 600 kyr are notch-filtered out. Coherence and phase estimates between are between eccentricity La2011 solution and benthic foraminiferal stable isotope datasets. The significance level represented by the red line for the coherence plots is 99%. For the phase estimates between the benthic foraminiferal series and eccentricity, eccentricity was multiplied by -1.*

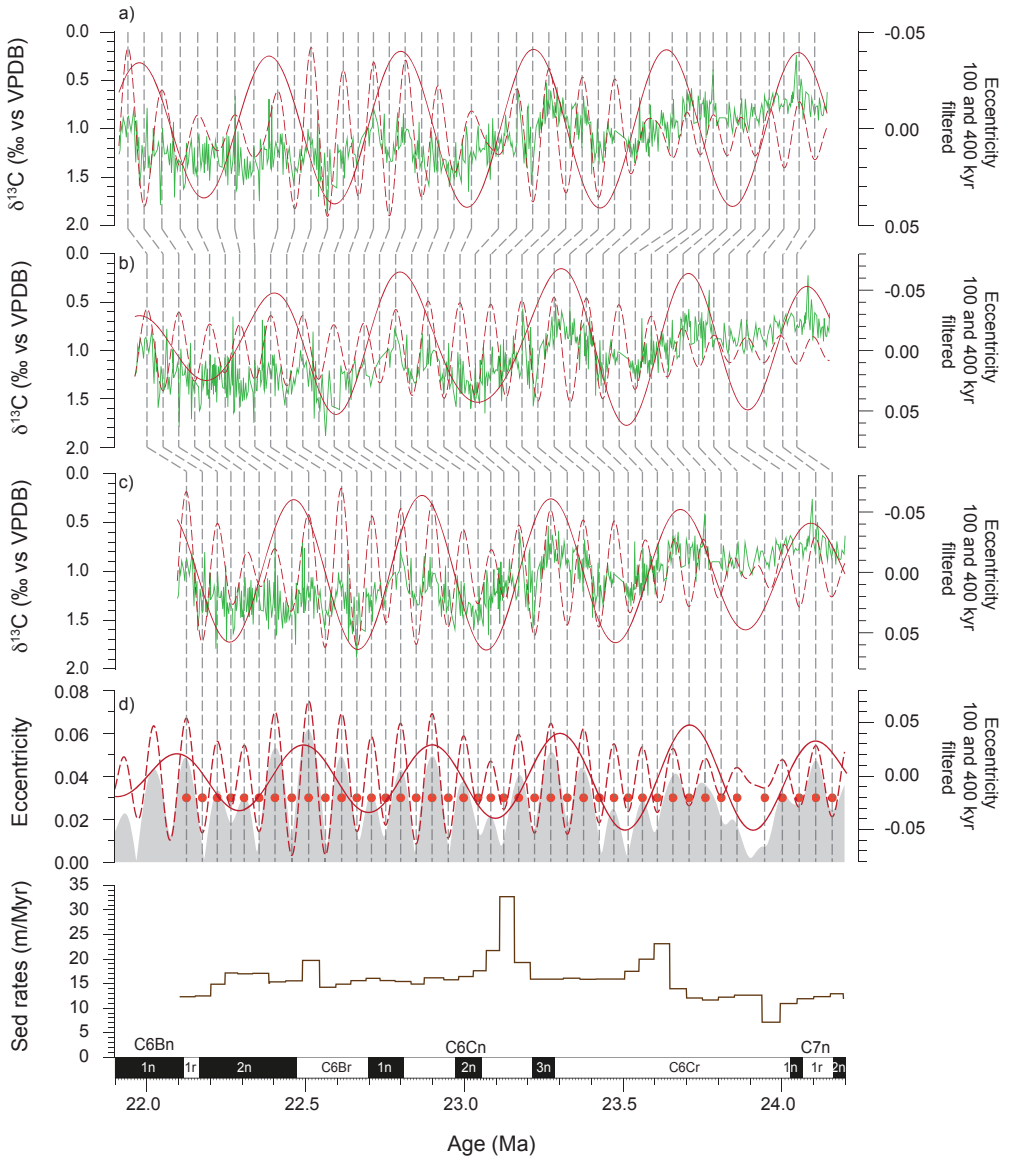

Figure 3.7. *Site U1334 $\delta^{13}C$ datasets (green line) and 405 kyr (solid red line) and ~110 kyr (dashed red line) Gaussian filters on the three independent age models. The $\delta^{13}C$ dataset and Gaussian filters plotted on the magenetostratigraphic age model (a), the option one age model, using $CaCO_3$ est. weights (%) as a tuning signal (b), and the option 2 age model, using the ~110 kyr filter of $\delta^{13}C$ as a tuning signal (c). Eccentricity is plotted in grey (d). Tie points between the ~110 kyr filter of the $\delta^{13}C$ dataset on magenetostratigraphic age model (a) and the ~110 kyr filter of eccentricity (d) are represented by red dots and dashed lines. Gaussian filters were calculated in AnalySeries [Palliard et al., 1996] with the following settings: 405 kyr – f: 2.5 bw 0.8, ~110 kyr – f: 10, bw: 3.*

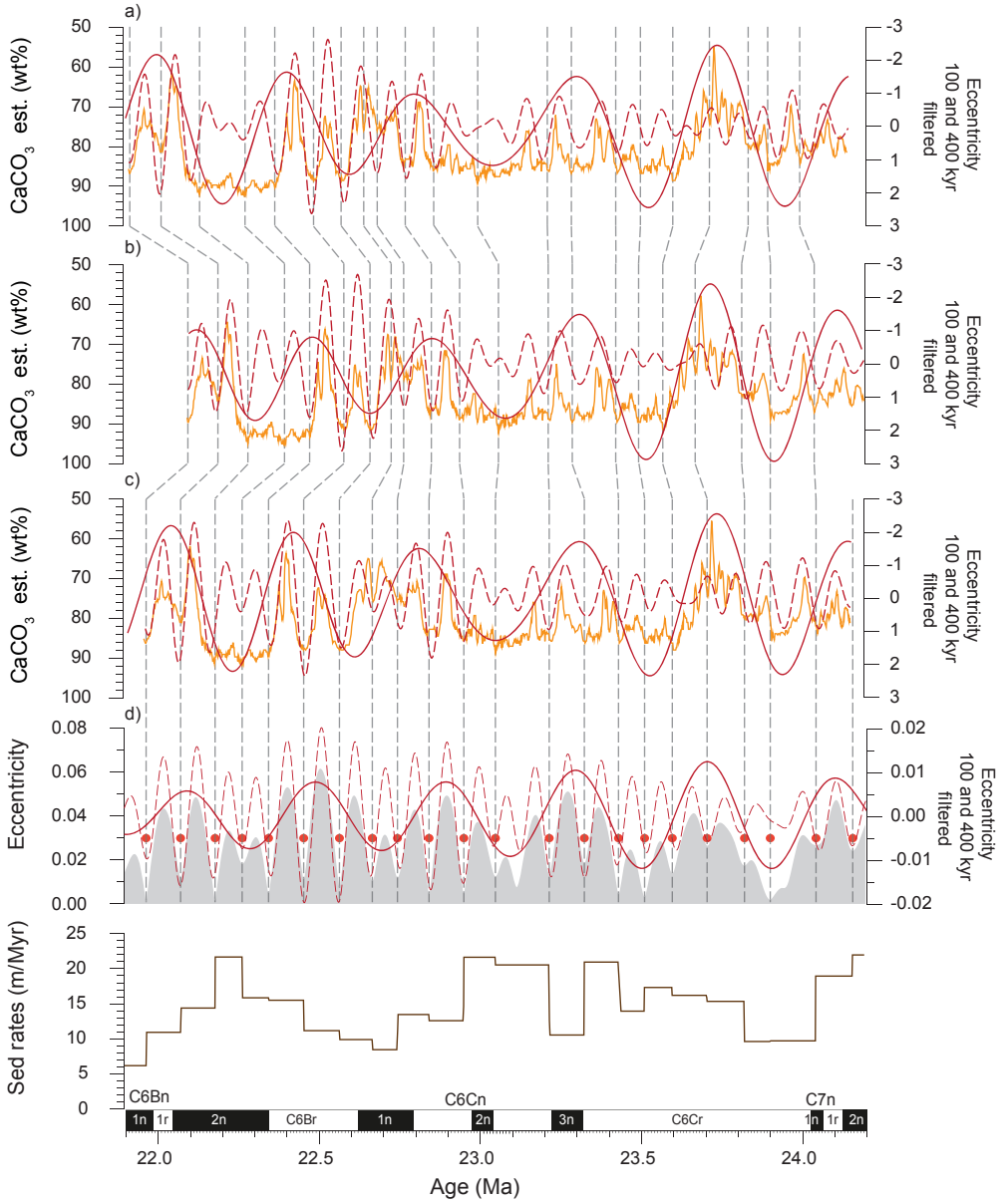

Figure 3.6. *Site U1334 $CaCO_3$ datasets (orange line) and 405 kyr (solid red line) and ~110 kyr (dashed red line) Gaussian filters on the three independent age models. Site U1334 $CaCO_3$ est. weights plotted on the magenetostratigraphic age model (a), the option one age model, using $CaCO_3$ est. weights (%) as a tuning signal (b) and the option 2 age model, using the ~110 kyr filter of $\delta^{13}C$ as a tuning signal (c). Eccentricity is plotted in grey (d). Tie points between eccentricity minima and est. $CaCO_3$ maxima are represented by red dots and dashed lines. Gaussian filters were calculated in AnalySeries [Palliard et al., 1996] with the following settings: 405 kyr – f: 2.5 bw 0.8, ~110 kyr – f: 10, bw: 3.*

in the $\delta^{13}C$ record (Fig. 5), which we assumed to be in-phase with the 405 kyr eccentricity cycle (Fig. 7d). We chose not to introduce a time lag between the solution and the $\delta^{13}C$ record, as beyond the Pliocene phases between orbital periodicities and climate response are uncertain [*Shackleton et al.*, 1999]. As a starting point for our $\delta^{13}C$ based time-scale, we identify 21 complete short (~110 kyr) eccentricity cycles within our initial age model using a Gaussian filter (Fig. 7a). We correlated minima and maxima in the Gaussian filtered ~110 kyr component of the $\delta^{13}C$ record from the initial age model to maxima and minima in the filtered short eccentricity time series (Fig. 7d).

As a result of our second astronomical tuning option, the $CaCO_3$ est. (%) and benthic stable isotope records span the interval between 22.1 and 24.2 Ma (2.1 Myr duration), resulting in an average time step of 3.4 kyr for the benthic stable isotope records. Linear sedimentation rates range from 7.2-32.7 m/Myr, with an abrupt, short-lived increase of ~17 m/Myr coincident with the ~1% positive shift in the $\delta^{18}O$ record across the OMT. On the $\delta^{13}C$ tuned age model, the $CaCO_3$ est. (%) record remains in anti-phase with respect to ~110 kyr eccentricity in the astronomical solution, but loses a cycle, and becomes ~110 kyr shorter in duration (Fig. 6 and 7). The evolutive analyses and power spectra are broadly consistent with the evolutive analyses from the $CaCO_3$ astronomically tuned age model, with dominant 405 kyr forcing in all three datasets, an increase in spectral power at ~110 kyr short eccentricity cycles after the OMT and intermittent significant power at lower periodicities. On the $\delta^{13}C$ tuned age model, all datasets exhibit a more significant response at the 95 kyr short eccentricity cycle rather than the 125 kyr periodicity, in contrast to the $CaCO_3$ tuned age model. Significant power at the 41 kyr obliquity periodicity is present in the late Oligocene, between ~ 23.3 and 23.8 Ma. We also find some expression of power in the evolutive spectra at precession related frequencies in the benthic stable isotope data, in $\delta^{18}O$ in particular, between 23.6 and 23.9 Ma.

Cross-spectral analyses on the $\delta^{13}C$ tuned age model (Fig. 5) indicate that $CaCO_3$, $\delta^{18}O$ and $\delta^{13}C$ are significantly coherent (99%) with eccentricity at the 405 kyr long and 125 and 95 kyr short eccentricity cycles. Phase estimates of $\delta^{13}C$ with respect to eccentricity (Fig. 5) indicate that on the $\delta^{13}C$ tuned age model, $\delta^{18}O$ lags eccentricity by 1-10º (1-9 kyr) at the 405 kyr period and 2-32º (1-10 kyr) at the 125 kyr periodicity, whilst $\delta^{13}C$ lags eccentricity by 1-8º (1-8 kyr) at the 405 kyr periodicity and 6-32º (2-10 kyr) at the 125 kyr short eccentricity cycle. In both the $\delta^{13}C$ and the $\delta^{18}O$, at the 95 kyr eccentricity cycle, both records lead eccentricity by -3 to -30º (1-9 kyr) and -4 to -30º (1-9 kyr) respectively. $CaCO_3$ leads eccentricity by -17 to -30 (15-40 kyrs) at the 405 kyr periodicity, and by -3 to -50º (1-13 kyrs) and-0 to -50º (0-14 kyrs) at the 96 kyr and 125 kyr eccentricity cycles respectively.

3.5 Discussion

3.5.1 Age model evaluation

The main rationale underlying the creation of two independent age models for Site U1334 is the shift in phasing between 405 kyr cycles in the $CaCO_3$ est. (%) and benthic stable isotope datasets, and the 405 kyr eccentricity [Figs. 5 and 6]. For both age models, we establish a final tuning to ~110 kyr short eccentricity, taking the 405 kyr cycle into account. Ideally, we would begin tuning by matching a 405 kyr signal in the proxy records to the eccentricity solution, before refining the tuning to the ~110 kyr cycle. This is complicated, however, as across the OMT the 405 kyr signal has a poor expression in the $CaCO_3$ est. (%) record, and in the $\delta^{13}C$ record the 405 kyr signal is attenuated by the OMT $\delta^{13}C$ maximum (Fig. 4)

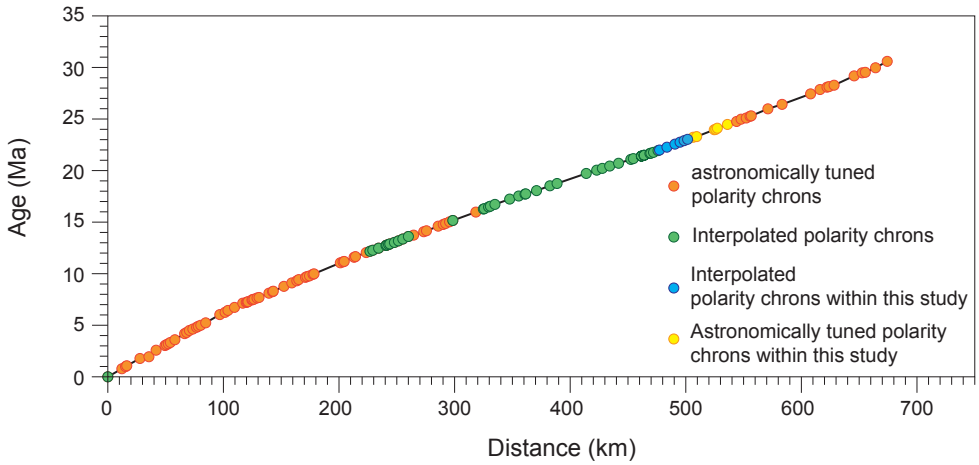

Figure 3.8. *Age calibration of marine magnetic anomalies from 0-30 Ma as compiled by Cande and Kent. (1992), indicating which polarity chrons have astronomically calibrated ages provided by this study.*

The two astronomical tuning approaches yield different age models for the late Oligocene and early Miocene time interval. The duration of the two age models for the Site U1334 stable isotope records differs by ~80 kyr, with the $\delta^{13}C$ tuned age model being ~1 eccentricity cycle shorter in duration than the $CaCO_3$ tuned age model. This is a direct result of the patterns observed in the 405 kyr and ~110 kyr cycles present in the datasets on the initial magnetostratigraphic age model. Although differences are present in the late Oligocene and early Miocene, the two astronomically tuned age models are consistent with each other across the positive $\delta^{18}O$ isotope excursion during the OMT, with the peak positive value in the $\delta^{18}O$ record, and the base of Chron C6Cn.2n (marking the Oligocene-Miocene boundary), occurring within 10 kyr on both age models. In the late Oligocene, the maximum difference between the two astronomically tuned age models is ~40-kyr, with the $CaCO_3$ tuned age model age model resulting in the youngest ages. This difference is within the duration of one obliquity cycle and could be explained by different phase relations between $\delta^{13}C$ and eccentricity and $CaCO_3$ and eccentricity. The largest point of difference between the two astronomically tuned age models occurs during the early Miocene, when the two age model options diverge at ~22.7 Ma by one short eccentricity cycle. This leads to the earliest part of the stable isotope record in the early Miocene being 130 kyr older in the $\delta^{13}C$ tuned age model than in the $CaCO_3$ tuned age model. This difference is age is accounted for by the difference of one short eccentricity cycle in the tuning, and by a difference of ~30-40 kyrs in the relative phasing between $CaCO_3$ and $\delta^{13}C$. In principle, the two age models can be made more consistent by tuning all ~110-kyr eccentricity related cycles in $CaCO_3$ est. (%) between 21.9 and 22.7 one short eccentricity cycle older. In that case the difference with the $\delta^{13}C$ based age model would be accounted for solely by the relative phasing of the two proxies to eccentricity and not by a difference in the tuning. Such a retuning may further eliminate the significant lag observed between the filtered 405 kyr cycles between $CaCO_3$ and the 405 kyr eccentricity cycle, and the dominance of the 125 kyr cycle relative to the 95 kyr cycles in the $CaCO_3$ est. (%), $\delta^{13}C$ and $\delta^{18}O$ on the $CaCO_3$ tuned age model.

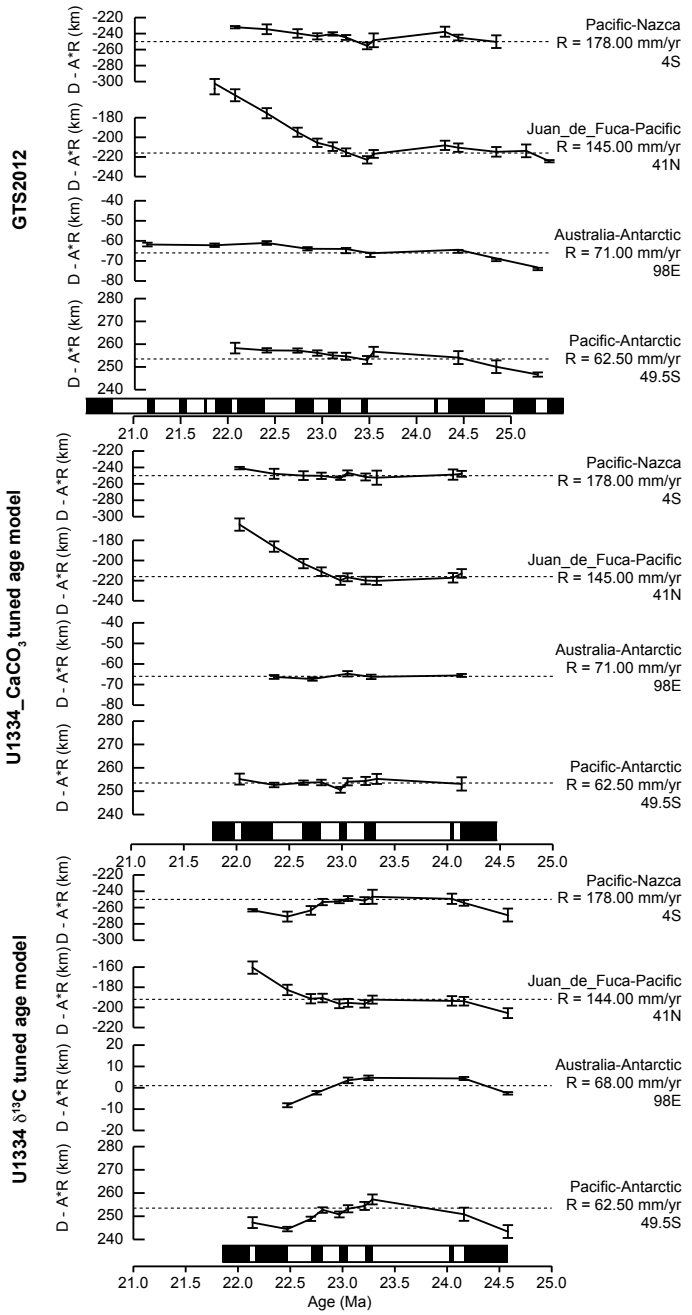

Figure 3.9. *Reduced-distance plots for the labeled plate pairs implied by the GTS2012 (a), the $CaCO_3$ tuned age model (b) and the $\delta^{13}C$ tuned age model (c). Reduced distance is the full spreading distance (D) minus the age (A) times the labeled spreading rate (R). Distance scale is plotted inversely with spreading rate so that for true constant spreading rate, age errors will cause uniform vertical departures from a straight line. Error bars are 95% confidence. The $CaCO_3$ based age model (b) gives the simplest spreading rate history.*

The evolutive and power spectra indicate that on the $\delta^{13}C$ tuned age model, all datasets exhibit a more significant response at the 95 kyr short eccentricity cycle, which is in contrast to the $CaCO_3$ tuned age model, where all datasets show a more significant response at the 125 kyr short eccentricity cycle. Previous OMT tunings (Fig. 10) have identified a stronger 125 kyr signal at other sites (Table 2 and Fig. 11), which is consistent with the $CaCO_3$ tuned age model [*Shackleton et al.*, 2000; *Zachos et al.*, 2001; *Pälike et al.*, 2006a,b]. However, the 95 kyr eccentricity cycle has a the stronger signal in the astronomical solution (Fig. 11) [*Laskar et al.*, 2011a,b], consistent with $\delta^{13}C$ tuned age model.

Comparing the evolutive spectra for the $\delta^{18}O$ dataset on both astronomical age models (Fig. 5), we see enhanced power at higher frequencies on the $\delta^{13}C$ tuned age model, including some variation at precession frequencies during the late Oligocene. Both age models show enhanced power in the $\delta^{18}O$ evolutive spectra potentially related to obliquity periodicities between ~23.3 Ma to ~23.8 Ma. On the $\delta^{13}C$ tuned age model, enhanced power corresponds to at 40-kyr periodicity, whereas on the $CaCO_3$ tuned age model, significant power during the same time period is found at a ~50-kyr periodicity.

3.5.2 Phase relationships

We need to take into consideration both potential phase relationships and global versus local influences on climate proxy signals when choosing the most optimal signal to tune to. We make a simple assumption when constructing both age model options that the proxy signal chosen as the tuning signal is directly in phase with insolation, and that this phase relationship between insolation and the tuning signal remains constant throughout the record. We do not introduce a time lag between the tuning signal and the tuning target largely because lead- and lag-relationships are difficult to determine [*Shackleton et al.*, 1999].

Variations in the $\delta^{13}C$ signal are generally considered to best reflect global ocean signals, but generally lag global climate by ~10% on all periodicities (Table 2) [*Billups et al.*, 2004; *Pälike et al.*, 2006a,b; *Liebrand et al.*, submitted). The $CaCO_3$ signal most likely represents a more regional response to insolation since it depends on regional carbonate productivity; export productivity and dissolution, probably as a more direct response to insolation forcing [*Hodell et al.*, 2001]. In addition, the amount of dissolution in $CaCO_3$ est. (%) is difficult to reconstruct, as the closed sum effect means that reconstructed values of $CaCO_3$ are dependent on the size of the terrigenous component, particularly at low levels of $CaCO_3$ est. (%) [*Broecker*, 1995; *Stap et al.*, 2009]. However, our tuning signal tie-points are based on $CaCO_3$ maxima, and we avoid tuning $CaCO_3$ minima. Furthermore, Site U1334, in the middle of the Pacific Ocean, is located far away from the Eurasian and North American landmasses, making the only source of terrigenous material a rather small wind-blown component.

However, in this respect, the $CaCO_3$ est. (%) record is more likely to be in-phase with insolation than the slower responding climate/cryosphere system and carbon cycle represented by the $\delta^{18}O$ and $\delta^{13}C$ stable isotope records [*Pälike* et al., 2006a,b; *Liebrand et al.*, 2011]. The in-phase assumption between the $CaCO_3$ est. (%) record and eccentricity (for the $CaCO_3$ tuned age model), is supported by the resulting phase relation on the ~110 kyr timescale between eccentricity and $\delta^{18}O$ and $\delta^{13}C$, which is in agreement with previously published astrochronologies (Table 2 and Figs. 5 and 10) [*Billups et al.*, 2004; *Pälike et al*, 2006a, b; *Liebrand et al.*, submitted]. The phasing of the 405 kyr periodicity between $\delta^{13}C$ and eccentricity on the $\delta^{13}C$ tuned age model is more in-phase than the 405 kyr component of $\delta^{13}C$ is with eccentricity on the $CaCO_3$ tuned age model, which starts to

Table 3.1. *Polarity Chron ages.*

Chron (old end)	CCSF-A [*Channell et al.*, 2013]	GTS2004 (Myrs) [*Lourens et al, 2004]*	GTS2012 (Myrs) [*Hilgen et al.*, 2012]	Onset (Myrs) *Billups et al*, 2004	Onset (Myrs) *Palike et al*, 2006	Onset (Myrs) $CaCO_3$ based astronomical tuning	Onset (Myrs) D13C based astronomical tuning	Difference Between GTS2012 and *Billups et al.*, 2004 (Myrs)	Difference Between GTS2012 and *Pälike et al.*, 2006 (Myrs)	Difference Between GTS2012 and $CaCO_3$ based tuning (Myrs)	Difference Between GTS2012 and $CaCO_3$ based tuning (Myrs)
C6AAr.3r	86.94	21.767	21.767	21.847	21.853			-0.080	-0.086		
C6Bn.1n	89.17	21.936	21.936	21.991	21.998	21.985	22.115	-0.055	-0.062	-0.049	-0.179
C6Bn.1r	89.79	21.992	21.992	22.034	22.062	22.042	22.165	-0.042	-0.070	-0.050	-0.173
C6Bn.2n	94.72	22.268	22.268	22.291	22.299	22.342	22.473	-0.023	-0.031	-0.074	-0.205
C6Br	98.26	22.564	22.564	22.593	22.588	22.621	22.697	-0.029	-0.024	-0.057	-0.133
C6Cn.1n	100.00	22.754	22.754	22.772	22.685	22.792	22.809	-0.018	0.069	-0.038	-0.055
C6Cn.1r	102.50	22.902	22.902	22.931	22.854	22.973	22.970	-0.029	0.048	-0.071	-0.068
C6Cn.2n	103.96	23.030	23.030	23.033	23.026	23.040	23.053	-0.003	0.004	-0.01	-0.023
C6Cn.2r	107.50	23.249	23.233	23.237	23.278	23.212	23.211	-0.004	-0.045	0.021	0.022
C6Cn.3n	108.68	23.375	23.295	23.299	23.340	23.318	23.286	-0.0026	-0.045	-0.023	0.009
C6Cr	119.10	24.044	23.962	23.988	24.022	24.025	24.026	-0.013	-0.060	-0.063	-0.064
C7n.1n	119.58	24.102	24.000	24.013	24.062	24.061	24.066	-0.029	-0.038	-0.061	-0.066
C7n.1r	120.76	24.163	24.109	24.138	24.147	24.124	24.161			-0.015	-0.052
C7n.2n	125.63	24.556	24.474				24.581				

become out-of phase during the OMT and into the early Miocene (Figs. 6 and 7). This phasing issue in the $CaCO_3$ tuned age model lends support to the $\delta^{13}C$ based tuning.

3.5.3 Magnetostratigraphy

Of the two independent astronomical age models for Site U1334, the chron ages of the $CaCO_3$ tuned age model are closest to those of the GTS2012 (within 60 kyrs) [*Hilgen et al.*, 2012; *Vandenberghe et al.*, 2012], especially for the early Miocene interval, where the two age models diverge at ~22.7 Ma (Table 1). Between C6Bn.1n and C6Br, in the early Miocene, the $\delta^{13}C$ tuned age model chron ages are a ~110-kyr eccentricity cycle older than GTS2012 (Table 1). On the $CaCO_3$ tuned age model, polarity chron ages are generally older by 15-55 kyr than the ages given in GTS2012, with the exception of C6Cn.2r, which is ~20-30 kyr younger on both our independent age models [*Hilgen et al.*, 2012; *Vandenberghe et al.*, 2012]. This is in agreement with the polarity ages given by *Billups et al.* (2004) and *Pälike et al.* (2006b) for the early Miocene, which are also consistently older than the GTS2012 ages (Table 1) [*Hilgen et al.*, 2012]. The late Oligocene chrons in GTS2012 are based on the astronomically tuned ages of *Pälike et al.* (2006b) [*Vandenberghe et al.*, 2012].

From C5Cn.1n in the mid Miocene, to the base of C6Cn.2n, which marks the Oligocene-Miocene boundary, numerical ages given for polarity chrons in the GTS2012 [*Hilgen et al.*, 2012] are based on assumed piecewise constant Australia-Antarctica spreading rates, and remain the same as the numerical ages given in the GTS2004 [*Lourens et al.,* 2004] (Fig. 8). Reversal ages for this period (16 Ma-23 Ma) based on high-resolution stable isotope datasets have been published since GTS2004 and are candidates to replace the polarity chron ages derived from spreading rates [*Billups et al.*, 2004; *Pälike et al.*, 2006b, *Hilgen et al.*, 2012]. However, the ages derived from these astronomically tuned stable isotope records are not consistent with the assumption of constant spreading rates which underlies the construction of the GTS2004, and the early Miocene part of the timescale between ~16 and 23 Ma is not astronomically calibrated [*Lourens et al.*, 2004; *Hilgen et al.*, 2012].

We use spreading rates as an independent check to discriminate between the two different age model options presented here, using techniques introduced by *Wilson* [1993] and applied subsequently independently testing astronomical tuning [e.g., *Krijgsman et al.*, 1999; *Hüsing et al.*, 2007]. The central idea is that when multiple plate pairs show simultaneous changes in spreading rate with the same ratio, this indicates errors in the timescale. Plate pairs used are, in order of decreasing spreading rate, Pacific-Nazca, Pacific-Juan de Fuca, Australia-Antarctic, and Pacfic-Antarctic. Data for the Pacfic-Nazca pair are only from the northern part of the system, where interest in initiation of the Cocos-Nazca boundary during C6Bn has focused on data collection [*Lonsdale*, 2005; *Barckhausen et al.,* 2008]. Pacific-Juan de Fuca data are from immediately north of the Mendocino fracture zone, an area used in previous timescale calibrations [e.g. *Cande and Kent*, 1992] even though only the Pacific-plate record survives. *Wilson* [1988] interpreted a sudden change of spreading-rate gradient for this pair from south faster prior to C6Cn.2n(o) to north faster afterward. The dataset for the Australia-Antarctic pair is similar to that presented by *Cande and Stock* [2004] and is slightly expanded from that used by *Lourens et al.* [2004] for early Miocene calibration. Data for Pacific-Antarctic come primarily from recent surveys near the Menard and Vacquier fracture zones [*Croon et al.*, 2008].

Of our two age models and GTS2012, the $CaCO_3$ tuned age model is most consistent with spreading rates (Fig. 9). On the $CaCO_3$ tuned age model, the Australia-Antarctica, Pacific-Nazca, and Pacific-Antarctic plate pairs are all very close to a constant spreading rate, at least prior to C6Bn. The Juan de Fuca-Pacific plate pair indicates a sudden decrease in spreading rate (145 to 105

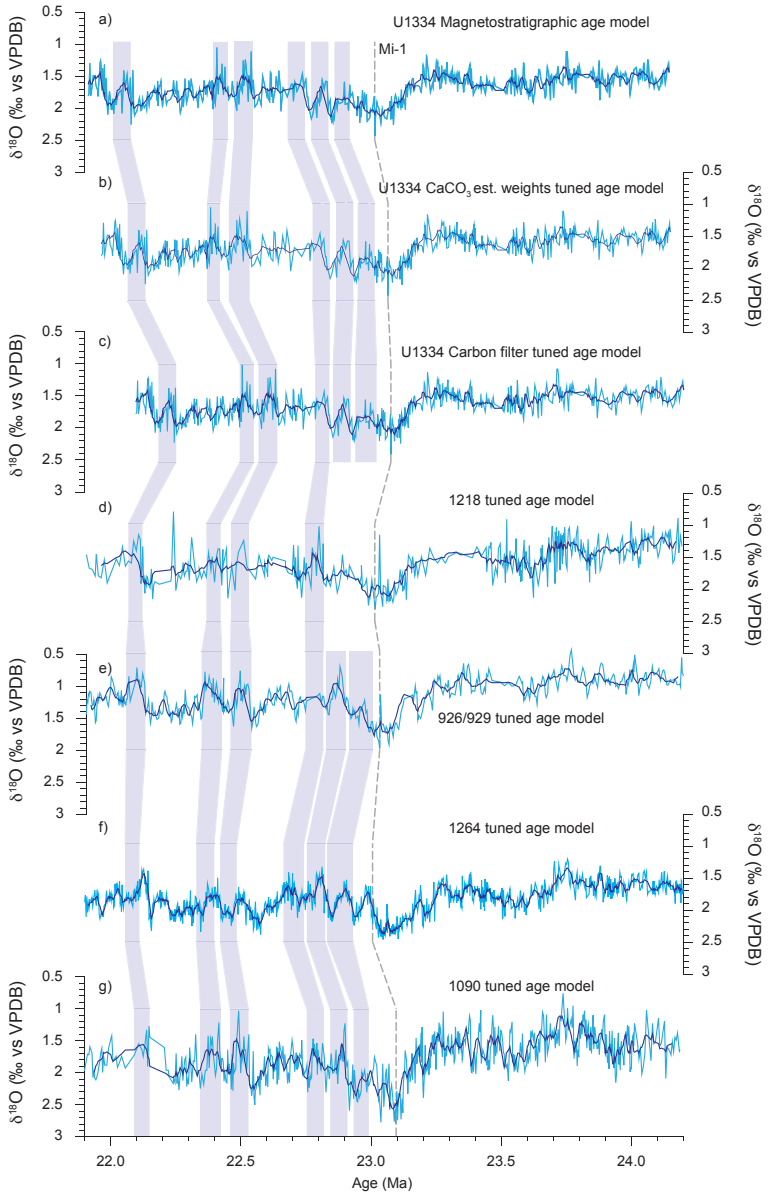

Figure 3.10. *Comparison of the Site U1334 $\delta^{18}O$ on all three independent age models with previously published high-resolution benthic foraminiferal $\delta^{13}C$ records. The datasets are plotted in light green, with a seven point moving average plotted in dark green. Plotted are Site U1334 $\delta^{18}O$ on the magenetostratigraphic age model (a), Site U1334 $\delta^{18}O$ dataset on the $CaCO_3$ based age model (b) Site U1334 $\delta^{18}O$ dataset on the carbon isotope based age model (this study) Site 1218 $\delta^{18}O$ (d) [Pälike et al., 2006b] Sites 926/929 $\delta^{13}C$ (e) [Flower et al., 1997; Zachos et al., 1997, 2001; Paul et al., 2000; Pälike et al., 2006a; Shackleton et al., 2000], Site 1264 $\delta^{18}O$ (f) [Liebrand et al., 2011] and Site 1090 $\delta^{18}O$ (g) [Billups et al., 2002, 2004]. Shaded purple lines highlight the timing of individual ~110 kyr cycles between independent age models.*

Table 3.2. *Tuning strategy comparison*

Site	Tuning signal	Tuning target	Lead/lag 405 kyr $\delta^{13}C$	Lead/lag ~110 kyr $\delta^{13}C$	Lead/lag ~405 kyr $\delta^{18}O$	Lead/lag ~110 kyr $\delta^{18}O$	Lead/lag ~405 kyr $CaCO_3$ est (%)	Lead/lag ~110 kyr $CaCO_3$ est (%)
Site U1334 (This study)	$CaCO_3$ est. %	Eccentricity	Lag ~30 kyrs	Lag ~10 kyrs	Lag ~25-30 kyrs	Lag ~10 kyrs	In phase	In phase
Site U1334 (This study)	Carbon isotopes	Eccentricity	In phase	Lag ~10 kyrs at 125 kyr, In phase at 96 kyr	In phase	Lag ~10 kyrs	Leads ~20 kyrs	Leads ~10 kyrs
Site 1090 (*Billups et al.*, 2004)	Oxygen isotopes	ETP	Lag ~20 -30 kyrs	Lag ~20 -30 kyrs	In phase	In phase at 125 kyr, ~10 kyr lag at 96 kyr	-	-
Site 926 (*Palike et al.*, 2006a)	Combination of magnetic susceptibility and colour reflectance (SusRef)	ETP	Lag ~35 kyrs	Lag ~30 kyrs	Lag ~ 10 kyrs	Lag ~20 kyrs	-	-
Site 1218 (*Palike et al.*, 2006b)	Carbon isotopes	ETP	Lag ~30 kyrs	In phase	Lag ~10 kyrs	In phase	-	-
Site 1264 (*Liebrand et al.*, submitted)	$CaCO_3$ est. (%)	Eccentricity	Lag ~36 kyrs	Lag ~12 kyrs	Lead ~14 kyrs	Lag ~12 kyrs	Unstable phase	In phase

mm/yr) at ~23 Ma, consistent with expectations [*Wilson*, 1988]. The implied synchronous changes for the Australia-Antarctica, Pacific-Nazca, and Pacific-Antarctic plate pairs in the $\delta^{13}C$ tuned age model, especially the faster spreading rates ~22.5-23.0 Ma implied by older ages for C6Bn, make this option less credible. Differences between the $CaCO_3$ tuned age model for Site U1334 and GTS2012 are more subtle. Most visible is the effect of our longer duration of C6Cn.3n (106 vs. 62 kyr), which eliminates a brief pulse of fast spreading implied by GTS2012. Over longer intervals, $CaCO_3$ tuned ages remove a slight but synchronous rate slowdown implied by GTS2012 at ~23.2 Ma.

The spreading rates implied by the $CaCO_3$ tuned age model suggest that the $CaCO_3$ tuned duration for C6Cn.2n may be up to ~30 kyr too short. Although our distance error bars imply only marginal significance of this discrepancy, it is worth mentioning because it might imply an age of up to 23.06 Ma for the Oligocene-Miocene boundary, in agreement with *Liebrand et al.*, [submitted]. This could indicate an uncertainty in the magnetostratigraphy, although this is unlikely as the C6Cn.2n reversal is clearly delineated in the VPG latitude signal [*Channell et al.*, 2013]. An alternative explanation is an uncertainty in the tuning signal. In both the $CaCO_3$ est (%) and $\delta^{13}C$ record, this short interval is difficult to align to the tuning target (Figs. 5 and 6). In this interval, $CaCO_3$ est. (%) values are high, with little variability. In the $\delta^{13}C$ record, this interval corresponds to the marked shift towards more enriched values at the Oligocene-Miocene carbon maximum [*Hodell and Woodruff*, 1994]. The 83 kyr duration of C6Cn.2n from the $\delta^{13}C$ tuned age model is more consistent with spreading rates than the 67 kyr duration from the $CaCO_3$ tuned age model.

3.5.4 Comparison of astronomical variability between sites

We compare our astronomically tuned age model from Site U1334 to four other drill localities with high-resolution astronomically tuned benthic stable isotope records encompassing the OMT (Fig.1 and Table 2). U1334 is compared with 1) a composite record constructed using stable isotope data from ODP Site 926 (Hole B, 3598 mbsl) and Site 929 (Hole A, 4358 mbsl) from Ceara Rise in the equatorial western Atlantic Ocean, [*Shackleton et al.*, 1999; *Zachos et al.*, 2001; *Pälike et al.*, 2006a], 2) ODP Site 1218 (composite of Holes A, B and C, 4827 mbsl) in the eastern equatorial Pacific [*Pälike et al.*, 2006b], 3) ODP Site 1090 (composite of Holes D and E, 3699 mbsl) from the Agulhas Ridge in the Atlantic sector of the Southern Ocean [*Billups et al.*, 2004], and 4) ODP Site 1264 (composite of Holes A and B, 2505 mbsl), from the Walvis Ridge in the south eastern Atlantic Ocean in the south-east Atlantic [*Liebrand et al.*, 2011, submitted]. The methodology for creating these age models is distinct from the astronomical age models presented here for IODP Site U1334, and for that from Site 1264, which are both tuned solely to eccentricity. For a summary of tuning signals, tuning targets and phase relations for these astronomical age models, see Table 2.

Comparing the two independent astronomical age models for Site U1334 with other independent age models from different sites, we find that the $CaCO_3$ tuned age model is more consistent with previous tunings for the OMT than the $\delta^{13}C$ tuned age model (Table one and Fig. 10), which is important in light of the different choices of both lithological and geochemical based tuning signals, and provides additional support for the $CaCO_3$ tuned age model. The $\delta^{13}C$ tuned age model deviates in the early Miocene at ~22.7 Ma, which is particularly clear in the timing of individual ~110 kyr cycles identified at all sites in the $\delta^{18}O$ datasets during the early Miocene (Fig. 10, purple bars represent visual identifications of contemporaneous ~110 kyr cycles).

Evolutive analyses and power spectra for the five high-resolution stable isotope records covering the OMT, indicates that all records exhibit cyclicity on astronomical time scales (Fig. 11). The most robust astronomical features present at all sites are the consistent 405 kyr cyclicity, present throughout the entire OMT interval, and the increase in power at ~110 kyr periodicity after the

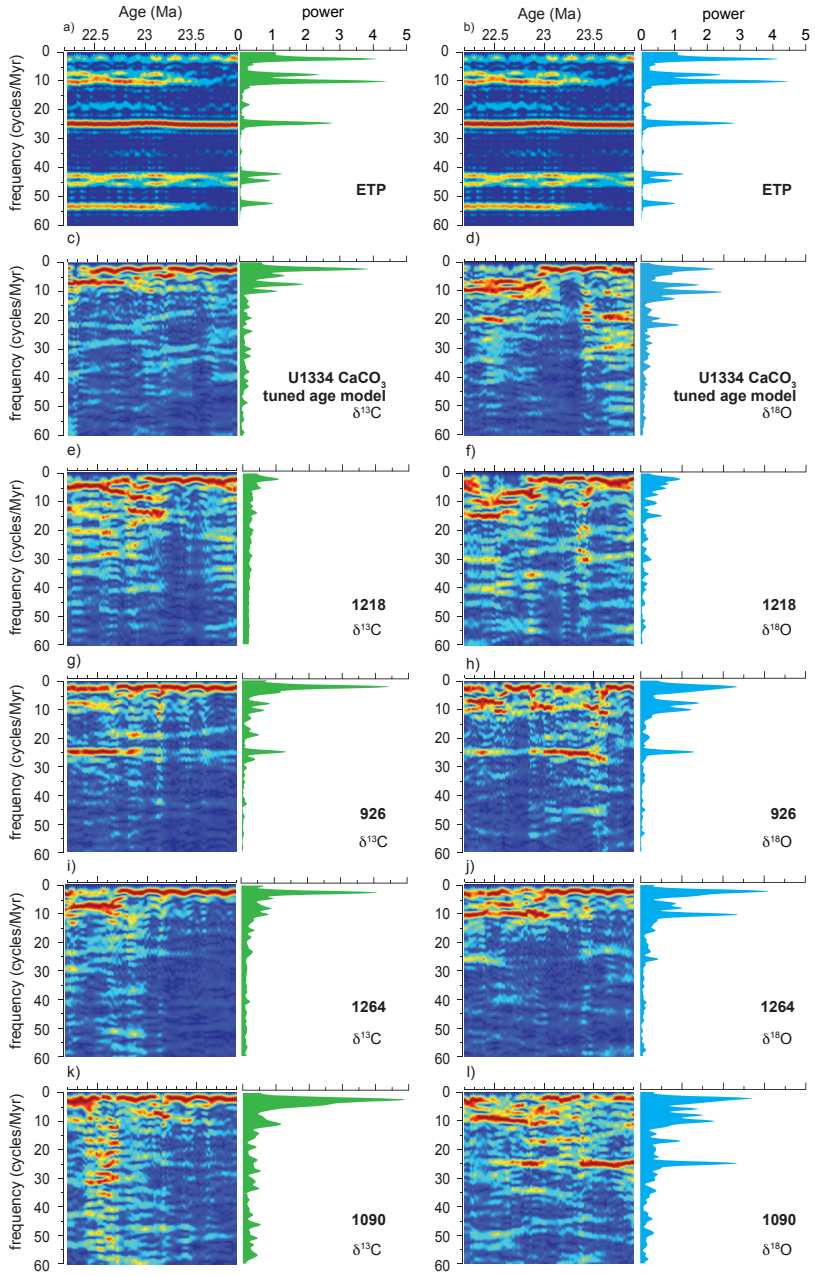

Figure 3.11. *A comparison of evolutive and Blackman-Tukey power spectra across several high-resolution records from different sites on independent age models. Plotted are evolutive and power spectra for ETP (a and b), calculated from La2010 [Laskar et al., 2011a,b] Site U1334 $\delta^{13}C$ (c) and $\delta^{18}O$ (d) datasets on the $CaCO_3$ tuned age model, Site 1218 $\delta^{13}C$ (e) and $\delta^{18}O$ (f) [Pälike et al., 2006b] Site 926/929 $\delta^{13}C$ (g) and $\delta^{18}O$ (h), [Pälike et al., 2006a], Site 1264 $\delta^{13}C$ (i) and $\delta^{18}O$ (j) [Liebrand et al., 2011] and Site 1090 $\delta^{13}C$ (k) and $\delta^{18}O$ (l) [Billups et al., 2004].*

positive $\delta^{18}O$ excursion across the OMT [*Zachos et al.*, 1997; 2001]. The significant climate response at the 405 kyr periodicity is a pervasive imprint on Cenozoic stable isotope records throughout the Miocene, Oligocene and Eocene [e.g. *Zachos et al.*, 2001; *Wade and Pälike*, 2004; *Pälike et al*, 2006a; *Holbourn et al.*, 2013; *Littler et al*, 2014].

During the $\delta^{18}O$ excursion at the OMT, there is weak significance at all periodicities shorter than 405 kyrs, followed by the strong expression at ~110 kyrs in the early Miocene. The low amplitude variability at all periodicities shorter than 405 kyr at ~23.0 Ma is indicative of a brief (~200 kyrs) interval with a large, stable, dry-based ice sheet on Antarctica during the OMT. Following the $\delta^{18}O$ excursion across the OMT, the increase in ~110 kyr high-amplitude variability, and the change in the $\delta^{18}O$ values and amplitude variability between the late Oligocene to Miocene values, suggests that climate transitioned to a more glaciated state, characterized by more variable ice volume, with large amplitude 100 kyr cycles in $\delta^{18}O$, which remained strong in the early Miocene of Site U1334 until 21.9 Ma.

The expression of obliquity is not consistent between isotope chronologies from different sites, with a strong response recorded at equatorial Atlantic Site 929 and in the Southern Ocean at Site 1090 [*Pälike et al.*, 2006a; *Billups et al.*, 2004], intermittent expression at Site U1334 [*Beddow et al.*, 2016] and a very weak obliquity response in the south-east Atlantic [*Liebrand et al.*, 2011]. If present, the obliquity signal seems most consistent in the late Oligocene interval prior to the OMT in all $\delta^{18}O$ records, implying that across the OMT, we see a change in spectral energy from shorter periodicities (higher frequencies) to longer periodicities (lower frequencies) [*Zachos et al.*, 2001; *Pälike et al.*, 2006a,b].

The large range in the obliquity response recorded at different deep-ocean could be a result of low sedimentation rates, where bioturbation can potentially remove shorter periodicity signals. The sedimentation rates at Site 1264 (~1.0 cm/kyr), are two-three times lower than those seen at equatorial Atlantic Sites 926 and 929, which do record a strong imprint of obliquity in both the depth and age domain [*Shackleton et al.*, 2000; *Pälike et al.*, 2006a]. Previous studies modeling the effect of bioturbation at low sedimentation rates have demonstrated that bioturbation can remove higher frequency signals, leading to a transfer of power to lower frequencies [*Ripepe and Fischer*, 1991; *Herbert*, 1994].

3.6 Conclusions

We explore the application of $CaCO_3$ est. (%) and benthic foraminiferal $\delta^{13}C$ records as tuning signals for the OMT record at IODP Site 1334 in the eastern equatorial pacific. These two tunings produce two very different age models, highlighting the importance of carefully considering the implications of tuning choices and assumptions when creating astronomical age models. The $CaCO_3$ tuned age model supports previously published tunings constructed using stable isotopes as a tuning signal, whilst the $\delta^{13}C$ tuned age model presents an alternative tuning option for the early Miocene. The new astronomically tuned age models provide astronomically calibrated ages for C6AAr.3r to C6Cn.1r, which in GTS2012 are not presently astronomically calibrated. Spreading rates provide an independent check on our age models, and are more consistent with the $CaCO_3$ tuned age model suggesting this as the more likely age model option. This suggests that lithological signals respond more directly to insolation forcing than stable isotope signals, which respond with a lag, and are suitable tuning targets for astronomical tuning. The polarity chron ages from the $CaCO_3$ tuned age model are generally older than the ages given in GTS2012, suggesting that the early

Miocene portion of the GTS will undergo adjustments of up to 60 kyrs. Astronomical periodicities shift from shorter to longer periodicities across the OMT, moving from significant 41 kyr forcing in the late Oligocene to a characteristic increase in power at ~110 kyrs in the early Miocene, suggesting a change in the astronomical pacing of climate variability occurs coincident with the OMT.

Acknowledgements

This research used samples provided by the Integrated Ocean Drilling Program (IODP), collected by the staff, crew and scientists of IODP Expedition 320/321. We thank Dominika Kasjanuk, Arnold van Dijk, Maxim Krasnoperov and Jan Drenth for laboratory assistance and Vittoria Lauretano and Frits Hilgen for useful discussions. This research was supported by NWO VICI grant no. [865.10.001] awarded to L. J. Lourens. A. Sluijs thanks the European Research Council (ERC) under the European Union Seventh Framework Program for ERC Starting Grant #259627. B S. Wade was supported by UK Natural Environment Research Council (NERC) reference number NE/G014817, and a Marie Curie Career Integration Grant "ERAS". This work was carried out under the program of the Netherlands Earth System Science Centre (NESSC). Data for the figures are available in the supporting information tables, and will be available online through Pangaea upon publication in the peer-reviewed literature. Data is also available on request (h.m.beddow-twigg@uu.nl).

Chapter 4:
Astronomically paced variations in vertical carbon and oxygen isotope gradients across the Oligocene Miocene Transition from Site U1334 (eastern equatorial Pacific)

Abstract

The response of high-latitude climate and cryosphere to astronomical climate forcing in the late Oligocene and early Miocene is relatively well understood. However, no continuous and high-resolution planktonic foraminiferal stable isotope records across this time interval exist. The absence of such records prevents investigations into surface water temperature variability and surface to deep oxygen and carbon isotope gradients, generally interpreted to reflect vertical temperature gradients and the strength of the biological pump, respectively. We present the first high-resolution astronomically tuned planktonic foraminiferal stable isotope ($\delta^{18}O$, $\delta^{13}C$) record for a ~2.2 Myr interval covering the Oligocene-Miocene transition (OMT) at IODP Site U1334 in the eastern equatorial Pacific. We utilize the thermocline dwelling species *Dentoglobigerina venezuelana* and compare this record to previously published benthic foraminiferal stable isotope records from the same site. Using this comparison, we reconstruct the surface water temperature/ice-volume signal and productivity across the OMT and find astronomically-paced variability in vertical water column gradients. Using the amplitude of the planktonic $\delta^{18}O$ shift across the OMT, we constrain the ice-volume component of the benthic foraminiferal $\delta^{18}O$ signal to a lower limit of ~0.45‰, which indicates an estimated sea level fall of ~45m assuming the modern $\delta^{18}O$ value of the Antarctic ice sheet. Spectral analysis reveals a strongly coherent synchronicity in planktonic and benthic foraminiferal $\delta^{13}C$ at the 405 kyr and ~110 kyr eccentricity cycles. Planktonic and benthic foraminiferal $\delta^{18}O$ show significant power and coherency with eccentricity at the ~110 kyr cycle. We find a steady increase in $\Delta\delta^{13}C$ (planktonic-benthic) between 22.2 and 23.2 Ma, driven by a sustained increase in planktonic foraminiferal $\delta^{13}C$, coincident with a sustained increase in benthic foraminiferal $\delta^{13}C$. Maxima in $\Delta\delta^{13}C$ and $\Delta\delta^{18}O$ occur during 110 kyr eccentricity minima, suggesting an increase in export productivity during cooler, glaciated climate conditions.

4.1 Introduction

The Oligocene Miocene transition (OMT) is a major episode in Cenozoic climate history, marked by a ~1‰ positive shift in oxygen isotope ratios ($\delta^{18}O$) of deep-sea benthic foraminiferal calcite. This signal is interpreted as an increase in ice volume on Antarctica and a cooling of high-latitudes, and deep-sea temperatures [*Woodruff and Savin*, 1989; *Miller et al.,* 1991; *Zachos et al.,* 1997; *Liebrand et al*., 2011; *Beddow et al*., 2016]. High-resolution astrochronologies have allowed for accurate time control across the OMT and have illuminated the complex interchange between astronomical forcing, ice volume/deep sea temperatures and the global carbon cycle as reflected in benthic foraminiferal $\delta^{18}O$ and $\delta^{13}C$ records, respectively [*Shackleton et al*., 2000, *Billups et al*., 2004; *Pälike et al.,* 2006a,b, *Liebrand et al*., 2011; *Hilgen et al, 2012*; *Vandenburghe et al*, 2012, *Beddow et al*., 2016].

Variability in the surface waters and the evolution of vertical $\delta^{13}C$ and $\delta^{18}O$ gradients between the surface and deep ocean across the Oligocene-Miocene are not well constrained. Surface-deep $\delta^{13}C$ gradients track the functioning of the biological pump and expand during intervals of high export productivity, as planktonic foraminiferal $\delta^{13}C$ becomes enriched with respect to benthic foraminiferal $\delta^{13}C$, reflecting the transfer of organic carbon between the surface and deep ocean [*Boyle*, 1988; *Togeweiler*, 1999; *Rohling and Cooke*, 1999; *Hodell et al*., 2003]. Crucially, very few high-resolution planktonic foraminifera stable isotope records have been published for the Oligocene and Miocene, and are only available from the mid Oligocene of ODP Site 1218 [*Wade and Pälike*, 2004] and the middle Miocene of Site U1337 [*Tian et al*., 2014]. Available records for the late Oligocene and early Miocene are of low-resolution, and no high-resolution records covering the OMT interval exist [*Pearson et al*., 1997; *Paul et al*., 2000].

In the modern day ocean, the eastern equatorial Pacific (EEP) is one of the largest ocean basins, with warm temperatures and strong wind-driven upwelling systems driving high biological productivity and rates of air-sea gas exchange, making it an important component of Earth's climate system [*Herbert et al*., 2010]. The EEP is a net source of CO_2 to the atmosphere, as wind-driven upwelling of CO_2 rich waters leads to high partial pressure of oceanic CO_2 ($p_{CO_2}^{aq}$) relative to the atmosphere, resulting in high rates of sea-to-air gas exchange [*Feely et al*., 1999; *Takahashi et al*., 2002] However, the high biological productivity means of the EEP means it plays a significant role in the biological sequestration of carbon to the deep-sea [*Takahashi et al*., 2002; *Lawrence et al*., 2006; *Dekens et al*., 2007]. This raises questions on how global and regional climate change across the OMT related to carbon cycling in the EEP.

Sediments recovered during Integrated Ocean Drilling Program (IODP) expedition 320/321, provide a valuable archive of paleoproductivity, carbon cycle shifts, the carbonate compensation depth (CCD) and cryosphere/temperature changes for the EEP over the past 56 Ma, including sediments across the Oligocene-Miocene interval [*Lyle et al*, 2008; *Pälike et al*, 2010; *Beddow et al*., 2016]. We have generated high-resolution (7 kyr) planktonic foraminiferal $\delta^{18}O$ and $\delta^{13}C$ records across the Oligocene Miocene transition from IODP Site U1334. We compare these results to a previously published astronomically tuned high-resolution benthic foraminiferal stable isotope records from the same site between 21.96 and 24.15 Ma [*Beddow et al*., 2016, *Beddow et al*., chapter 2]. These combined results allow us to reconstruct variability tracking temperature/ice volume changes in the Pacific surface water and compare astronomically paced climate variability in the surface ocean with the deep ocean. Moreover, by reconstructing vertical carbon gradients in foraminiferal $\delta^{13}C$ in the Pacific, we reconstruct variability in export productivity during the cooling event across the OMT.

4.2 Methods

4.2.1 Site location

IODP Site U1334 is located in the eastern equatorial Pacific (7°59.998ºN, 131°58.408ºW) at a present day water depth of 4704 metres below sea level (mbsl) (Fig. 1) The estimated paleodepth of Site U1334 during the OMT interval is ~4200 mbsl [*Pälike et al*, 2010]. We follow the latest splice for Site U1334 constructed as a composite from Holes A, B and C [*Westerhold et al.* 2012]. The section presented here runs from 88.93 m CCSF-A (core composite depth below seafloor) (U1334A-9H-3) to 121.29 m CCSF-A (U1334B-11H-5). The Oligocene to Miocene sediments of Site U1334 primarily consist of nannofossil ooze and chalk, with $CaCO_3$ concentrations for the OMT interval varying between ~50 and ~90%. [*Pälike et al*., 2010; *Beddow et al*., chapter 2].

4.2.2 Paleoecology of *Dentoglobigerina venezuelana*

The planktonic foraminiferal $\delta^{18}O$ and $\delta^{13}C$ records are generated using the species *Dentoglobigerina venezuelana,* which is a suitable species for paleoclimatic investigation due to its large size, wide geographic distribution, abundance in Oligocene-Miocene sediments and long (early Oligocene-early Pliocene) range [*Spezzaferri*, 1994]. *Dentoglobigerina venezuelana,* during the OMT interval, is recognised as a lower thermocline dweller at equatorial Atlantic Site 926 [*Stewart et al*., 2012]. During the middle Oligocene, *D. venezuelana* has been identified as an upper thermocline dweller at Pacific Site 1218 [*Wade and Pälike*, 2004], indicating that a possible shift in the depth of calcification from the upper to the lower thermocline takes place between the Oligocene and the late Oligocene/early Miocene [*Stewart et al*., 2012].

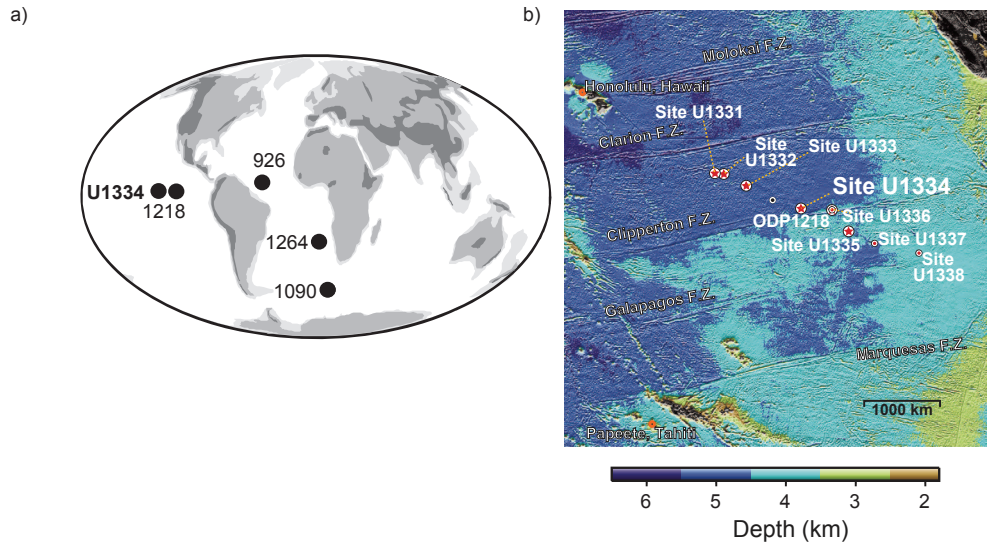

Figure 4.1. *(a) Location of IODP Site U1334. (b) Bathymetric overview map of Site U1334 and PEAT drilling locations, with previous ODP and DSDP sites, including ODP Site 1218 [adapted from Pälike et al., 2010 2010.]*

As planktonic foraminifera calcify at a range of depths and temperatures within the water column, we assess the depth habitat of *D. venezuelana* at Site U1334, in comparison with three other species of planktonic foraminifera, *Paragloborotalia siakensis* and *Trilobatus primordius* and *Globigerinoides altiaperturusa*, before interpreting the paleoclimatic signal in the planktonic foraminiferal record. *Paragloborotalia siakensis* is a thermocline dwelling species [*Iaccorino*, 1985; *Pearson and Wade*, 2009], whilst *T. primordius* and *G. altiaperturusa* dwell higher in the water column [*Gasperi and Kennet*, 1993].

4.2.3 Taxonomy of selected planktonic foraminiferal species

Planktonic foraminifera species assignment relied primarily on taxonomic descriptions from *Kennett and Srinivasan* [1983], *Spezzaferri* [1994], *Zachariasse and Sudijono*, [2012] and the forthcoming Atlas of Oligocene Planktonic Foraminifera [*Wade et al.*,in prep]. *Dentoglobigerina venezuelana* is variable in morphology [*Pearson and Chaisson, 1997*] with three distinct morphotypes described as *D. venezuelana* [*Stewart et al., 2012; Fox and Wade, 2013*]. We restrict the specimens picked as *D. venezuelana* to those with a circular outline and 3½-4 embracing, reniform (i.e. kidney-shaped) chambers that slowly increase in size. The final chamber of *D. venezuelana* is commonly reduced in size and flattened. The sutures are weakly depressed. The umbilicus is commonly triangular in shape, aperture umbilical, often concealed, may be bordered by an irregular triangular tooth or a lip with no tooth (*Wade et al.*, submitted). In the case of *P. siakensis*, the species has been commonly synonymized with *Paragloborotalia mayeri* [*e.g. Bolli and Saunders,* 1982,1985*; Chaisson and Leckie,* 1993*; Chaisson and Pearson,* 1997], while other studies have differentiated between the two [*e.g. Hilgen et al.,* 2003*; Stewart et al.,* 2004*; Pearson and Wade*, 2009]. We follow the new genetic and morphological classification of *Spezzaferri et al.* [2015] and place *G. altiaperturus* in the new genus *Trilobatus*.

4.2.4 SEM analysis

To assess the preservation and morphological variability of the foraminifera, 14 specimens of *D. venezuelana* and *P. siakensis* were picked for scanning electron microscope (SEM) analysis. These specimens were all mounted in umbilical view on a 10mm SEM stub and coated in gold using a sputter coater. The samples were then imaged using a JEOL JSM-6480LV variable pressure SEM at University College London. All specimens were imaged with a view of the whole test to ensure both species were consistent with the taxonomic descriptions, and the test wall of the majority of the specimens was imaged at a high magnification (>1000 x) to analyse the preservation state of the sample.

4.2.5 Stable isotope analyses

The Site U1334 planktonic foraminiferal stable isotope data were generated from the same samples used to construct the benthic foraminiferal stable isotope record [*Beddow et al.*, 2016]. Planktonic foraminifera *D. venezuelana* were picked from the 250-355 μm size fraction. Specimens of three additional species, *P. siakensis*, *T. primordius* and *G. altiaperturus,* were picked from the 212-355 μm size fraction for stable isotope analysis, to assess the depth habitat of *D. venezuelana*. We combine multiple specimens of each species for measurement, to reduce the effect of seasonal or depth differences at the time of calcification [*Pearson*, 2012]. Prior to analysis, foraminifer specimens were ultrasonically cleaned for two seconds while suspended in ethanol, to remove any nannofossils potentially attached to the surface of the foraminifera, and then crushed. Excess ethanol was pipetted out and the samples dried at 40°C.

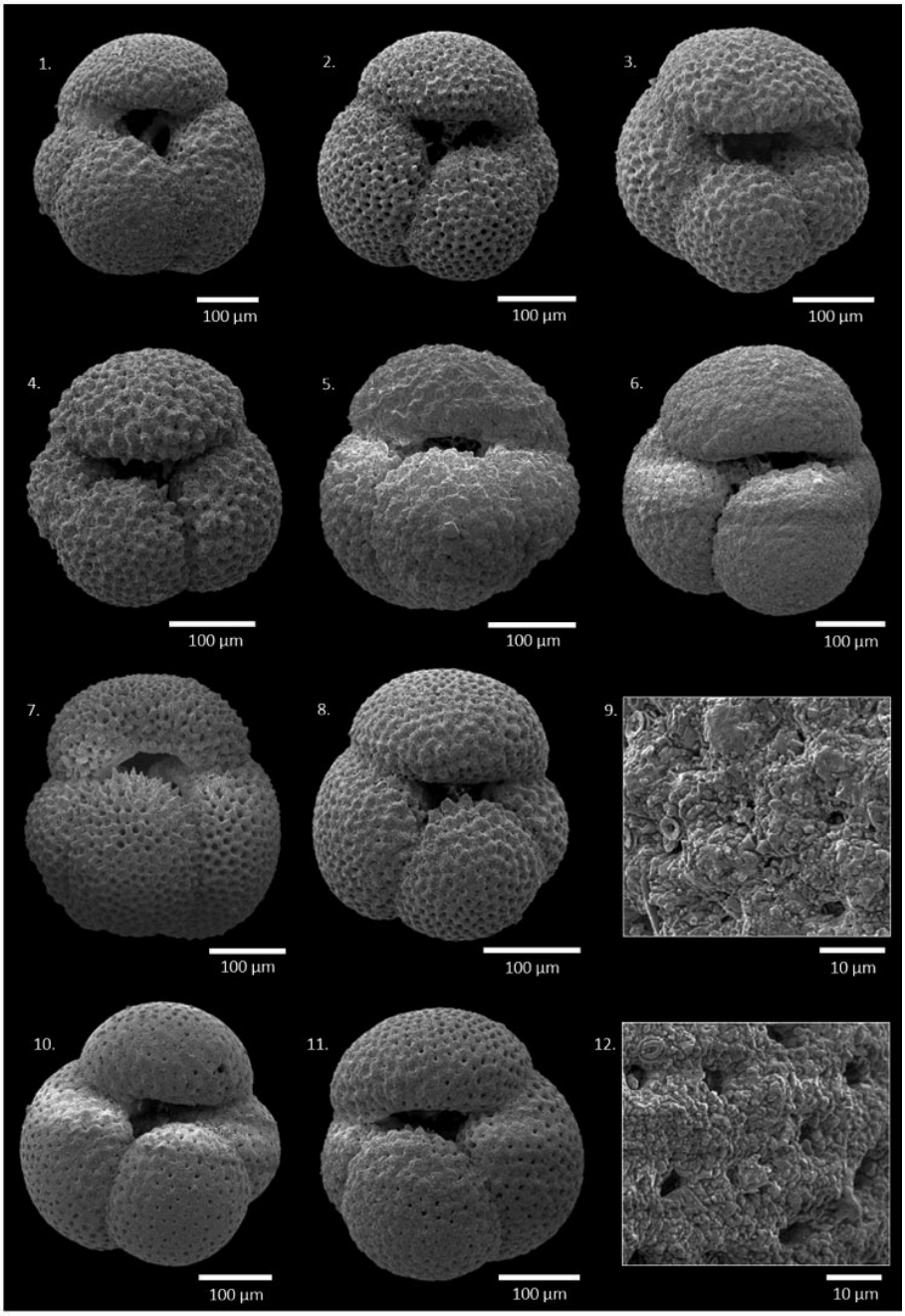

Figure 4.2. *Dentoglobigerina venezuelana.* **(1)** *U1334A-11H-4, 46-47 cm, 111.59 m CCSF-A.* **(2)** *U1334A-11H-4, 110-111 cm, 112.23 m CCSF-A.* **(3)** *U1334A-11H-5, 28-29 cm, 112.91 m CCSF-A.* **(4-5)** *U1334-A-11H-5, 68-69 cm, 113.31 m CCSF-A.* **(6)** *U1334A-11H-5, 96-97 cm, 113.59 m CCSF-A.* **(7)** *U1334A-11H-5, 100-101 cm, 113.63 m CCSF-A.* **(8-9)** *U1334A-11H-5, 108-109 cm, 113.71 m CCSF-A.* **(10-12)** *U1334A-11H-5, 116-117 cm, 113.79 m CCSF-A.*

Stable isotope analyses were conducted at Utrecht University, using a Thermo-Finnigan Kiel III automated preparation system coupled to a Thermo-Finnigan MAT 253 isotope ratio mass spectrometer. The standard NBS-19 and an in-house marble standard "Naxos" were used to calibrate isotope values to Vienna Pee Dee Belemnite (VPDB). Analytical precision is 0.03 ‰ and 0.08 ‰ for $\delta^{13}C$ and $\delta^{18}O$, respectively. We remove 12 outlying values by eye from the *D. venezuelana* planktonic foraminiferal $\delta^{18}O$ and $\delta^{13}C$ dataset. (Figure S1, Supplementary information).

4.2.6 Age model

Two independently tuned astronomical age models have been proposed for Site U1334 [*Beddow et al.*, chapter 2]. Within this study, we place the planktonic and benthic foraminiferal data on the $CaCO_3$ tuned age model, which is independently supported by spreading rate assumptions and more consistent with previously published OMT tunings [*Billups et al.*, 2004; *Pälike et al.*, 2006a,b; *Hilgen et al.*, 2012; *Beddow et al.*, Chapter 2]. This age model was based on matching maxima in $CaCO_3$ est. (%) from Site U1334 to 100 kyr eccentricity minima in the most recent astronomical solution [*Laskar et al.*, 2011a,b]. On the $CaCO_3$ tuned age model, the planktonic and benthic foraminifera stable isotope datasets run from 21.96 to 24.15 Ma, with average sedimentation rates of ~1.6 cm/kyr. This results in ~3.6 and ~7 kyr time steps for the benthic and planktonic foraminiferal stable isotope records from Site U1334, respectively.

4.2.7 Spectral analysis

Blackman-Tukey power spectra, cross-spectral analysis and evolutive spectral analyses were conducted on planktonic foraminiferal $\delta^{13}C$ and $\delta^{18}O$ in the age domain to examine astronomical characteristics present in the proxy records. The data were re-sampled and detrended using version 2 of the software package AnalySeries [*Paillard et al.*, 1996] prior to time series analyses. To calculate phase relationships of the stable isotope records with eccentricity, we multiplied the datasets by -1. We compare the Blackman-Tukey power spectra and evolutive analyses for the planktonic foraminiferal stable isotopes to those of the benthic foraminiferal stable isotopes [*Beddow et al.*, Chapter 2].

4.2.8 Calculation of vertical gradients

We calculated the vertical water column gradient between planktonic (*D. venezuelana*) and benthic foraminiferal stable isotopes on ~40 kyr time scales, subtracting benthic values from planktonic values (Figs. 6 and 7). To calculate the short-term average, the planktonic and benthic foraminifera stable isotope time series were recalculated at a 7 kyr time step, matching the lower resolution of the planktonic foraminifera sampling interval, and a 5 point moving average placed through the resampled dataset to avoid a potential over-estimation of gradients resulting from the more extreme values in the planktonic foraminiferal $\delta^{18}O$.

4.3 Results

3.3.1 SEM analyses, morphology and preservation

The specimens of *D. venezuelana* (Fig. 2) are relatively consistent in terms of morphology, with only a small degree of variance in their morphological characteristics. For *P. siakensis* (Fig. 3), the majority of specimens have 5-6 chambers in the final whorl, moderately depressed radial sutures, and an umbilical to extra-umbilical aperture bordered by a distinctive lip. While some specimens

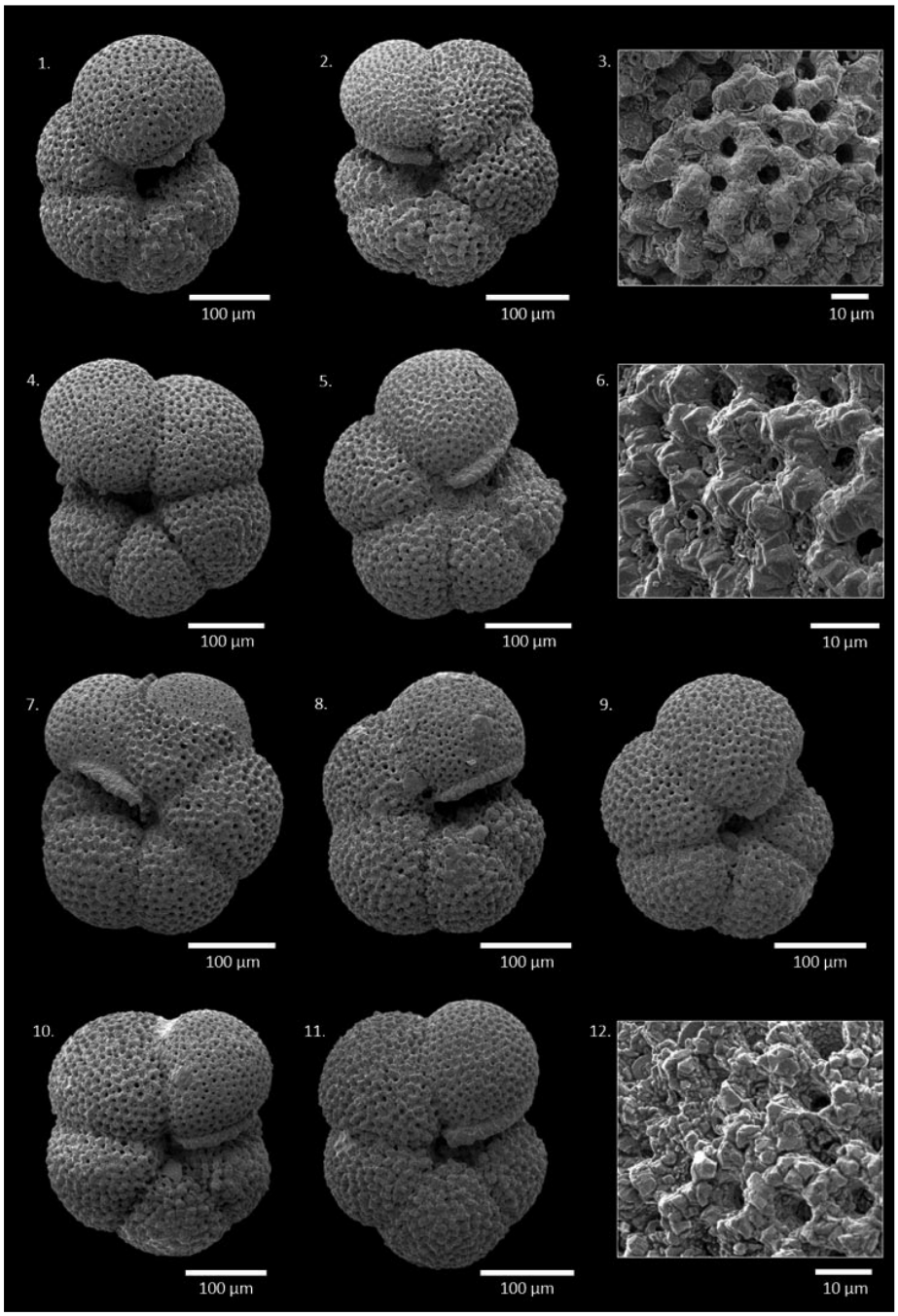

Figure 4.3. *Paragloborotalia siakensis.* **(1)** *U1334A-11H-4, 110-111 cm, 112.23 m CCSF-A.* **(2-3)** *U1334A-11H-5, 28-29 cm, 112.91 m CCSF-A.* **(4)** *U1134A-11H-5, 68-69 cm, 113.31 m CCSF-A.* **(5-7)** *U1334A-11H-5, 100-101 cm, 113.63 m CCSF-A.* **(8-9)** *U1334A-11H-5, 108-109 cm, 113.71 m CCSF-A.* **(10-12)** *U1334A-11H-5, 116-117 cm, 113.79 m CCSF-A.*

have more enveloping and kummerform (small and stunted) final chambers (e.g. Fig. 3, specimens 2, 10 and 11), the imaged specimens are consistent with specimens from the type locality presented in *Zachariasse and Sudijono* [2012].

Foraminifera at Site U1334 are less well preserved than Site U1338 [*Fox and Wade*, 2013], with a high abundance of radiolarians in the <150 mm size fractions [*King and Wade*, submitted]. In general, foraminifer specimens indicate infilling is rare but show some recrystallization and are moderately preserved. The most common post burial alteration was the presence of coccoliths on the foraminiferal test wall. The degree of recrystallization appears to increase downcore, in particular in the older, Oligocene samples (e.g. Fig. 2, specimen 12; Fig. 3 specimen 12).

4.3.2 Planktonic foraminiferal abundances

Of the four planktonic foraminiferal species selected, we find the occurrence of *D. venezuelana* consistently present throughout the record, the occurrence of *P. siakensis* intermittent and two small intervals where *Globigerinoides/Trilobatus* spp. specimens are present in low amounts. Species abundances are given in specimens per gram of sediment. For samples where *D. venezuelana*, *P. siakensis* or *Globigerinoides/Trilobatus* spp. are found, *D. venezuelana* ranges between 0.1 and 3.9 specimens per gram, with an average of 0.8 specimens/g, *P. siakensis* ranges between 0.1 and 15 specimens/g and *Globigerinoides/Trilobatus* spp. numbers range between 0.1 and 1 specimens/g, with *T. primordius* being more abundant than *G. altiaperturus* (Fig. 4). Abundances of *D. venezuelana* and *P. siakensis* increase concurrently across three intervals: between ~ 23.7 and 24 Ma, ~22.8 and 23.1 Ma and ~22.1 to 22.4 Ma (Fig. 4). *Paragloborotalia siakensis* specimen numbers are generally low, with the exception of a significant spike in abundance of 15 specimens/g at ~23.9 Ma. During the more abundant intervals between ~22.8 and 23.1 Ma and 22.1 and 22.4 Ma, we also see occurrences of low numbers of *Globigerinoides/Trilobatus* spp.

4.3.3 Planktonic foraminiferal stable carbon isotopes ($\delta^{13}C$)

Dentoglobigerina venezuelana $\delta^{13}C$ values range from 0.35‰ at 23.7 Ma to 2.26‰ at 22.1 Ma (Fig. 4). The planktonic $\delta^{13}C$ dataset has less variance than the planktonic $\delta^{18}O$, and the long-term trend clearly follows the benthic $\delta^{13}C$ long-term trend (Fig. 4). Planktonic $\delta^{13}C$ values during the late Oligocene are generally low, ranging between 0.35‰ and 1.90‰, with baseline values of ~1‰. A positive shift of ~0.5 ‰ occurs at ~23.2 Ma, coincident with positive shifts in the planktonic foraminiferal $\delta^{18}O$, and in the benthic foraminifera $\delta^{18}O$ and $\delta^{13}C$ associated with the OMT (Fig. 4).

The $\delta^{13}C$ maximum during the OMT is 2.05‰ at 23.07 Ma, coincident with OMT maxima in the benthic $\delta^{18}O$ and $\delta^{13}C$ values (2.43 and 1.53‰ respectively) (Fig. 4). After the termination of the OMT, baseline $\delta^{13}C$ values increase by ~0.4‰, with higher $\delta^{13}C$ values in the early Miocene relative to the OMT. This is in contrast to the benthic foraminifera $\delta^{13}C$, where $\delta^{13}C$ values appear to stabilize at a baseline of ~1.2 ‰ during the OMT and extending into the early Miocene. Towards

Figure 4.4. *Planktonic $\delta^{13}C$ (a) and $\delta^{18}O$ (c) foraminifera stable isotopes from Site U1334 compared to previously published benthic $\delta^{13}C$ (b) and $\delta^{18}O$ (d) foraminifera stable isotopes from Site U1334 [Beddow et al., Chapter 2] plotted against Age (Ma). Carbon isotopes are in light green, with a 5 point moving average running through the data in dark green. Oxygen isotopes are in light blue, with a 5-point moving average running through the data in dark blue. Foraminiferal abundances are plotted for the species D. venezuelana (e), P. siakensis (f) and Globigerinoides/Trilobatus spp. (g) in specimens per gram of sediment.*

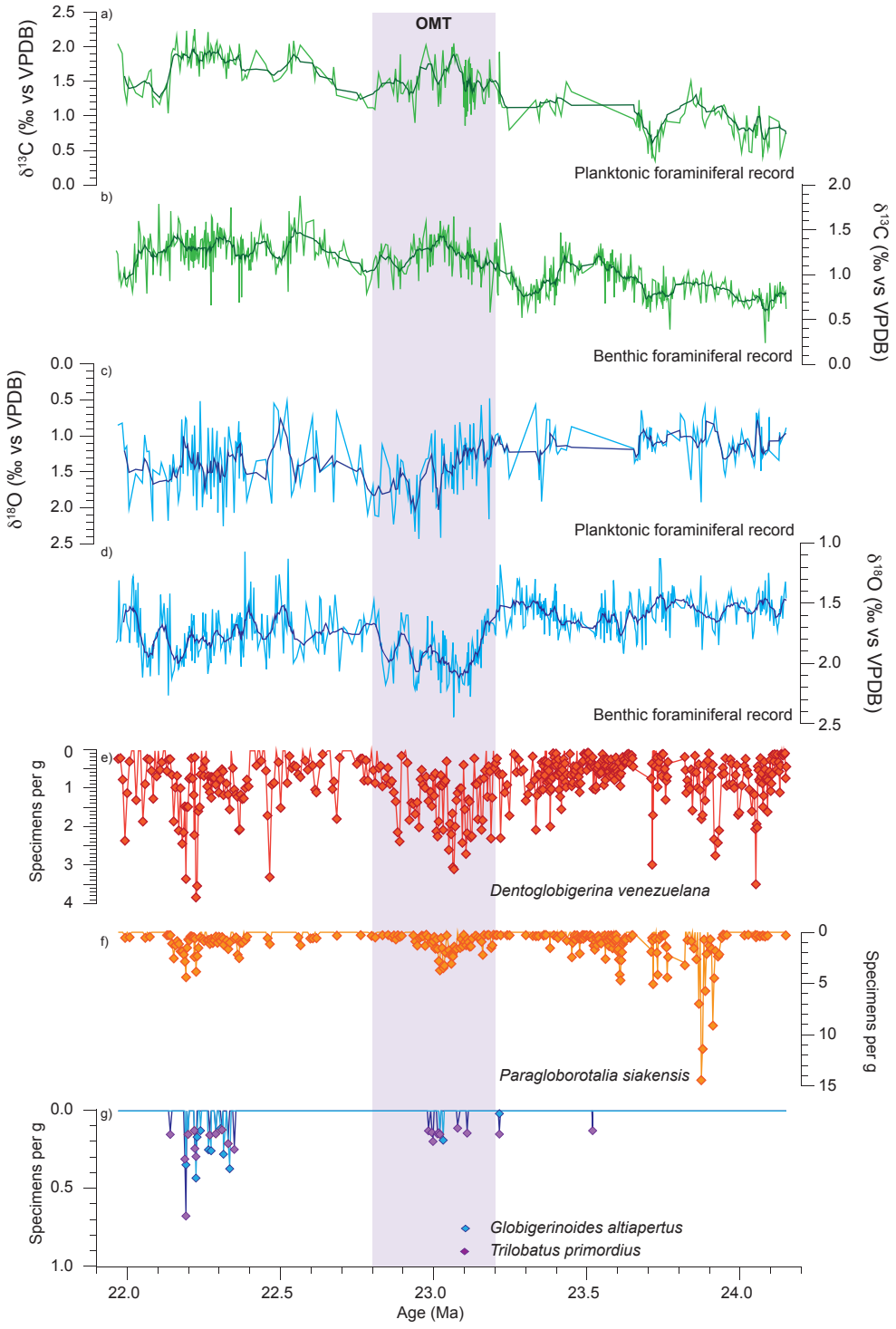
OMT
a)
b)
c)
d)
e)
f)
g)
δ13C (‰ vs VPDB)
Planktonic foraminiferal record
Benthic foraminiferal record
δ18O (‰ vs VPDB)
Specimens per g
Dentoglobigerina venezuelana
Paragloborotalia siakensis
Globigerinoides altiapertus
Trilobatus primordius
Age (Ma)
22.0
22.5
23.0
23.5
24.0

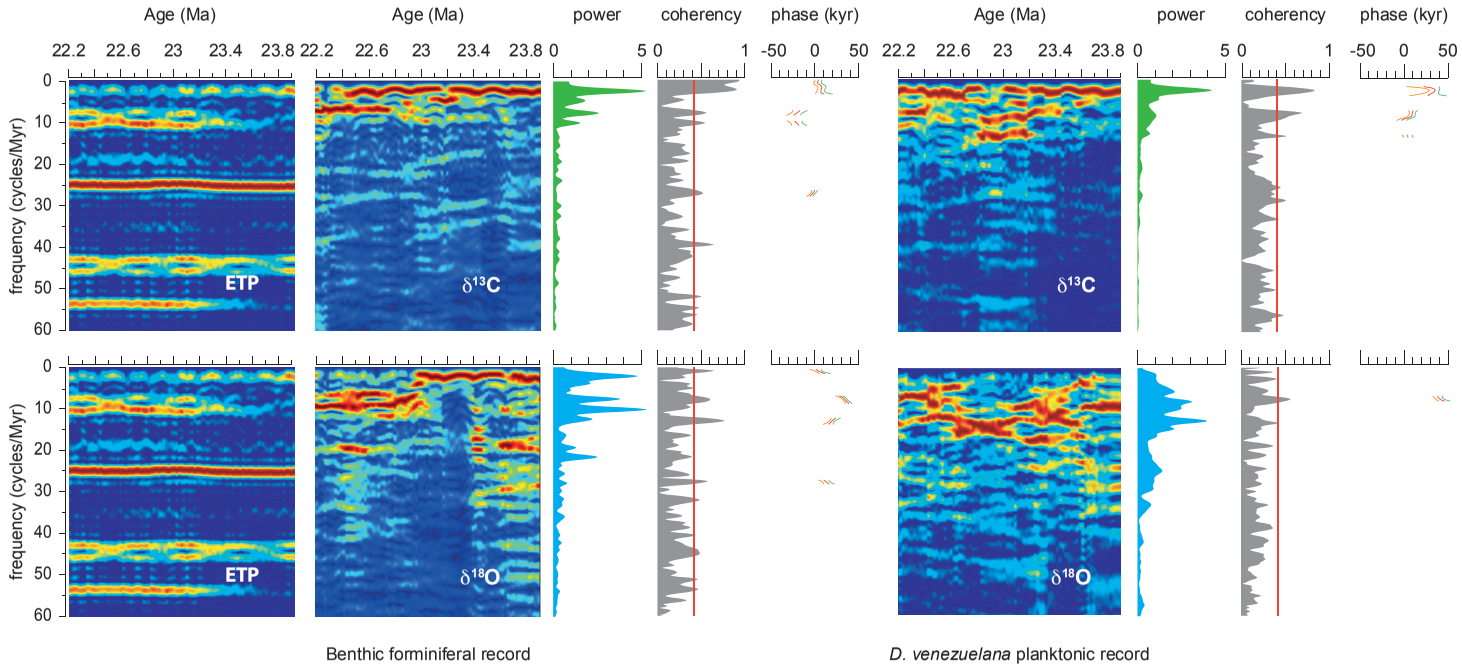
Age (Ma)
22.2 22.6 23 23.4 23.8
frequency (cycles/Myr)
0 10 20 30 40 50 60
ETP
δ13C
δ18O
power
0 5
coherency
0 1
phase (kyr)
-50 0 50
Benthic forminiferal record
D. venezuelana planktonic record

the youngest part of the record, at ~22 Ma, there is a prominent shift of ~0.4 and ~0.8 ‰ towards negative values in the benthic and planktonic foraminiferal $\delta^{13}C$, respectively.

4.3.4 Planktonic foraminiferal stable oxygen isotopes ($\delta^{18}O$)

Dentoglobigerina venezuelana $\delta^{18}O$ values range from 0.07 at 23.20 Ma to 2.02‰ at 23.02 Ma. Although the $\delta^{18}O$ dataset for *D. venezuelana* contains a lot of variance, a 5-point running average indicates that the long-term trend present in the data follows the benthic foraminiferal $\delta^{18}O$ record (Fig. 4).

During the late Oligocene, $\delta^{18}O$ values are relatively low, with a shift towards higher values beginning ~23.2 Ma, coincident with the onset of the positive benthic foraminifera $\delta^{18}O$ excursion. At ~23.2 Ma, planktonic foraminiferal $\delta^{18}O$ shifts towards positive values for ~400 kyrs. The planktonic foraminiferal $\delta^{18}O$ maximum occurs within 40-50 kyrs of the benthic foraminiferal $\delta^{18}O$ maxima of 2.43‰ (Mi-1) at 23.07 Ma. After ~22.8 Ma, planktonic foraminiferal $\delta^{18}O$ values decrease to a baseline value of ~ 1.0‰, 0.3‰ higher than late Oligocene baseline values, with a marked increase in the amplitude variability.

Due to the high level of variance, cyclical amplitude variability within the $\delta^{18}O$ record is difficult to quantify. Using absolute maxima and minima in $\delta^{18}O$ could lead to an overestimation of the $\delta^{18}O$ paleoclimatic signal. The moving average indicates an increase in high frequency amplitude variability during the early Miocene, consistent with the increase in high frequency amplitude variability (~ 1‰) present in the early Miocene interval of the benthic foraminiferal $\delta^{18}O$.

4.3.5 Spectral analyses of the stable isotope records

Amplitude variability in planktonic foraminiferal $\delta^{13}C$ varies on 405 kyr eccentricity timescales, with clear variability of ~0.7 to 1.0‰ present throughout the record, synchronous with 405 kyr variability in the benthic foraminiferal $\delta^{13}C$, which has a lower amplitude of ~0.3 to 0.5 ‰ (Fig. 4). Additionally, we find clear ~110-kyr paced variability of ~1.0 ‰ in the planktonic foraminiferal $\delta^{13}C$ during the OMT, with two clear ~110-kyr cycles at ~22.9 Ma and 23.0 Ma, which intriguingly are not prominent in the benthic foraminiferal $\delta^{13}C$ record. In the early Miocene interval, between ~21.9 and 22.8 Ma, variability on ~110-kyr timescales in the planktonic foraminiferal $\delta^{18}O$ is coincident with high-amplitude ~110 kyr cycles in the benthic foraminifera $\delta^{18}O$ (Fig. 4).

Power spectra and evolutive analyses indicate that the dominant periodicity in the planktonic foraminifera $\delta^{13}C$ is at 405 kyr, with an increase in ~110 kyr power between 22.8 and 23.2 Ma, across the OMT (Fig. 5). The strong 405 kyr signal in planktonic foraminiferal $\delta^{13}C$ is consistent with the strong 405 kyr signal in the benthic foraminifera $\delta^{13}C$ evolutive spectrum. Power at the ~110 kyr periodicity between 22.8 and 23.2 Ma increases in the planktonic foraminiferal $\delta^{13}C$, but is weak in the benthic foraminifera $\delta^{13}C$ until ~22.8 Ma, after the OMT.

Both the power spectra and evolutive analyses indicate a weak 405 kyr signal in the planktonic foraminifera $\delta^{18}O$, in contrast to the strong 405 kyr periodicity present in the benthic $\delta^{18}O$, and in the planktonic and benthic $\delta^{13}C$. The dominant signal in the planktonic $\delta^{18}O$ is present at the ~110 kyr eccentricity periodicity. We find some power in the $\delta^{18}O$ evolutive spectrum at the 40 kyr

Figure 4.5. *Evolutive analyses, power spectra and coherence and phase plots for the benthic foraminiferal stable isotopes and for the D. venezuelana planktonic foraminifera stable isotopes for Site U1334. Coherence and phase estimates between are between eccentricity La2011 solution and benthic foraminiferal stable isotopes. The significance level on the coherence plots is 99%.*

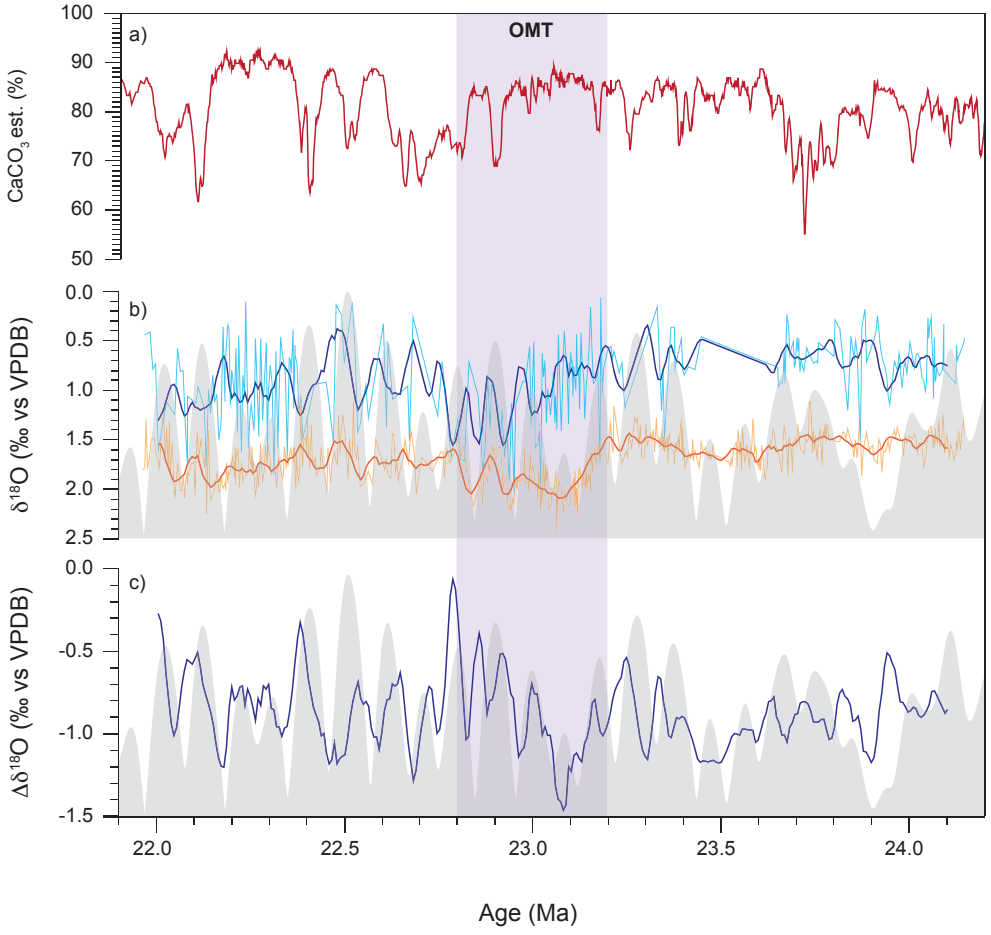

Figure 4.6. *Short eccentricity pacing of planktonic-benthic foraminiferal $\delta^{13}C$ gradients for Site U1334. Plotted are (a) $CaCO_3$ est (%), (b) benthic (orange) and planktonic (green) foraminifera $\delta^{13}C$ with 5 point moving averages, (c) $\Delta\delta^{13}C$ calculated using the 5 point moving averages in panel b. The grey shaded area in panel b and c is eccentricity [Laskar et al., 2011a,b].*

obliquity period, similar to the evolutive spectrum of the benthic foraminifera $\delta^{18}O$, between 23.2-23.7 Ma.

Planktonic foraminiferal $\delta^{18}O$ and $\delta^{13}C$ are significantly coherent (99%) with benthic foraminiferal $\delta^{18}O$ and $\delta^{13}C$ and with eccentricity at 405 kyr and ~110 kyr eccentricity cycles and 40 kyr obliquity cycles (Fig. 5). Phase estimates of planktonic $\delta^{13}C$ with respect to benthic foraminiferal $\delta^{13}C$ indicate that planktonic $\delta^{13}C$ lags benthic foraminifera $\delta^{13}C$ by ~10 kyr at the 405 kyr period and leads benthic foraminifera $\delta^{13}C$ by ~20 kyr at the ~110 kyr periodicity, whilst planktonic $\delta^{18}O$ lags benthic foraminifera $\delta^{18}O$ by ~30-35 kyr at the ~110 kyr eccentricity periodicity (Fig. 5). On obliquity time scales, planktonic $\delta^{13}C$ leads benthic foraminifera $\delta^{13}C$ slightly by ~5 kyr, and planktonic $\delta^{18}O$ record lags benthic foraminifera $\delta^{18}O$ by ~10kyr.

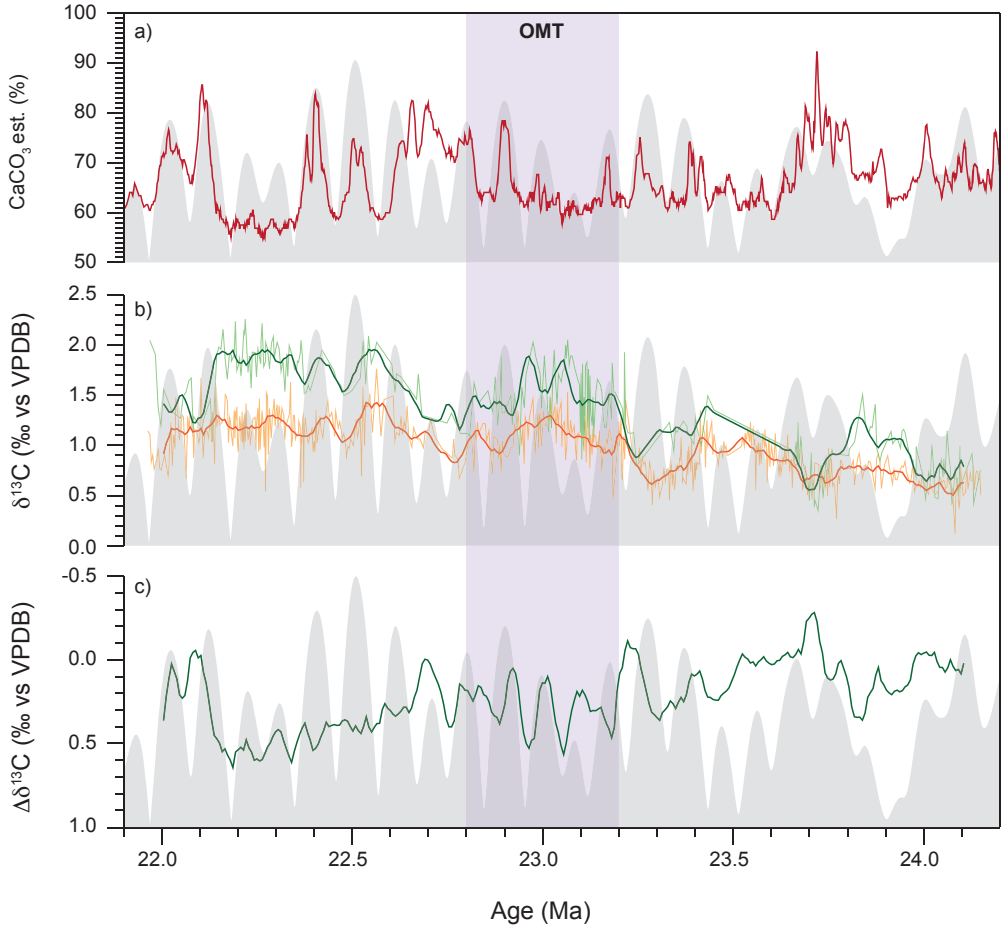

Figure 4.7. *Short eccentricity pacing of planktonic-benthic foraminifera $\delta^{18}O$ gradients for Site U1334. Plotted are (a) $CaCO_3$ est (%), (b) benthic (orange) and planktonic (green) foraminifera $\delta^{13}C$ with 5 point moving averages, (c) $\Delta\delta^{18}O$ calculated from the 5 point moving averages in panel b. The grey shaded area in panel b and c is eccentricity [Laskar et al., 2011a,b].*

Phase estimates of planktonic foraminiferal stable isotope records to eccentricity indicate that planktonic $\delta^{18}O$ lags eccentricity by ~45 kyrs at the ~110 kyr periodicity, whilst planktonic $\delta^{13}C$ lags eccentricity by ~20-30 kyr at the 405 kyr periodicity and is roughly in phase at the ~110 kyr eccentricity periodicity (Fig. 5).

4.3.6 Vertical $\delta^{13}C$ and $\delta^{18}O$ gradients

The long-term trend in $\Delta\delta^{13}C$ indicates that thermocline to deep water gradients across the OMT interval expand, with higher-frequency variability in $\Delta\delta^{13}C$ indicating expansions in $\delta^{13}C$ gradients are coincident with increases in $\delta^{13}C$ and $\delta^{18}O$ (Figs. 6 and 7). Between ~22.1 to 24.1 Ma, $\Delta\delta^{13}C$ shows a steady increase of ~0.5‰, with the exception of a notable ~100 kyr drop in $\Delta\delta^{13}C$ to 0.0 ‰ at ~23.7 Ma, coincident with a sharp decrease in $CaCO_3$ est. (%) to ~54 % [*Beddow et al.*, Chapter 2] (Fig. 7). The increase in gradients is driven by enrichment in the planktonic foraminiferal

$\delta^{13}C$, which shows a positive increase over time relative to the benthic foraminiferal $\delta^{13}C$. This increase in $\Delta\delta^{13}C$ values ends abruptly at ~22.1 Ma, where there is a ~100 kyr decrease in $\Delta\delta^{13}C$ to ~0.0 ‰, coincident with a shift towards negative $\delta^{13}C$ values in both the benthic and planktonic foraminiferal $\delta^{13}C$.

In contrast to the steady increase in $\Delta\delta^{13}C$ values, long-term $\Delta\delta^{18}O$ values indicate a slight long-term reduction of ~ 0.1‰ in vertical gradients between the late Oligocene and early Miocene, although they indicate significant variability on higher-frequency timescales. There is a notable an increase of ~0.2‰ at ~22.8 and a decrease of ~ 0.4‰ at ~23.2 Ma (Fig. 7).

Both $\Delta\delta^{13}C$ and $\Delta\delta^{18}O$ vary on ~110 kyr eccentricity timescales, with maxima in $\Delta\delta^{13}C$ and $\Delta\delta^{13}O$ occurring during eccentricity minima. In general, maxima in $\Delta\delta^{13}C$ and $\Delta\delta^{18}O$ occur during positive shifts in benthic and planktonic $\delta^{13}C$ and $\delta^{18}O$ and coincide with intervals of higher $CaCO_3$ est. wt (%)(Figs. 6 and 7). The amplitude of ~110 kyr $\Delta\delta^{18}O$ variability is higher in the early Miocene than in the late Oligocene, reflecting the increase in variability in the early Miocene in both planktonic and benthic foraminiferal $\delta^{18}O$.

4.5 Discussion

4.5.1 Depth habitat of *D. venezuelana*

Our multispecies planktonic stable isotope data from Site U1334 indicate that *G. altiaperturus* and *T. primordius* record relatively negative $\delta^{18}O$ and positive $\delta^{13}C$, indicative of mixed-layer calcification and a photosymbiotic relationship with dinoflagellates (Fig. 8). The stable isotope values of *P. siakensis* are more positive in $\delta^{18}O$ and more negative in $\delta^{13}C$, compared to *Globigerinoides* and *Trilobatus* species. This probably indicates an upper thermocline dwelling, asymbiotic lifestyle for *P. siakensis*, consistent with *Pearson and Wade* [2009], as planktonic foraminifera without symbionts have more negative foraminiferal $\delta^{13}C$ signatures relative to symbiotic foraminifera.

The depth at which *D. venezuelana* calcified has been discussed in detail in *Wade et al.* [2007], *Stewart et al.* [2012] and *Beltran et al.* [2014]. Stable isotope determination of the depth habitat of *D. venezuelana* is complicated by an increase in $\delta^{18}O$ values with test size [*Wade et al.*, 2007; *Stewart et al.*, 2012]. Ideally a restricted size range should be used in all planktonic foraminiferal geochemical analyses to limit vital effects. We restricted our stable isotope analyses of *D. venezuelana* to the 250-355 mm size fraction. Our weight vs. $\delta^{18}O$ single specimen analyses (see Fig. S3, supplementary information) suggest an increase in $\delta^{18}O$ with test weight (size), indicative of movement through the water column during ontogeny.

Overall, our stable isotope data indicate that *D. venezuelana* has more positive $\delta^{18}O$ values than co-occurring paragloborotaliids and *Globigerinoides*/*Trilobatus* species, suggesting a deeper habitat, lower in the thermocline. Carbon isotope values are similar to *P. siakensis*, confirming an asymbiotic lifestyle. A lower thermocline depth habitat is consistent with several previous studies (e.g. *Gasperi and Kennett*, 1993; *Pearson et al.*, 1997; *Pearson and Wade*, 2009), while both early Oligocene and late Miocene studies from the equatorial Pacific indicate a shallower calcification depth [e.g., *Beltran et al.*, 2014, *Moore et al.*, 2014]. *Wade et al.* (2007) record an increase in $\delta^{18}O$ values in *D. venezuelana* in the late Oligocene (~28 Ma) and suggested this represented an increase in the depth habitat of *D. venezuelana*. Changes in depth habitat through time, as well as the size/$\delta^{18}O$ relationship may account for the controversy over *D. venezuelana* calcification depth habitats.

4.5.2 Diagenesis

SEM imaging indicates that *D. venezuelana* from Site U1334 show recrystallization, particularly in the downcore late Oligocene samples (Figs. 2 and 3). Previous studies have indicated that recrystallization of planktonic foraminifera preserved in pelagic oozes is a common occurrence in deep ocean sediment archives, leading to a potential underestimation of the temperature component of the planktonic $\delta^{18}O$ signal, as recrystallized calcite is formed at shallow burial depths in lower temperatures than the original calcite [*Schlanger and Douglas*, 1974; *Pearson et al*., 2001; *Sexton and Wilson*, 2009]. The "frosty" appearance, low-latitude setting and lithology of the sediments at Site U1334 indicate that diagenesis could affect the $\delta^{13}C$ and $\delta^{18}O$ isotope signals in the planktonic foraminifera [*Schrag et al*., 1995; *Pearson et al*., 2001; *Sexton et al*., 2006].

The multi-species stable isotope cross plot (Fig. 8) indicates that the planktonic foraminifera from different species retain substantial $\delta^{13}C$ and $\delta^{18}O$ isotope differentials, due to differences in the isotopic signature of the ambient seawater and temperature at the point of calcification, suggesting a significant sea-surface signal is retained despite recrystallization [*Pearson et al*., 2001]. Whilst the planktonic foraminiferal $\delta^{13}C$ and $\delta^{18}O$ from Site U1334 could therefore reflect a combined thermocline and deep-water signal in their isotopic composition, studies of well-preserved "glassy" planktonic foraminiferal isotope values compared with "frosty" recrystallized planktonic foraminiferal isotope values indicate that, as long as not used for absolute paleotemperature estimates, recrystallized planktonic foraminiferal calcite still preserves a surface water isotopic signal [*Sexton et al*., 2006].

Diagenesis effects in foraminiferal stable isotopes are mainly dependent on their early recrystallization histories, where recrystallization occurs at shallow burial depths, and affect $\delta^{18}O$ isotope signatures more than $\delta^{13}C$ [*Rudnicki et al*., 2001; *Sexton et al*., 2006; *Edgar et al*., 2013]. We see a significant long-term change in $\Delta\delta^{13}C$, and not in $\Delta\delta^{18}O$ suggesting that our calculation of $\Delta\delta^{18}O$ and $\Delta\delta^{13}C$ reflects a real climate signal, rather than a linear scaling of $\Delta\delta^{13}C$ due to increasing diagenesis with core depth.

There is one interval, between ~23.6 and 23.8 Ma, where we find anonymously negative planktonic $\delta^{13}C$ relative to the benthic $\delta^{13}C$ values. The depletion signal in the planktonic $\delta^{13}C$ during this interval is not reflected in the benthic $\delta^{13}C$. A diagenetic overprint, perhaps due to lower sedimentation rates (~0.7 cm/kyr) [*Beddow et* al., Chapter 2], could explain the depletion of planktonic $\delta^{13}C$ values relative to the benthic signal [*Schrag et al*., 1995; *Sexton and Wilson*, 2009]. However, in the $\delta^{18}O$ record, planktonic-benthic gradients remain steady during this interval. As $\delta^{18}O$ is generally more affected by diagenesis than $\delta^{13}C$ [*Sexton et al*., 2006], this suggests that this a real climate signal reflecting changes in thermocline paleo-productivity that are not reflected in the deep water.

4.5.3 Climate evolution across the OMT.

Both the $\delta^{18}O$ and $\delta^{13}C$ *D. venezuelana* records exhibit similar long-term trends and characteristic features as the benthic foraminiferal $\delta^{18}O$ and $\delta^{13}C$, demonstrating a clear synchronicity, particularly in the $\delta^{13}C$ (Figs. 4 and 6). These trends are most notable during the OMT between ~22.8 and 23.2 Ma, and during marked 405 kyr variability in benthic and planktonic $\delta^{13}C$, providing further comfirmation that these stable isotope trends and oscillations are representative of global climate signals [*Billups et al*., 2004, *Wade and Pälike*, 2004; *Pälike et al*, 2006a,b; *Liebrand et al*., 2011; *Tian et al*., 2014; *Beddow et al*, 2016].

The shift towards heavier values in both benthic and planktonic foraminiferal $\delta^{13}C$ records between 22.1 and 23.2 Ma coincides with the previously described Oligocene-Miocene Carbon

Maximum [*Hodell and Woodruff*, 1994]. The similarity in response in the $\delta^{13}C$ during this interval suggests a whole ocean shift in the marine carbon cycle occurs, in conjunction with the ice sheet expansion and global cooling at the OMT. A long-term shift towards more enriched $\delta^{13}C$ in both the benthic and planktonic stable isotopes is indicative of an increase in export productivity and subsequent organic carbon burial in deep ocean sediments [*Delaney and Boyle*, 1985; *Diester-Haass et al.,* 2011; *Mawbey and Lear*, 2013].

The foraminiferal $\delta^{18}O$ signal is controlled by three main environmental factors: ice volume, temperature and salinity [*Shackleton,* 1974]. As the global ice volume component of the $\delta^{18}O$ signal affects the $\delta^{18}O$ values of both benthic and planktonic foraminifera equally, the presence of a positive shift in the planktonic foraminiferal $\delta^{18}O$ record between ~22.8-23.2 Ma, coincident with the ~1‰ positive excursion in the benthic $\delta^{18}O$, supports suggestions of an increase in Antarctic ice volume across the OMT [*Miller et al*., 1991; *Shackleton et al*., 2000; *Zachos et al*., 2001; *Billups et al*., 2004; *Pälike et al*., 2006a,b; *Liebrand et al*., 2011].

Comparing absolute values, the amplitude in the benthic $\delta^{18}O$ of the transient excursion associated with the OMT is ~0.9‰, versus one of ~1.6‰ in the planktonic $\delta^{18}O$ (~0.7‰ higher). As the ice volume component of the $\delta^{18}O$ signal is equal in both records, this would suggest that ice volume changes cannot exceed ~0.9‰ in the most extreme, hypothetical scenario. Previous estimates, however, suggest that 50% or more of the benthic $\delta^{18}O$ signal is linked to an increase in Antarctic ice volume, meaning that ice volume accounts for a lower limit of ~0.45‰, around 30% of the planktonic $\delta^{18}O$ signal [*Lear et al*., 2004; *Mawbey and Lear*, 2013; *De Boer et al*., 2010, 2012]. This would suggest a lower limit for sea-level fall of ~ 45 m [*Fairbanks and Mathews*, 1978], consistent with previous sea-level fall estimates for the OMT, which range between 30 and 90m [*Miller et al.,* 1991; *Pekar et al.*, 2002; *Pekar and Deconto*, 2006; *Liebrand et al.*, 2011; *Mawbey and Lear*, 2013; *Beddow et al*., 2016], although this estimate assumes an ice sheet $\delta^{18}O$ similar today, and could be potentially larger if the Antarctic ice sheet is less depleted in $\delta^{18}O$ across the OMT [*Lhomme et al., 2005*]. The remaining 1.15‰ in the *D. venezuelana* $\delta^{18}O$ change across the OMT would relate to a ~4-5°C cooling of surface waters in the equatorial Pacific Ocean across this interval, although we cannot preclude any associated changes with depth habitat. Sea surface cooling estimates are complicated by evidence of recrystallization in Site U1334 foraminifera specimens, which could lead to an diagenetic overprint of the $\delta^{18}O$ signal, as recrystallization occurs during the early burial history of foraminifera, in ambient interstitial waters at a lower temperature [*Schrag et al.*, 1995; *Pearson et al*., 2001]. The large variance in the planktonic $\delta^{18}O$ record could reflect seasonal variability in temperatures and depth during calcification of *D. venezuelana* specimens. Sites with well-preserved "glassy" planktonic foraminifera [*Sexton et al*, 2006], and alternative temperature proxies e.g., Mg/Ca or Tex_{86} are needed to confirm or refute sea surface temperature changes across the OMT.

4.5.4 Climatic response to astronomical forcing

The dominant astronomical signal in the planktonic and benthic foraminiferal $\delta^{13}C$ is at the 405 kyr periodicity, consistent with previous high-resolution benthic foraminifera $\delta^{13}C$ stable isotope studies illustrating the pervasive imprint of a strong 405 kyr signal present throughout the Eocene, Oligocene and Miocene time period [*Zachos et al*., 2001; *Wade and Pälike*, 2004; *Pälike et al*., 2006a; *Holbourn et al*., 2013, 2015; *Littler et al*., 2015]. The synchronicity in 405 kyr variability, demonstrated by the coherence and phase relationships (Fig. 6) between benthic and planktonic foraminifera $\delta^{13}C$, confirms that this global signal involves the entire water column. Coherent 405 kyr forcing in planktonic and benthic foraminifera $\delta^{13}C$ is also present in the middle Miocene

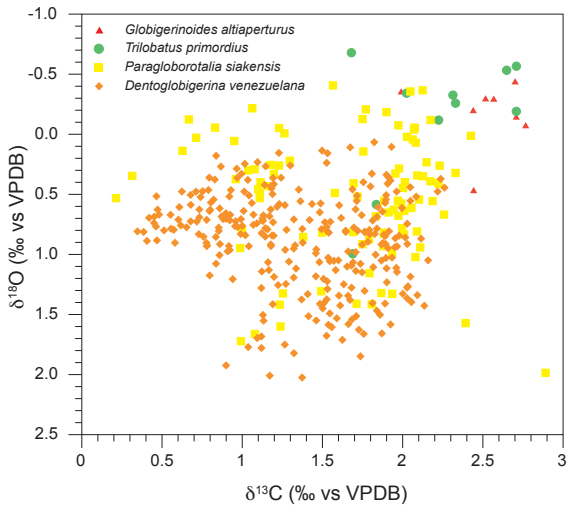

Figure 4.8. *$\delta^{18}O$ vs $\delta^{13}C$ crossplot for the four planktonic species selected for this study, D. venezuelana (orange diamonds), P. siakensis (yellow squares) Globigerinoides altiaperturus (red triangles) and Trilobatus primordius (green circles).*

and mid Oligocene, suggesting coherent variation between planktonic and benthic $\delta^{13}C$ is a consistent feature of the the Oligocene and Miocene time interval [*Wade and Pälike*, 2004; *Tian et al.*, 2014]. Box modeling studies have proposed an internal feedback system chemical resulting in eccentricity paced variations in weathering driving changes in the DIC pool [*Ma et al.*, 2011] and the long-residence time of carbon in the oceans leading to an amplification of higher astronomical periodicities within the $\delta^{13}C$ record as mechanisms to explain the prominent 405 kyr $\delta^{13}C$ cycles seen throughout the Cenozoic $\delta^{13}C$ record [*Pälike, et al.*, 2006b].

At the 405 kyr periodicity, the weak power in the planktonic $\delta^{18}O$ is not consistent with the dominant 405 kyr signal in benthic $\delta^{18}O$. One possibility is that variability in the $\delta^{18}O$ at the 405 kyr periodicity is obscured due to variance in planktonic foraminifera $\delta^{18}O$ and the sampling resolution of the dataset. The mid Oligocene record from ODP Site 1218 also expresses lower power in planktonic foraminifera $\delta^{18}O$ at the 405 kyr periodicity than in the benthic foraminifera $\delta^{18}O$ [*Wade and Pälike*, 2004].

Both benthic and planktonic foraminifera $\delta^{13}C$ show a strong response at the ~125 kyr periodicity, but this signal is stronger in the evolutive spectra for planktonic foraminifera $\delta^{13}C$ between ~22.8 Ma and 23.2 Ma, in comparison to benthic foraminifera $\delta^{13}C$ (Fig. 6). This, combined with an increase in foraminiferal abundances and relatively high $CaCO_3$ est (%) (Figs. 4 and 6), suggests that during the glacial expansion at the OMT, thermocline waters experienced an increase in productivity on 100 kyr time scales. In general, there is a correlation between positive $\delta^{18}O$ values, inferred as intervals of global cooling, and enhanced species abundances, which is particularly noticeable during the OMT, and in the early Miocene between 21.9 and 22.3 Ma (Fig. 4).

At Site 1264, inverse modeling constrained by benthic $\delta^{18}O$ has shown that phases of high-amplitude ~110 kyr variability coincides with phases of lower ice volume, following large expansions of the Antarctic ice sheet occurring between 23.4 and 22.6 Ma, and 22.3 and 21.9 Ma [*Liebrand*

et al., 2011]. The two ice sheet expansions occur during 405 kyr minima, when ~110 kyr cyclicity is weaker, although notably not during every 405 kyr minima, suggesting a potential relationship to 1.2 Myr long-term modulation of obliquity or 2.4 Myr modulation of eccentricity [*Palike et al*., 2006a, *Liebrand et al*., 2011, submitted]. This suggests that surface water productivity/preservation during export productivity increases during phases of Antarctic Ice sheet expansion, and decreases during phases of lower ice sheet volume with increased ~110 kyr paced $\delta^{18}O$ variability within 405 kyr minima. Increases in ice volume could drive increases in meridonal temperature gradients, which would lead to an increase in upwelling and subsequent nutrient availability, increasing export productivity and organic carbon burial, driving the biological pump during phases of Antarctic ice sheet expansion [*Zachos et al*., 1997; *Diester-Haass et al*., 2011]

The 40 kyr obliquity signal is not strongly expressed in either the planktonic or benthic foraminiferal $\delta^{13}C$ and $\delta^{18}O$ at Site U1334. This is in contrast to a low-resolution OMT planktonic foraminifera record from equatorial Atlantic Site 926, which is dominated by strong variation on obliquity time-scales, even in the depth domain [*Pearson et al.,* 1997; *Paul et al*., 2000]. The difference in the obliquity response between sites in the Atlantic basin across the OMT has been discussed extensively in *Liebrand et al.,* [submitted] and is potentially due to different approaches in age model construction, or bioturbation at low sedimentation rates [*Beddow et al*., Chapter 2].

4.5.5 The evolution of $\delta^{13}C$ vertical water column gradients across the OMT

The long-term increase in $\Delta\delta^{13}C$ between 22.2 and 24.1 Ma indicates an increase in thermocline-deep ocean $\delta^{13}C$ gradients. A marked shift in $\Delta\delta^{13}C$ begins after the $\delta^{18}O$ and $\delta^{13}C$ maxima at the OMT, indicating the expansion of vertical water column gradients in the Pacific is associated with a global shift in the carbon cycle that occurs across the OMT and is either coincident with or triggered by the expansion of the Antarctica ice sheet/cooling deep sea temperatures (Fig. 7) [*Hodell and Woodruff*, 1994; *Diester-Haass et al*., 2011]. There are two notable short-lived interruptions to the trend in increasing $\Delta\delta^{13}C$. The first is at 23.7 Ma, during which $\delta^{13}C$ gradients collapse to ~0.0 ‰, simultaneous with enriched benthic $\delta^{13}C$ values relative to planktonic $\delta^{13}C$. A second interruption occurs at the end of the Oligocene-Miocene Carbon Maximum (22.1 Ma), when both benthic and planktonic foraminifer $\delta^{13}C$ shift abruptly towards negative values. Both reductions in gradients are coincident with marked decreases in $CaCO_3$ est (%) and occur during intervals of general foraminifer abundance in sediments, indicating that these collapses in $\delta^{13}C$ reflect short intervals of low productivity, although we cannot exclude the potential influence of diagenesis.

4.5.6 Eccentricity pacing of thermocline to deep-water stable isotope gradients

On ~110 kyr time scales, increases in $\Delta\delta^{18}O$ values and $\delta^{18}O$ maxima occur during eccentricity minima, suggesting that thermocline-to-deep water $\delta^{18}O$ gradients expand during colder, more glacial conditions paced by short eccentricity. The thermocline-deep-water $\Delta\delta^{18}O$ signal exhibits a high level of variability, in particular in the early Miocene, reflecting the increase of ~110 kyr paced variability in both $\delta^{18}O$, and differences in the amplitude of ~110 kyr variability between planktonic and benthic $\delta^{18}O$ (Fig. 7).

Expansions in $\Delta\delta^{18}O$ coincide with increases in $\Delta\delta^{13}C$ and $\delta^{13}C$ maxima, and maxima in $CaCO_3$ est (%), suggesting a link between cooler, glaciated climate conditions and changes in the carbon cycle [*Zachos et al*., 1997; *Wade and Palike*, 2004; *Liebrand et al*., 2011]. The coherent cyclical variation on eccentricity timescales between the benthic and planktonic $\delta^{13}C$ driven by enriched planktonic $\delta^{13}C$ suggests an increase in strength of the biological pump, driven by an increase in export production and carbon burial [*Zachos et al., 1997*; *Rohling and Cooke*, 1999; *Diester-Haass*

et al., 2011]. Eccentricity pacing of enhanced thermocline to deep-water gradients on ~110 kyr timescales associated with increased planktonic $\delta^{13}C$ values (peak productivity) during cooler, more glacial climate conditions are also present in Oligocene and Pleistocene planktonic foraminiferal stable isotope records, suggesting this is a persistent feature of Cenozoic glaciated climates [*Wade and Pälike,* 2004; *Hodell et al*., 2003]. Increases in wind-driven transport of nutrients to the sea surface during cooler, more glacial climates could account for an increase in productivity and organic carbon export on ~110 kyr timescales, suggesting the biological pump, and therefore biological carbon sequestration from the atmosphere, is enhanced during glacials [*Wade and Pälike*, 2004].

4.6 Conclusions

We present the first high-resolution (~7kyrs) planktonic isotope record for the OMT, using the lower thermocline dwelling foraminiferal species, *Dentoglobigerina venezuelana,* providing a 2.2 Myr record of climate evolution in the thermocline waters of the EEP. Using a previously published benthic record, we explore vertical carbon and oxygen gradients in the Pacific. Using the amplitude of the positive shift in $\delta^{18}O$ at the OMT, we estimate a lower limit of ~0.45‰ for the ice volume component of the benthic foraminiferal $\delta^{18}O$ signal, implying a global sea level fall of~ 45m and thermocline cooling of 4-5°C across the OMT. We find a steady increase in $\delta^{13}C$ gradients between ~23.3 and 22.2 Ma, coincident with the Oligocene-Miocene carbon maximum, driven by an enrichment of planktonic foraminiferal $\delta^{13}C$. This increase ends abruptly at 22.2 Ma, as benthic and planktonic foraminiferal $\delta^{13}C$ decreases. High amplitude cyclical variations in $\delta^{13}C$ and $\delta^{18}O$ gradients indicate that vertical gradients expand during colder, more glacial conditions, paced by 100 kyr eccentricity, suggesting an eccentricity-paced control on export productivity and the biological pump. Major phases of Antarctic Ice Sheet expansion, between 23.4 and 22.6 and between 23.1 and 21.9 Ma, are characterized by the largest fluxes of planktonic specimens/g, suggesting surface water productivity is highest during intervals of increased ice-sheet accumulation.

Acknowledgements
This research used samples provided by the Integrated Ocean Drilling Program (IODP), collected by the staff, crew and scientists of IODP Expedition 320/321. IODP is sponsored by the U.S. National Science Foundation and participating countries. We thank Dominika Kasjanuk, Arnold van Dijk, Maxim Krasnoperov and Jan Drenth for laboratory assistance, and Frits Hilgen and Heiko Pälike for useful discussions. This research was supported by NWO VICI grant no. [865.10.001] awarded to L. J. Lourens. A. Sluijs thanks the European Research Council (ERC) under the European Union Seventh Framework Program for ERC Starting Grant #259627. DK is funded through the London Doctoral Training Programme. AH was funded by a University Research and Leadership Scholarship from the University of Leeds. BW was supported by UK Natural Environment Research Council (NERC) reference number NE/G014817, and a Marie Curie Career Integration Grant "ERAS". Data are available in the supporting information tables and online through Pangaea.

Appendix A. Supplementary data

List of species
Planktonic foraminifera species
Globigerinoides altiaperturus Bolli, 1957
Trilobatus primordius (Blow and Banner, 1962)
Paragloborotalia siakensis (LeRoy, 1939)
Dentoglobigerina venezuelana (Hedberg, 1937)

Benthic foraminifera species
Cibicidoides mundulus (Brady, Parker, and Jones, 1888)
Oridorsalis umbonatus (Reuss, 1851)

Appendix B. Supplementary figures

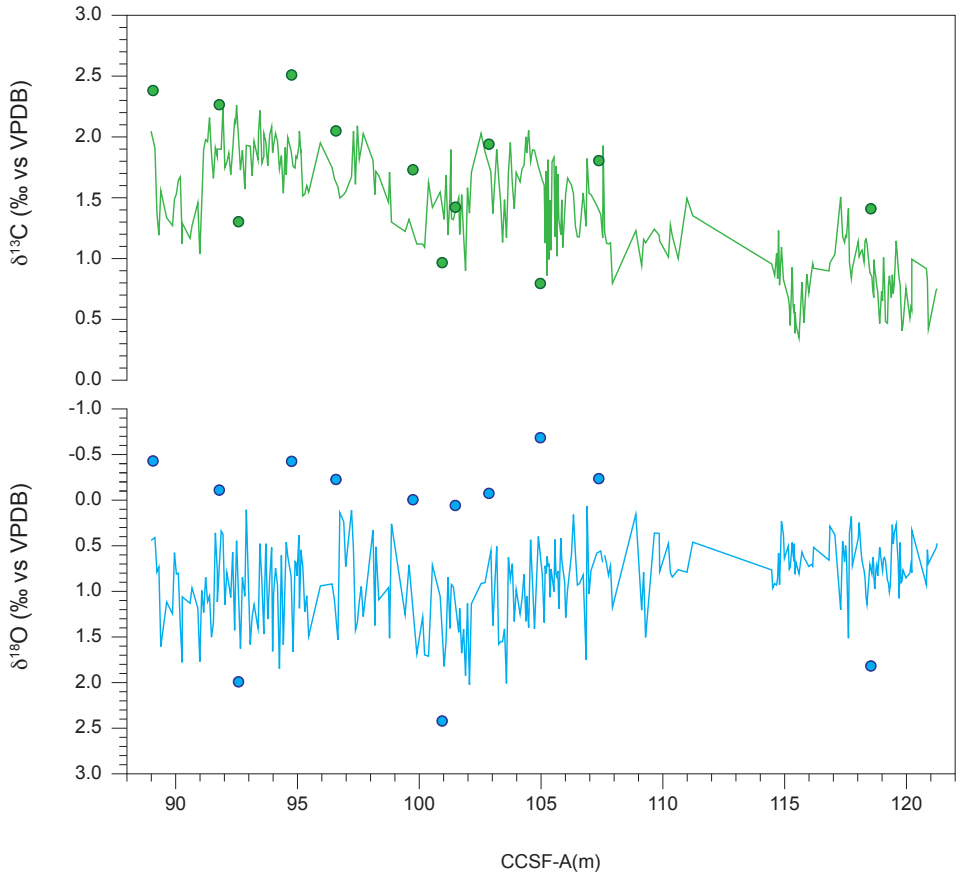

Figure S1. *Planktonic foraminferal $\delta^{13}C$ (a) and $\delta^{18}O$ (b) plotted on CCSF-A depth scale. Circles represent outlying values removed from the dataset.*

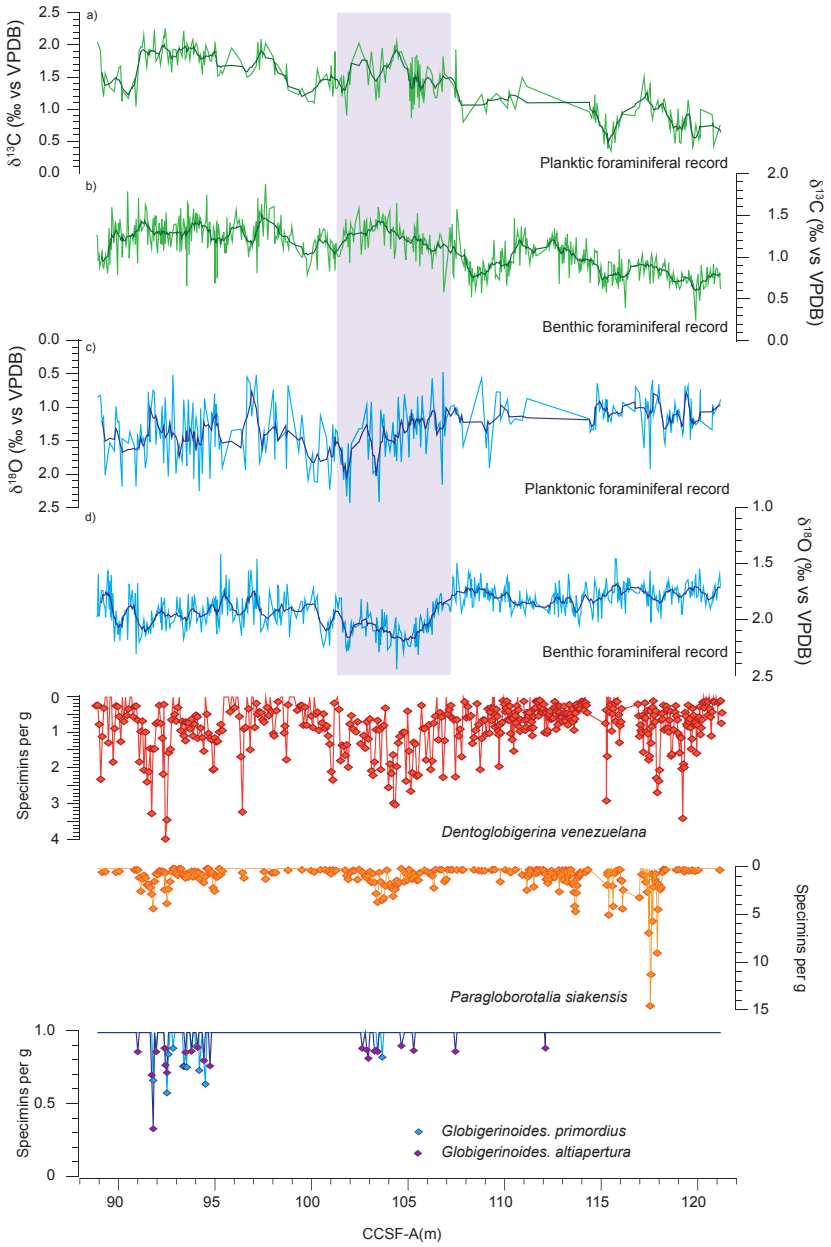

Figure S2. *Planktonic $\delta^{13}C$ (a) and $\delta^{18}O$ (c) foraminifera stable isotopes from Site U1334 compared to previously published benthic $\delta^{13}C$ (b) and $\delta^{18}O$ (d) foraminifera stable isotopes from Site U1334 [Beddow et al., Chapter 2] plotted against CCSF-A. Carbon isotopes are in light green, with a 5 point moving average running through the data in dark green. Oxygen isotopes are in light blue, with a 5-point moving average running through the data in dark blue. Foraminiferal abundances are plotted for the species D. venezuelana (e), P. siakensis (f) and Globigerinoides/Trilobatus spp. (g) in specimens per gram of sediment.*

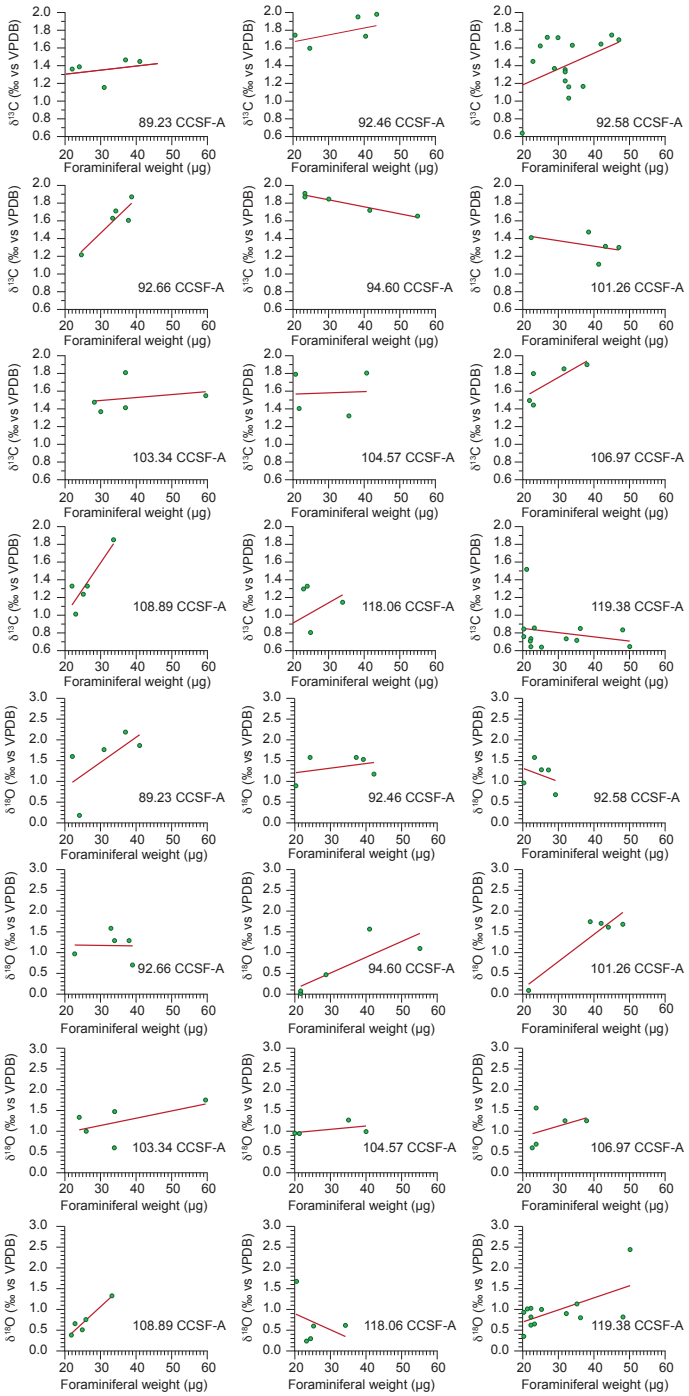

Figure S3. *Intra-sample comparisons of weight vs $\delta^{18}O$ isotope value and weight vs $\delta^{13}C$ isotope value for individual D. venezuelana specimens.*

Chapter 5:
Early to middle Miocene climate evolution: benthic oxygen and carbon isotope records from Walvis Ridge Site 1264.

Abstract

Across the early to middle Miocene, high-resolution records from the Pacific Ocean indicate a dynamic climate system, encompassing a 2 Myr global warming event from 17 Ma to 14.7 Ma, followed by a major Cenozoic cooling step at 14.2 Ma -13.8 Ma. Currently, no high-resolution benthic record from the Atlantic Ocean exists covering both events, limiting global coverage of this intriguing period in Cenozoic climate evolution. Here, we present the first early to middle Miocene high-resolution from the Atlantic basin. These records, from Site 1264 on the Walvis Ridge, span a ~5.5 Myr long interval (13.24-18.90 ma) in high temporal resolution (~4 kyr) and are tuned to eccentricity. The $\delta^{18}O$ record shows a sudden (high-latitude) warming/deglaciation on Antarctica at ~17.1 Ma, a rapid cooling/glaciation of Antarctica at ~13.8 Ma, and high-amplitude (~1‰) variability on astronomical time-scales throughout this interval. Together with other records from this time interval located in the Pacific, which show similar features, the data strongly suggests a highly dynamic global climate system. We find cooling steps in $\delta^{18}O$ at 14.7, 14.2 and 13.8 Ma, suggesting concurrent cooling in the Pacific and Atlantic deep waters during the MMCT. The benthic foraminiferal stable isotope records reveal that the dominant astronomical frequencies present at ODP Site 1264 during the early to middle Miocene interval are the 405 kyr and ~110 kyr eccentricity periodicities. This is a contrast to other early to middle Miocene records from drill-sites in the Pacific and South China Sea, which show a strong expression of obliquity in particular between 14.2 and 14.7 Ma.

5.1 Introduction

The early to middle Miocene is a dynamic period of Earth's climate history, containing a two million year long period of prolonged warmth, the Miocene Climatic Optimum (MCO; between ~17 and 14.7 Ma). The MCO is followed by a steady decline in temperatures culminating in a global climate transition towards colder, more glaciated conditions, the Middle Miocene Climate Transition (MMCT; between ~14.2 Ma and ~13.8 Ma). Understanding the MCO is vital in the context of modern day climate change, as the MCO is the geologically most recent interval of global warmth during a unipolar climate system, presenting an ideal opportunity to study Antarctic ice sheet dynamics in a warmer world. The MMCT is the second of three major Cenozoic global cooling/glaciation steps in the long-term cooling trend towards modern day climate systems with large continental ice sheets at both poles [*Zachos et al.*, 2001]. In the last decade**,** current understanding of early to middle Miocene climate has made substantial progress, underpinned by the generation of high-resolution, astronomically tuned benthic and planktonic stable isotope records from deep-sea drill cores. This has allowed us to track the evolution of Early Neogene climate variability in unprecedented detail and with precise time control [*Holbourn et al.*, 2005, 2007, 2013a,b, 2014, 2015; *Tian et al.*, 2013, 2014].

The early Miocene (~23-17 Ma) is characterized by relatively cold, glaciated climate conditions in comparison to the late Oligocene, as indicated by strong high-amplitude ~110 kyr variability (between ~0.5 and 1‰) and positive $\delta^{18}O$ values in benthic foraminiferal stable isotope records, suggesting the significant waxing and waning of ice sheets on Antarctica [*Zachos et al.*, 1992; *Liebrand et al.*, 2011; *Holbourn et al.*, 2015]. This relatively cool/glaciated phase shifts abruptly to warmer/less glaciated conditions during the onset of the MCO at ~17 Ma [*Woodruff and Savin*, 1991; *Miller et al.*, 1991; *Flower and Kennett*, 1993, 1995; *Shevenell et al.*, 2004, 2008; *Holbourn et al.*, 2005, 2007, 2013, 2014, 2015], with more negative benthic $\delta^{18}O$ values varying around ~0.5 to 1‰ lighter than in the early Miocene. The MCO stands out in the benthic $\delta^{18}O$ stable isotope record as one of the few major events running counter to the long-term trend of climate cooling in the Cenozoic [*Zachos et al.*, 2001, 2008].

The termination of the MCO is followed by a gradual positive shift in $\delta^{18}O$, indicating steady decreasing deep-sea temperatures/increasing in ice volume between ~14.7 to 14.2 Ma, modulated by obliquity in Pacific high-resolution stable isotope records [*Holbourn et al.,* 2007; 2013; 2014; 2015]. It culminates in a large shift towards positive $\delta^{18}O$ values between ~14.2 Ma and 13.8 Ma at the MMCT [*Flower and Kennett*, 1993; *Flower and Kennett*, 1994; *Tian et al.*, 2013]. The maximum $\delta^{18}O$ values of the MMCT at ~13.8 Ma is recognized as isotope event Mi3b [*Miller et al.*, 1991, 1996], marking the transition into colder climate conditions and a large expansion of the East Antarctic Ice sheet (EAIS) [*Woodruff and Savin*, 1989; *Miller et al.*, 1991; *Flower and Kennett*, 1994; *Zachos et al.*, 2001; *Holbourn et al.*, 2007; 2013; *Tian et al.*, 2013, 2014]. Mi zones were traditionally designated as oxygen isotope zones containing peak $\delta^{18}O$ values at their base [*Miller et al.*, 1991], but have come to designate the $\delta^{18}O$ maxima [e.g. *Miller et al.*, 1996; *Abels et al.*, 2005; *Husing et al.*, 2009; *Mourik et al.*, 2011]. Within this study, we refer to Mi3b to mean the rapid $\delta^{18}O$ increase at the base of the MMCT.

Across the middle Miocene (~17 Ma-13.5 Ma) the $\delta^{13}C$ record shows several transient $\delta^{13}C$ maxima. This $\delta^{13}C$ carbon excursion was first identified at DSDP Site 216 in the tropical Indian Ocean and termed the "Monterey" Carbon Isotope Excursion due to its synchronous timing with the deposition of the organic carbon rich Monterey formation [*Vincent and Berger*, 1985; *Woodruff and Savin*, 1991]. The six $\delta^{13}C$ maxima (CM events) encompassed by the Monterey carbon isotope

excursion are paced by the long-period (405 kyr) eccentricity cycle, and the last $\delta^{13}C$ maxima, CM6, coincides with the termination of Mi3b in the $\delta^{18}O$ record at ~13.8 Ma [*Woodruff and Savin*, 1991, *Holbourn et al.*, 2007; 2013; *Tian et al.*, 2013]. These CM events are generally interpreted as an episodic increase in carbon burial leading to an increase in pCO_2 drawdown, contributing towards global cooling [*Vincent and Berger*, 1985; *Woodruff and Savin*, 1991, *Flower and Kennet*, 1993, 1994, *Holbourn et al.*, 2007, 2015; *Greenop et al.*, 2014].

The early to middle Miocene is comparatively understudied, with only four high-resolution (3-7 kyr) stable isotope records, all located in or adjacent to the Pacific, with no single high-resolution stable isotope stratigraphy available that captures both the MCO and the MMCT at an Atlantic site. A record from Site 1090 in the Atlantic sector of the southern ocean extends to ~16 Ma, but is of relatively low resolution in the early Miocene. Here, we present the first astronomically tuned high-resolution (~4 kyr) benthic stable isotope records from Site 1264 in South Atlantic Ocean resolving the early to middle Miocene (13.24 to 17.1 Ma). In addition, we use existing data from Site 1264 between 17.1 and 18.9 that encompasses the early Miocene interval in the lead-up to the MCO [*Liebrand et al.*, submitted]. We assess the global significance of climate and carbon cycle events reconstructed on the basis of existing high-resolution stable isotope records from the circum-Pacific Sites ODP Sites 1237 and 1146, and IODP sites U1337 and U1338 [*Holbourn et al.*, 2005; 2007, 2013, 2014, 2015]. We discuss the interval from 13.24-18.90 Ma, encompassing the MCO, the MMCT, Mi3b and the six CM events, and compare the amplitude and timing and astronomical pacing of these events between the Atlantic and Pacific basins.

5.2 Site Description

ODP Site 1264 (28°31.955'S, 2°50.730'E) is located 2505 metres below sea level (mbsl) on the Walvis Ridge in the south-eastern Atlantic Ocean, and was drilled in 2003, during expedition Leg 208 (Fig. 1). A shipboard composite depth scale and spliced record was constructed using Holes A and B [*Zachos et al.*, 2004]. Following the shipboard splice, the section used for this study runs from 184.25 (1264 B18 H 4) to 216.57 (1264 B21 H5) metres composite depth (mcd) (Fig. 2). Miocene sediments consist of a foraminifer-bearing nannofossil ooze. Shipboard data indicate $CaCO_3$

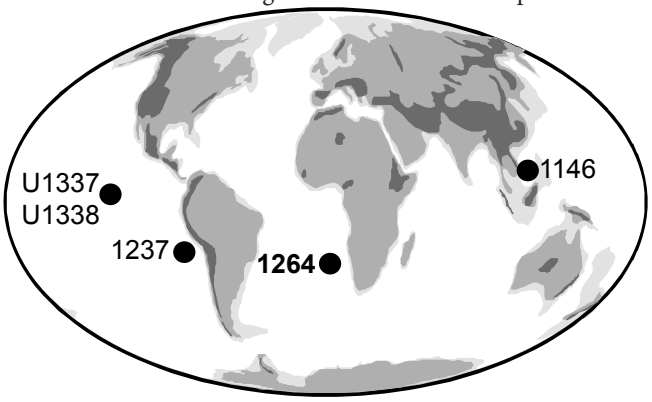

Figure 5.1. *Location of the newly generated high-resolution records generated from ODP Site 1264 with reference to other high-resolution sites discussed within this study, ODP Site 1237, ODP Site 1146, IODP Site U1337 and IODP Site U1338.*

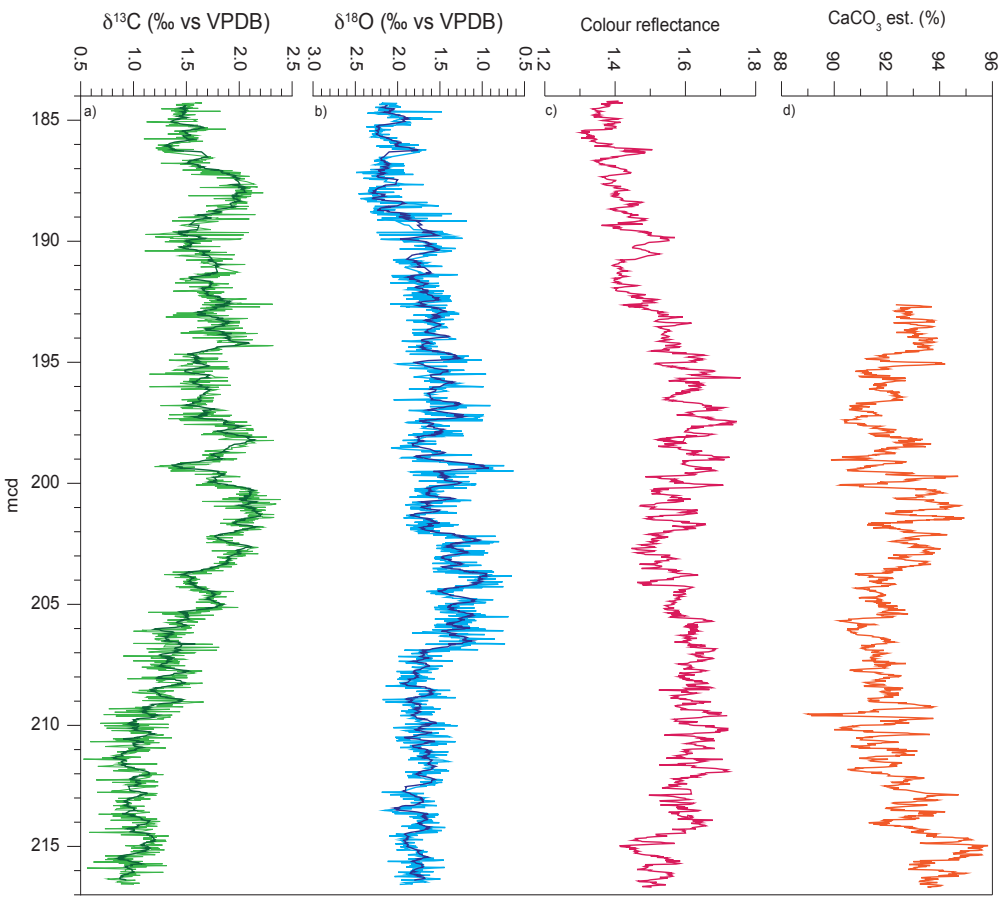

Figure 5.2. *Site 1264 benthic foraminiferal $\delta^{13}C$ (a) and $\delta^{18}O$ (b) stable isotope records, colour reflectance (c) and $CaCO_3$ est. (%) record (d) on the mcd depth scale based on the shipboard splice [Wang et al., 2012]. The orange bar marks the potential hiatus at Site 1264.*

concentrations are consistently high within this section, greater than 92 wt%, with well-preserved foraminifera [*Zachos et al.*, 2004].

We compare our benthic foraminiferal stable isotope data with high-resolution stable isotope datasets from ODP Site 1237, located in the South east Pacific (3212 mbsl) [*Holbourn et al.*, 2005; 2007], ODP site 1146 (2902 mbsl) located in the South China Sea [*Wang et al.*, 2000; *Holbourn et al.*, 2005; *Holbourn et al.*, 2007; *Holbourn et al.*, 2013], and IODP Sites U1337 (4200mbsf) [*Pälike et al.,* 2010, *Holbourn et al.*, 2015] and U1338 in the eastern equatorial Pacific (4200 mbsf, paleodepth during Middle Miocene ~3000-3500) [*Pälike et al.*, 2010; *Holbourn* et al., 2014], which were both drilled during Expedition 320/321 (Fig. 1).

5.3 Methods

5.3.1 Stable isotope analysis

Samples of approximately 15cm^2 (half core slices) of sediment were taken every 2cm, following the shipboard splice. The samples were freeze-dried, washed over 38 µm, 63 µm and 150 µm sieves, and oven-dried at 40ºC. Samples were dry-sieved and the benthic foraminifer species, *Cibicides mundulus* was picked from the 250-355 µm size fraction. Between 1 and 6 foraminifera were picked, crushed for homogeneity and ultrasonically cleaned for two seconds while suspended in ethanol. Excess ethanol was pipetted out and the samples dried overnight at 40°C. Stable isotope analyses were conducted at Utrecht University, using a Thermo-Finnigan Kiel III automated preparation system coupled to a Thermo-Finnigan MAT 253 mass spectrometer. The standard NBS-19 and an in-house marble standard "Naxos" were used to calibrate isotope values to Vienna Pee Dee Belemnite (VPDB). This methodology is consistent with the methodology for the Site 1264 benthic foraminiferal stable isotope record constructed for the interval between 17.1 and 30.1 Ma [*Liebrand et al.*, submitted]. Analytical precision is 0.03 ‰ and 0.08 ‰ for $\delta^{13}C$ and $\delta^{18}O$, respectively. In total, 26 outliers were identified by eye and were removed from both the $\delta^{13}C$ and $\delta^{18}O$ series, leaving a total of 1389 measurements within each dataset.

5.3.2 X-ray fluorescence data

X-ray fluorescence (XRF) element counts were generated at the MARUM XRF-laboratory, University of Bremen. Calibrations ($r^2_{(1264)}$ = 0.84, $r^2_{(1265)}$ = 0.95) between ln(Ca/Fe) and shipboard

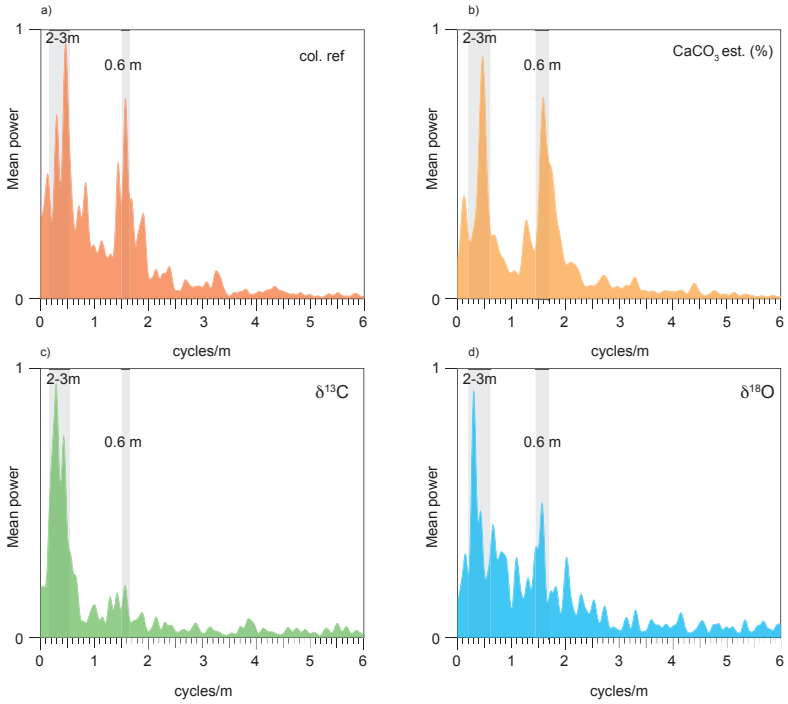

Figure 5.3. *Blackman-Tukey spectral analysis of colour reflectance (a), $CaCO_3$ est (%),* $\delta^{13}C$ *(c) and* $\delta^{18}O$ *(d) in the depth domain. Datasets are notch-filtered in analyseries to remove cycles longer than 6m.*

coulometric $CaCO_3$ measurements from Sites 1264 and 1265 [*Zachos et al.*, 2004] are used to estimate the $CaCO_3$ content ($CaCO_3$ est.) for the studied interval (see supplementary Fig. S1 in *Liebrand et al.*, submitted].

5.3.3 Spectral analyses

Spectral analysis methods are conducted on colour reflectance and benthic stable isotope datasets in the depth domain and on the astronomical age model presented within this study. Before analysis, data were re-sampled, linearly detrended and long-term trends longer than 6m or 600 kyr were removed using a notch-filter in version 2 of the software package AnalySeries [*Paillard et al.*, 1996]. Spectral analysis methods were conducted on the $CaCO_3$ est. (%) and benthic foraminiferal $\delta^{13}C$ and $\delta^{18}O$ datasets in the depth domain to examine spectral characteristics present in the datasets prior to being placed on the initial or tuned age models. We use Blackman-Tukey power spectral analysis to identify dominant periodicities present within the data and filter significant spectral peaks using a Gaussian filter in AnalySeries. To identify coherence and phase relationships between datasets and the astronomical curve of *Laskar et al*, [2011a,b], we perform Blackman-Tukey cross-spectral analysis at 95% significance. Wavelet spectra were calculated using an adapted script of *Grinsted,* [2004].

5.4 Results

5.4.1 Colour reflectance and $CaCO_3$ est (%)

Variability in the $CaCO_3$ est. record between 192.61 and 216.58 mcd ranges between 89 and 96 wt% $CaCO_3$ of the dry sediment, with an average of ~92%. The highest percentages of $CaCO_3$ occur between ~205 to ~212 mcd and ~214 to 216 mcd, with a maximum value at 214.86 mcd (Fig. 2). Reduced amplitude variability is recorded between ~191 to 196 mcd and ~204 to 209 mcd, with a minimum value of ~89 wt% at ~209.45 mcd.

The colour reflectance record is derived using a ratio of the 600 and 450 nm wavelength. This ratio of wavelength was also used during Leg 208 to establish hole-to-hole correlations and a shipboard composite depth scale and splice in $CaCO_3$-rich intervals where the magnetic susceptibility record did not show clear variability [*Zachos et al.*, 2004]. The colour reflectance record follows the $CaCO_3$ est (%) record with a large degree of synchronicity. Variability in the colour reflectance 600/450 ratio ranges between 1.30 and 1.75. The highest values are present between ~197 mcd and ~212 mcd (Fig. 2). Colour reflectance values begin to decline at ~212, and reach a minimum value at 185.45 mcd. Regular variations in $CaCO_3$ content with an amplitude of 2-3% are observed with at an even spacing of ~0.6 and ~2-3m throughout the record (Fig. 2).

5.4.2 Benthic stable isotopes

At Site 1264, in the interval between 184 and 217 mcd, benthic foraminiferal stable carbon isotope ratios ($\delta^{13}C$) vary between 0.52‰ (211.40 mcd) and 2.39‰ (200.67 mcd) (Fig. 2). After detrending, the $\delta^{13}C$ record has a standard deviation of ~0.13‰ and a range (representing maximum variability in the record) of ~1.0‰. The $\delta^{13}C$ record shows relatively low values and amplitude variability between ~216 and ~203 mcd. Above this interval, between ~203 and ~183 mcd, we observe a long-term increase in $\delta^{13}C$ and amplitude variability characterized by six prominent $\delta^{13}C$ maxima. Following the last $\delta^{13}C$ maximum at ~184 mcd, there is a shift towards lower $\delta^{13}C$ values.

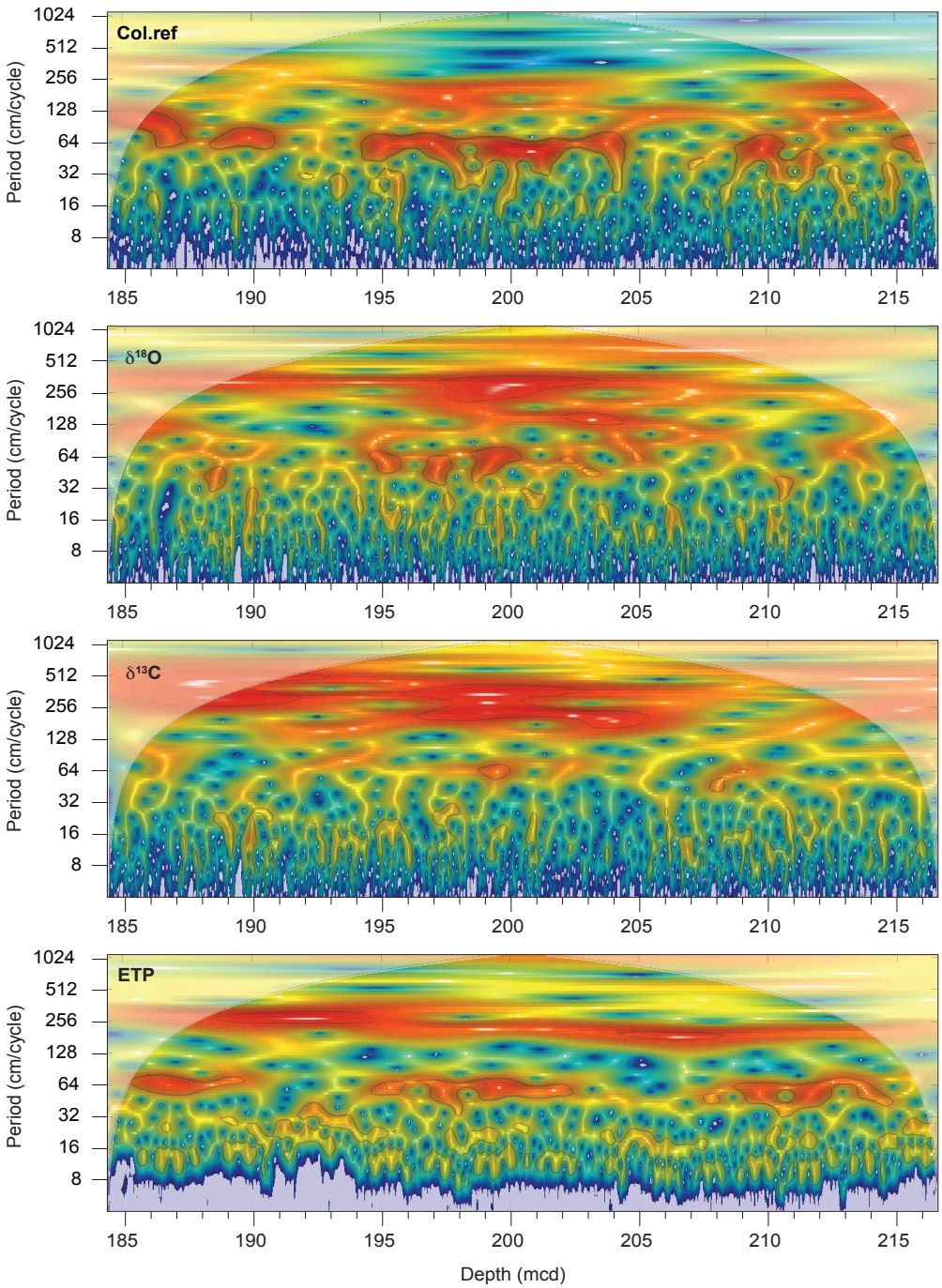

Figure 5.4. *Wavelet analyses for colour reflectance (a), $\delta^{13}C$ (b) and $\delta^{18}O$ (c) indicating periodicities present with the datasets in the depth domain, compared with a smooth depth-rescaled ETP curve (d) based on La2011 [Laskar et al., 2011a,b] and La2004 (Laskar et al., 2004).*

Benthic foraminiferal stable oxygen isotope ratios ($\delta^{18}O$) vary between 0.63‰ (199.49 mcd) and 2.49‰ (187.16 mcd) (Fig. 2). After detrending, the $\delta^{18}O$ record has a standard deviation of ~0.16‰ and a maximum variability of ~0.9‰. An interval of low $\delta^{18}O$ values is recorded between ~199 and 207 mcd with several minima reaching below ~1.0‰. There is a ~1.0‰ decrease in $\delta^{18}O$ values between 189 and 192 mcd.

5.4.3 Spectral analyses in the depth domain

In the depth domain, we find strong spectral peaks in the colour reflectance, $CaCO_3$ est (%), $\delta^{18}O$ and $\delta^{13}C$ datasets at ~0.6 m cycle and a broader 3.3-2m cycle (Fig. 3). High-amplitude periodicities in the colour reflectance, $CaCO_3$ est (%), $\delta^{18}O$ and $\delta^{13}C$ datasets occur at a roughly 1:4 ratio, suggesting that they are related to 405 and ~110 kyr eccentricity cycles, which have a similar ratio of occurrence (Fig. 3). This finding is supported by the initial biostratigraphic age model [*Zachos et al.*, 2004], which suggests that the study interval covers approximately 5.6 Myr, indicating that our main periodicities found in the depth domain have a duration of ~405 and ~110 kyr.

Wavelet analyses in the depth domain (Fig. 4) reveal that the broad cycle at 3.3-2 m is best expressed in the $\delta^{13}C$ dataset. This cycle shows an increase in power ~205 mcd, which remains strong until the top of the dataset. The cycle at ~0.6 m is has the highest amplitudes in the colour reflectance and $\delta^{18}O$ datasets, notwithstanding several short intervals of significantly reduced power.

5.4.4 Age model

As a starting point for our age model, we use an initial age model created by *Liebrand et al.* [submitted], based on a polynomial fit through selected biostratigraphic and magnetostratigraphic tie-points between 184 and 318 mcd (see *Liebrand et al.*, [submitted] supplementary information Fig S2). Liebrand et al., [submitted] revised the splice for the interval below ~216 mcd, producing a new splice and depth scale, but these revisions do not affect the interval above ~216 mcd. For the interval studied here, between 184.27 and 216.57 mcd, the initial age-control points are based mainly on biostratigraphy, as there is no clear discernable magnetostratigraphy available for the middle Miocene sediments from Site 1264 [*Bowles*, 2006; *Zachos et al.*, 2004].

Fine-tuning of the Site 1264 records was accomplished using the combined XRF core scanning (ln(Ca/Fe; between ~192 and ~216 mcd only), magnetic susceptibility (shipboard and discrete samples) and 600/450 nm colour reflectance. Variance in these three physical/chemical property records is predominantly controlled by the $CaCO_3$ content of the sediment, allowing a comparable tuning approach across the early and middle Miocene as the approach used to tune the early Oligocene through early Miocene interval at Site 1264 [*Liebrand et al*, submitted].

Eccentricity is chosen as the tuning target primarily because of the strong expression of 405 and ~110 kyr periodicities in the dataset shown on the initial age model. The weak expression of

Figure 5.5. *Site 1264 benthic foraminiferal $\delta^{13}C$ (a) and $\delta^{18}O$ (b) stable isotope records placed on the astronomical age model. The 405 kyr (c) and ~110 kyr (d) periodicities are extracted from the datasets and the La2011 astronomical solution [Laskar et al., 2011] using a Guassian filter (405 kyr: f =0.0025, bw =0.0008 and ~110 kyr kyr: f=0.01, bw=0.003). The $\delta^{13}C$ 405 and ~110 kyr periodicities are in green, the $\delta^{18}O$ 405 and ~110 kyr periodicities are in blue and the periodicities derived from the astronomical solution are in red. Eccentricity based on the astronomical solution is shown is grey (e), with ~110 kyr filter represented by the dotted red line, and the 405 kyr filter represented by the red line. Colour reflectance is plotted in panel (f). Sedimentation rates based on the astronomical age model are show in panel (g). The orange bar marks the potential hiatus at Site 1264.*

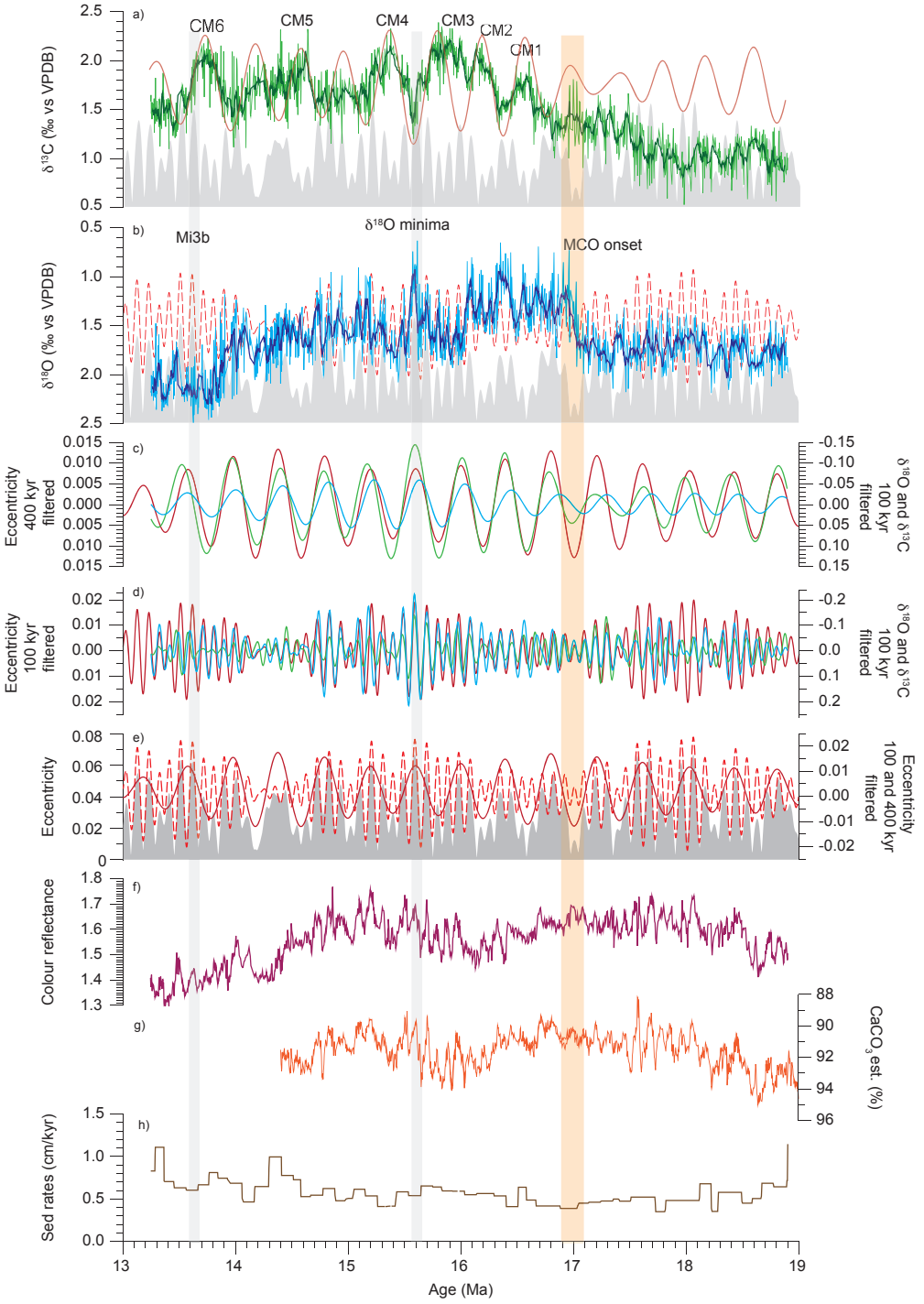
a)
CM6
CM5
CM4
CM3
CM2
CM1
δ13C (‰ vs VPDB)
b)
Mi3b
δ18O minima
MCO onset
δ18O (‰ vs VPDB)
c)
Eccentricity 400 kyr filtered
δ18O and δ13C 100 kyr filtered
d)
Eccentricity 100 kyr filtered
δ18O and δ13C 100 kyr filtered
e)
Eccentricity
Eccentricity 100 and 400 kyr filtered
f)
Colour reflectance
g)
CaCO3 est. (%)
h)
Sed rates (cm/kyr)
Age (Ma)

obliquity excludes it from serving as an appropriate component of the tuning target for Site 1264 records. As an additional consideration, the stability of obliquity and precession periods beyond 10 Ma is uncertain due to limited constraints on tidal dissipation values and dynamical ellipticity [*Lourens et al.,* 2004*; Husing et al.,* 2007*; Zeeden et al.*, 2014].

The phase relation between the $CaCO_3$ proxy records from Site 1264 and the eccentricity tuning target is derived from the known phase relation between $\delta^{18}O$ and eccentricity during the early and middle Miocene on the ~110-kyr time scales (*Holbourn et al.*, 2007, 2013, 2014, 2015; *Pälike et al.*, 2006a). As $\delta^{18}O$ and $CaCO_3$ maxima occur synchronously with ~110 kyr eccentricity minima in the intervals with the strongest ~110 kyr expression throughout our study interval, we link $CaCO_3$ maxima to eccentricity minima and assume that this phase relationship between $CaCO_3$ and eccentricity remains stable for the Oligocene and Miocene at Site 1264 (for further discussion see *Liebrand et al*. submitted).

We obtained a preliminary tuning by matching 405 kyr maxima in $CaCO_3$ est. to 405 kyr minima in the La2011 astronomical solution [*Laskar et al.,* 2011a,b]. We then tuned maxima in $CaCO_3$ est. and minima in colour reflectance to ~110-kyr eccentricity minima. On the astronomically tuned age model, the newly generated benthic stable isotope records cover the interval 13.24-17.1 Ma. For the interval between 17.1 Ma and 18.9 Ma, we use the benthic stable isotope data and astronomical tuning of *Liebrand et al*. [submitted] which is based on similar phase assumptions (Fig. 5). Sedimentation rates at Site 1264 are relatively low, with an average sedimentation rate of 0.6 cm/kyr, and remain fairly steady throughout the record, with the exception of a slight increase between ~14.5 and 13.2 Ma (Fig. 5h). This results in average sample resolution of 4 kyr for the benthic stable isotope records.

Tuning the $CaCO_3$ proxy records of Site 1264 to eccentricity is straightforward across the study interval, with possible exception of the interval around ~207 mcd, corresponding broadly to ~17 Ma or the onset of the MCO (Figs. 2 and 5, orange bar) During this interval, sedimentation rates derived from the tuning are relatively low and the 405 kyr filtered component of the stable isotopes shows a reduced amplitude, which could indicate an uncertainty in the tuning (Figs. 5c and 5d). Alignment of $CaCO_3$ and color proxy records with eccentricity within this interval is less straightforward, and one ~110-kyr cycle could be missing when we approach the tuning from clear tie-points on either side of the interval. This might suggest the presence of a condensed interval, or minor hiatus at this level. However, core photographs do not indicate any change in lithology [*Zachos et al.*, 2004], and we adhere to our age model in view of the lack of physical evidence for a hiatus.

5.4.5 Benthic foraminiferal stable oxygen isotopes ($\delta^{18}O$)

In the early Miocene, between 18.9 to 17 Ma, $\delta^{18}O$ values are relatively positive, with a baseline value of ~1.7 ‰ (Fig. 5). During this interval, there is high-frequency, low-amplitude $\delta^{18}O$ variability between ~ 0.4 to 0.8‰. This interval is followed by a prominent shift towards negative values of ~0.8‰, beginning at ~17.1 Ma, marking the base of the MCO. A sustained interval of more negative $\delta^{18}O$ values is present between ~16.9-14.7 Ma, with a minimum $\delta^{18}O$ value of 0.63‰ occurring at 15.6 Ma. During this interval, high-frequency $\delta^{18}O$ amplitude variability increases, varying between ~0.6 and 1.0‰.

Between ~14.7 and 13.24 Ma, the $\delta^{18}O$ record reveals an overall long-term shift towards more positive values, with steps in $\delta^{18}O$ towards more positive values occurring at 14.7, 14.2 and 13.8 Ma. During this interval, amplitude variability remains relatively high, ranging between ~0.4 and 1.0‰. Between 14.2 Ma and 13.8 Ma, $\delta^{18}O$ shifts by ~1.2 ‰ towards positive values, which can be

identified as the MMCT. The $\delta^{18}O$ record reaches a maximum value of 2.49‰ at ~13.75 Ma, which we identify as Mi3b (Fig. 5) [*Miller et al*., 1991; *Woodruff and Savin*, 1991; *Tian et al*., 2013].

5.4.6 Benthic foraminiferal stable carbon isotopes ($\delta^{13}C$)

The $\delta^{13}C$ record reveals a long-term shift towards increased $\delta^{13}C$ values beginning at ~18 Ma, with a sustained interval of higher $\delta^{13}C$ values present between ~13.5 and 16.8 Ma, containing six clear carbon maxima events (Fig. 5). This is followed by a decrease in $\delta^{13}C$ values at ~13.8 Ma, with a minimum at 13.75 Ma, coincident with third step towards more positive values in the $\delta^{18}O$ record.

The $\delta^{13}C$ record between 18 and 18.9 Ma contains relatively negative $\delta^{13}C$ values, with a steady baseline of ~1.1 ‰, and a minima of 0.53 ‰ at 18.0 Ma. At ~18 Ma, the $\delta^{13}C$ record begins a gradual increase towards more positive values, with the exception of a small decrease back to negative $\delta^{13}C$ values at ~17 Ma, just after the negative shift in $\delta^{18}O$ at the base of the MCO. There is a sharp increase towards positive $\delta^{13}C$ at ~16.8 Ma, and $\delta^{13}C$ values remain relatively postive until ~13.8 Ma. This period of enriched $\delta^{13}C$, containing 6 prominent carbon cycles, is synonymous with the Monterey carbon isotope excursion, and the carbon maxima with CM events 1-6 (Fig. 5). The highest $\delta^{13}C$ value (2.39 ‰) is reached at ~15.6 Ma, the peak of CM3, coincident with the minimum $\delta^{18}O$ value. CM6 has the largest amplitude (~1.1 ‰) of the six CM events identified. Following CM6, there is a sharp decline of ~0.8 ‰ in $\delta^{13}C$ values, beginning at ~13.8 Ma, coincident with the $\delta^{18}O$ maximum at Mi3b.

At the beginning of the record, prior to the onset of the MCO at ~17 Ma, amplitude variability on high-frequency time scales is between ~0.4 and 0.8 ‰. After the positive $\delta^{13}C$ excursion, beginning at ~16.8 Ma, amplitude variability is reduced during CM events 1-3 and varies between ~0.2 and 0.4 ‰. At ~15.4 Ma, following CM4, amplitude variability increases again to between ~0.4 and 0.8 ‰.

5.4.7 Time series analysis

The $\delta^{13}C$ record shows strong variability on 405 kyr timescales, with all CM events occurring during 405 kyr eccentricity minima (Fig. 4). There are eight complete 405 kyr cycles present between 13.8 and 16.8 Ma, during the carbon isotope excursion, with two smaller peaks in $\delta^{13}C$ values occurring in 405 kyr eccentricity minima after CM4 and CM5 (Fig. 5). The dominant astronomical signals in the benthic $\delta^{13}C$ and $\delta^{18}O$ records correspond to 405 kyr and 125 and 96 kyr eccentricity cycles. The expression of shorter periodicities, including 41 kyr obliquity, is weak in both the benthic $\delta^{13}C$ and $\delta^{18}O$ records (Fig. 6), although there are short intervals displaying high-frequency variability that could be obliquity-paced, in particular between ~14.2 and 14.7 Ma (Fig. 5a and Fig 5b)

The 405 kyr periodicity in the benthic $\delta^{13}C$ wavelet spectra shows an increase in power at ~17 Ma, close to the increase in $\delta^{13}C$ values beginning at ~16.8 Ma and signifying the onset of the Monterey carbon isotope excursion (Fig 7c). Power at the 405 kyr periodicity remains strong until at least 13.5 Ma, when $\delta^{13}C$ values decrease. At the ~110 kyr periodicity, the $\delta^{13}C$ wavelet spectrum reveals two intervals of increased power, between and ~14.5 and 16 Ma and ~17 and 18 Ma.

The benthic $\delta^{18}O$ record indicates the presence of significant power at the 405 kyr and ~110 kyr periodicities (Fig. 7b). The wavelet spectrum indicates that the 405 kyr signal in the benthic $\delta^{18}O$ record is strong between ~14.5 and 16 Ma. The ~110 kyr periodicity exhibits strong power between 14.5 and 17.5 Ma during the negative $\delta^{18}O$ excursion at the MCO (Fig. 7). Between ~15.5 and 17 Ma, there is power expressed at a ~200 kyr periodicity, which could represent a multiple of the ~110 kyr eccentricity cycle. Between ~13.9 and 14.8 Ma, there is also the weak expression of power at the ~41 kyr obliquity periodicity.

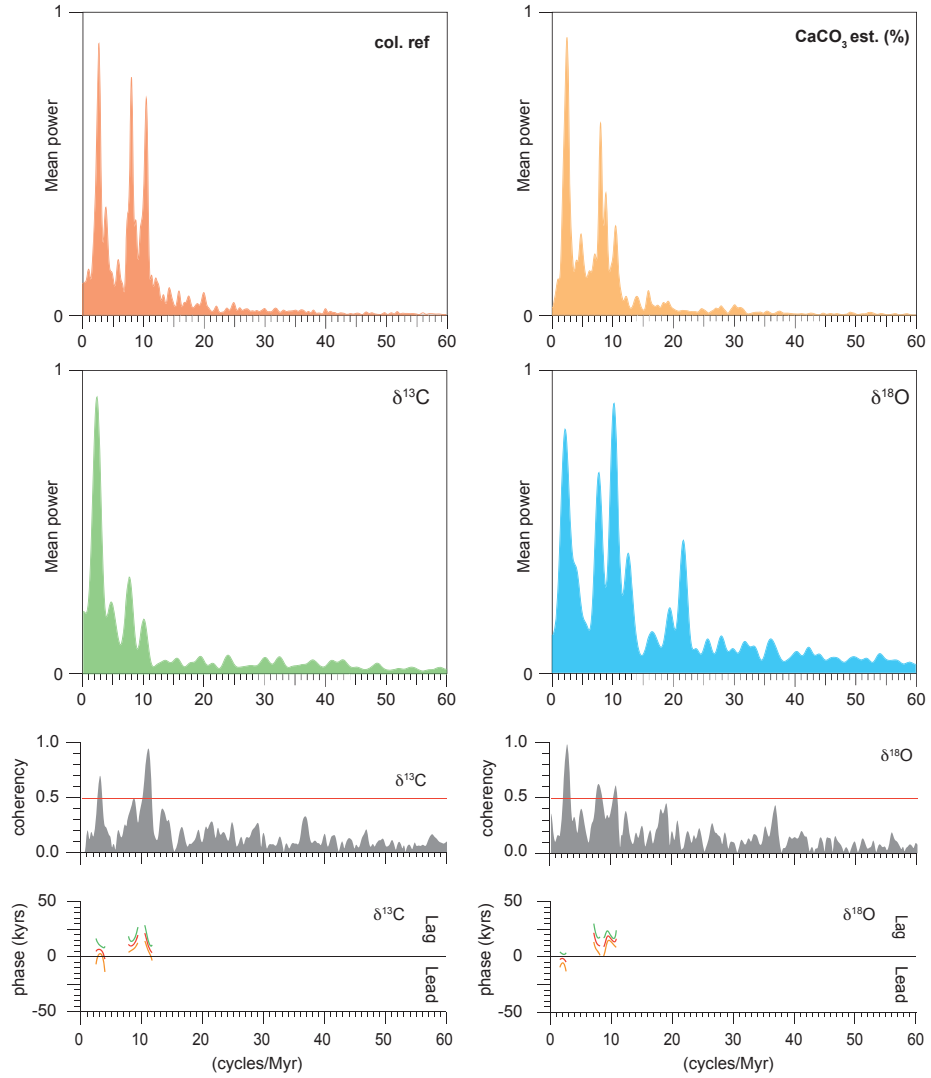

Figure 5.6. *Wavelet analyses for colour reflectance (a), $\delta^{13}C$ (b) and $\delta^{18}O$ (c) indicating periodicities present with the datasets on the astronomically tuned age model, compared with ETP (d) based on La 2011 [Laskar et al., 2011a,b]*

At the 405, 125 and 95 kyr period eccentricity cycles, both $\delta^{18}O$ and $\delta^{13}C$ are significantly coherent (99%) with eccentricity (Fig. 6). Phase estimates of $\delta^{18}O$ and $\delta^{13}C$ with respect to eccentricity indicate that on the eccentricity tuned age model, $\delta^{18}O$ leads eccentricity by 29-42 kyr at the 405 kyr period and lags eccentricity by 10 -23 kyr at the 125 kyr eccentricity periodicity and by 2-7 kyrs at the 96 kyr eccentricity periodicity, whereas $\delta^{13}C$ is in-phase with eccentricity at the 405 kyr periodicity, and lags between 4-21 kyr at the ~110 kyr eccentricity cycles (Fig. 6).

5.4.8 SiZer analysis

We calculated a 'family of smooths" for Atlantic Site 1264, and Pacific Sites 1146, 1237, U1337 and U1338 (Fig. 8) using a space-scale statistical programme SiZer (Significant Zero crossing of derivatives), to compare the long-term trends and changes in the amplitude of the MCO and MMCT between the Pacific and the Atlantic basin [*Chaudhuri and Marron*, 1999]. Of the 41 smooths calculated by SiZer, we have selected the 30th and the 20th smooths as they resolve variability on ~100 kyr and >250 kyr timescales, respectively (Figs. 9a, 9b, 10a and 10b). We calculate the relative change in amplitude at each site for both the $\delta^{18}O$ and $\delta^{13}C$ records, using a baseline average value determined between 15.1 and 15.4 Ma for the MMCT and 18.1 and 18.4 Ma for the MCO (Figs. 9 and 10, panels c, d, e and f) similar to the approach used by *Bohaty et al.* [2012] and *Beddow et al.* [2016] to compare relative amplitudes of the Eocene-Oligocene transition (EOT) and Oligocene-Miocene transition (OMT), respectively.

5.5 Discussion

5.5.1 The onset of the MCO

In general, the record from Site 1264 is in good correspondence with the records from the Pacific sites [*Holbourn et al.*, 2007, 2013, 2014, 2015] showing a large degree of synchronicity between records on the long-term trend and at astronomical time-scales, although there are small differences in timing and amplitude between sites.

At Site 1264, the onset of the MCO is present in the $\delta^{18}O$ record as a steep shift of ~1‰ beginning at 17.1 Ma (Fig. 5). Constraining the timing of the onset is complicated by the possible presence of a condensed section or hiatus during this interval. Although the correspondence between Atlantic site 1264 and the Pacific sites is for the majority of the record very good, at Pacific Site U1337 and 1237, the onset of the MCO occurs 100 kyrs later than at Site 1264, at ~17.0 Ma. The difference in timing could be a result of approaches in age model construction or the potential hiatus at 1264 coincident with the onset of the MCO.

The onset of the MCO at Site 1264 is followed by a decrease in benthic $\delta^{13}C$ lasting ~200 kyr, coincident with a small decrease in $CaCO_3$ est (%), just prior to the onset of the $\delta^{13}C$ isotope event at ~16.8 Ma (Fig. 5). This stable isotope feature in the $\delta^{13}C$ following the onset of the MCO is also found at Pacific Site U1337, coincident with a drop in $CaCO_3$ to ~ 30%, and is interpreted as a perturbation of the carbon cycle, with a shoaling of the CCD [*Holbourn et al.*, 2015]. At Site 1264, $CaCO_3$ est. (%) only drops by 2% to ~89% during the decrease in $\delta^{13}C$ following the onset of the MCO (Fig. 5), suggesting that the CCD in the Atlantic does not shoal as shallow as the paleo-location of Site 1264. Site 1264 has a present day water depth of ~2500 msbf, which is around 1.5 km shallower than that of Site U1337 [*Zachos et al.*, 2004; *Pälike et al.*, 2010]. Although no CCD shoaling has been observed at Site 1264, we cannot exclude a coeval lysocline migration in the Atlantic basin.

5.5.2 Peak warming during the MCO at ~15.6 Ma

At Site 1264, the minimum $\delta^{18}O$ value occurs at 15.6, coincident with a large minimum in the $\delta^{13}C$ record. These indicate a negative shift of ~1.0‰ during an interval of already relatively depleted $\delta^{18}O$ values, and a prominent negative shift of ~0.8‰ during an interval of relatively positive $\delta^{13}C$ values (Fig. 5a and 5b) This short interval (~100 kyrs) is interpreted as a peak in global warmth/ minimum ice volume during the MCO, occurring simultaneously with a shift in the global carbon

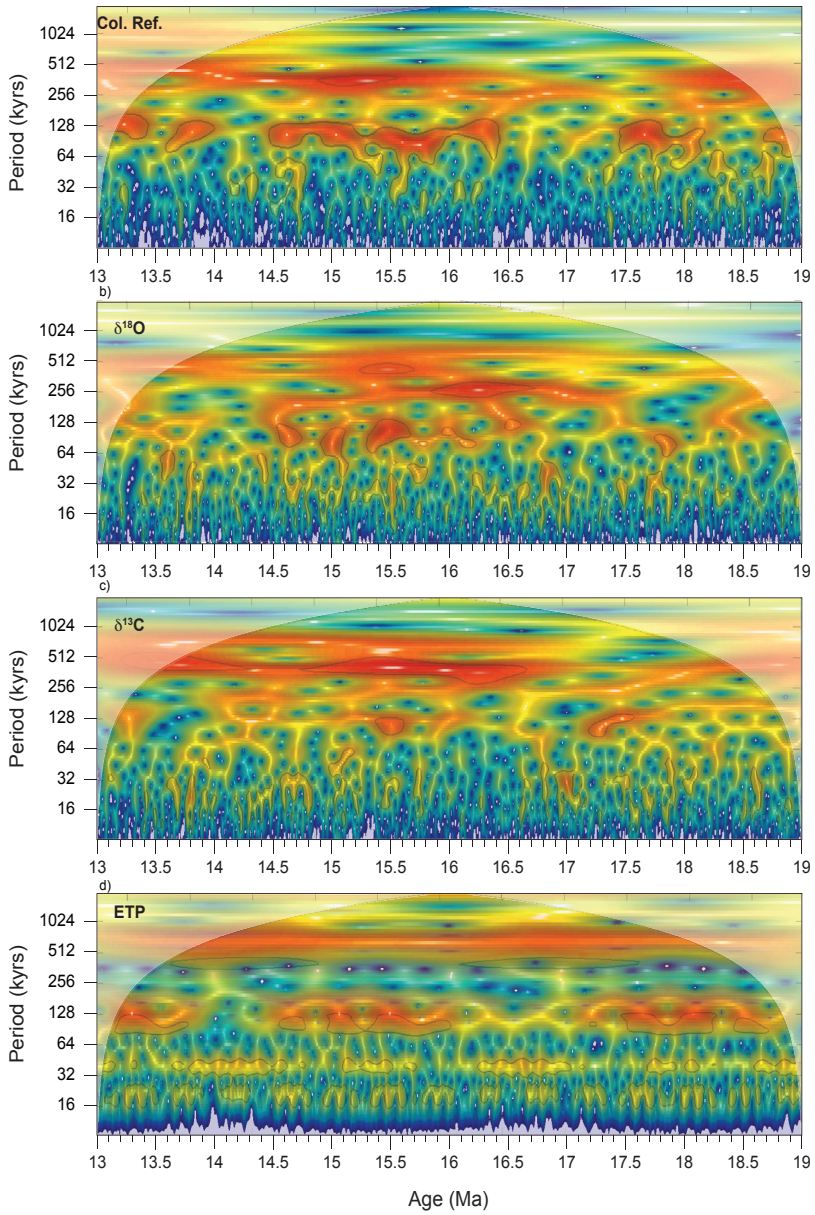

Figure 5.7. *Power spectra and coherence and phase plots for benthic stable isotope records from ODP Site 1264. Power spectra are plotted in panel (a) with $\delta^{13}C$ in green and $\delta^{18}O$ in blue. (d). Coherence and phase estimates are between performed between eccentricity from the La2011 astronomical solution [Laskar et al., 2011a,b] and benthic foraminiferal stable isotope datasets. Coherence is in grey for $\delta^{13}C$ (c) and $\delta^{18}O$ (d). The significance level represented by the red line for the coherence plots is 99%. For the phase estimates between the benthic foraminiferal series and eccentricity, eccentricity was multiplied by -1. For $\delta^{13}C$ (e) and $\delta^{18}O$ (f), the calculated phase is in red, with the 95% upper limit estimate in green and 95% lower limit estimate in orange.*

cycle. This co-variance between $\delta^{18}O$ and $\delta^{13}C$ has been previously observed in all the (circum-) Pacific Sites U1146, U1337, U1338 and 1237 [*Holbourn et al*., 2005, 2007, 2013, 2014, 2015]. A comparison of the available isotope records (Fig. 8) indicates a very close correspondence between all sites during this interval in both the Atlantic and Pacific basins, confirming the global nature of this event. The strong decrease in $\delta^{13}C$ indicates a transient supply of isotopically light carbon to the deep waters, which has been linked to a potential rapid release of methane [*Holbourn et al*., 2013], by similar mechanisms driving hyperthermal carbon isotope excursions in the Eocene [*Dickens et al*., 1995; *Lourens et al*., 2005; *Sluijs et al*., 2007; *Bohaty et al*., 2009; *Littler et al.*, 2015; *Lauretano et al*., 2015], driving an increase in deep sea temperatures/Antarctic ice sheet melting. At Site 1146, the record extends to ~ 8 Ma, and a similar shift in $\delta^{18}O$ and $\delta^{13}C$ is observed between 10.7 and 10.8 ~Ma, running counter to the long-term cooling trend during that interval, suggesting periodic rapid releases of CO_2 occur during the Miocene interval [*Holbourn et al*., 2013]. High-resolution records for this interval are lacking, and extending the record at 1264 could potentially reveal a similar event during the same interval, confirming the global nature of this event.

5.5.3 Eccentricity paced climate variability during the MCO

The MCO at Site 1264 is characterized by rapid, high amplitude variability (between 0.6 and 1.0 ‰) in the $\delta^{18}O$ record, and longer-paced, high amplitude variability (~1‰) in the $\delta^{13}C$ record (Fig. 5). Whilst on tectonic timescales, $\delta^{13}C$ and $\delta^{18}O$ are anti-correlated across the mid-Miocene, on ~110 kyr astronomical timescales, minima in $\delta^{18}O$, inferred as peaks of maximum warmth/minimum ice volume, coincide with minima in $\delta^{13}C$ across the MCO. Wavelet spectra reveal a strong expression of the ~110 kyr periodicity in $\delta^{18}O$ and the $\delta^{13}C$, in particular in the interval between 14.5 and 16.5 Ma (Fig. 7). High-frequency amplitude fluctuations are also present in Pacific records across the middle Miocene, indicating that this is a global climate signal suggesting a tightly coupled cryosphere-carbon cycle climate system is operating on astronomical timescales [*Holbourn et al*., 2007; 2013, 2014, 2015].

The most likely mechanism driving global warmth at the MCO is the sustained degassing of large igneous provinces, in particular the mid-Miocene Columbia River Basalt, leading to elevated pCO_2 levels across the early to middle Miocene [*Hodell and woodruff*, 1994; *Kender et al*., 2009; *Foster et al*., 2012; *Mckay et al*., 2014; *Holbourn et al*., 2007, 2013, 2015]. Although *p*CO2 estimates increase across the MCO, they appear to be relatively low (~400-500 ppm) [*Kurschner et al*., 2008; *Foster et al*., 2012; *Badger et al*., 2013; *Zhang et al*., 2013; *Greenop et al*., 2014] when compared to modeled threshold values for sustaining ice sheets on Antarctica, which assume a strong hysteresis effect on the ice sheet [*Deconto and Pollard*, 2003; *Pollard and Deconto*, 2005; *Deconto et al*, 2008]. To account for the large fluctuations seen in the $\delta^{18}O$ record across the MCO at both the Atlantic and Pacific sites, it has been suggested that either the behavior of the Antarctic Ice Sheet is more dynamic than climate models suggest [*Lear et al*., 2004] and/or there is continental ice in the Northern Hemisphere [*Moran et al., 2006*], or proxies for atmospheric CO_2 are not at a high enough resolution to capture the full extent of variability [*Greenop et al*., 2014]. A dynamic Antarctic ice sheet across the MCO, with large-scale fluctuations on ~110 kyr timescales, could be responding sensitively to smaller scale variations in CO_2 [*Greenop et al*., 2014], or ~110 kyr eccentricity paced variability in insolation [*Holbourn et al*., 2013, 2014, 2015]. Variations in ice volume have been reproduced by modeling studies, which suggest that the Antarctic ice sheet may have decreased by around 10-25% across the middle Miocene, compared with its modern extent [*De Boer et al*., 2010].

5.5.4 Astronomical pacing of climate cooling during MMCT

At Site 1264, a decline in $\delta^{18}O$ indicates deep-sea cooling/increasing ice volume begins at ~14.7 Ma, after the termination of the MCO. Further cooling/ice volume steps are present at 14.2 Ma, the onset of the MMCT, and at 13.8 Ma, synonymous with isotope event Mi3b (Fig. 5). The $\delta^{18}O$ maximum at Mi3b is inferred as the point of maximum cooling/Antarctic ice volume extent during the MMCT. These cooling steps have also been recognised in the Pacific with similar amplitudes, suggesting concurrent cooling occurs in the Atlantic and Pacific basins [*Holbourn et al*., 2013, 2014, 2015].

At Site 1264, the wavelet spectra indicate the consistent expression of ~110 kyr between ~14.7 and 13.8 Ma in the benthic $\delta^{13}C$ and an increase in the expression of ~110 kyr power in the $\delta^{18}O$ record between ~14.2 and 13.8 Ma, during the MMCT (Fig. 7). Within both the $\delta^{18}O$ and $\delta^{13}C$ wavelet spectra there is some expression of power at the obliquity periodicity between 14.2 and 14.7 Ma. This is in contrast with the Pacific sites, which reveal a strong expression of obliquity between ~14.7 and 14.2 Ma [*Holbourn et al*., 2005, 2007, 2013, 2014, 2015]. The period between 14.7 and 14.2 Ma is coincident with a minimum in the 2.4 Myr eccentricity cycle when the amplitude of the ~110-kyr eccentricity cycle is relatively constant and low (Figs. 5e and 7d) [*Laskar et al*., 2011a,b]. The Pacific sites indicate a switch takes place at ~14.7 Ma from ~110 kyr eccentricity paced climate variability to 41 kyrs obliquity paced climate variability, and then switches back to ~110 kyr eccentricity paced climate variability at ~14.2 Ma, which is not recorded in the Site 1264 record.

The strong expression of ~110 kyr short period eccentricity and the weak expression of 41 kyr obliquity seems to be a persistent feature of Site 1264, which also displays weak obliquity during the OMT and the Oligocene, in contrast to obliquity signals present at other sites [*Liebrand et al., 2011*, submitted]. Several mechanisms have been suggested to explain this difference in forcing between Site 1264 and high-resolution records from different sites across the OMT and into the Late Oligocene, including differences in age model construction and the effect of bioturbation at low sedimentation rates [*Ripepe and Fischer*, 1991; *Herbert*, 1994]. Site 1264 has lower sedimentation rates than the Pacific sites, which range between ~1.0 cm/kyr and ~4.0 cm/kyr. For a more detailed discussion see *Liebrand et al*. [submitted].

5.5.5 405 kyr eccentricity pacing of the carbon cycle

Long period (405 kyr) eccentricity is the dominant astronomical periodicity in both stable isotope datasets, and is particularly strong in the $\delta^{13}C$ dataset (Figs. 5, 6 and 7). There is a marked association between the $\delta^{13}C$ CM events and the 405 kyr eccentricity cycle in the astronomical solution, with peak CM $\delta^{13}C$ values occurring during 405 kyr eccentricity minima [*Laskar et al*., 2011a,b]. The strong response at the 405 kyr periodicity present in the $\delta^{13}C$ record is a persistent global feature of Miocene, Oligocene and Eocene climate, although the signal appears to be obscured in deep-sea records from the more recent Pleistocene and Pliocene [*Zachos et al*., 2001; *Wade and Pälike*, 2004; *Pälike et al*., 2006a; *Wang et al*., 2010; *Holbourn et al*., 2013, 2015; *Littler et al*., 2014; *Tian et al*., 2014; *Beddow et al*., 2016]. The strong 405 kyr cycle in the benthic $\delta^{13}C$ represents a nonlinear response to insolation, and modelling studies have suggested it could be a result of the long residence time of carbon in the deep ocean, which would lead to an amplification of the higher astronomical periodicities within the $\delta^{13}C$ record [*Pälike et al*., 2006b]. Alternatively an internal feedback present within earth's climate system, resulting from astronomically controlled fluctuations in weathering, changing the ratio of carbonate to organic carbon burial, could have led to a change in deep ocean $\delta^{13}C$ values [*Ma et al., 2011*; *Tian et al*., 2013.]

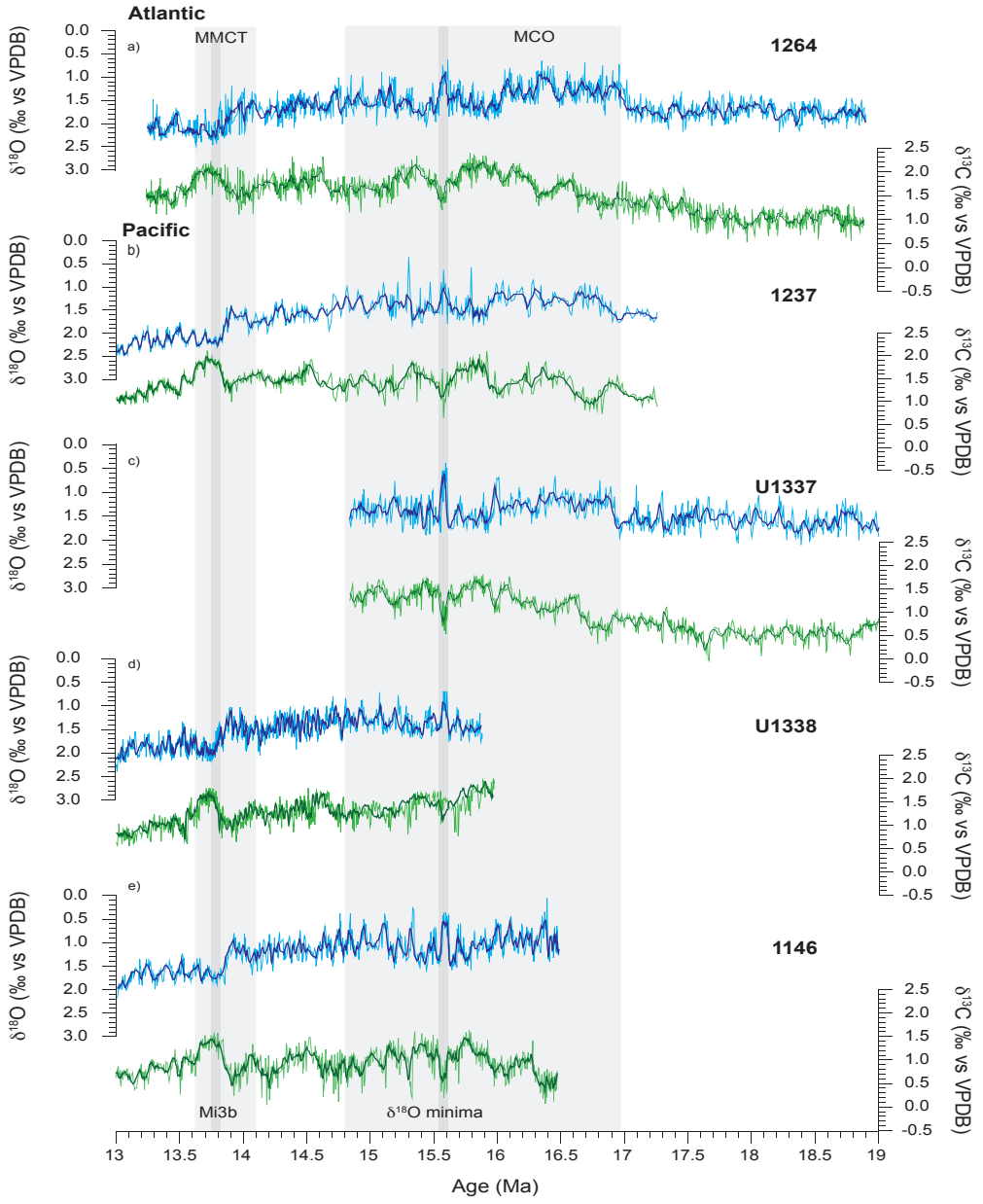

Figure 5.8. *Comparison of Site 1264 with previously published high-resolution benthic foraminiferal $\delta^{13}C$ and $\delta^{18}O$ records. Light green lines represent $\delta^{13}C$ datasets and dark green lines are a statistical smooth created using SiZer [Chaudhuri and Marron, 1999]. Light blue lines represent the datasets and dark green lines are a statistical smooth created using SiZer. Plotted above is IODP Site 1237 (a) [Holbourn et al., 2005; 2007] ODP Site 1264 (b) IODP Site U1337 (c) and U1338 (d) [Holbourn et al., 2014, 2015], and Site 1146 (e) [Liebrand et al., 2011].*

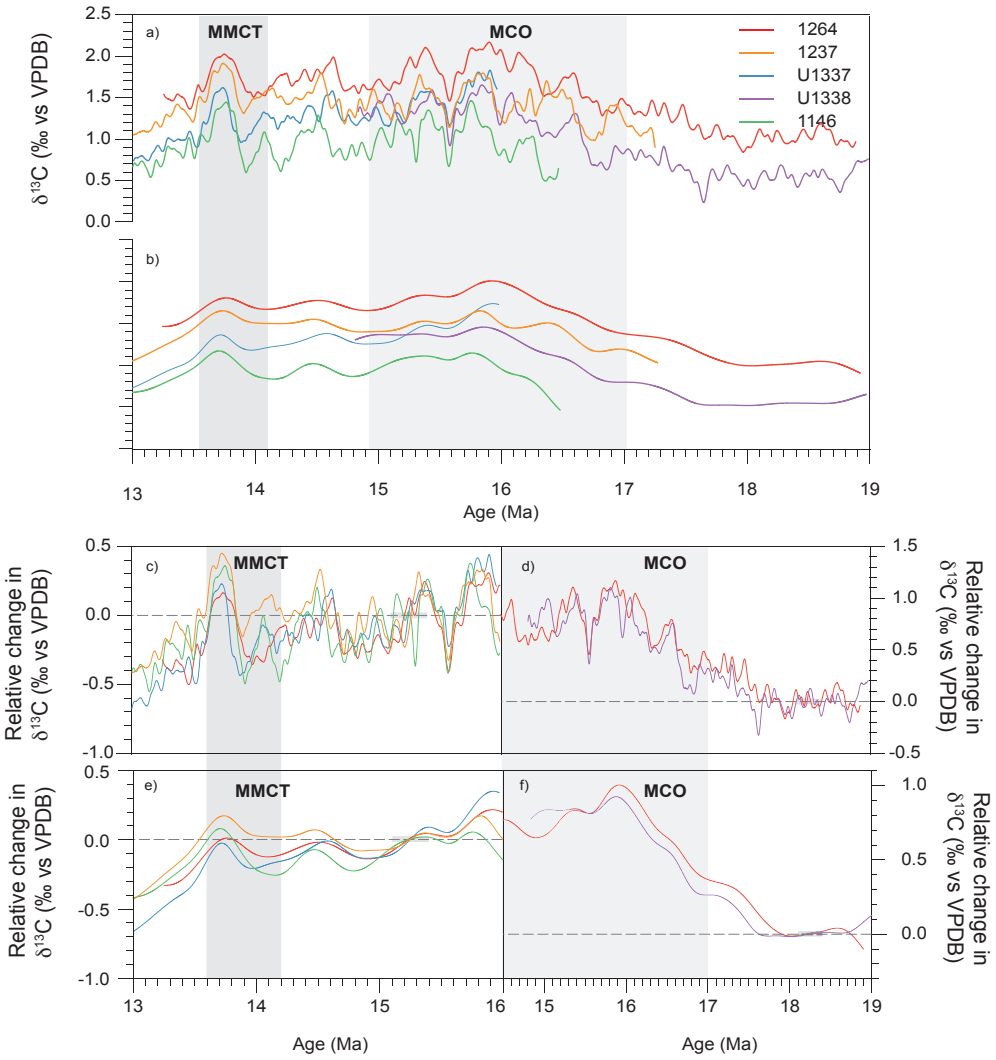

Figure 5.9. *Statistically smoothed $\delta^{13}C$ datasets from Site U1334 (this study) and previously published datasets from Sites 1237, 1146, U1337, 1264 and U1338 indicating the intermediate (~100 kyr) trend (a) and the long-term (>250 kyr) trend (b). Relative change in $\delta^{13}C$ record based on the intermediate and long-term $\delta^{18}O$ SiZer smooths, is calculated for the MMCT (c and e) using a baseline average determined between 15.1 and 15.4 Ma (grey shaded box) and for the MCO (d and f) using a baseline average determined between 18.1 and 18.4 Ma (grey shaded box)..*

5.5.6 Spectral peaks at eccentricity and obliquity harmonics

The $\delta^{18}O$ power spectra at Site 1264 further indicates the presence of spectral peaks at ~200 kyr and ~80 kyr periodicities (Fig. 6). Spectral peaks at these periodicities have also been found in $\delta^{18}O$ records at Site 1237 and Site 1146, suggesting that these are not a regional signal, or drifting

periodicities within the record as a result of age model construction [*Holbourn et al*., 2007; *Tian et al*., 2013]. The peak at ~200 kyrs, coherent with eccentricity, has also been found during the OMT in Site U1334, Site 1264 and Sites 926 and 929 at Ceara Rise [*Liebrand et al*., submitted; *Pälike et al*., 2006a; *Beddow et al*., 2016]. The ~200 kyr periodicity is particularly clear in the $\delta^{18}O$ wavelet spectrum (Fig. 7b), between ~15.5 and 17 Ma, suggesting non-linearity in the response of deep-water temperatures/ice sheet extent to the eccentricity cycle during the MCO [*King*, 1996]. The ~200 kyr periodicity could be either the first harmonic of the 405 kyr eccentricity cycle, or could represent a doubling of the ~110 kyr eccentricity cycle or the 170 kyr modulation of obliquity also detected in a magnetic susceptibility record from ODP Site 926 in the equatorial Atlantic during the Oligocene-Miocene interval [*Shackleton et al.,* 1999]. The 80-kyr peak in the power spectra may be due to a non-linear response to two 40-kyr cycles. Such harmonics would indicate a highly non-linear climate/carbon cycle dynamics, likely resulting from the slow response of the ice sheets/ carbon cycle.

5.5.7 ~2.4 Myr climate pacing between 13.2-30.1 Ma

Between 13.24 and 18.90 Ma, we find periods of high amplitude $\delta^{18}O$ variability coincide with high amplitude ~110 kyr intervals in the astronomical solution, during maxima of 2.4 Myr amplitude modulation of eccentricity. The Gaussian 405 kyr and ~110 kyr filters of $\delta^{13}C$ and $\delta^{18}O$ are indicative of 2.4 Myr pacing, with high amplitude ~110 kyr cycles during ~2.4 Myr eccentricity maxima (Fig 5c, 5d and 5e). Prominent high amplitude $\delta^{18}O$ variability at ~110 kyr cycles during 2.4 Myr maxima is also found at Site 1264 between 18.9 Ma and 30.1 Ma, suggesting the 2.4 Myr amplitude modulation is pacing periods of high-amplitude ~110 kyr $\delta^{18}O$ variability from the middle Oligocene to the middle Miocene [*Liebrand et al*., submitted]. An association between climate variability and the ~2.4 Myr cycle has also been found in the Pacific Sites, where prominent obliquity paced climate variability between ~14.6 and ~14.1 Ma and ~9.8 and 9.2 Ma coincides with 2.4 Myr eccentricity minima, when the amplitude of the ~110 kyr eccentricity cycle is low [*Holbourn et al*., 2007; 2013].

5.5.8 Comparison of the MCO and MMCT in the Atlantic and Pacific basins

Comparing the intermediate (<100 kyr) and long-term (>250 kyrs) SiZer smooths and calculations of the relative amplitude of the shifts at the MCO and the MMCT in the Atlantic and Pacific high-resolution records highlights the synchronicity in timing and amplitude of $\delta^{13}C$ and $\delta^{18}O$ long-term trends and climate events between the Atlantic and Pacific basins. The relative amplitude of shifts in $\delta^{13}C$ and $\delta^{18}O$ at the MCO and the MMCT is very similar between the Atlantic and Pacific basins, indicating the global nature of these events (Figs. 9 and 10).

Site 1264 is consistently offset to more positive $\delta^{13}C$ values by ~0.5 ‰, indicating a persistent 0.5 ‰ gradient is present between Site 1264 and the Pacific Sites. When we consider Site 1264 in isolation, as the only Atlantic high-resolution site, this could be interpreted as evidence for a persistent offset between the Atlantic and the Pacific across the early to middle Miocene. However, a comparison of Atlantic and Pacific records across the OMT, between 21.9 and 24.2 Ma, found that Site 1264 was consistently offset from other Atlantic sites by 0.5‰, and no significant $\delta^{13}C$ gradient was present between the Atlantic and Pacific Sites at deeper locations [*Beddow et al*., 2016]. Lower resolution stable isotope records from the Atlantic suggest that this is a regional influence on the $\delta^{13}C$ of Site 1264, rather than a true deep-water increase in Atlantic-Pacific $\delta^{13}C$ gradients between the late Oligocene into the early and middle Miocene [*Delaney and Boyle*, 1987; *Woodruff*

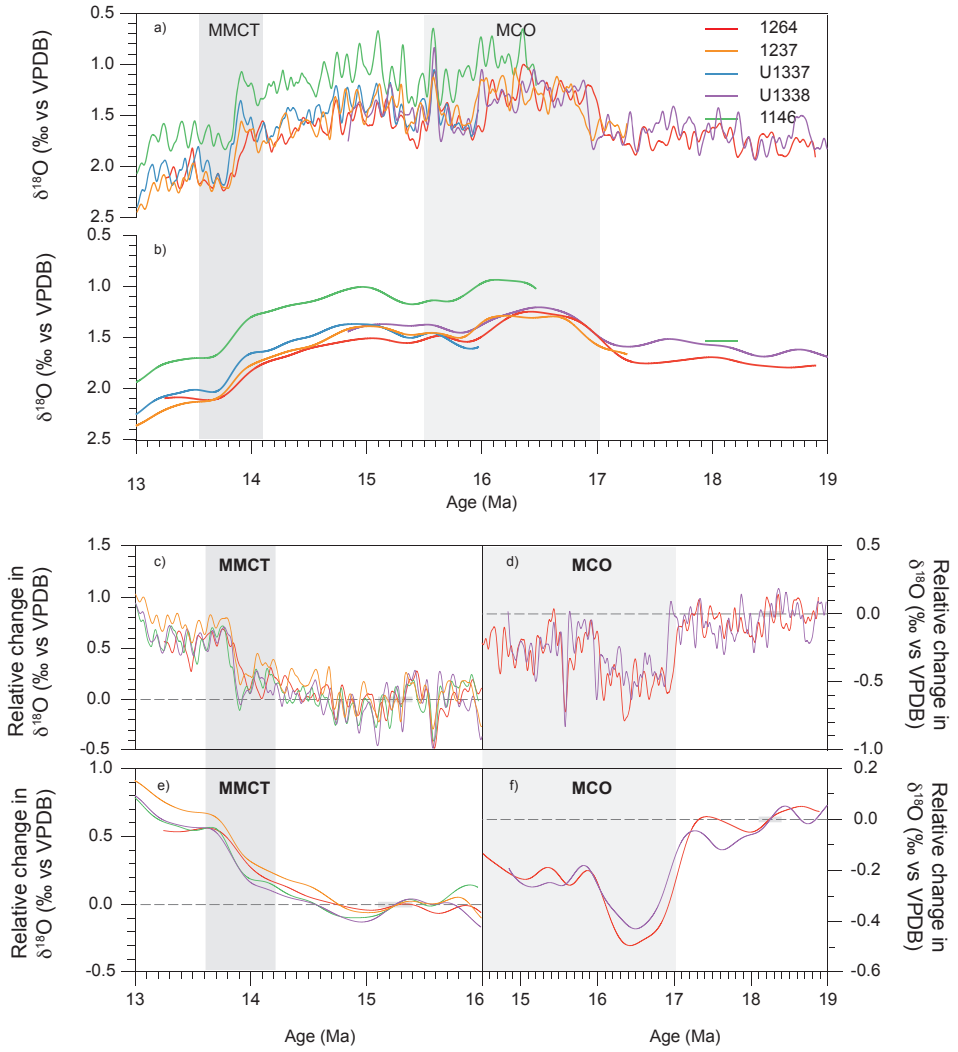

Figure 5.10. *Statistically smoothed $\delta^{18}O$ datasets from Site U1334 (this study) and previously published datasets from Sites 1237, 1146, U1337, 1264 and U1338 indicating the intermediate (~100 kyr) trend (a). and the long-term (>250 kyr) trend (b) Relative change in $\delta^{18}O$ record based on the intermediate and long-term $\delta^{18}O$ SiZer smooths, is calculated for the MMCT (c and e) using a baseline average determined between 15.1 and 15.4 Ma (grey shaded box) and for the MCO (d and f) using a baseline average determined between 18.1 and 18.4 Ma (grey shaded box).*

and Savin, 1991; *Wright et al.*, 1991; *Billups et al.*, 2002]. Site 1146 is consistently offset towards more depleted values by ~ 0.5 ‰ from the other Pacific Sites, and by ~ 1.0 ‰ from Atlantic Site 1264. The relatively depleted $\delta^{13}C$ signal at Site 1146 is probably due to its shallower location in a marginal sea, despite its open connection to the Pacific Ocean [*Holbourn et al.*, 2007; 2013].

Offsets in $\delta^{18}O$ values between the Atlantic and Pacific sites indicate regional differences in temperature and salinity present in the water masses at different sites, as the ice volume component of the foraminiferal $\delta^{18}O$ signal is a global signal affecting all sites equally [*Shackleton*, 1974]. With the exception of Site 1146, in the South China Sea, $\delta^{18}O$ offsets between Site 1264 and the Pacific sites are minimal. Site 1146 is consistently offset to depleted $\delta^{18}O$ values relative to the open ocean Pacific and Atlantic sites values by ~0.5‰, most likely a reflection of its location in a marginal sea with regional controls on temperature/salinity. Minimal $\delta^{18}O$ offsets and the concurrent cooling steps at 14.7 Ma, 14.2 Ma and 13.8 Ma between the Atlantic and Pacific basins [*Holbourn et al.*, 2013, 2014], are consistent with suggestions of a deep-water Southern Ocean source supplying most of the deep ocean during the early to Middle Miocene [*Woodruff and Savin*, 1989; *Billups et al.*, 2002].

On 100 kyr time scales, high-amplitude ~110 kyr paced variability in $\delta^{18}O$ between the different sites occurs is generally synchronous, with minor differences suggesting regional influences on temperature, salinity or mixing and advection on the $\delta^{18}O$ of the water masses at different sites [*Shackleton*, 1974]. Higher-frequency fluctuations in $\delta^{13}C$ between sites indicate more variability than in the $\delta^{18}O$ records, which could reflect regional differences in nutrient availability and ventilation, driving surface water productivity and export production, and organic carbon burial, or differences in the deep water source caused by advection and mixing of intermediate water masses [*Rohling and Cooke*, 1999].

5.6 Conclusions

Here we present as astronomically tuned stable isotope record for Site 1264 in the Atlantic, between 13.2 and 18.9 Ma. Our high-resolution benthic stable isotope records reveal middle Miocene climate evolution and capture stable isotope variability during the MCO and the MMCT. There is a close correspondence between long-term trends and higher frequency variability between the Pacific and Atlantic Sites, particularly during a transient prominent minimum in $\delta^{13}C$ and $\delta^{18}O$, confirming the global nature of this event. We find the dominant astronomical frequency present at Site 1264 is the 405 kyr periodicity in the $\delta^{13}C$ record, and the ~110 kyr periodicity in the $\delta^{18}O$ record. Expression of power at ~200 kyrs periodicity on the $\delta^{18}O$ during the MCO suggests a non-linear response in deep-water temperatures/ice volume to the eccentricity cycle during this interval of global warmth. We find the amplitude of the shifts at the MCO and MMCT to be very similar between the Atlantic and the Pacific basins, with concurrent cooling steps at 14.7, 14.2 and 13.8 Ma, suggesting they experience similar changes in temperature/salinity across the events.

References

Abels, H. A., F. J. Hilgen, W. Krijgsman, R. W. Kruk, I. Raffi, E. Turco, and W. J. Zachariasse (2005), Long-period orbital control on middle Miocene global cooling: Integrated stratigraphy and astronomical tuning of the Blue Clay Formation on Malta, *Paleoceanography*, *20*.

Badger, M. P. S., C. H. Lear, R. D. Pancost, G. L. Foster, T. R. Bailey, M. J. Leng, and H. A. Abels (2013), CO2 drawdown following the middle Miocene expansion of the Antarctic Ice Sheet, *Paleoceanography*, 28, 42-53, doi:10.1002/palo.20015.

Bailey, I., G. M. Hole, G. L. Foster, P. A. Wilson, C. D. Storey, C. N. Trueman, M. E. Raymo (2013), An alternative suggestion for the Pliocene onset of major northern hemisphere glaciation based on the geochemical provenance of North Atlantic Ocean ice-rafted debris. *Quat. Sci. Rev*. 75, 181-194.http://dx.doi.org/10.1016/j.quascirev.2013.06.004

Barckhausen, U., C. R. Ranero, S. C. Cande, M. Engels and W. Weinrebe (2008), Birth of an intraoceanic spreading center. *Geology*, *36*(10), 767-770.

Barker, P. F (2001), Scotia Sea regional tectonic evolution: implications for mantle flow and palaeocirculation, *Earth-Sci. Rev*. 55,1-39.

Bassinot, F. C., L. D. Labeyrie, E. Vincent, X. Quidelleur, N. J. Shackleton and Y. Lancelot (1994), The astronomical theory of climate and the age of the Brunhes-Matuyama magnetic reversal. *Earth and Planetary Science Letters*, *126*(1-3), 91-108.

Beddow, H. M., D. Liebrand, A. Sluijs, B. S. Wade, and L. J. Lourens (2016), Global change across the Oligocene-Miocene transition: High-resolution stable isotope records from IODP Site U1334 (equatorial Pacific Ocean), *Paleoceanography*, *31*, doi:*10.1002/2015PA002820.*

Beltran, C., G. Rousselle, J. Backman, B. S. Wade and M. A. Sicre, (2014), Paleoenvironmental conditions for the development of calcareous nannofossil acme during the late Miocene in the eastern equatorial Pacific. *Paleoceanography*, *29*, 210-222, doi:10.1002/2013PA002506.

Berger, A. (1980), The Milankovitch astronomical theory of paleoclimates: a modern review. *Vistas in Astronomy*, *24*, 103-122.

Billups, K., J. E. T. Channell, and J. Zachos (2002), Late Oligocene to early Miocene geochronology and paleoceanography from the subantarctic South Atlantic, *Paleoceanography*, 17(1).

Billups, K., H. Pälike, J. E. T. Channell, J. Zachos, and N. J. Shackleton (2004), Astronomic calibration of the late Oligocene through early Miocene geomagnetic polarity time scale, *Earth and Planetary Science Letters*, *224*, 33-44.

Bijl, P.K., A.J.P Houben, S. Schouten, S. M. Bohaty, A. Sluijs, G-J. Reichart, J. S. Sinninghe-Damsté, H. Brinkhuis, (2010), Transient middle Eocene atmospheric CO_2 and Temperature variations. *Science* 330, 819-821

Birch, H., H. K. Coxall, N. P. Pearson, D. Kroon, and M. O'Regan (2013), Planktonic foraminifera stable isotopes and water column structure: Disentangling ecological signals. *Marine Micropaleontology*, *101*, 127-145.

Bohaty, S. M., J. C. Zachos, F. Florindo, and M. L. Delaney (2009), Coupled greenhouse warming and deep-sea acidification in the middle Eocene, *Paleoceanography,* 24, PA2207, doi:10.1029/2008PA001676.

Bohaty, S. M., J. C. Zachos, and M. L. Delaney (2012), Foraminiferal Mg/Ca evidence for Southern Ocean cooling across the Eocene-Oligocene transition. *Earth and Planetary Science Letters*, *317*, 251-261.

Bolli, H. M., and J. B Saunders (1982), *Globorotalia mayeri* and its relationship to *Globorotalia siakenesis* and *Globorotalia continuosa*. *The Journal of Foraminiferal Research*, *12*(1), 39-50.

Bolli, H. M., and J.B Saunders (1985), Oligocene to Holocene low latitude planktonic foraminifera, in Bolli, H.M., Saunders, J.B., and Perch-Nielsen, K. (eds.), Plankton Stratigraphy: Cambridge, Cambridge University Press, p. 155-262.

Bowles, J. (2006), Data report: revised magnetostratigraphy and magnetic mineralogy of sediments from Walvis Ridge, Leg 208, Ocean Drilling Program, College Station, TX.

Boyle, E. A. (1988), The role of vertical chemical fractionation in controlling late Quaternary atmospheric carbon dioxide, *J. Geophys. Res.*, 93, 15,701-15,714.

Broecker, W. S. (1995), *The Glacial World According to Wally*, Eldigio, Palisades, N. Y.

Brown, R. E., L. D Anderson, E. Thomas and J.C. Zachos (2011), A core-top calibration of B/Ca in the benthic foraminifers Nuttallides umbonifera and Oridorsalis umbonatus: A proxy for Cenozoic bottom water carbonate saturation. *Earth and Planetary Science Letters*, *310*(3), 360-368 doi:10.1016/j.epsl.2011.08.023

Cande, S. C., and D. V. Kent (1992), A new geomagnetic polarity time scale for the Late Cretaceous and Cenozoic, *J. Geophys. Res.*, *97*(B10), 13917-13951.

Cande, S. C., and J. M. Stock (2004), Pacific-Antarctic-Australia motion and the formation of the Macquarie plate, *J. Geophys. Int.*, 157, 399-414.

Chaisson, W. P., and M. R. Leckie (1993), High-resolution Neogene planktonic foraminiferal biostratigraphy of Site 806, Ontong Java Plateau (western equatorial Pacific). In: Berger, W.H., Kroenke, L.W., Janecek, T.R., Sliter, W.V. (Eds.), *Proceedings of the Ocean Drilling Program, Scientific Results*, *130*, pp. 137-178.

Chaisson, W. P. and P. N. Pearson (1997), Planktonic foraminifer biostratigraphy at Site 925: Middle Miocene-Pleistocene. In: Shackleton, N. J., Curry, W. B., Richter, C., Bralower, T. J. (Eds.), *Proceeding of the Ocean Drilling Program, Scientific Results 154*, 3-31.

Channell, J. E. T., S. Galeotti, E. E. Martin, K. Billups, H. Scher, and J. S. Stoner (2003), Eocene to Miocene magnetic, bio- and chemo-stratigraphy at ODP Site 1090 (sub-Antarctic South Atlantic), *Geol. Soc. Amer. Bull. 115,* 607-623.

Channell, J. E. T., C. Ohneiser, Y. Yamamoto, and M. S. Kesler (2013), Oligocene-Miocene magnetic stratigraphy carried by biogenic magnetite at sites U1334 and U1335 (equatorial Pacific ocean) *Geochemistry, Geophysics, Geosystems, 14*(2) pp1525-2027doi:10.1029/2012GC004429

Chaudhuri, P., and J. S. Marron (1999), SiZer for exploration of structures in curves. *Journal of the American Statistical Association* 94.447: 807-823.

Coxall, H. K., and P. A. Wilson (2011), Early Oligocene glaciation and productivity in the eastern equatorial Pacific: Insights into global carbon cycling. *Paleoceanography*, *26*(2).

Croll, J. (1875), *Climate and Time, in their Geological Relations: A Theory of Secular Changes of the Earth's Climate*. Daldy, Tbister and Company, London, 577 p.

Croon, M. B., S. C. Cande, and J. M. Stock (2008), Revised Pacific-Antarctic plate motions and geophysics of the Menard Fracture Zone: *Geochemistry, Geophysics, Geosystems*, v. 9, Q07001, doi:10.1029/2008GC002019.

DeConto, R. M and D. Pollard (2003a), Rapid Cenozoic glaciation of Antarctica induced by declining atmospheric CO2, *Nature* 421, 245-249.

DeConto, R. M., and D. Pollard (2003b), A coupled climate-ice sheet modeling approach to the Early Cenozoic history of the Antarctic ice sheet, *Palaeogeography, Palaeoclimatology, Palaeoecology*, *198*, 39-52.

DeConto, R. M., D. Pollard, P. A. Wilson, H. Pälike, C. H. Lear and M. Pagani (2008), Thresholds for Cenozoic bipolar glaciation. *Nature*, *455*(7213), 652-656.

Dekens, P. S., A. C. Ravelo and M. D. McCarthy (2007), Warm upwelling regions in the Pliocene warm period. *Paleoceanography*, *22*(3).

De Boer, B., R. S. W. van de Wal, R. Bintanja, L. J. Lourens, and E. Tuenter (2010), Cenozoic global ice volume and temperature simulations with 1-D ice-sheet models forced by benthic $\delta^{18}O$ records, *Annals of Glaciology*, *51* (55), 23-33.

De Boer, B., R. S. W. Van de Wal, L. J. Lourens, and R. Bintanja (2012), Transient nature of the Earth's climate and the implications for the interpretation of benthic $\delta^{18}O$ records. *Palaeogeography, Palaeoclimatology, Palaeoecology,* 335-336, 4-11.

Delaney, M. L., and E. A. Boyle (1987), Cd/Ca in late Miocene benthic foraminifera and changes in the global organic carbon budget, *Nature,* 330, 156-159.

Dickens, G. R., J. R. O'Neil, D. K. Rea, and R. M. Owen (1995), Dissociation of oceanic methane hydrate as a cause of the carbon isotope excursion at the end of the Paleocene, *Paleoceanography*, 10, 965-971.

Diester-Haass, L., K. Billups, and K. Emeis (2011), Enhanced paleoproductivity across the Oligocene/Miocene boundary as evidenced by benthic foraminiferal accumulation rates. *Palaeogeography, Palaeoclimatology, Palaeoecology* 302, 464-473 doi:10.1016/j.palaeo.2011.02.006.

Diz, P., C. Barras, E. Geslin, G. J. Reichart, E. Metzger, F. Jorissen and J. Bijma. (2012), Incorporation of Mg and Sr and oxygen and carbon stable isotope fractionation in cultured Ammonia tepida. *Marine Micropaleontology*, *92*, 16-28.

Edgar, K. M., H. Pälike, and P. A. Wilson (2013), Testing the impact of diagenesis on the $\delta^{18}O$ and $\delta^{18}O$ of benthic foraminiferal calcite from a sediment burial depth transect in the equatorial Pacific, *Paleoceanography*, 28, 468-480, doi:10.1002/palo.20045.

Ehrmann, W. U. and A. Mackensen (1992), Sedimentological evidence for the formation of an East Antarctic ice sheet in Eocene/Oligocene time, *Palaeogeogr. Palaeoclimatol. Palaeoecol*., 93, 85-112, doi:10.1016/0031-0182(92)90185-8.

Elderfield, H., M. Greaves, S. Barker, I. R. Hall, A. Tripati, P. Ferretti, S. Crowhurst, L. Booth, and C. Daunt (2010), A record of bottom water temperature and seawater $\delta^{18}O$ for the Southern Ocean over the past 440 kyr based on Mg/Ca of benthic foraminiferal Uvigerina spp. *Quat. Sci. Rev., 29, 160-169,* doi:10.1016/j.quascirev.2009.07.013.

Emiliani, C. (1955), Pleistocene temperatures. *Journal of Geology*, 63:538-578.

Fairbanks, R. G., and R. K. Matthews (1978), The marine oxygen isotope record in Pleistocene coral, Barbados, West Indies. *Quaternary Research,* 10(2), 181-196.

Feely, R. A., R. Wanninkhof, T. Takahashi, and P. Tans (1999), Influence of El Nino on the Equatorial Pacific contribution to atmospheric CO_2 accounts. *Nature* 398, 597-601.

Flower, B. P. and J. P. Kennett (1993), Middle Miocene ocean-climate transition: high- resolution oxygen and carbon isotopic records from Deep Sea Drilling Project Site 588A, southwest Pacific. *Paleoceanography* 8 (6), 811-843.

Flower, B. P. and J. P. Kennett (1994), The middle Miocene climatic transition: East Antarctic ice sheet development, deep ocean circulation and global carbon cycling. *Palaeogeography, palaeoclimatology, palaeoecology*, *108*(3-4), 537-555.

Flower, B. P. and J. P. Kennett (1995), Middle Miocene deep water paleoceanography in the southwest Pacific: Relations with East Antarctic ice sheet development. *Paleoceanography*, 10, 1095-1112.

Flower, B. P., J. C. Zachos, and H. Paul (1997), Milankovitch-scale variability recorded near the Oligocene/Miocene Boundary: Hole 929A. In: Shackleton, N.J., Curry, W.B., Richter, C., Bralower, T.J. (Eds.), *Proceedings of ODP Science Research. vol. 154*. Ocean Drilling Program, College Station, TX, pp. 433-439.

Friedrich, O., G. Schmiedl, and H. Erlenkeuser (2006), Stable isotope composition of Late Cretaceous benthic foraminifera from the southern South Atlantic: Biological and environmental effects. *Marine Micropaleontology*, *58*(2), 135-157.

Friedrich, O., R. Schiebel, P. A. Wilson, S. Weldeab, C. J. Beer, M. J. Cooper and J. Fiebig (2012), Influence of test size, water depth, and ecology on Mg/Ca, Sr/Ca, $\delta^{18}O$ and $\delta^{13}C$ in nine modern species of planktic foraminifers. *Earth and Planetary Science Letters* 319-320, 133-145.

Foster, G., Lear, C. H. and Rae, J., (2012), The evolution of pCO2, ice volume and climate during the middle Miocene, *Earth and Planetary Science Letters*, 341-344, 243-254.

Fox, L. R., and B. S Wade (2013), Systematic taxonomy of early-middle Miocene planktonic foraminifera from the equatorial Pacific Ocean: Integrated Ocean Drilling Program, Site U1338. *The Journal of Foraminiferal Research*, 43(4), 374-405.

Gasperi, J. T., and J. P. Kennett (1993), Vertical thermal structure evolution of Miocene surface waters: western equatorial Pacific DSDP Site 289. *Marine Micropaleontology*, *22*(3), 235-254.

Gradstein, F. M., et al. (2012), *The Geologic Time Scale 2012*: Boston, Elsevier, USA, doi:10.1016/B978-0-444-59425-9.00004-4.

Greenop, R., G. L. Foster, P. A. Wilson and C. H Lear (2014), Middle Miocene climate instability associated with high-amplitude CO2 variability. *Paleoceanography*, 2 9, doi:10.1002/2014PA002653.

Grinsted, A., J. C. Moore, and S. Jevrejeva (2004), Application of the cross wavelet transform and wavelet coherence to geophysical time series, *Nonlinear Processes in Geophysics*, *11*, 561-566.

Hamon, N., P. Sepulchre, V. Lefebvre and G. Ramstein (2013), The role of eastern Tethys seaway closure in the Middle Miocene Climatic Transition (ca. 14 Ma). *Climate of the Past*, *9*(6), 2687-2702.

Hays, J. D., J. Imbrie, and N. J. Shackleton (1976), Variations in the Earth's Orbit: Pacemaker of the Ice Ages, *Science*, *194*(4270), 1121-1132.

Hemleben, C., M. Spindler and O.R. Anderson (1989), *Modern Planktonic Foraminifera*. Springer-Verlag, New York.

Herbert, T. D (1994), Reading orbital signals distorted by sedimentation: models and examples. *Orbital forcing and cyclic sequences*, 483-507.

Herbert, T. D. (1995), *Orbital chronology of Cretaceous-Paleocene marine sediments*.

Herbert, T. D., L. C. Peterson, K. T. Lawrence and Z. Liu (2010), Tropical ocean temperatures over the past 3.5 million years. *Science*, *328*(5985), 1530-1534.

Hilgen, F. J., W. Krijgsman, C.G. Langereis, L. J Lourens, A. Santarelli and W.J. Zachariasse (1995), Extending the astronomical (polarity) time scale into the Miocene. *Earth Planet. Sci. Lett*. 136, 495-510.

Hilgen, F. J., L. Bissoli, S. Iaccarino, W. Krijgsman, R. Meijer, A. Negri, G. Villa (2000), Integrated stratigraphy and astrochro- nology of the Messinian GSSP at Qued Akrech (Atlantic Mo- rocco). *Earth Planet. Sci. Lett*. 182, 237-251.

Hilgen, F. J., H.A. Aziz, W. Krijgsman, I. Raffi, and E. Turco (2003), Integrated stratigraphy and astronomical tuning of the Serravallian and lower Tortonian at Monte dei Corvi (Middle-Upper Miocene, northern Italy). *Palaeogeography, Palaeoclimatology, Palaeoecology*, *199*(3), 229-264.

Hilgen, F. J., L. J. Lourens, and J. A. Van Dam (2012), The Neogene Period. *The geologic time scale*, *2*, 923-978.

Hodell, D. A., and F. Woodruff (1994), Variations in the strontium isotopic ratio of seawater during the Miocene: Stratigraphic and geochemical implications. *Paleoceanography* **9**, 405-426.

Hodell, D. A., C. D. Charles and F.J. Sierro (2001), Late Pleistocene evolution of the ocean's carbonate system. *Earth and Planetary Science Letters*, *192*(2), pp.109-124.

Hodell, D. A., K. A. Venz, C. D. Charles, and U. S. Ninnemann (2003), Pleistocene vertical carbon isotope and carbonate gradients in the South Atlantic sector of the Southern Ocean, *Geochem. Geophys. Geosys.*, 4(1), 1004, doi:10.1029/2002GC000367.

Hohbein, M. W., P. F. Sexton, and J. A. Cartwright (2012), Onset of North Atlantic Deep Water production coincident with inception of the Cenozoic global cooling trend, *Geology*, *40*(3), 255-258.

Holbourn, A., W. Kuhnt, J. T. Simo and Q. Li (2004), Middle Miocene isotope stratigraphy and paleoceanographic evolution of the northwest and southwest Australian margins (Wombat Plateau and Great Australian Bight). *Palaeogeography, Palaeoclimatology, Palaeoecology*, *208*(1), 1-22.

Holbourn, A.E., W. Kuhnt, M. Schulz and H. Erlenkeuser (2005), Impacts of orbital forcing and atmospheric CO_2 on Miocene ice-sheet expansion: Nature, v. 438, p. 483-487, doi:10.1038/nature04123.

Holbourn, A.E., W. Kuhnt, M. Schulz, J-A Flores and N. Andersen (2007), Middle Miocene long-term climate evolution: Eccentricity modulation of the "Monterey" carbon-isotope excursion: *Earth and Planetary Science Letters*, v. 261, p. 534-550, doi:10.1016/j.epsl.2007.07.026.

Holbourn, A., W. Kuhnt, S. Clemens, W. Prell, and N. Andersen (2013), Middle to late Miocene stepwise climate cooling: Evidence from a high-resolution deep-water isotope curve spanning 8 million years, *Paleoceanography, 28*, doi:10.1002/2013PA002538.

Holbourn, A. E., W. Kuhnt, M. Lyle, L. Schneider, O. Romero and N. Andersen. N., (2014), Middle Miocene climate cooling linked to intensification of eastern equatorial Pacific upwelling. *Geology,* 42, 19-22.

Holbourn, A., W. Kuhnt, K. G. Kochhann, N. Andersen, and K.S. Meier (2015), Global perturbation of the carbon cycle at the onset of the Miocene Climatic Optimum. *Geology*, *43*(2), 123-126.

Hoogakker, B., H. Elderfield, K. Oliver, and S. Crowhurst (2010), Benthic foraminiferal oxygen isotope offsets over the last glacial-interglacial cycle. *Paleoceanography*, *25*(4).

Houben, A. J., C. A. van Mourik, A. Montanari, R. Coccioni and H. Brinkhuis (2012), The Eocene-Oligocene transition: Changes in sea level, temperature or both?. *Palaeogeography, Palaeoclimatology, Palaeoecology*, 335, 75-83.

Hüsing, S. K., F. J. Hilgen, H. Abdul Aziz, and W. Krijgsman (2007), Completing the Neogene geological time scale between 8.5 and 12.5 Ma, *Earth and Planetary Science Letters*, *253*, 340-358.

Hüsing, S. K., W-J. Zachariasse, D. J. J Van Hinsbergen, W. Krijgsman, M. Inceöz, M. Harzhauser, O. Mandic, and A. Kroh (2009), Oligocene-Miocene basin evolution in SE Anatolia, Turkey: constraints on the closure of the eastern Tethys gateway. *Geological Society, London, Special Publications* 311, no. 1: 107-132.

Iaccarino, S., (1985), Mediterranean Miocene and Pliocene planktonic foraminifera. In: *Plankton stratigraphy* Eds: Bolli, H.M.Saunders, J.B.Perch-Nielsen, K. p. 283-314.

Imbrie, J., J. D. Hays, D. G. Martinson, A. McIntyre, A. C. Mix, J. J. Morley, N. G. Pisias, W. L. Prell and N. J. Shackleton. "The orbital theory of Pleistocene climate: Support from a revised chronology of the marine $\delta^{18}O$ record." In *Milankovitch and climate: Understanding the response to astronomical forcing*, vol. 1, p. 269. 1984.

Ivany, L. C., S. Van Simaeys, E. W. Domack and S. D. Samson (2006), Evidence for an earliest Oligocene ice sheet on the Antarctic Peninsula, *Geology*, 34, 377-380, doi:10.1130/G22383.1.

Katz, M. E., D. R. Katz, J. D. Wright, K. G. Miller, D. K. Pak, N. J. Shackleton, and E. Thomas (2003), Early Cenozoic benthic foraminiferal isotopes: Species reliability and interspecies correction factors. *Paleoceanography, 18*(2), 1024, doi:10.1029/2002PA000798.

Katz, M. E., B. S. Cramer, J. R. Toggweiler, G. Esmay, C. Liu, K. G. Miller, Y. Rosenthal, B. S. Wade, and J. D. Wright (2011), Impact of Antarctic Circumpolar Current development on late Paleogene ocean structure, *Science*, *332*.

Kender, S., V. L. Peck, R. W. Jones and M. A. Kaminski (2009), Middle Miocene oxygen minimum zone expansion offshore West Africa: evidence for global cooling precursor events. *Geology*, 37, 699-702.

Kennett, J. P., and N. J. Shackleton (1976), Oxygen isotopic evidence for the development of the cryosphere 38 Myr ago, *Nature*, 260, 513-515, doi:10.1038/260513a0.

Kennett, J. P (1977), Cenozoic evolution of Antarctic glaciation, the circum-Antarctic ocean, and their impact on global paleoceanography, *J. Geophys. Res*. 82, 3843-3859.

Kennett, J. P., and M. S Srinivasan (1983), *Neogene Planktonic Foraminifera: a Phylogenetic Atlas*. Hutchinson Ross.

King, T. (1996). Quantifying nonlinearity and geometry in time series of climate. *Quaternary Science Reviews*, *15*(4), 247-266.

King, D.J., and B. S. Wade (submitted), The Extinction of Chiloguembelina cubensis in the Pacific Ocean: Implications for Defining the Base of the Chattian (upper Oligocene). Submitted to *Newsletters on Stratigraphy*, December 28th, 2015.

Krijgsman, W., F.J. Hilgen, I. Raffi, F.J. Sierro and D. S. Wilson (1999), Chronology, causes and progression of the Messinian salinity crisis. *Nature* 400, 655-662.

Kürschner, W. M., Z. Kvacek, and D. L. Dilcher (2008), The impact of Miocene atmospheric carbon dioxide fluctuations on climate and the evolution of terrestrial ecosystems, *Proceedings of the National Academy of Sciences of the USA*, *105*(2), 449-453.

Lanci, L., J. M. Pares, J. E. T. Channell, and D. V. Kent (2004), Miocene magnetostratigraphy from equatorial Pacific sediments (ODP Site 1218, Leg 199). *Earth and Planetary Science Letters*, *226*(1), 207-224.

Lanci, L., J. M. Parés, J. E. Channell, and D. V. Kent (2005), Oligocene magnetostratigraphy from equatorial Pacific sediments (ODP Sites 1218 and 1219, Leg 199). *Earth and Planetary Science Letters*, *237*(3), 617-634.

Laskar, J., P. Robutel, F. Joutel, M. Gastineau, A. C. M Correia, and B. Levrard (2004), A long-term numerical solution for the insolation quantities of the Earth. *Astronomy & Astrophysics*, *428*(1), 261-285.

Laskar, J., A. Fienga, M. Gastineau, and H. Manche (2011a), La2010: A new orbital solution for the long-term motion of the Earth, *Astronomy and Astrophysics*, *532*(A89).

Laskar, J., M. Gastineau, J.-B. Delisle, A. Farrés, and A. Fienga (2011b), Strong chaos induced by close encounters with Ceres and Vesta, *Astronomy and Astrophysics*, *532*(L4), 1-4.

Lauretano, V., K. Littler, M. Polling, J. C. Zachos, and L. J. Lourens (2015), Frequency, magnitude and character of hyperthermal events at the onset of the Early Eocene Climatic Optimum. *Climate of the Past*, *11*(10).

Lawrence, K. T., Z.-H. Liu, and T. D. Herbert (2006), Evolution of the eastern tropical Pacific through Plio-Pleistocene glaciation, Science, 312, 79-83.

Le Verrier, U. J. (1856), Recherches astronomiques:(suite). In *Annales de l'Observatoire de Paris* (Vol. 2).

Lear, C. H., Y. Rosenthal, H. K. Coxall, and P. A. Wilson (2004), Late Eocene to early Miocene ice-sheet dynamics and the global carbon cycle, *Paleoceanography, 19*, PA4015, doi:10.1029/2004PA001039.

Lhomme, N., G. K. C. Clarke, and C. Ritz (2005), Global budget of water isotopes inferred from polar ice sheets, Geophys. Res. Lett., 32, L20502, doi:10.1029/2005GL023774.

Liebrand, D., L. J. Lourens, D. A. Hodell, B. De Boer, R. S. W. Van de Wal, and H. Pälike (2011), Antarctic ice sheet and oceanographic response to eccentricity forcing during the early Miocene, *Climate of the Past*, *7*, 869-880.

Liebrand, D (2015). Astronomical forcing during the Oligo-Miocene. (Unpublished doctoral thesis). National Oceanography Centre, Southampton

Liebrand, D., H. M. Beddow, L. J. Lourens, H. Pälike, I. Raffi, S. M. Bohaty, F. J. Hilgen, Mischa J. M. Saes., P.A. Wilson, A. E. van Dijk, D. A. Hodell, D. Kroon., C. E. Huck and S. J. Batenburg, *submitted,* Cyclostratigraphy and eccentricity tuning of the early Oligocene through early Miocene (30.1-17.1 Ma): Cibicides mundulus stable oxygen and carbon isotope records from Walvis Ridge Site 1264.

Lisiecki, L. E. and P. A. Lisiecki (2002), Application of dynamic programming to the correlation of paleoclimate records, Paleoceanography, 17(4), 1049, doi:10.1029/2001PA000733.

Lisiecki, L.E., and M. E. Raymo (2005), A Pliocene-Pleistocene stack of 57 globally distributed benthic $\delta^{18}O$ records. *Paleoceanography* 20.http://dx.doi.org/10.1029/2004PA001071

Littler, K., U. Röhl, T. Westerhold, and J.C. Zachos (2014). A high-resolution benthic stable-isotope record for the South Atlantic: Implications for orbital-scale changes in Late Paleocene-Early Eocene climate and carbon cycling. *Earth and Planetary Science Letters*, *401*, 18-30.

Livermore, R., A. Nankivell, G. Eagles, and P. Morris (2005), Paleogene opening of Drake Passage, *Earth Planet. Sci. Lett.,* 236, 459-470, doi:10.1016/j.epsl.2005.03.027.

Lonsdale, P., (2005), Creation of the Cocos and Nazca plates by fission of the Farallon plate: *Tectonophysics*, v. 404, p. 237-264, doi: 10.1016/j.tecto.2005.05.011.

Lourens, L., Hilgen, F., Shackleton, N.J., Laskar, J. and Wilson, D., 2004.'Chapter 21:The Neogene Period'. In: Gradstein, F., Ogg, J. and Smith,A., (eds).,A Geologic Time Scale 2004, Cambridge University Press, Cambridge, pp. 409-440.

Lourens, L. J., A. Sluijs, D. Kroon, J. C. Zachos, E. Tomas, U. Röhl, J. Bowles, and I. Raffi (2005), Astronomical pacing of late Paleocene to early Eocene global warming events, *Nature*, 435, 1083-1087, doi:10.1038/nature03814.

Lyle, M., P. A. Wilson, T. R. Janecek et al. (2002), Proc. ODP, Init. Repts.,199: College Station, TX (Ocean Drilling Program). doi:10.2973/odp.proc.ir.199.2002

Lyle, M., J. Barron, T. J. Bralower, M. Huber, A. Olivarez Lyle, A. C. Ravelo, D. K. Rea, and P. A. Wilson (2008), Pacific Ocean and Cenozoic evolution of climate, *Rev. Geophys., 46*, RG2002, doi:10.1029/2005RG000190.

Lyle, M., H. Pälike, H. Nishi, I. Raffi, K. Gamage, A. Klaus, and the IODP Expeditions 320/321 Science Party (2010), The Pacific Equatorial Age Transect, IODP Expeditions 320 and 321: building a 50-million-year-long environmental record of the equatorial Pacific Ocean. *Scientific Drilling 9*:4-15. doi:10.2204/iodp.sd.9.01.

Ma, W. T., J. Tian, Q. Y. Li, and P. X. Wang (2011), Simulation of long eccentricity (400-kyr) cycle in ocean carbon reservoir during Miocene climate optimum: Weathering and nutrient response to orbital change, *Geophys. Res. Lett*., 38, L10701, doi:10.1029/2011GL047680.

Macdonald, R.W., D. W. Paton, E.C. Carmack, and A. Omstedt (1995), The freshwater budget and under-ice spreading of Mackenzie River water in the Canadian Beaufort Sea based on salinity and $^{18}O/^{16}O$ measurements in water and ice. *Journal of Geophysical Research* 100 (C1), 895-919.

Maslin, M.A., X.S. Li, M-F Loutre and A. Berger (1998), The contribution of orbital forcing to the progressive intensification of Northern Hemisphere glaciation. *Quat. Sci. Rev*. 17, 411-426.http://dx.doi.org/10.1016/S0277-3791(97)00047-4.

Mawbey, E. M., and C. H. Lear (2013), Carbon cycle feedbacks during the Oligocene-Miocene transient glaciation. *Geology*, doi:10.1130/G34422.1.

McConnaughey, T., (1989a), 13C and 18O isotopic disequilibrium in biological carbonates: I. Patterns. Geochim. Cosmochim. Acta 53, 151-162.

McConnaughey, T., (1989b), 13C and 18O isotopic disequilibrium in biological carbonates: II. Invitro simulation of kinetic isotope effects. Geochimica et Cosmochimica Acta, 53: 163- 171.

McConnaughey, T.A., J. Burdett, J.F. Whelan, C.K. Paull (1997), Carbon isotopes in
biological carbonates: Respiration and photosynthesis. Geochim. Cosmochim. Acta 61, 611-622.

McKay, D. I. A., T. Tyrrell, P. A Wilson and G. L. Foster (2014), Estimating the impact of the cryptic degassing of Large Igneous Provinces: A mid-Miocene case-study. *Earth and Planetary Science Letters*, *403*, 254-262.

Milankovitch, M. (1941), *Canon of Insolation and the Ice-Age Problem*, 1st ed., Zavod za udžbenike i nastavna sredstva & Muzej nauke i tehnike Srpske akademije nauka i umetnosti, Beograd.

Miller, K. G., R. G. Fairbanks, and G. S. Mountain (1987), Tertiary oxygen isotope synthesis, sea level history, and continental margin erosion, *Paleoceanography*, 2, 1-19, doi:10.1029/PA002i001p00001.

Miller, K. G., J. D. Wright, and A. N. Brower (1989), Oligocene to Miocene stable isotope stratigraphy and planktonic foraminifer biostratigraphy of the Sierra Leone Rise (DSDP Site 366 and ODP Site 667), *Proceedings of the Ocean Drilling Program, Scientific Results.*, *108*, 279-294.

Miller, K. G., J. D. Wright, and R. G. Fairbanks (1991), Unlocking the Ice House: Oligocene- Miocene Oxygen Isotopes, Eustacy and Margin Erosion, *Journal of Geophysical Research*, *96*(B4), 6829-6848.

Miller, K. G., et al. (1996), Drilling and dating New Jersey Oligocene-Miocene sequences: Ice volume, global sea level, and Exxon records, *Science*, 271, 1092-1095, doi:10.1126/science. 271.5252.1092.

Molnar, P. (2008), Closing of the Central American Seaway and the Ice Age: A critical review. *Paleoceanography*, *23*(2).

Moore, T.C., Jr., B. S. Wade, T. Westerhold, A.M. Erhardt, H. K. Coxall, J. Baldauf and M. Wagner (2014), Equatorial Pacific productivity changes near the Eocene-Oligocene boundary. *Paleoceanography*, 29, 825-844. doi:10.1002/2014PA002656.

Moran, K., J. Backman, H. Brinkhuis, S.C. Clemens, T. Cronin, G.R Dickens et al. (2006), The cenozoic palaeoenvironment of the arctic ocean. *Nature*, *441*(7093), 601-605.

Montes, C., A. Cardona, C. Jaramillo, A. Pardo, J.C Silva, V. Valencia, C. Ayala, L.C. Perez-Angel, L.A. Rodrıguez-Parra, V. Ramirez and H. Nino (2015), Middle Miocene closure of the Central American Seaway. *Science*, 22, 6-228.

Mourik, A. A., H. A. Abels, F. J. Hilgen, A. Di Stefano, and J. W. Zachariasse (2011), Improved astronomical age constraints for the middle Miocene climate transition based on high-resolution stable isotope records from the central Mediterranean Maltese Islands. *Paleoceanography*, *26*(1).

Mudelsee, M., and M. E. Raymo (2005), Slow dynamics of the Northern Hemisphere glaciation. *Paleoceanography*, *20*(4).

Mudelsee, M., T. Bickert, C. H. Lear, and G. Lohmann (2014), Cenozoic climate changes: A review based on time series analysis of marine benthic $\delta^{18}O$ records, *Rev. Geophys., 52,* doi:10.1002/2013RG000440.

Pagani, M., J. C. Zachos, K. H. Freeman, B. Tipple, and S. Bohaty (2005), Marked decline in atmospheric carbon dioxide concentrations during the Paleogene, *Science*, 309, 600-603, doi:10.1126/science.1110063.

Pälike, H. (2005), Orbital variation (including Milankovitch cycles). *Encyclopedia of Geology*, *1*, 410-421.

Pälike, H., J. Frazier, and J. C. Zachos (2006a), Extended orbitally forced palaeoclimatic records from the equatorial Atlantic Ceara Rise, *Quaternary Science Reviews*, *25*(23-24), 3138- 3149.

Pälike, H., R. D. Norris, J. O. Herrle, P. A. Wilson, H. K. Coxall, C. H. Lear, N. J. Shackleton, A. K. Tripati, and B. S. Wade (2006b), The Heartbeat of the Oligocene Climate System, *Science*, *314*, 1894-1898.

Pälike, H., M. W. Lyle, H. Nishi, I. Raffi, K. Gamage, A. Klaus and the Expedition 320/321 Scientists (2010), *Proceedings of the Integrated Ocean Drilling Program*, Volume 320/321. Tokyo (Integrated Ocean Drilling Program Management International, Inc.)

Pälike, H., M. W. Lyle, H. Nishi, I. Raffi, A. Ridgewell, K. Gamage, et al (2012), A Cenozoic record of the equatorial Pacific carbonate compensation depth, *Nature*, *488*(7413), 609-614.

Paillard, D., L. Labeyrie, and P. Yiou (1996), Macintosh program performs time-series analysis, *Eos Trans. AGU*, *77*, 379, doi:10.1029/96EO00259.

Paul, H. P., J. C. Zachos, B. P. Flower, and A. Tripati (2000), Orbitally induced climate and geochemical variability across the Oligocene/Miocene boundary, *Paleoceanography*, 15, 471-485.

Pearson, P. N., and W. P. Chaisson (1997). Late Paleocene to middle Miocene planktonic foraminifer biostratigraphy of the Ceara Rise. In: Shackleton, N.J., Curry, W.B., Richter, C., Bralower, T.J. (Eds.), *Proceedings of the Ocean Drilling Program, Scientific Results*, 154, pp. 33-68.

Pearson, P. N., N. J. Shackleton, G. P. Weedon and M. A. Hall (1997), Multi- species planktonic foraminifer stable isotope stratigraphy through Oligocene/Miocene boundary climatic cycles, Site 926, *in* Shackleton, N.J., et al., eds., *Proceedings of the Ocean Drilling Program, Scientific Results*, Volume 154: College Station, Texas, Ocean Drilling Program, p. 441-449.

Pearson, P. N., and M. R. Palmer (2000), Atmospheric carbon dioxide concentrations over the past 60 million years, *Nature*, 406, 695-699, doi:10.1038/35021000.

Pearson, P. N., P. W. Ditchfield, J. Singano, K. G. Harcourt-Brown, C. J. Nicholas, R. K. Olsson, N. J. Shackleton and M. A. Hall (2001), Warm tropical sea surface temperatures in the Late Cretaceous and Eocene epochs, *Nature,* 413, 481-487, doi:10.1038/35097000.

Pearson, P. N., G. L. Foster and B. S. Wade (2009), Atmospheric carbon dioxide through the Eocene-Oligocene climate transition. *Nature*, *461*(7267), 1110-1113.

Pearson, P. N., and B. S. Wade (2009), Taxonomy and stable isotope paleoecology of well-preserved planktonic foraminifera from the uppermost Oligocene of Trinidad. *Journal of Foraminiferal Research* 39 (3), 191-217.

Pearson, P.N., (2012), Oxygen isotopes in foraminifera: overview and historical review. In: Ivany, L., Huber, B.T. (Eds.), *Reconstructing Earth's Deep-Time Climate: The State-of-the-art in 2012: Paleontological Society Short Course*, 18, pp. 1-38.

Pekar, S. F., N. Christie-Blick, M. A. Kominz and K.G Miller (2002), Calibration between eustatic estimates from backstripping and oxygen isotopic records for the Oligocene*, Geology,* 30(10), 903-906.

Pekar, S. F., and R. M. DeConto (2006), High-resolution ice-volume estimates for the early Miocene: Evidence for a dynamic ice sheet in Antarctica, *Palaeogeography, Palaeoclimatology, Palaeoecology*, *231*, 101-109.

Pollard, D., and R. M. DeConto (2005), Hysteresis in Cenozoic Antarctic ice-sheet variations, *Global and Planetary Change*, *45*(1-3), 9-21.

Ravelo, A. C., and C. Hillaire-Marcel (2007), Chapter Eighteen the use of oxygen and carbon isotopes of foraminifera in Paleoceanography. *Developments in Marine Geology*, *1*, 735-764.

Raymo, M. E., W. F. Ruddiman, and P. N. Froelich (1988), Influence of late Cenozoic mountain building on ocean geochemical cycles, *Geology*, *16*, 649-653.

Raymo, M. E and W. F. Ruddiman (1992), Tectonic forcing of late Cenozoic climate, *Nature* 359, 117-122.

Ripepe, M., and A. G. Fischer (1991), Stratigraphic rhythms synthesized from orbital variations. In *Sedimentary Modeling* (Vol. 233, pp. 335-344).

Rohling, E., and S. Cooke (1999), Stable oxygen and carbon isotopes in foraminiferal carbonate shells. In: Barum, K., Gupta, S. (Eds.), *Modern foraminifera*. Kluwer Academic.

Rudnicki, M. D., P. A. Wilson, and W. T. Anderson (2001), Numerical models of diagenesis, sediment properties, and pore fluid chemistry on a paleoceanographic transect: Blake Nose, Ocean Drilling Program Leg 171B, *Paleoceanography,* 16, 563-575, doi:10.1029/2000PA000551.

Scher, H. D., and E. E. Martin (2006), Timing and Climatic Consequences of the Opening of Drake Passage, *Science*, *312*, 428-430.

Schlitzer, R. (2010), Ocean Data View 4, version 4.3.6, http://odv.awi.de, edited.

Schmiedl, G., M. Pfeilsticker, C. Hemleben, and A. Mackensen (2004), Environmental and biological effects on the stable isotope composition of recent deep-sea benthic foraminifera from the western Mediterranean Sea. *Marine Micropaleontology*, *51*(1), 129-152, doi:10.1016/j.marmicro.2003.10.001

Schmiedl, G., and A. Mackensen (2006), Multispecies stable isotopes of benthic foraminifers reveal past changes of organic matter decomposition and deepwater oxygenation in the Arabian Sea. *Paleoceanography*, *21*(4).

Schlanger, S. O. and R. G. Douglas (1974), The pelagic ooze-chalk-limestone transition and its implication for marine stratigraphy, in Pelagic Sediments: on Land and under the Sea, *Int. Ass. Sedimentol. Spec. Publ., vol. 1*, edited by K. J. Hsü, and H. C. Jenkyns, pp. 117-148, Blackwell Scientific Publications, Oxford, UK.

Schrag, D. P., D. J. DePaolo, and F. M. Richter (1995), Reconstructing past sea surface temperatures: Correcting for diagenesis of bulk marine carbonate, *Geochim. et Cosmochim. Acta* 59, 2265-2278, doi:10.1016/0016-7037(95)00105-9.

Sexton, P. F., P. A. Wilson, and P. N. Pearson (2006), Microstructural and geochemical perspectives on planktonic foraminiferal preservation: "Glassy" versus "Frosty", *Geochem. Geophys. Geosyst.,* 7, Q12P19. doi:10.1029/2006GC001291.

Sexton, P. F. and P. A. Wilson (2009), Preservation of benthic foraminifera and reliability of deep-sea temperature records: Importance of sedimentation rates, lithology, and the need to examine test wall structure, *Paleoceanography,* 24, doi:10.1029/2008PA001650.

Shevenell, A.E., J. P. Kennett, and D.W. Lear, (2004), Middle Miocene Southern Ocean cooling and Antarctic cryosphere expansion. *Science*, 305, 1766-1770.

Shevenell, A. E., and J. P. Kennett (2007), Cenozoic Antarctic cryosphere evolution: tales from deep-sea sedimentary records. *Deep Sea Research Part II: Topical Studies in Oceanography*, *54*(21), 2308-2324.

Shevenell, A.E J. P. Kennett, and D.W. Lear (2008), Middle Miocene ice sheet dynamics, deep-sea temperatures, and carbon cycling: A Southern Ocean perspective. *Geochemistry, Geophysics, Geosystems*, 9, 1-14.

Shackleton, N.J., and N.D. Opdyke (1973), Oxygen isotope and paleomagnetic stratigraphy of equatorial Pacific core V28-238: oxygen isotope temperatures and ice volumes on a 10^5 and 10^6 year scale. *Quaternary Research* 3, 39-55.

Shackleton, N. J. (1974), Attainment of isotopic equilibrium between ocean water and the benthonic foraminifera genus Uvigerina: isotopic changes in the ocean during the last glacial.

Shackleton, N. J. and J. P. Kennett (1975), Paleotemperature history of the Cenozoic and the initiation of Antarctic glaciation: oxygen and carbon isotope analyses in DSDP Sites 277, 279, and 281. *Initial reports of the deep sea drilling project*, *29*, 743-755.

Shackleton, N.J., (1977), $\delta^{13}C$ in *Uvigerina*: tropical rainforest history and the equatorial Pacific carbonate dissolution cycles. In: Anderson, N., Malahof, A. (Eds.), *Fate of Fossil Fuel CO_2 in the Oceans*. Plenum, New York, pp. 401-427.

Shackleton, N.J., M. Hall, and A. Boersma (1984), Oxygen and carbon isotope data from Leg 74 foraminifers, *Initial Rep. Deep Sea Drill. Proj. 74*, 599-612.

Shackleton, N. J., S. Crowhurst, T. Hagelberg, N. G. Pisias and D. A. Schneider (1995), 6. A new late Neogene time scale: application to Leg 138 sites. In *Proceedings of the Ocean Drilling Program, Scientific Results* (Vol. 138, pp. 73-101).

Shackleton, N. J., S. J. Crowhurst, G. P. Weedon, and J. Laskar (1999), Astronomical Calibration of Oligocene-Miocene Time, *Philosophical Transactions: Mathematical, Physical and Engineering Sciences*, *357*(1757), 1907-1929.

Shackleton, N.J., M. A. Hall, I. Raffi, L. Tauxe, and J. C. Zachos (2000), Astronomical calibration age for the Oligocene/Miocene boundary. *Geology 28* (5), 447-450.

Sluijs, A., H. Brinkhuis, S. Schouten, S. M. Bohaty, C. M. John, J. C. Zachos, G.-J. Reichart, J. S. Sinninghe Damsté, E. M. Crouch, and G. R. Dickens (2007), Environmental precursors to rapid light carbon injection at the Palaeocene/Eocene boundary. *Nature* 450, 7173: 1218-1221.

Spezzaferri, S., (1994), Planktonic foraminiferal biostratigraphy and taxonomy of the Oligocene and lower Miocene in the oceanic record. An overview. *Palaeontographia Italica* 81, 188.

Spezzaferri, S., M. Kucera, P. N. Pearson, B. S. Wade, S. Rappo, C. R. Poole, R. Morard, and C. Stalder (2015), Fossil and genetic evidence for the polyphyletic nature of the planktonic foraminifera "Globigerinoides", and description of the new genus Trilobatus. *PLoS ONE* 10(5): e0128108. doi:10.1371/journal.pone.0128108

Stap, L., A. J. Sluijs, E. Thomas, and L. J. Lourens (2009). Patterns and magnitude of deep sea carbonate dissolution during Eocene Thermal Maximum 2 and H2, Walvis Ridge, southeastern Atlantic Ocean. *Paleoceanography*, *24*(1).

Stewart, D. R., P. N. Pearson, P. W. Ditchfield and J. M. Singano (2004), Miocene tropical Indian Ocean temperatures: evidence from three exceptionally preserved foraminiferal assemblages from Tanzania. *Journal of African Earth Sciences*, *40*(3), 173-189.

Stewart, J. A., P. A. Wilson, K. M. Edgar, P. Anand and R. H. James (2012), Geochemical assessment of the palaeoecology, ontogeny, morphotypic variability and palaeoceanographic utility of "Dentoglobigerina" venezuelana. *Marine Micropaleontology* 84-8

Takahashi, T., S. C. Sutherland, C. Sweeney, A. Poisson, N. Metzl, B. Tilbrook, N. Bates, R. Wanninkhof, R. A. Feely, C. Sabine, J. Olafsson and Y. Nojiri (2002), Global sea-air CO_2 flux based on climatological surface ocean pCO_2, and seasonal biological and temperature effects, Deep-Sea Res. II, 49(9-10), 1601-1622, doi:10.1016/S0967-0645(02)00003-6.

Thornalley, D. J., H. A. Bauch, G. Gebbie, W. Guo, M. Ziegler, S. M Bernasconi, S. Barker, L. Skinner and J. Yu (2015), A warm and poorly ventilated deep Arctic Mediterranean during the last glacial period. *Science*, *349*(6249), 706-710.

Tian, J., M. Yang, M. W. Lyle, R. Wilkens and J.K Shackford (2013), Obliquity and long eccentricity pacing of the Middle Miocene climate transition. *Geochemistry Geophysics Geosystems*, 14, 1740-1755.

Tian, J., W. Ma, M. W. Lyle and J. K. Shackford, (2014). Synchronous mid-Miocene upper and deep oceanic $\delta^{13}C$ changes in the east equatorial Pacific linked to ocean cooling and ice sheet expansion. *Earth and Planetary Science Letters*, *406*, 72-80.

Toggweiler, J. R., (1999), Variation of atmospheric CO_2 by ventilation of the ocean's deepest water, *Paleoceanography*, 14, 571-588.

Torrence, C., and G. P. Compo (1998), A practical guide to wavelet analysis, *Bull. Am. Meteorol. Soc.*, 79, 61-78.

Uchikawa, J., and R. E. Zeebe (2010), Examining possible effects of seawater pH decline on foraminiferal stable isotopes during the Paleocene-Eocene Thermal Maximum, Paleoceanography, 25, PA2216, doi:10.1029/2009PA001864.

Urey, H. C. (1947), The thermodynamic properties of isotopic substances. *Journal of the Chemical Society of London*, 1947:562-581.

Vandenberghe, N., F. J. Hilgen, and R. P. Speijer (2012), The paleogene period. *The geologic time scale*, *2012*, 855-921.

Vincent, E., and W. H. Berger (1985), Carbon dioxide and polar cooling in the Miocene: The Monterey Hypothesis, in The Carbon Cycle and Atmospheric CO2: Natural Variations Archean to Present, *Geophys. Monogr, American Geophysical Union, Washington, D.C.*, vol. 32, pp. 455-468.

Wade, B. S., and H. Pälike (2004), Oligocene climate dynamics. *Paleoceanography*, *19*(4).

Wade, B. S., W. A. Berggren and R. K. Olsson (2007), The biostratigraphy and paleobiology of Oligocene planktonic foraminifera from the equatorial Pacific Ocean (ODP Site 1218). *Marine Micropaleontology*, 62: 167-179.

Wang, P., W. L. Prell, P. Blum, and et. al. (2000), Initial Reports: Leg 184*Rep.*, College Station, TX.

Wang, P., J. Tian and L. J. Lourens (2010), Obscuring of long eccentricity cyclicity in Pleistocene oceanic carbon isotope records. *Earth and Planetary Science Letters*, *290*(3), 319-330.

Westerhold, T., et al. (2012a), Revised composite depth scales and integration of IODP Sites U1331-U1334 and ODP Sites 1218-1220, in *Proceedings of the Integrated Ocean Drilling Program*, vol. 320/321, edited by H. Pälike et al., Integ. Ocean Drill. Progr. Manage. Int., College Station, Tex.

Westerhold, T., U. Röhl and J. Laskar (2012b), Time scale controversy: Accurate orbital calibration of the early Paleogene. *Geochemistry, Geophysics, Geosystems*, *13*(6).

Westerhold, T., U. Röhl, T. Frederichs, S. M. Bohaty and J. C. Zachos (2015), Astronomical calibration of the geological timescale: closing the middle Eocene gap. *Climate of the Past*, *11*(9), 1181-1195.

Wilson, D. S (1988). Tectonic history of the Juan de Fuca ridge over the last 40 million years. *Journal of Geophysical Research: Solid Earth (1978-2012)*, *93*(B10), 11863-11876.

Wilson, D. S. (1993), Confirmation of the astronomical calibration of the magnetic polarity time scale from rates of sea-floor spreading, *Nature, 364*, 788-790.

Wilson, D. S., and B. P. Luyendyk (2009), West Antarctic paleotopography estimated at the Eocene-Oligocene climate transition, *Geophysical Research Letters*, *36*.

Wilson, D. S., S. S. Jamieson, J. P. Barrett, G. Leitchenkov, K. Gohl, and R. D. Larter (2012). Antarctic topography at the Eocene-Oligocene boundary. *Palaeogeography, Palaeoclimatology, Palaeoecology*, *335*, 24-34.

Woodruff, F., and S. M. Savin (1989), Miocene deepwater oceanography, *Paleoceanography*, *4*(1), 87-140.

Woodruff, F. and S. M. Savin (1991), Mid-Miocene isotope stratigraphy in the deep sea: High resolution correlations, paleoclimatic cycles, and sediment preservation, *Paleoceanography*, 6, 755-806.

Wright, J. D., K. G. Miller, and R. G. Fairbanks (1991), Evolution of modern deep water circulation: Evidence from the late Miocene Southern Ocean, *Paleoceanography*, 6, 275-290.

Zacharisse,W. J. and Sudijuno (2012), New data on the morphology and classification of the Oligocene-Miocene planktonic foraminifer Paragloborotalia siakensis (LeRoy, 1939): *Journal of Foraminiferal Research*, v. 42, p. 156-168.

Zachos, J. C., J. R. Breza and S. W. Wise (1992), Early Oligocene ice-sheet expansion on Antarctica: Stable isotope and sedimentological evidence from Kerguelen Plateau, southern Indian Ocean. *Geology*, *20*(6), 569-573.

Zachos, J. C., B. P. Flower, and H. A. Paul (1997), Orbitally paced climate oscillations across the Oligocene/Miocene boundary, *Nature*, *388*(6642), 567-570.

Zachos, J. C., M. Pagani, L. Sloan, E. Thomas, and K. Billups (2001), Trends, Rhythms, and Aberrations in Global Climate 65 Ma to Present, *Science*, *292*, 686-693.

Zachos, J.C., N. J. Shackleton, J. S. Revenaugh, H. Pälike, and B. P. Flower (2001), Climate response to orbital forcing across the Oligocene-Miocene boundary, *Science* 292, 274-278.

Zachos, J. C., D. Kroon, P. Blum, and et. al. (2004), Initial Reports: Leg 208*Rep. Volume 208*, Ocean Drilling Program.

Zachos, J. C., G. R. Dickens, and R. E. Zeebe (2008), An early Cenozoic perspective on greenhouse warming and carbon-cycle dynamics, *Nature*, *451*(7176), 279-283.

Zeebe, R. E (1999), An explanation of the effect of seawater carbonate concentration on foraminiferal oxygen isotopes. *Geochimica et Cosmochimica Acta*, *63*(13), 2001-2007.

Zeeden, C., F. J. Hilgen, S. K. Hüsing, and L. J. Lourens (2014), The Miocene astronomical time scale 9-12 Ma: new constraints on tidal dissipation and their implications for paleoclimatic investigations. *Paleoceanography*, *29*(4), 296-307.

Zhang, Y. G., M. Pagani, Z. Liu, S. Bohaty, and R. DeConto (2013), A 40-million-year history of atmospheric CO2, *Phil. Trans. R. Soc. A*, *371*

Acknowledgements

This thesis has been a long time in the making, and would not have been possible without the support and help of so many people. I feel incredibly grateful to have so many good memories, and I would like to everyone who made my time here in Utrecht so special.

Firstly, I would like to thank my supervisor Luc, for giving me the opportunity to come to Utrecht and be part of the earth sciences department at the university. I've had so many great experiences during my PhD, and been to some fantastic places, and met so many wonderful people, which would not have been possible if I had not been part of this project. Thank you for all your personal guidance and support over the last five years.

I've collaborated with some truly brilliant people on the chapters in this thesis, and the questions, discussions and advice from all of you really helped me grow and develop as a researcher. A special thanks to Diederik, who encouraged me every step of the way – from the very beginning when applying for the PhD to the very end during the final stages of writing. You guided me through the toughest parts of my PhD and were always ready to answer any questions and offer me help. I'm truly grateful for all your help and support. I'd like to thank Frits for always being enthusiastic and encouraging, and for all his help in understanding astronomical forcing and in creating age models. Thank you to Doug, who was enthusiastic and helpful when contributing the spreading rates. Thank you very much to Appy, who gave really useful insight and advice on my chapters, and who helped collect the material on the PEAT cruise back in 2009. I'd especially like to thank Bridget, who gave me an introduction to planktic foraminfera and was always cheerful and happy to help. I really enjoyed all my visits to Leeds, and to UCL. Thanks to David at UCl, for all his hard work and input on the planktonics.

I'd also like to thank all the enthusiastic students from Utrecht and Leeds, who's hard work during their bachelors and masters projects contributed to the stable isotope records in this thesis. Thank you to Julian, Mischa, Cindy, Anja, and Annelotte in Utrecht and Alex in Leeds.

Without the technical staff there would not be a thesis. So, thank you Arnold, for putting up with many many phone calls about the broken mass spec on your day offs and even on the weekends. Many thanks to Dominika for washing so many samples, and for always being there as a good friend. Thanks also to Natasja, Maxim and Jan.

Being part of the Earth Sciences at Utrecht University has meant working alongside so many great people. Particular thanks go to all my strat/pal colleagues - Antonio, Hemmo, Wilma, Jelle, Ivo, Martin, Tiuri, Maria, Stef, Christian, Joyce, Maria and Frits. I've met so many talented scientists and it's been a pleasure to work and spend time with everyone over the years- Karin, Dan, Dirk, Nathan, Mariette, Karolina, Gert, Gert-Jan, Fatimah, Mathilde, Matthias, Tom, Alwina, Joost, Tjerk, Alejandra, Marie-Louise, Peter, Sandor, Itzel, Linda, Jiawang, Wout, Francesca and so many others!

I'd like to give a special thank you to all my friends and family both here and at home, who make all the time spent on the thesis worthwhile. First and foremost, thank you to my family, Mum Tony, Matthew ,Beth, Claire ,Phil, and Andrew. Without your encouragement and support, I would not be where I am today.

I need to give a special thanks to Vittoria, housemate, officemate, PhD co-conspirator and very good friend. We started on the same day, and spent almost every day together since, so it's only appropriate that we are finishing on the same day. We've been on a rollercoaster together the last five years, shared all the ups and downs. You have always listened and supported me and I wouldn't have wanted to share my PhD journey with any one else. Thank you for being such a good friend over the last five years.

To my paranymphs – Izzy and Fiona. Thank you for being behind me both today, and every day over the last five years. You've both been great friends, always ready to listen and offer support and it's an honour to have you as part of my graduation day.

One of the best experiences of my PhD was the summer school in Urbino, where I made so many friends and great memories. Niels, Rick and Vittoria we stuck together since day one in Italy, and we have been great friends ever since. Thanks for all the fun dinners , the tequila, and the science we did on beermats! Lynsey – thanks for all the times you put me up in Leeds, and all the tea and sympathy. Anna Joy, Wendy, Tom, Rosanna, Kendra, Julien and too many other names to mention!

I've been in Utrecht for five years now, and it's been wonderful, mostly because of the friends I have made. I'd like to thanks to all the people who made my time in Utrecht so special – Janneke, Alice, Noel, Blaise, Kevin, Fiona, Tina, Carol-Ann, Maria, Stef, Pacella, Aleksandra, Nathan, Christian, Meri, Clement. To all my housemates over the years – Noel, Fiona, Alex, Sebas, Angela, Ricardo and Gabi - you guys have been absolute stars. I have to thank also all of my friends outside of Utrecht who are now spread all over the world, from my hometown in the UK to Australia. Thank you to Vanessa, Fiona, Dave, Gareth, John, Roisin, Lucy, Roanna, Josh, Vicki, Katy, Sam, Katie, Megan, Cristina, Claire. Even though we are seperated by seas and oceans, we can always just pick up where we left off, as if we have never been apart!

The final thank you is for Alistair, who is my favourite person in the whole world. Thank you for always being so positive and encouraging, and having so much faith in me. Thanks for all the good advice, the sense of perspective, and, most importantly, for making me laugh and keeping it fun. I love you and I'm truly grateful for your support. Now that the PhD is done, I can't wait for all the fun and adventures we've got coming next!

Samenvatting in het Nederlands

Aanleiding en doel

Vanwege de door de mens veroorzaakte toename van het koolstofdioxidegehalte in de atmosfeer is het van groot belang om de mogelijke invloed hiervan op klimaatsverandering te voorspellen. De mondiale klimaatsystemen zijn complex en worden beïnvloed door een veelvoud aan factoren. Voorspellingen over klimaatsveranderingen zijn dan ook lastig te maken. Door onderzoek te doen naar klimaatsveranderingen in het verleden kunnen grenzen worden gesteld aan scenario's voor de toekomst.

Om inzicht te krijgen in de veranderingen in de klimaatsystemen in de geologische geschiedenis van de aarde maken wij gebruik van zogenaamde proxies. De meest gebruikte proxies zijn stabiele zuurstof- en koolstofisotopen. Die kunnen eveneens worden gebruikt om toekomstige klimaatscenario's te schetsen.

Het doel van dit onderzoek is het in beeld brengen van de klimaatsveranderingen door middel van het reconstrueren van de temperatuurontwikkeling van het oceaanwater en de veranderingen in het volume van de verschillende ijskappen en in de koolstofkringloop. Daarbij richten wij ons op de geologische periodes van het Oligoceen en Mioceen, tussen de 24 en 13 miljoen jaren geleden. In de eerste plaats is daar de extreem koude periode van de Oligoceen-Mioceen transitie (OMT, 23 miljoen jaar geleden). In de tweede plaats wordt deze transitie miljoenen jaren later gevolgd door een warme periode, genaamd het Mioceen Klimaatoptimum, die twee miljoen jaar duurde (MCO, 17-15 miljoen jaar geleden). Tenslotte wordt dit optimum op zijn beurt gevolgd wordt door een overgang naar een zeer koude periode, de Midden-Miocene Klimaattransitie (MMCT, 14 miljoen jaar geleden).

Stabiele isotopen als klimaatproxies

Voor de reconstructie van de klimaatparameters in deze drie kritieke tijdsintervallen gebruiken we zuurstof- en koolstofisotopen zoals we die aantreffen in de kalkskeletjes (calciumcarbonaat) van zeer kleine fossielen afkomstig uit sedimentkernen van de diepzee. Met behulp van de zuurstofisotopen kunnen de temperatuur van het zeewater en het volume van de ijskapppen worden gereconstrueerd. De koolstofisotopen worden met name gebruikt om de ontwikkelingen in de koolstofkringloop in de oceaan vast te stellen.

Voor de nauwkeurige datering van de stabiele zuurstof-en koolstofisotopen meetreeksen wordt gebruik gemaakt van de zogenaamde 'astronomische tuning methode'. Deze methode is gebaseerd op de variaties in de baan van de aarde om de zon, veroorzaakt door de zwaartekracht van de zon, maan en planeten in ons zonnestelsel. De schommelingen in de baan van de aarde en de stand van de aardas beïnvloeden de lengte van de seizoenen en zorgen voor variatie in de instraling van de zon die we op aarde ontvangen. Beide resulteren in een voorspelbaar patroon in de veranderingen van het klimaat. Dit patroon is vastgelegd in sedimentaire gesteenten die als het ware een klimaatarchief vormen. Door dit archief te koppelen aan reeds eerder opgestelde modellen voor de variatie in de baan van de aarde en de stand van de aardas voor de afgelopen 50 miljoen jaar, kunnen we de meetreeksen van onze stabiele isotopen dateren.

Onderzoeksmateriaal

In dit onderzoek analyseren we twee boorkernen van diepzeesediment. De boorkern van site U1334 komt uit het oostelijke equatoriale deel van de Grote Oceaan. De tweede kern, site 1264, komt uit het zuidoostelijk deel van de Atlantische Oceaan. Van U1334 genereren we meetreeksen

van zuurstof- en koolstofisotopen aan de hand van benthonische foraminiferen (kalkdiertjes) die op de bodem van de oceaan leefden. De planktonische foraminiferen, die in het oppervlakte water leefden, leveren de gegevens voor vaststelling van de thermocline in de vroegere oceanen. De zuurstof-en koolstofisotopen reeksen van U1334 beslaan het late Oligoceen, de OMT en het vroege Mioceen (24.2 tot 21.9 miljoen jaar geleden). Van site 1264 genereren we meetreeksen van benthonische foraminiferen van 18.9 tot 13.2 miljoen jaar geleden. Hierbinnen vallen de MMCT en MCO. Aan de hand van de zuurstof-en koolstof isotopen samenstelling van deze foraminiferen kunnen we de veranderingen in temperatuur en ijskapvolume bepalen.

Resultaten

Het verband tussen de zuurstof- en koolstofisotopen enerzijds en het ijsvolume, temperatuur van het oceaanwater en de mariene koolstofkringloop anderzijds tijdens het Oligoceen en Mioceen is duidelijk zichtbaar in de meetreeksen. Het OMT en MMCT worden gekenmerkt door de toename in de ratio van de zuurstofisotopen in zowel kern U1334 als 1264. Dit duidt op een grootschalige uitbreiding van de ijskap op Antarctica en een afname van de temperatuur in de oceaan. Door de daling van de temperatuur en groei van de ijskap is de mariene koolstofcyclus veranderd. Gedurende het MCO vertonen de zuurstof- en koolstofisotopen (van site 1264) een verandering naar negatieve waarden wat duidt op hogere temperaturen in de oceaan en een afname van het volume van de Antarctische ijskap.

In de meetreeksen van beide locaties is er bovendien een duidelijke verandering zichtbaar in de bijdrage van de astronomische cycli met periodes van 100.000 en 405.000 jaar. De dominante astronomische cyclus in de koolstofisotopenreeks van beide sites is de cyclus met een periode van 405.000 jaar. Daarentegen treffen we een zeer sterke 100.000 jaar cyclus aan in de zuurstofisotopenreeks van het vroege Mioceen (direct na de OMT) en tijdens de MCO en MMCT.

De isotopenreeksen van beide sites duiden dan ook op een wereldwijd zeer instabiel klimaat. Het ritme van de veranderingen wordt bepaald door de astronomische cycli van 405.000 en 100.000 kyr. Deze bevindingen worden ondersteund door de uitkomsten van vergelijkbaar onderzoek naar de klimaatsveranderingen in het Oligoceen en Mioceen.

Curriculum Vitae

Helen Beddow-was born on 27th January 1986 in London, UK. She completed her secondary school education at Cromwell Community College, and took her A-levels at Neale Wade Sixth Form. In 2004, she began her undergraduate degree at the University of St Andrews in Scotland, graduating with an MA (Hons) in Geography in 2008. Helen worked as a technician on paleoclimate projects at Newcastle University and the British Antarctic Survey in Cambridge, before beginning her masters degree at the National Oceanography Centre, Southampton in 2009. She graduated with an MSc in Oceanography in 2010. In 2011, Helen moved to the Netherlands to begin a PhD in paleoclimatology with Lucas Lourens at Utrecht University.